SIRIUS-T: A Study of a Symmetrically Illuminated Inertial Confinement Fusion Tritium Production Facility Final Report

B. Badger, I.N. Sviatoslavsky, D. Bruggink, R.L. Engelstad, G.L. Kulcinski, E.M. Larsen, E.G. Lovell, J.J. MacFarlane, E.A. Mogahed, G.A. Moses, A. Moucha, R.R. Peterson, J. Powers, M.E. Sawan, L.J. Wittenberg

December 1990

UWFDM-850

FUSION TECHNOLOGY INSTITUTE

UNIVERSITY OF WISCONSIN

MADISON WISCONSIN

SIRIUS-T: A Study of a Symmetrically Illuminated Inertial Confinement Fusion Tritium Production Facility Final Report

B. Badger, I.N. Sviatoslavsky, D. Bruggink, R.L. Engelstad, G.L. Kulcinski, E.M. Larsen, E.G. Lovell, J.J. MacFarlane, E.A. Mogahed, G.A. Moses, A. Moucha, R.R. Peterson, J. Powers, M.E. Sawan, L.J. Wittenberg

Fusion Technology Institute
University of Wisconsin
1500 Engineering Drive
Madison, WI 53706

http://fti.neep.wisc.edu

December 1990

UWFDM-850

SIRIUS-T

A Study of a Symmetrically Illuminated Inertial Confinement Fusion Tritium Production Facility

Final Report

B. Badger, I.N. Sviatoslavsky, D. Bruggink, R.L. Engelstad, G.L. Kulcinski,
E.M. Larsen, E.G. Lovell, J.J. MacFarlane, E.A. Mogahed, G.A. Moses, A. Moucha,
R.R. Peterson, J. Powers, M.E. Sawan, L.J. Wittenberg

Fusion Technology Institute
University of Wisconsin-Madison
1500 Johnson Drive
Madison, WI 53706

December 1990

UWFDM-850

TABLE OF CONTENTS

13. COMPARISON OF TRITIUM PRODUCTION REACTORS

Preface

There are two main motivations behind the present study. First, to demonstrate the usefulness of symmetric illumination in driving targets for thermonuclear energy release, a series of reactors called SIRIUS has been postulated. These range from SIRIUS-M, for materials testing, to SIRIUS-C for power production. Secondly, the need for tritium in the United States defense program has become critical. New and innovative techniques for producing tritium have been proposed and because of the unique properties of the DT reaction, it is important to examine the implications of a DT-ICF production facility operating after the year 2000.

The study was conducted over a three year (1988-90) period by the University of Wisconsin Fusion Technology Institute. The project was funded by the Inertial Confinement Division of the Department of Energy under Contract DOE/DE-AS03-88DP10754-1. We wish to acknowledge helpful discussions and assistance from scientists at the Laboratory for Laser Energetics at the University of Rochester. The authors would also like to thank Dr. David Bixler of the U.S. Department of Energy for his help and guidance in this study.

We hope that the reader recognizes that projecting the performance of materials and certain technologies by more than 10-20 years is difficult at best. However, it has often been noted that scientists are notorious for overestimating what can be done in 5 years and underestimating what can be done in 20 years. We fully expect that we may have been too conservative in this study and events may prove to be more favorable than we predict now. Even without that caveat, it is clear from this study that SIRIUS-T could be an extremely attractive option for production of tritium in the future and the ICF technology embodied in this design deserves further investigation.

1. EXECUTIVE SUMMARY

1.1. Introduction

The aging U.S. tritium production reactors are slowly being phased out and the U.S. Department of Energy has initiated a "New Production Reactors Program" which will provide for the design, construction and operation of new facilities for the production of tritium and other special nuclear materials. Preliminary requirements are currently being prepared, leading to construction and operation by the year 2000. Unfortunately, inertial confinement fusion (ICF) cannot possibly be ready to perform such a task on this short time scale. However, it is instructive to see how well it can do in producing tritium when ICF has been demonstrated and a comparison with the other proposed production schemes is conducted here. SIRIUS-T is a conceptual design study of a tritium production facility utilizing direct drive symmetrically illuminated inertial confinement fusion. The "T" designation distinguishes it from SIRIUS-M, a materials facility, and SIRIUS-C, a commercial power plant.

As in any other fusion related design study, a certain amount of technical extrapolation has been made in SIRIUS-T. It should be said early on, however, that in areas of uncertainty, we have always taken the conservative approach. This is evident in our choice of target gain, number of beams selected for symmetric illumination and elsewhere throughout the study. In performing the economic analysis we have also attempted to err on the conservative side. This too is evident in our costing of the driver and the reactor chamber. For these reasons, we feel that this study projects enough confidence as to make it worthy of comparison with the other proposed production systems. Such a comparison is made in Chapter 13 of this report.

1.2. General Description

The SIRIUS-T reactor utilizes a 2 MJ KrF laser to symmetrically illuminate a single shell direct drive target with 92 beams uniformly distributed around a spherical chamber. A conservative target gain of 50 is used at a 10 Hz repetition rate, giving 1000 MW of fusion power. The effective blanket energy multiplication is 1.41, providing a total thermal power of 1410 MW, which, when converted at a 36% power cycle efficiency, yields 507 MWe. This power makes the reactor self

sufficient with respect to electricity, even if the laser driver efficiency is only 5%. A helium gas intermediate loop is used between the lithium and the steam cycle to prevent excessive permeation of T_2 into the steam.

The gain of 50 with 2 MJ of KrF laser energy chosen for this study is shown in Fig. 1.1 in comparison with the latest gain estimates.[1] It is about a factor of two below the optimistic gain curve and very near to the lower conservative gain curve. The SIRIUS-T target performance corresponds to designs that are optimized to minimize Rayleigh-Taylor instabilities on capsule performance. This is accomplished by imploding the target along a higher isentrope that might otherwise be used, thus trading some implosion efficiency for improved stability. This conservative design has less restrictive requirements on drive and capsule uniformity than the most optimistic designs.

The critical issue in direct drive target performance is illumination uniformity and subsequent uniformity of the ablatively driven implosion. These aspects depend on several parameters, the most important being the number of laser beams and the roundness and uniformity of the spherical shell target. This study has not addressed target fabrication issues. However, the large number of beams, 92, although complicating the design, provides the possibility of creating a very uniform irradiation of the target. It also provides protection against power imbalances in the beams and some tolerance to beam pointing errors, thus relaxing the laser design constraints and allowing a more conservative design.

The spherical chamber is supported on a pedestal in the center of a spherical containment building 22 m in radius as shown in Fig. 1.2. The 92 beams originate from a single KrF laser. Two groups of 46 beams, which are routed such that they approach the containment building from opposite sides, are positioned in a horizontal configuration. Mirrors placed outside the building then direct each beam radially through the spherical wall of the containment building. At this point the beams pass through windows which constitute the vacuum barrier between the containment building and the laser hall. After passing through the window the beams are incident onto turning

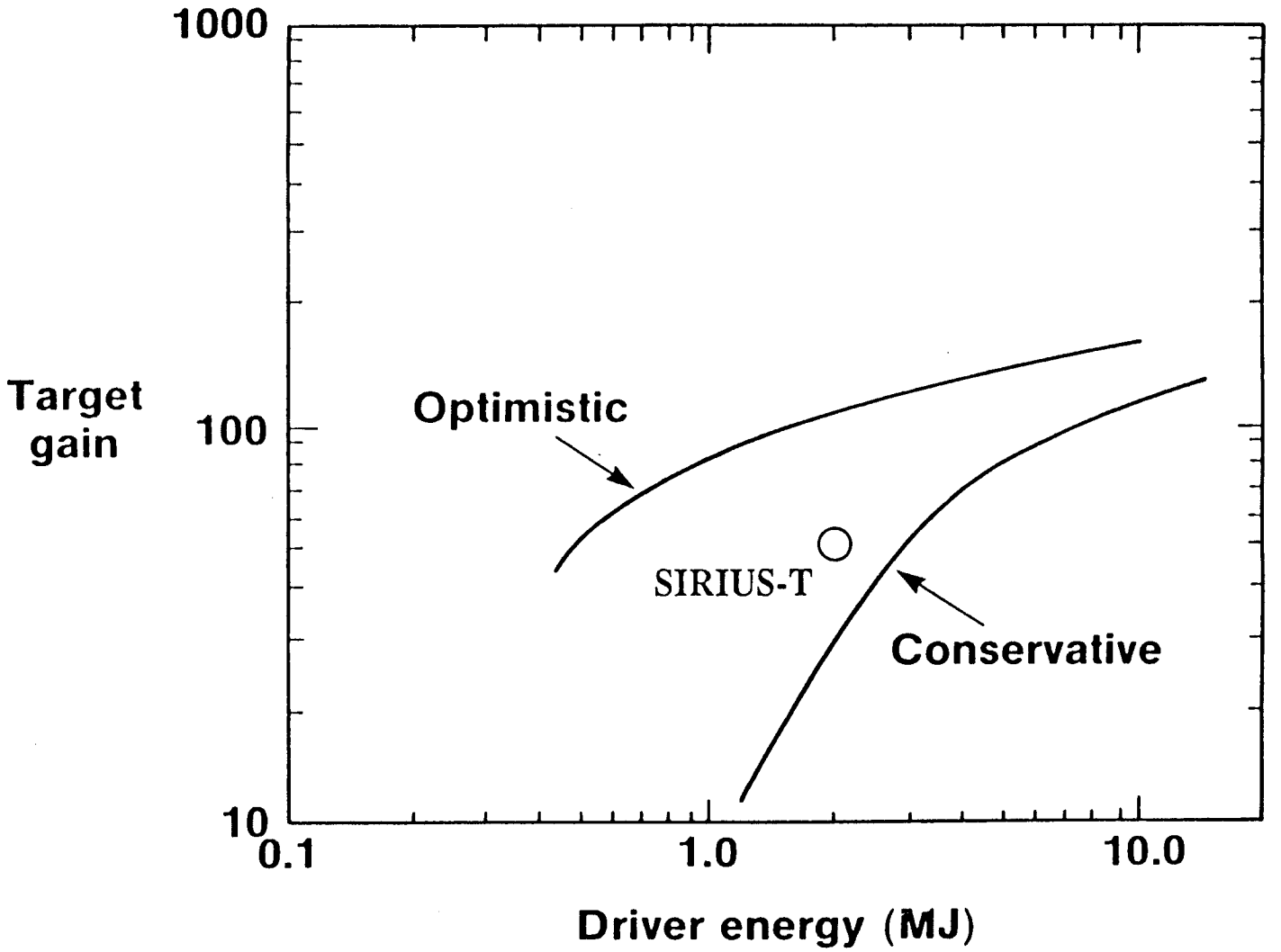

Fig. 1.1. Target gain as a function of driver energy (symmetric illumination).

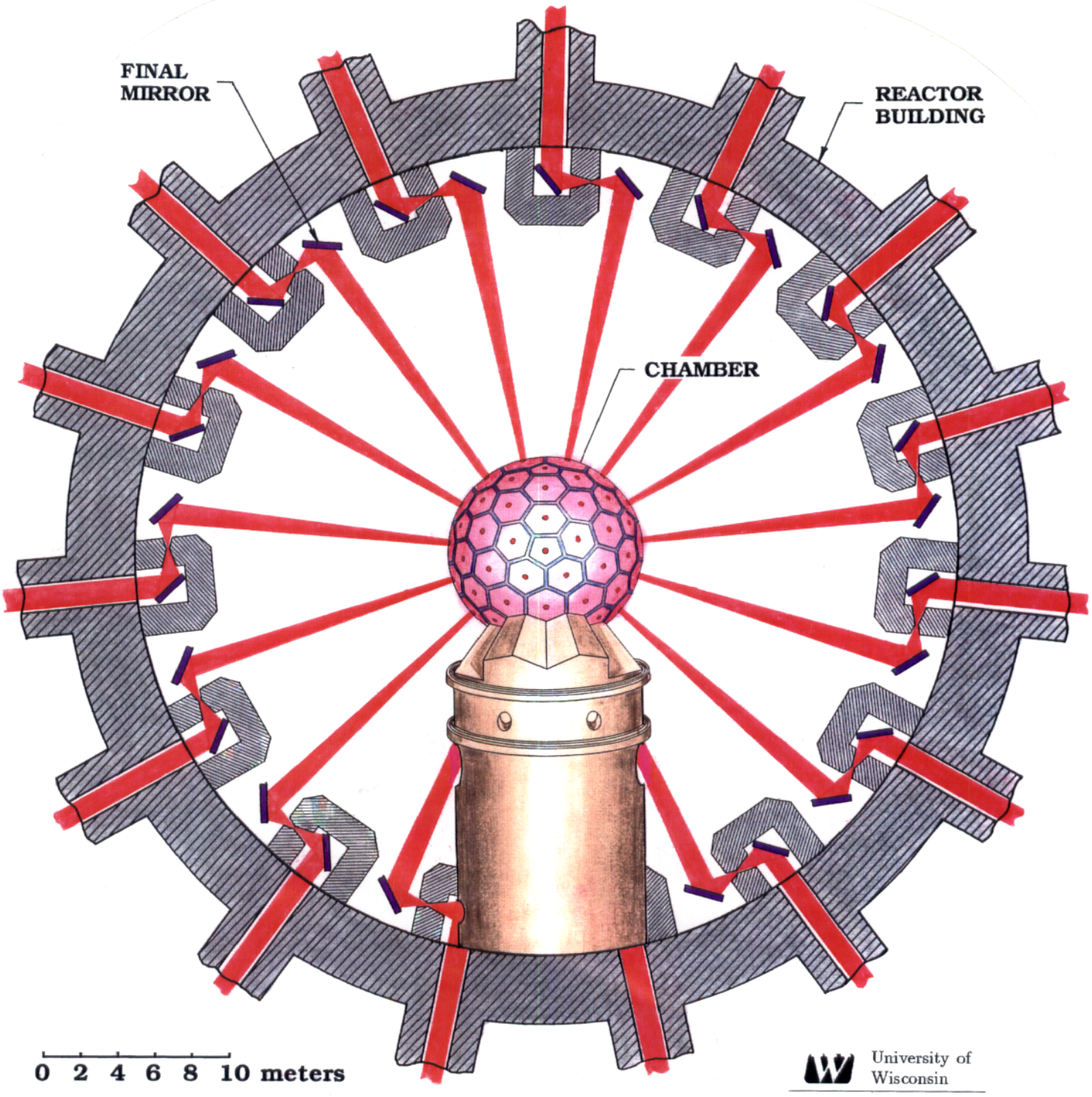

Fig. 1.2. Overall view of the SIRIUS-T reactor.

and focusing mirrors which focus them through a 5 cm diameter aperture. These next to last mirrors are housed in shielded enclosures and are adequately protected to be reactor lifetime components. The beam crossover points through the 5 cm diameter aperture are provided to minimize neutron streaming to the next to last mirrors and out of the containment building. Once the beams pass through the crossover point they expand to their original size and are incident onto the final focusing mirrors. The final focusing mirrors, which are mounted on the wall of the containment building at a radius of 20 m from the center of the chamber, then focus the beams through ports in the chamber to converge onto the target in the center of the chamber. Between the final focusing mirrors and the chamber, the beams travel through vacuum without the benefit of beam tubes. The implications of such a transport mechanism is that the chamber and containment building share the same vacuum space and the unburned tritium in the targets is exhausted into the building from which it is pumped out. The main advantage of this scheme is that the space between the chamber and the containment building wall is not cluttered with beam tubes making maintenance of the reactor and the final focusing mirrors much easier.

The spherical reactor chamber has a radius of 4 m to the first wall and has a blanket thickness of 97 cm. It has 92 blanket modules, each with a beam tube in the center. Division of the spherical surface is based on the Platonic icosahedron which has twenty equilateral triangles joined together along common sides. The triangles form the background against which the spherical surface is further subdivided into pentagonal and hexagonal shapes. Each pentagonal shape is located at the confluence of the equilateral triangles' vertices of which there are twelve locations. For this configuration, there are 12 pentagonal and 80 hexagonal modules.

The structure used for the reactor is the vanadium alloy V-3Ti-1Si and the breeding/cooling material is liquid lithium 90% enriched in ^{6}Li. This combination was one of the primary recommendations of BCSS[2] (Blanket Comparison and Selection Study). Vanadium alloys have a low neutron absorption cross section making them ideal for tritium breeding, and they are acceptable from a waste disposal rating standpoint. The V-3Ti-1Si alloy has displayed the best radiation damage characteristics of all the vanadium alloys tested thus far.

The first wall consists of carbon-carbon composite tiles bonded to a backing of liquid lithium cooled vanadium alloy. The spherical void in the chamber is filled with xenon gas at a density of 3.5×10^{16} atoms/cm^3 (1.0 torr at STP). The x-rays and ions released by the microexplosion are absorbed in the xenon gas and their energy is then reradiated to the carbon-carbon composite tiles over a time that is comparable to the thermal diffusion time in the tiles. The active cooling of the tiles keeps the maximum temperature at the front carbon surface within acceptable limits while recovering the energy of the target x-rays and ions.

We have used the CONRAD[3] code to simulate the deposition of target x-rays and ions in the xenon and the subsequent reradiation. It has been found that 180 photon energy groups must be used in the radiation diffusion calculation to accurately represent the pulse shape of reradiated energy. We then used the WALL code to calculate the thermal diffusion of energy through the 1 cm thick carbon composite. To obtain the possible range of operating conditions, three types of graphites were analyzed; two unirradiated and one irradiated with fission neutrons to the equivalent of 10 dpa (displacements per atom). Because of the reduced thermal conductivity in irradiated graphite, the maximum surface temperature reached was 1900 K, while in the unirradiated case it was <1500 K. All three materials displayed thermal stresses which in the worst case were a factor of 1.9 below their respective compressive strengths.

The 92 breeding blanket modules are held together in the reactor chamber by means of a homogeneous structural frame made of V-3Ti-1Si. This structural frame, shown in Fig. 1.3, consists of a network of pentagonal and hexagonal tapered cells into which the modules are inserted from the outside. The inner radius of the frame is 4.3 m, i.e., the inner edge is 30 cm within the blanket. This is done to make the frame a lifetime component, and to allow the tiles to close the spherical surface at the first wall without interference from the frame.

Figure 1.4 is a cross-section of a typical hexagonal blanket module. It is shown nested between two webs of the structural frame. Two first wall tiles are shown flush with each other at the 4 m inner chamber radius. The tile is shown attached to two concentric tubes, the outer of

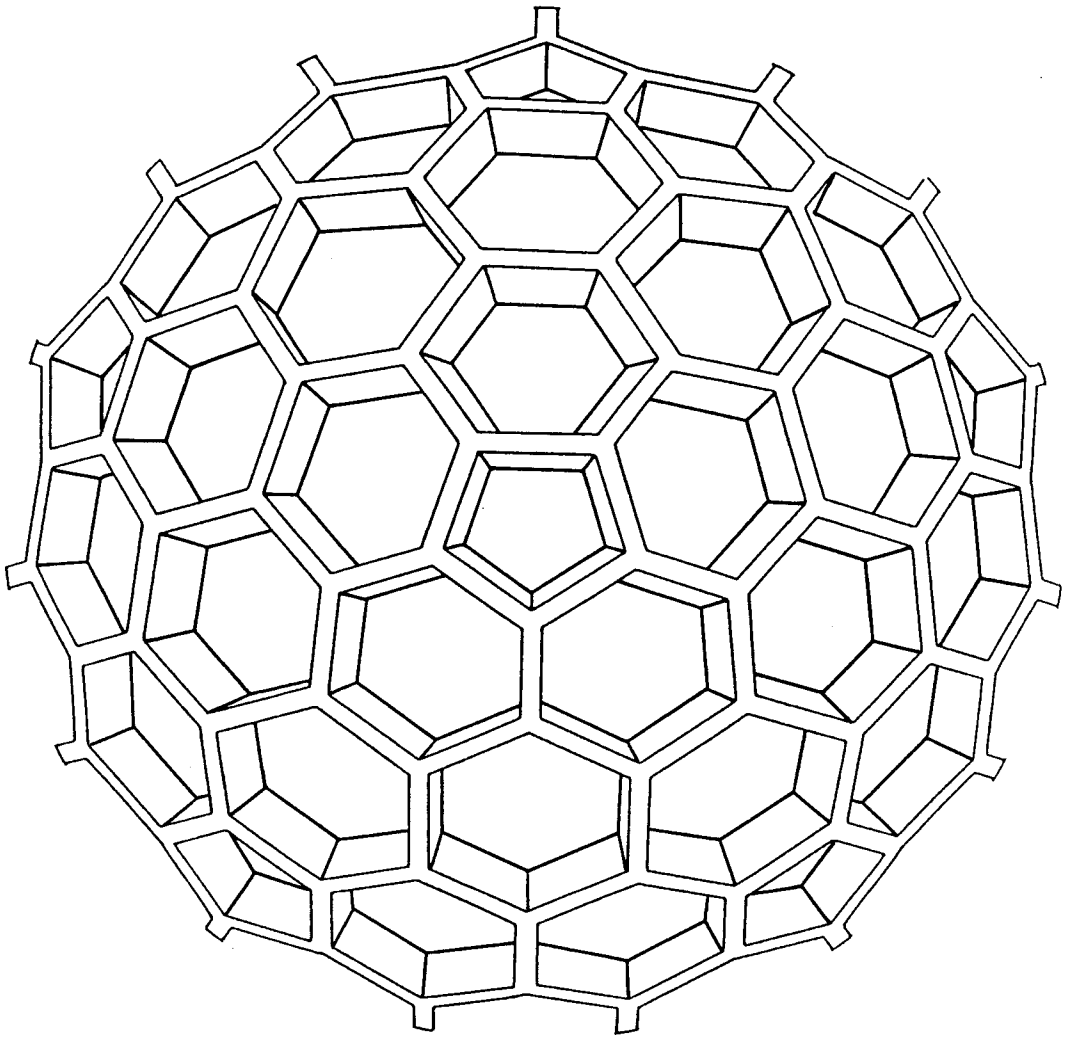

Fig. 1.3. Reactor structural frame.

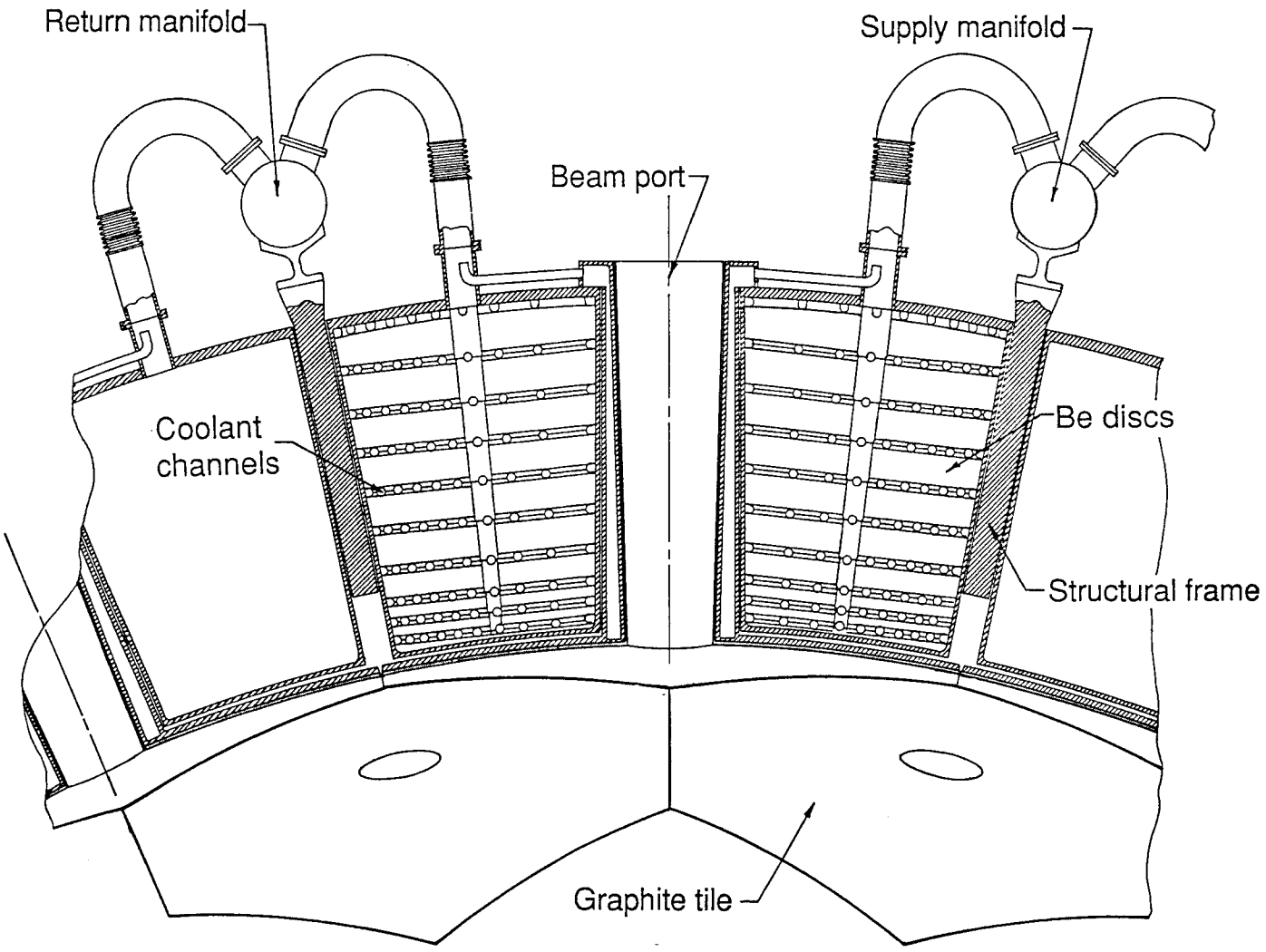

Fig. 1.4. Cross section of a typical hexagonal blanket module.

constant diameter and the inner a tapered tube through which the laser beam passes. The annular space between the tubes is used to duct coolant to the metallic backing of the tile. This figure shows the distribution of beryllium discs within the module. A large fraction of the module is occupied by beryllium discs to provide neutron multiplication. A single supply and a single return coolant connection are shown. The coolant supply line channels lithium down one side of the module with channels radiating from it to the inner and outer perimeters of the module. Circumferential channels then carry the coolant between the beryllium discs to the other side collecting in a single return line leading to the return manifold. Figure 1.5 shows the coolant distribution within the metallic backing of the first wall tiles.

The structural frame has been stress analyzed by finite element methods for regions which are the most highly loaded by dead weight of the frame, modules and coolant. Stresses were found to be well below yield limits for the V-3Ti-1Si vanadium alloy. The frame is quite robust and the deflection of the individual frame cells were sufficiently small to accommodate module removal and replacement without difficulty.

Table 1.1 gives the major parameters for SIRIUS-T.

1.3. Neutronics Analysis

The neutronics analysis performed for SIRIUS-T is aimed at optimizing the blanket design to maximize the tritium breeding ratio (TBR). Based on the mechanical design and structural analysis for the blanket support frame, the webs of the frame and the blanket module side walls were determined to occupy 12.77% of the volume in the blanket region. In addition, the beam penetrations correspond to 1.97% of the blanket volume. The lithium in the radial tubes feeding the coolant layers amounts to 2.3% of the blanket volume.

The neutronics calculations were performed using the one-dimensional discrete ordinates code ONEDANT[4] with cross section data based on the ENDF/B-V evaluation. The 4 m inner radius spherical chamber is modeled in spherical geometry with the target at the center emitting neutrons with energy distribution given by the SIRIUS target spectrum. As a result of neutron target interactions the source spectrum has only 78% of the neutrons at 14.1 MeV. Two

Table 1.1. Major SIRIUS-T Parameters

Driver Energy	2 MJ
Target Gain	50
Driver Efficiency	5-10%
Repetition Rate	10 Hz
Pulse Length	10 ns
Fusion Power	1000 MW
Thermal Power	1410 MW
Electrical Conversion Efficiency	36%
Capacity Factor	70%
Chamber Inner Radius	4 m
Number of Beams	92
Tile Thickness	2 cm
Gap Between Tile and Blanket	1 cm
Blanket Thickness	97 cm
Structural Material	V-3Ti-1Si
Breeding Material	Li (90% enr. ^{6}Li)
Breeding Ratio	1.9
Blanket Energy Multiplication	1.4
Inlet Lithium Temperature	350°C
Outlet Lithium Temperature	550°C
Maximum Blanket Structural Temperature	650°C
Lifetime of Tiles	2 FPY
Lifetime of Modules	3 FPY
Containment Building Radius	22 m
Distance to Final Focusing Mirrors	20 m
Diameter of Final Focusing Mirrors	1.35 m
Lifetime of Final Focusing Mirrors	1 FPY
Containment Wall Thickness	3.2 m
Mass of Graphite in Reactor	3.44 tonnes
Mass of Lithium Inside Chamber	8.97 tonnes
Mass of Lithium Outside Chamber	17.94 tonnes
Mass of Vanadium in Reactor	272 tonnes
Mass of Beryllium Purchased (includes 33% extra)	324.9 tonnes
Annual Tritium Production	33.32 kg
Maximum Routine T_2 Release	29 Ci/d
Maximum Accidental T_2 Release	19.9 g
Total Tritium Inventory	183.6 g

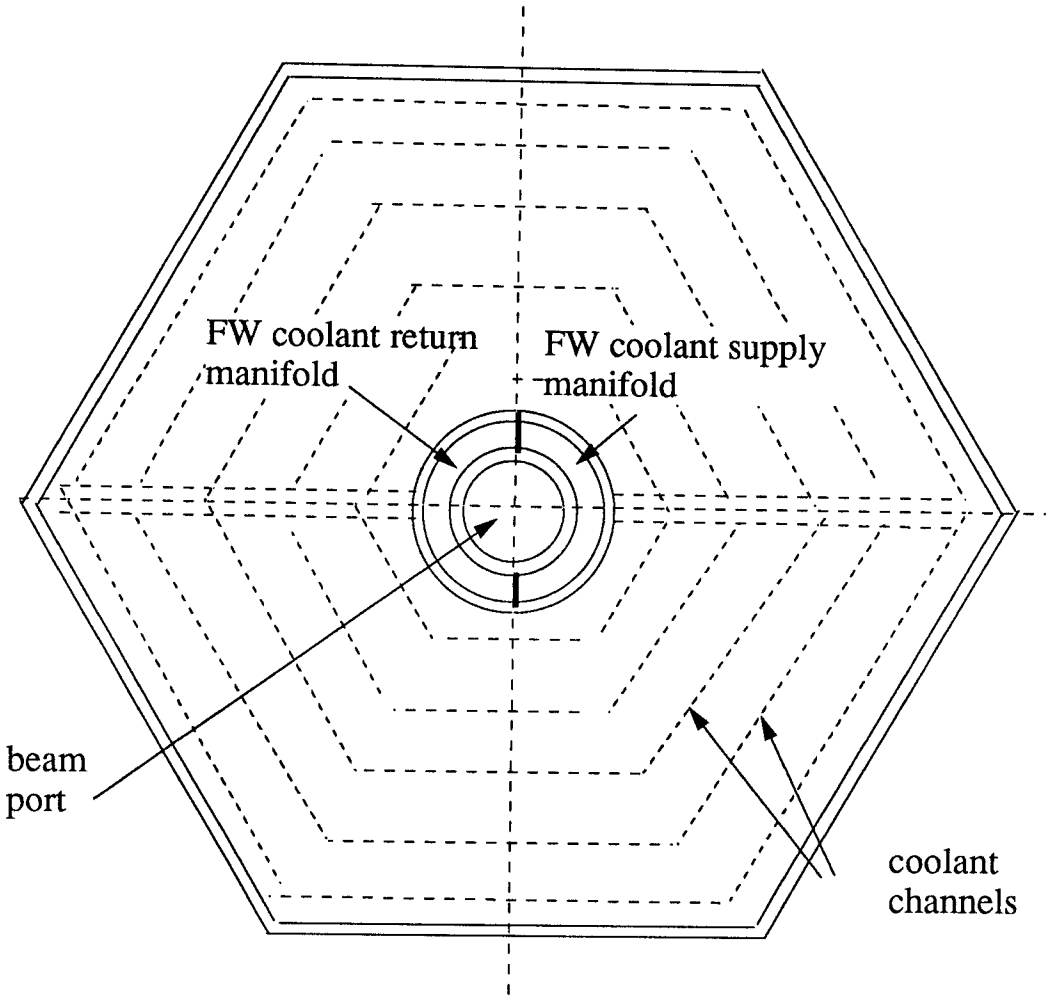

Fig. 1.5. Coolant distribution in first wall tile metallic backing.

approaches were considered to calculate the overall TBR. One approach is based on performing the neutronics calculations using the local blanket composition excluding the structural support webs and beam penetrations. The results are then modified to account for the reduced blanket coverage. The other approach uses a homogenized composition for each blanket layer taking into account the beam penetrations and structural frame. This yields conservative estimates for the overall TBR and is utilized here. In the neutronics calculations, each lithium layer is considered to consist of 85.26% lithium, 12.77% vanadium, and 1.97% void. On the other hand, each beryllium layer has 82.96% beryllium, 2.3% lithium, 12.77% vanadium, and 1.97% void.

Extensive optimization has been performed for arriving at the optimum layering of beryllium and lithium with respect to layer thickness and distribution, holding as a major constraint, the maximum temperature and its gradients.

Varying the lithium enrichment for the optimum layered configuration, the TBR was found to increase as the enrichment increases as shown in Figure 1.6(a). Although the TBR enhancement appears to be small, the cost impact will be significant since an enhancement of 0.001 in the TBR results in an additional 1.65 kg of tritium produced over the 30 FPY reactor life. At a tritium cost of $10,000/g, this translates into a $16.5 M enhancement in the value of tritium produced. A simple cost tradeoff analysis has been performed to assess the economic impact of increasing the lithium enrichment. The analysis indicates that using 90% ^{6}Li results in a net economic gain in spite of the increased lithium cost. The effect of varying the total tile and blanket thickness is shown in Figure 1.6(b). The cost tradeoff analysis indicated that increasing the thickness to 1.1 m leads to a net economic loss with the increase in tritium produced for the thicker blanket being negated by the increased chamber cost. A 1 m thick blanket is chosen for SIRIUS-T with the radial build given in Fig. 1.7 and the lithium is enriched to 90% ^{6}Li. This yields an overall TBR of 1.903.

The radial variation of dpa and helium production rates in the vanadium alloy structure is shown in Fig. 1.8. The results indicate that the peak dpa and helium production rates in the vanadium back structure of the tiles are 30 dpa/FPY and 94 appm/FPY, respectively. The peak

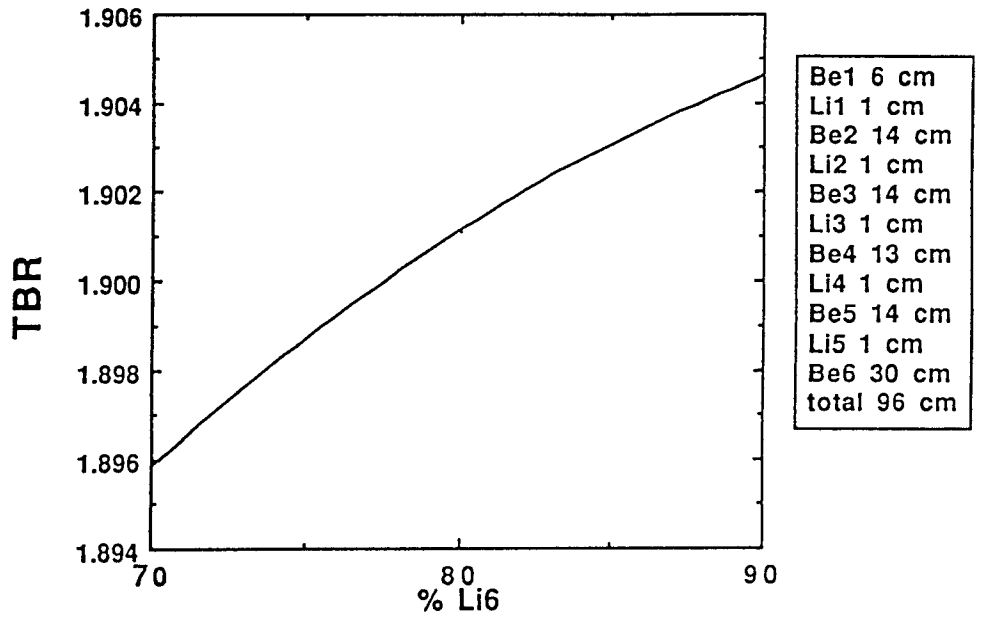

Fig. 1.6(a). Effect of Li enrichment on the TBR.

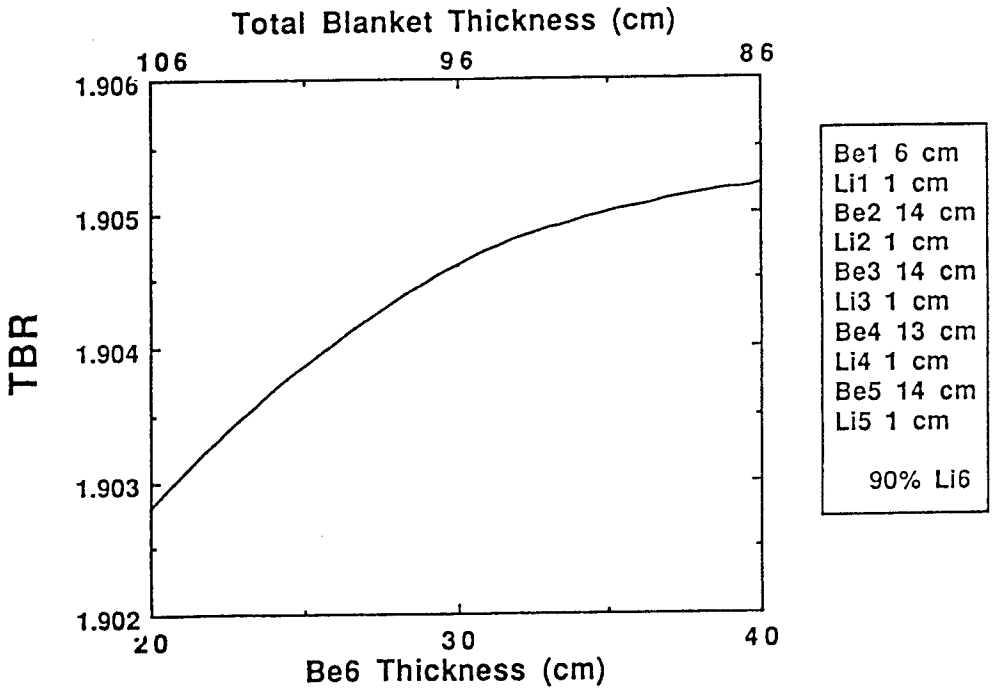

Fig. 1.6(b). Effect of overall blanket thickness on TBR.

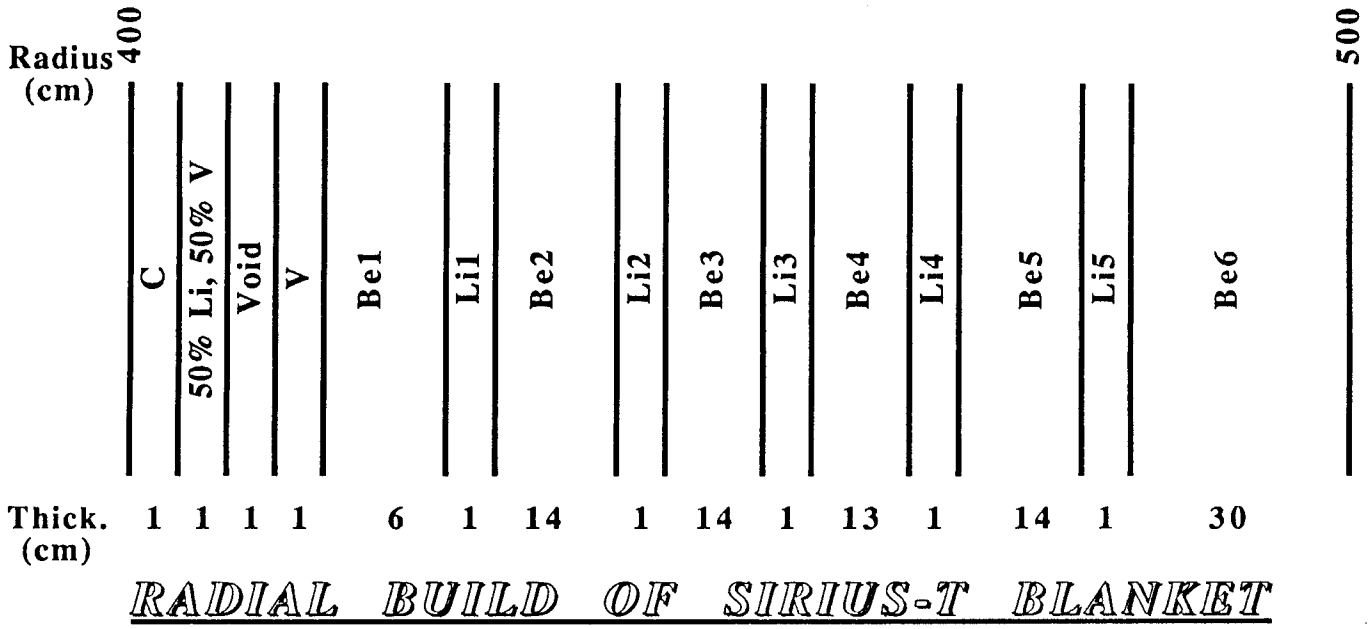

Be zone: 82.96% Be, 2.3% Li, 12.77% V, 1.97% void

Li zone: 85.26% Li, 12.77% V, 1.97% void

Fig. 1.7. Radial build of SIRIUS-T blanket.

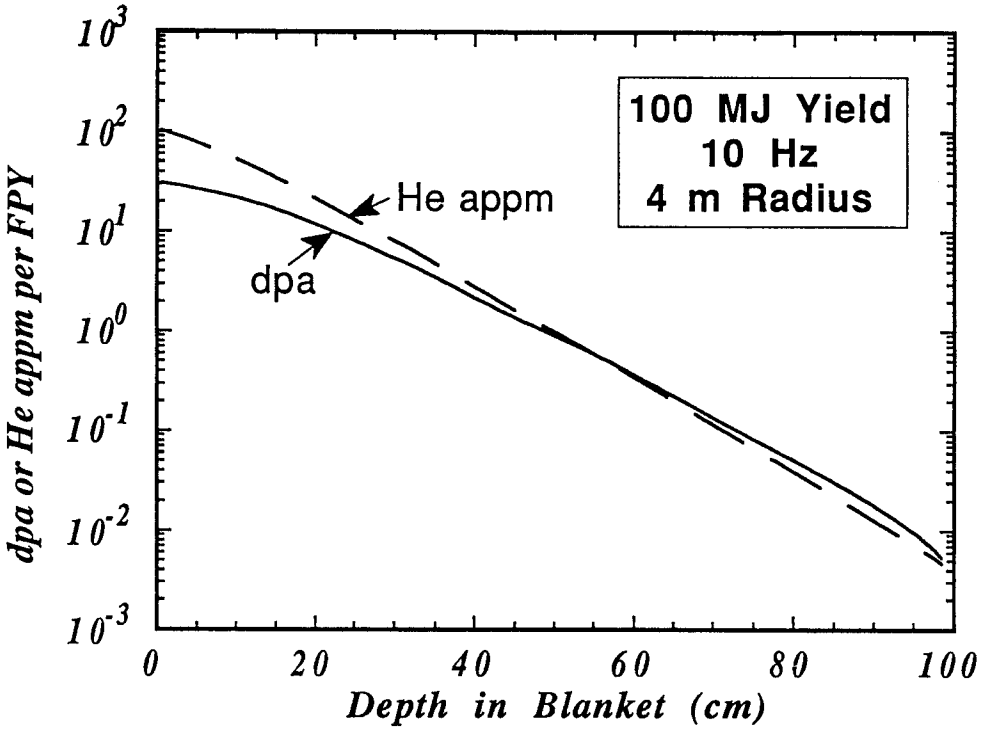

Fig. 1.8. Radial variation of dpa and helium production in vanadium alloy structure.

dpa rate in the front wall of the blanket module is 24 dpa/FPY and the helium production rate is 70 appm/FPY. Detailed lifetime analysis for the V-3Ti-1Si alloy that takes into account swelling and radiation embrittlement indicated that the vanadium alloy lifetime in the SIRIUS-T blanket is expected to be ~3-4 FPY. The peak dpa rate in the graphite tiles is 18 dpa/FPY. The lifetime of graphite is determined by the damage level at which the graphite passes through the shrinkage phase and crosses the zero dimensional change axis on the way to runaway swelling. Data on irradiation of several forms of graphite show that the useful life in SIRIUS-T is 2 FPY.[5]

Neutron irradiation of beryllium in fusion reactors results in the production of tritium. The tritium inventory in the beryllium depends on the rate of tritium production and the retention and transport characteristics of tritium in beryllium. The limited data available on tritium retention in beryllium show that the retention rate drops as the temperature increases.[6] The tritium production rate determined from the neutronics calculations along with the calculated temperature distribution have been used to determine the tritium inventory in the different beryllium layers of the blanket at the end of the blanket lifetime. The total tritium inventory in the beryllium in the blanket is 19 g assuming that it is annealed at 650°C every 2 months.

Table 1.2 gives the major neutronics parameters for SIRIUS-T.

1.4. Thermal Hydraulics

The configuration and parameters of the coolant system must be optimized simultaneously with the neutronics and thermal stress calculations to achieve the maximum possible TBR, while satisfying the engineering constraints imposed on the design. Iterations are needed to determine the optimum configuration of lithium coolant and beryllium multiplier in the blanket. Figure 1.9 is a detailed cross section of a hexagonal blanket module. The coolant traverses each channel to the other side where it finds its way up and out through the return manifold. The first wall is composed of graphite tiles bonded to lithium cooled vanadium structure. Cooling the first wall is achieved by feeding the coolant down an annulus around the beam port to the coolant channels which have the same geometrical configuration as the blanket coolant channels. The annulus is divided into two separate channels, one for supply and the other for return.

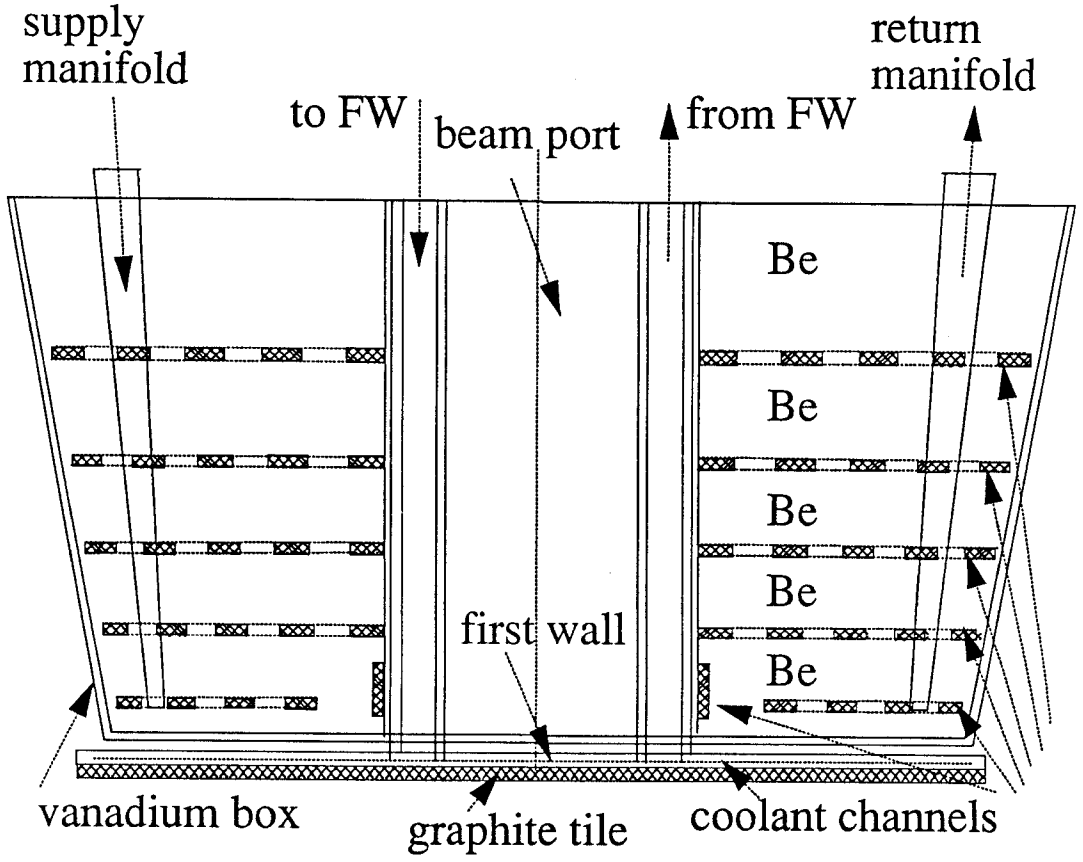

Fig. 1.9. Cross-section of hexagonal module showing direction of coolant flow.

Table 1.2. Neutronics Parameters for the Reference SIRIUS-T Blanket Design

Tritium breeding ratio:	^{6}Li	1.8993
	^{7}Li	0.0032
	Total	1.9025
Nuclear heating (MeV/fusion):	Neutron	16.88
	Gamma	3.44
	Total	20.32
Nuclear energy multiplication	1.55	
Overall energy multiplication	1.41	
Peak dpa rate in graphite tiles	18 dpa/FPY	
Peak helium production rate in graphite	4420 appm/FPY	
Peak dpa rate in vanadium alloy	30 dpa/FPY	
Peak helium production rate in vanadium alloy	94 appm/FPY	
Total tritium inventory in beryllium	19 g	

A two-dimensional finite-element thermal model has been generated for use with the ANSYS code,[7] to examine the thermal performance of the proposed configuration utilizing the nuclear heating results obtained from the neutronics analysis. It is assumed that the liquid lithium enters at a temperature of 350°C and exits at 550°C. The temperature of the vanadium structure should be in the range between 350°C and 650°C. The lower limit is needed to eliminate any concern about DBTT and the upper limit is required to avoid helium induced degradation on ductility. In the mean time, the temperature of the beryllium should be kept as high as possible to allow tritium to diffuse out. Figure 1.10 shows the reference coolant routing through the blanket and first wall. Velocity and temperature rises and absolute temperatures are included in this figure.

The two-dimensional thermal model uses temperature dependent properties for the different materials used. Moreover, it allows heat to be radiated between the blanket and FW. The two

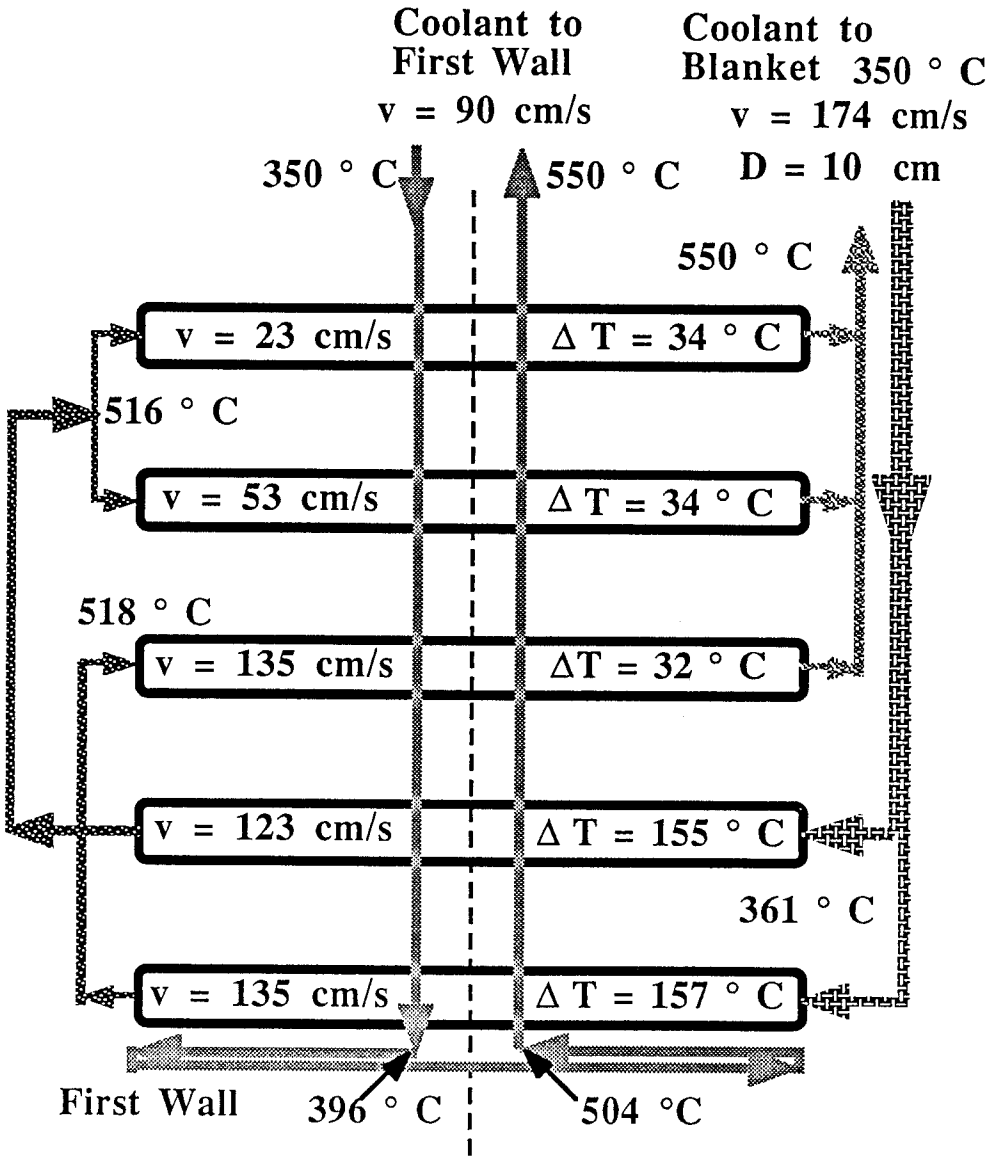

Fig. 1.10. Reference coolant routing through a blanket module.

sides of the model have been modeled separately. Different boundary conditions are imposed on each side during the calculations since the thermal model handles each module side separately. The maximum beryllium temperature is 718°C in the middle of the first beryllium layer while the maximum vanadium temperature is 650°C at the front surface of the module. The steady state temperature distribution in the first wall has been calculated. The maximum steady state temperature of the graphite tile surface has been determined to be 834°C.

1.5. Materials Lifetime Analysis

Lifetimes have been determined for the graphite tiles, the vanadium blanket modules and the final focusing mirrors.

The main problem for the graphite is the dimensional stability of the tiles operating at 700-850°C in a neutron environment for long periods of time. During high temperature irradiation, the graphite first shrinks and then expands at a very rapid rate. A useful lifetime is usually determined when the dimensional change reverses and crosses the $\Delta V = 0$ line. The useful life of isotropic graphite is ≈49 dpa (3×10^{22} n/cm^2) at 400°C. This lifetime gets shorter as the temperature increases, dropping to ≈18 dpa at 800°C and to ≈10 dpa at 1000°C. At temperatures higher than 1000°C, the lifetime increases with increasing temperatures as the defects anneal out. Since the damage level in SIRIUS-T is ≈18 dpa/FPY, we might expect a useful life of only 1 FPY from isotropic graphite. Fortunately, there are other forms of graphite more resistant to radiation damage. Birch and Brocklehurst[5] have reported data on three forms of graphite and show that Graphnol-N3M would not reach the zero swelling point until ≈1.5 FPY's in SIRIUS-T at 700°C. Since the graphites tested thus far have not been optimized for the fusion environment, and because SIRIUS-T is a device that would not operate for at least 10 years, we feel comfortable in projecting the Graphnol-N3M data by 33%, to 2 useful FPY's.

There are usually 3 key indicators of the useful lifetime of metallic structural members in a fusion reactor; swelling, embrittlement, and corrosion. The two parameters that have the most impact on the first 2 properties are the dpa level and the amount of helium generated at high

temperatures in the alloy. For SIRIUS-T, the maximum conditions at the first wall just behind the graphite are:

- 30 dpa/FPY
- 100 appm He/FPY
- T = 687°C.

Unfortunately there is relatively little information on neutron damage in vanadium alloys at fusion reactor conditions. Braski,[8] as well as Loomis and Smith[9] have studied the V-3Ti-1Si alloy after irradiation in the fission spectrum of a fast breeder reactor. The irradiation temperatures were lower (420 to 600°C) than the maximum (687°C) anticipated in SIRIUS-T and the helium production rate was only ≈0.05 appm He/dpa compared to ≈3 appm/dpa in SIRIUS-T. Nevertheless, reference 8 showed that at low helium contents, the swelling at damage levels equivalent to 2.7 FPY's in SIRIUS-T is slightly over 0.2% at 420°C and reference 9 showed 0.5 to 4.3% swelling at 600°C. When 20 appm helium is preinjected into the samples before 420°C irradiation, the level of swelling is tripled, and when the equivalent of 2.7 FPY's of helium generation had been preinjected, swelling had reached ≈1.2%. It is felt that swelling on the order of a few percent can be tolerated. Without further high temperature data, we have assumed that irradiation at 687°C will not increase the swelling by more than a factor of 2-3 over the 420°C results (with preinjected helium) or by more than a factor of 1 to 3 times over the 600°C results with low helium contents. This would indicate that a useful lifetime would be conservatively on the order of 3 FPY's from a dimensional stability standpoint.

Irradiation of a V-3Ti-1Si alloy at 420°C, with low helium content (4 appm), makes this alloy stronger and less ductile. The ductility drops rapidly within the first 5 dpa (≈4 full power months in SIRIUS-T) and after that, the total elongation at failure remains relatively constant at ≈5%. However, the low helium content does not properly simulate the fusion conditions and adding more helium before irradiation causes the total elongation to drop even further to ≈2% at dpa levels equivalent to 2.7 FPY's. One might expect that irradiation at higher temperatures would aggravate this effect but data obtained by Braski[8] shows that preinjected helium contents equivalent to 10 full

power months do not cause further degradation at higher temperatures. With the above limited information in hand and using a 1 to 2% total elongation as a limit, we estimate that the useful life due to a loss of ductility is ≈4 FPY's for the vanadium alloy. From the corrosion standpoint the material lifetime will be >10 FPY assuming a thinning of the material of 100 μm (0.1 mm).

The above analysis indicated that swelling is the controlling mechanism and thus, we have used 3 FPY as the lifetime of the blanket modules.

The useful lifetime of the final focusing mirrors is determined by the degradation of the reflective properties of the laser mirror coating. We have used the criterion that no more than 10^{11} rads to the mirror coating is desirable. Assuming that some of the damage can be annealed by high temperature treatments, one can determine the lifetime if the minimum time between anneals, and the fraction of damage annealed out in each anneal is known.

The damage rate at the final optics (20 m from the target) in SIRIUS-T is 5×10^{11} rads/FPY. This means that the first anneal must be conducted after 0.2 of a FPY (2.4 full power months, or 3.4 calendar months at 70% availability). If we assume that the minimum time between anneals is 1 calendar month at 70% availability (0.0583 FPY), then the lifetime can be expressed as a function of recovery fraction. This analysis reveals that if we wish to have a 1 FPY life for the mirrors, the recovery fraction needs to be ≥85% per anneal.

Figure 1.11 summarizes the critical lifetime components in SIRIUS-T. It can be seen that the most limiting materials are the mirrors at 1 FPY and the graphite tiles at 2 FPY's. These are followed by the beryllium neutron multiplier and by radiation damage to the vanadium alloy structure at 3 FPY's. Finally, the corrosion of the vanadium alloy does not pose significant problems in availability for the SIRIUS-T reactor.

1.6. Tritium Considerations

In this section we are mainly concerned with T_2 recovery from the lithium, the tritium inventory in the various reactor systems and safety issues related to routine and accidental releases.

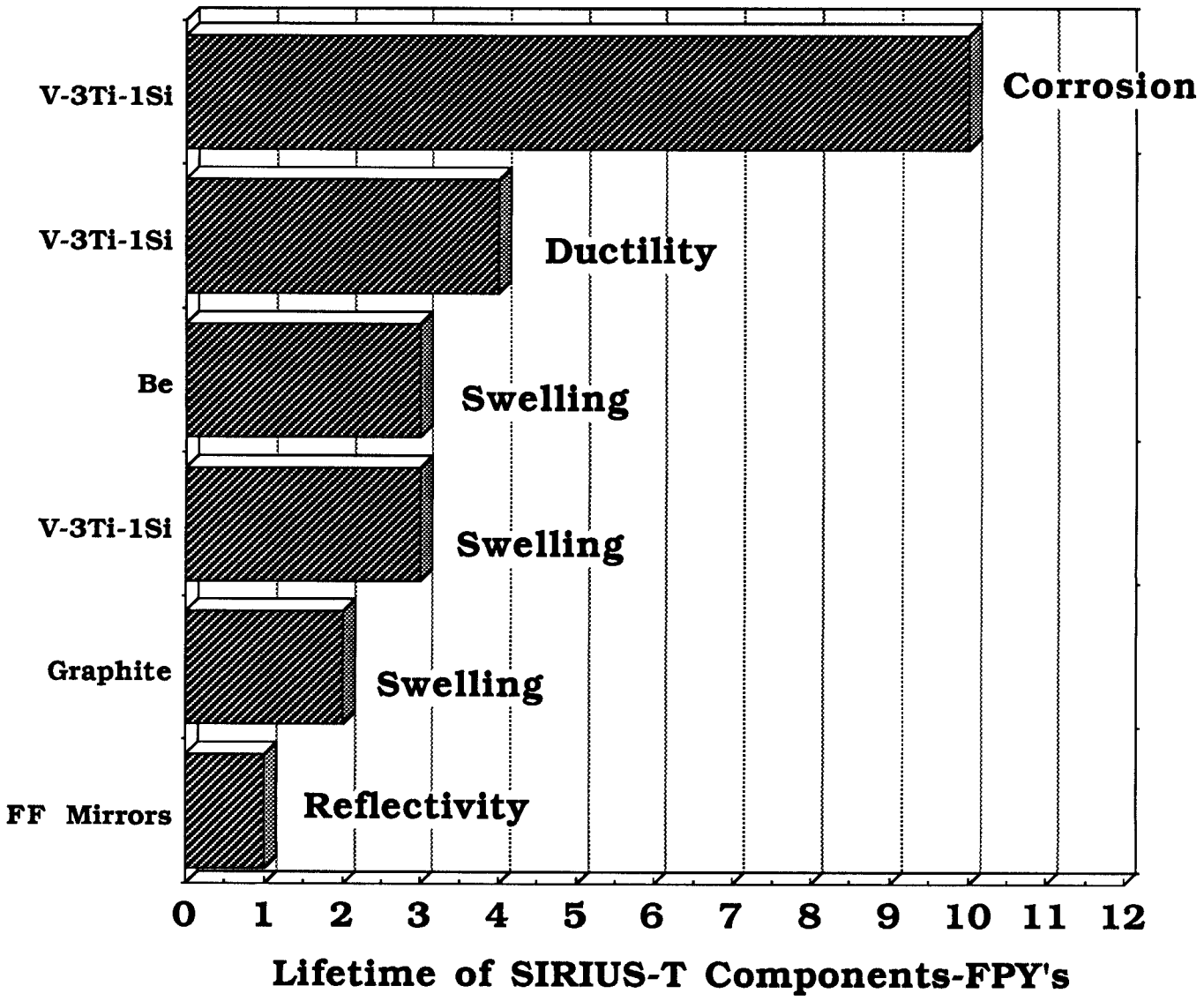

Fig. 1.11. Life limiting mechanisms for SIRIUS-T components.

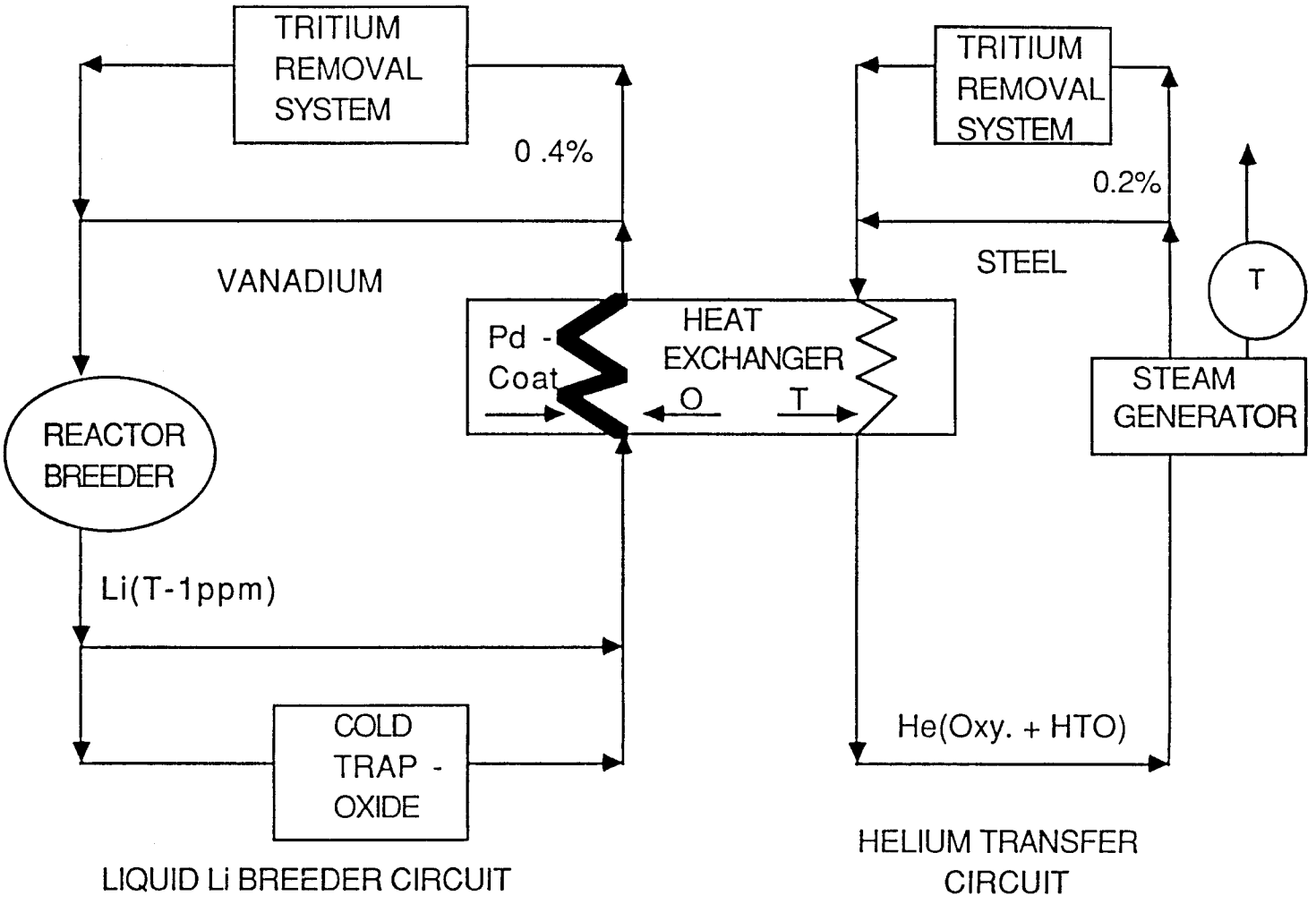

Fig. 1.12. Tritium removal system for the lithium breeder and the helium intermediate heat transfer circuits.

The concentration of the tritium in the liquid lithium is determined by the operation of the Tritium Removal System (TRS), Fig. 1.12, which is located external to the reactor cavity. As the lithium flows from the reactor cavity to the heat exchanger a portion of the liquid is diverted to the TRS which removes tritium at the rate it is generated in the reactor blanket. By the use of the TRS, the concentration of tritium in the lithium is maintained at 1 wppm.

The TRS, which has been experimentally demonstrated,[10] initially mixes a portion of the lithium containing tritium with a second liquid phase of a fused salt composed of LiF-LiCl-LiBr. During this contact, the LiT present transfers from the liquid metal to the molten salt phase. The lithium is returned to the reactor and the tritium is released as gaseous T_2 from the molten salt during electrolysis. This system has demonstrated approximately 50% efficiency for the extraction of tritium from lithium at a tritium concentration of 1 wppm. In order to remove tritium at the rate it is produced in the lithium breeder, 3.37×10^{-3} g(T)/s, approximately 1.35×10^{-2} m^3/s of lithium must be sent to the TRS which is only 0.4% of the lithium stream circulating at 3.24 m^3/s. The recycle time for the lithium is ~17 s for thermal extraction, but the mean residence time for a tritium atom in the lithium is ~134 min. With ~9 tonnes of lithium in the reactor chamber and ~18 tonnes in the remainder of the lithium circuit, the total tritium inventory in the lithium is 27 g (9 g in the reactor chamber and 18 g in the external circuit).

Although the tritium pressure in the lithium is very low, 10^{-7} Pa, some tritium, ~17 g/day (2×10^{-4} g(T)/s) would permeate through the intermediate heat exchanger (IHX) into the helium circuit and continue to accumulate; consequently, a tritium removal system (TRS) is installed in the helium circuit. This TRS removes tritiated water (HTO) by adsorption on a desiccant bed which yields a dew point of -60°C and a HTO pressure of ~1.33 Pa. In order to ensure the oxidation of the tritium, the exterior surface of the vanadium tubes in the IHX is coated with a thin, ~7-10 μm layer of palladium, as described by Hsu and Buxbaum.[11] Sufficient O_2 pressure is maintained in the helium so that the palladium is saturated with oxygen; consequently, as the tritium atoms permeate through this palladium coating they are oxidized when they desorb into the gaseous stream. As a result the entire helium circuit contains only 2 g of tritium and only ~4 Ci/d of tritium

permeates into the steam generator. The desiccant beds are recycled every 4 hours so that they contain only 3 g of tritium.

The atmosphere within the containment structure contains xenon at a pressure of 1 torr (133 Pa) and the unburned fuel from the exploded fuel targets exits from the reactor cavity through the open penetrations provided for the laser beams. At this time, it is assumed that xenon is continually admitted into the reactor cavity at a rate so that the cavity gas is replenished once per second requiring 14.4 moles of Xe/s. This xenon contains, therefore, the target debris for one second (10 targets) which includes 1.4×10^{-3} moles of DT (1×10^{-4} mole fraction DT/Xe). The entire building contains 2.4×10^{3} moles of xenon, and consequently 0.24 moles of (DT) equivalent to 0.75 g of tritium.

Other inventories of T_2 in the containment building are those adsorbed on the graphite tiles and on the stainless steel coating on the inside of the containment building. Based on data on the solubility of DT in graphite and the observation that hydrogen saturates in the grain boundaries of graphite[12] to a concentration of 5 ppm atom of hydrogen per atom of carbon, we calculate a total inventory of 4.3 g of tritium in the graphite tiles. Assuming that DTO will be present in the gases within the containment building, the tritium adsorbed on the building walls will be negligible, at $\sim 6 \times 10^{-8}$ g.

An additional source of tritium is contained in the fuel target injector which must reside within the containment building (at a location which has not been defined at this time). The injector will contain a supply of cryogenically-cooled targets which are prepared in the Target Fabrication Facility. The targets are injected at 10 Hz delivering 6 mg/s of tritium. A 30 min supply of targets would contain 10.8 g(T) (18 g of DT).

A conceptual design of a simple gas handling system is presented which processes the exhaust gases from the containment building, prepares decontaminated xenon gas for reinsertion into the reactor cavity, and recovers, purifies, and isotopically-separates DT for the preparation of new target fuel. This processing must be accomplished with low loss and minimal inventories of xenon and tritium because of the high cost of xenon and tritium and the potential radiological

hazard caused if tritium escapes to inhabited areas. Briefly, the purification technique considers the oxidation of all the reactor exhaust to form water (containing H, D and T) and carbon dioxide in the xenon carrier gas. The oxidized gases are next absorbed on molecular sieve desiccant beds at an ambient temperature, ~25°C. The desiccants are selected for preferential adsorption of water and CO_2. Finally, the helium is removed from the xenon by cryogenic distillation.

The inventories of tritium in the various locations and components are summarized in Table 1.3. Review of this table indicates that the majority of the tritium exists in the Exhaust Recycle System which is located in a basement below the reactor cavity but would share the single containment structure. Because this is a tritium production reactor, the tritium produced would be packaged for storage in the facility near the TRS for the lithium coolant. When they are securely sealed, the tritium containers would be transported to a separate storage vault away from the reactor.

The routine release of tritium from the containment building via a stack of 100 m high is very low because most of the equipment is within double or triple containment structures. Experience at the Tritium Systems Test Assembly (TSTA)[13] has shown that these multiple containment structures release very small amounts of tritium off-site.

The quantity of tritium which would be released following an accident within the containment building would require an assessment of potential accident scenarios, which was not undertaken. A very conservative assumption would be that all the tritium in all the components might be released to the atmosphere. In such a case, up to 109 g of tritium would become airborne. (The Target Fabrication Facility has not been included in this analysis since targets will be purchased from a vendor.) Based upon the FUSECRAC model,[14] which is currently being used in the USA for fusion reactor studies, the radiation dose to the most exposed individual at the 1 km site boundary would be only 1 rem. A comprehensive accidental safety analysis would also consider other radioactive isotopes which might be released with the tritium, such as the vanadium structure. Fortunately, vanadium is a low activation material and would contribute only a small additional

Table 1.3. Tritium Inventory and Potential Off-Site Release

Location	Components	Inventory Tritium, g	Tritium Release Routine Ci/d	Tritium Release Accidental g
Containment building	Fuel injector	11	-	11
	Atmosphere	0.8	2	0.8
	Surfaces	<0.1	-	-
Reactor cavity	Beryllium	18	-	18
	Vanadium	1.2	-	1.2
	Graphite	4.3	-	4.3
Coolant circuits	Lithium	27	-	27
	Li-TRS	0.03	-	0.03
	Helium	2	4	2
	He-TRS	3	6	3
	Steam generator	-	4	-
Exhaust recycle	Desiccant beds	16	-	16
	Isotopic separator	24	-	24
	Other	1	2	1
Vault storage		2800	-	-
		2909	18	109

hazard off-site. This brief review suggests that the dose to the most exposed individual off-site can be kept below 25 rem, which is the guideline requiring evacuation of the neighborhood.

1.7. Reactor Maintenance

The three important components of the reactor that must be periodically maintained are the first wall tiles, the blanket modules and the final focusing mirrors.

The first wall tiles are the closest components to the incident neutrons and are thus subjected to the most severe radiation damage, having a projected lifetime of 2 FPY.

The first wall tiles are designed to be removed in two ways. They can be removed separately from the inside of the chamber, or they can be removed along with the whole module from the outside of the chamber. Figure 1.4 shows a cross section of a typical module with the first wall tile in place and Fig. 1.13 is the same cross section showing the tile being removed from inside the chamber. To disconnect the tile from the module the flange which makes up the rear of the coolant distribution header must be machined off as shown in Fig. 1.13. Further, the weld that seals the constant diameter tube connected to the tile, to the constant diameter tube connected to the module must be machined off. The tile can then be withdrawn radially into the chamber. The procedure is reversed when a new tile is inserted. After insertion, the two constant diameter tubes are welded together to provide the seal which prevents coolant from leaking in between them into the chamber. A new rear flange is then welded to provide closure for the coolant distribution header. Although the lifetime of a blanket module is ~3-4 FPY, we have assumed that they will be replaced every 2 FPY to be consistent with the replacement of the first wall tiles.

A blanket module replacement has to be performed from the outside of the chamber. Figure 1.14 shows a blanket module being extracted from the chamber. Note that the first wall tile is still attached and clears the structural frame. Two functions have to be performed before the module can be extracted. The inlet and outlet coolant lines have to be disconnected and the clamps (not shown in the drawing) which hold the module within the structural frame have to be unfastened. These functions are performed from the outside of the reactor by a remote maintenance machine which rides on a set of rails provided on the support pedestal as shown in

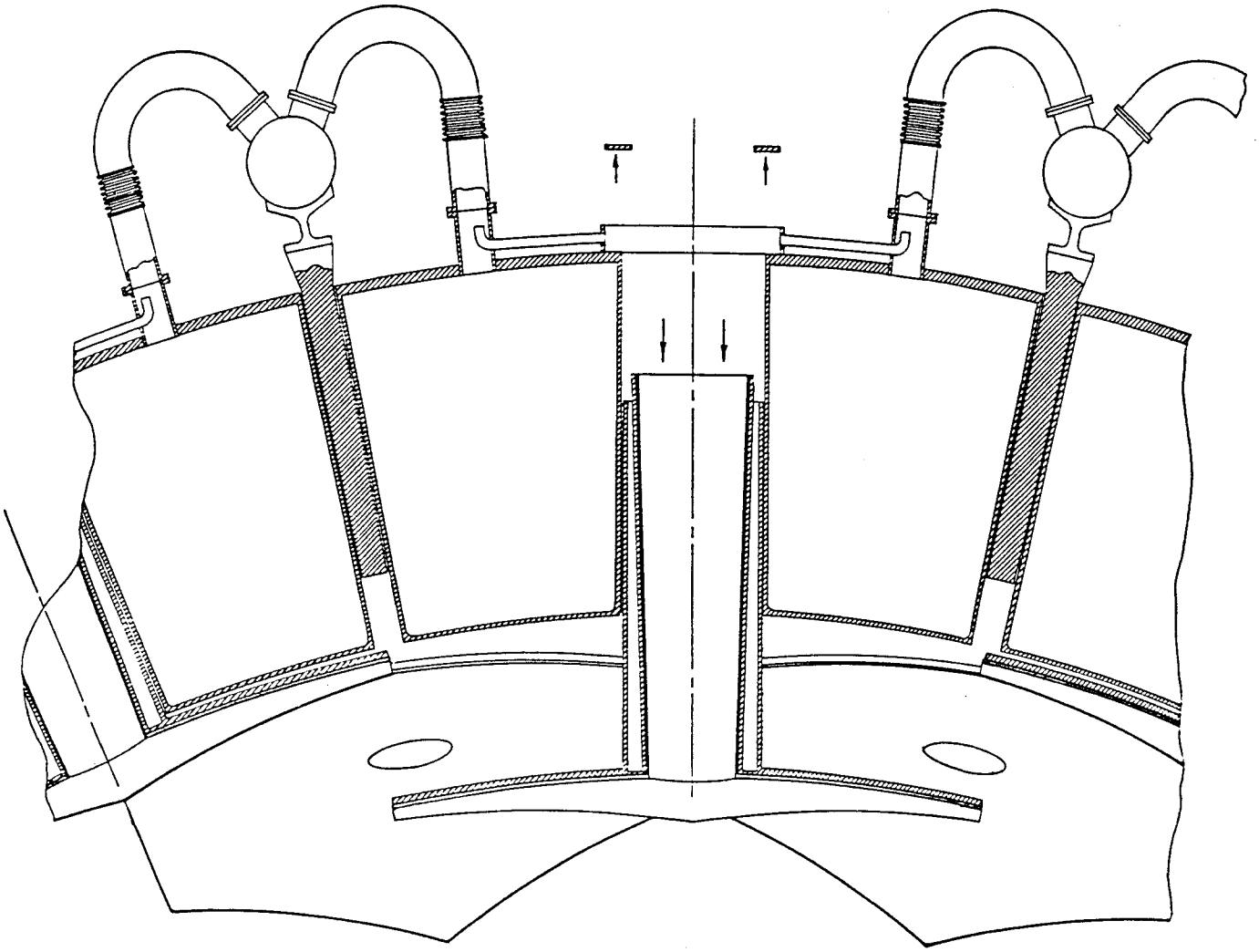

Fig. 1.13. Blanket module showing tile replacement from inside the reactor.

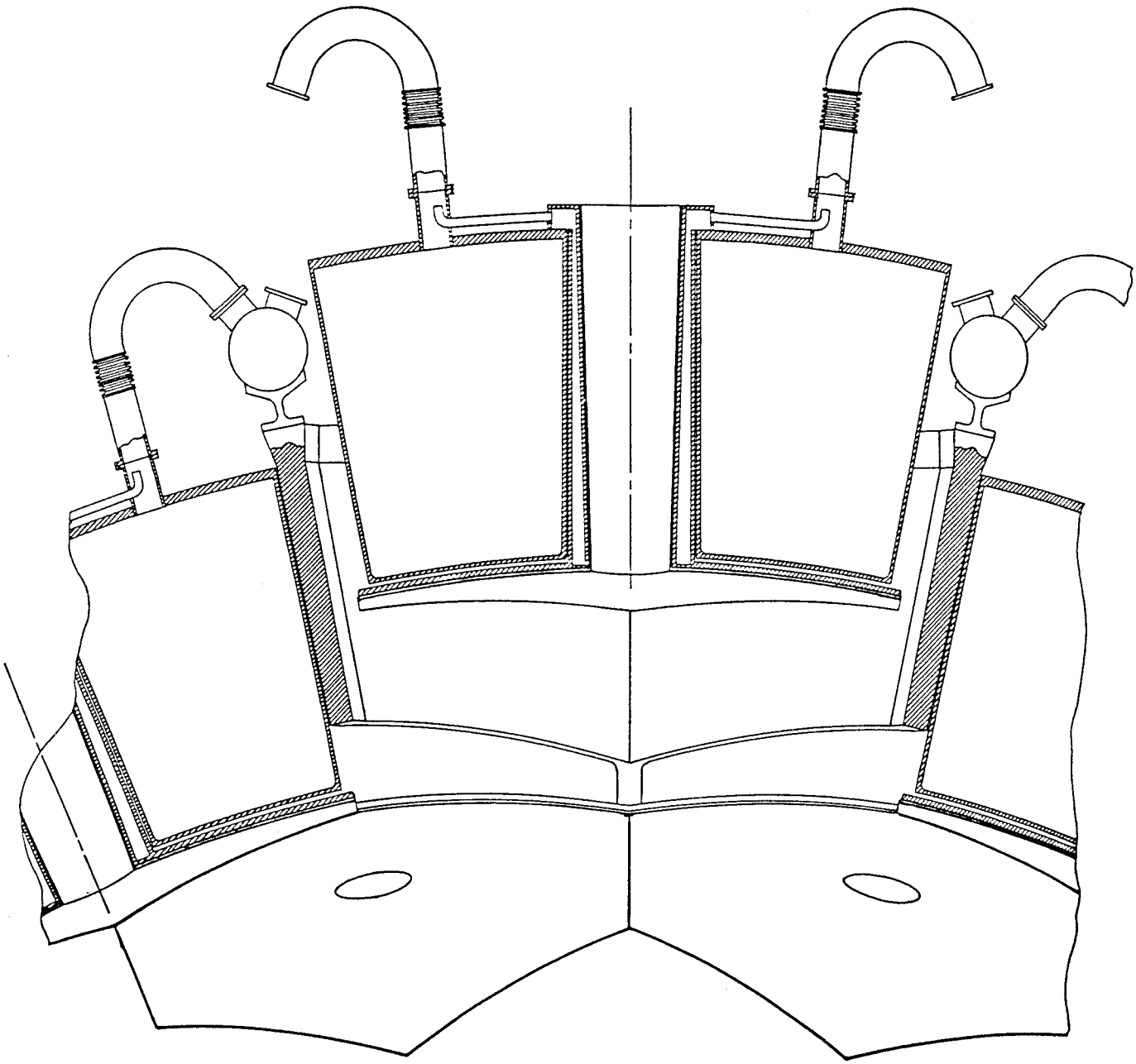

Fig. 1.14. Blanket module replacement from outside the reactor.

Fig. 1.2. The machine will be capable of circumnavigating the chamber on 360° and will be capable of reaching all of the 86 modules outside the support pedestal. Obviously, the remaining 6 modules trapped within the support pedestal will be maintained separately.

Figure 1.2 shows that the support pedestal has been designed to permit maintenance of the 6 modules trapped within it. The convoluted conical surfaces interface with the chamber along the support frame which defines the perimeter of the 6 module cluster. These surfaces provide the needed clearance for the modules to be extracted radially outward within the support pedestal.

The final focusing mirrors have a lifetime of 1 FPY assuming they are periodically annealed and have an 85% damage recovery.

Replacing the final focusing mirrors will be performed on an 8.5 calendar month schedule when one half (46) of the mirrors will be replaced. Several special purpose remote maintenance machines will operate simultaneously aided by the main machine riding on the pedestal tracks. The special purpose machines will index onto a turning mirror shield module and attach themselves to it. From that perch, they can reach a cluster of mirrors, one at a time. The spent mirrors will be unfastened from this support and handed to the main machine which will deposit them into a retrieval hatch. New mirrors are taken from a supply hatch and handed to the special purpose machine which then fastens it in place. These operations will be fairly repetitive and automatic. Recognition of the station being serviced will automatically program the location, distance and orientation needed for the main machine to handle the mirrors.

Two machines operating simultaneously can replace all 46 mirrors in a 48 hour period, allowing on the average, two hours per mirror. This seems to be a reasonable time for such an operation. The impact on availability is <1%. Further, this maintenance can be performed in parallel with routine maintenance of the power generating equipment.

1.8. Economic Evaluation

A special effort has been made to be conservative in arriving at a cost of tritium (COT) in SIRIUS-T. This conservatism is reflected in both technical as well as economic assumptions.

Table 1.4. Assumptions Used in T_2 Cost Determination

Plant capacity factor (%)	70
Operation and maintenance (% of TOC*)	3
Construction time (years)	8
Plant amortization period (years)	30
Construction factor (%)	15
Home office factor (%)	15
Field office factor (%)	15
Owners cost factor (%)	5
Project contingency (%)	10
Fraction of capital borrowed (%)	100
Interest rate (%)	5-10
Levelized annual interim replacement cost fraction (% of TDC**)	1
Reference year costs	1986
(4.2% interest rate used from 1986-1990)	

*TOC = Total overnight costs or total direct + indirect costs
**TDC = Total direct costs

The cost code used in the economic analysis is FUSCOST,[15] a PC based menu driven program for economic evaluation of fusion facilities. Cost algorithms and scaling laws have been taken from SAFIRE[16] and from industrial experience whenever possible. The basic economic assumptions are given in Table 1.4.

Table 1.5 gives the SIRIUS-T costs in 1990 dollars for the interest rates of 5% and 10%. The assumptions in both cases are: 8 year construction period, 100% debt financing, 30 FPY reactor lifetime, 70% availability, 15¢ target cost. Tritium production is 33.3 kg/calendar year.

Table 1.5. SIRIUS-T Costs

	Costs in M$ (1990)	
Interest Rate	5%	10%
Reactor chamber	411	411
Driver	375	375
Turbine plant	136	136
Heat transfer equipment	115	115
Electric plant	115	115
Buildings	98	98
Maintenance equipment	43	43
Miscellaneous plant	39	39
Heat rejection	26	26
Instrumentation and control	26	26
Fuel handling	24	24
Land acquisition	6	6
Total direct costs	1,413	1,413
Total overnight costs	2,332	2,332
Total capital costs	2,838	3,465
Annual operation and maintenance	70	70
Annual component replacement	39	39
Annual target costs	33	33
Annual principal and interest	161	352
Total annual payment	303	494
Cost of T_2 production $/g (1990)	9,099	14,835

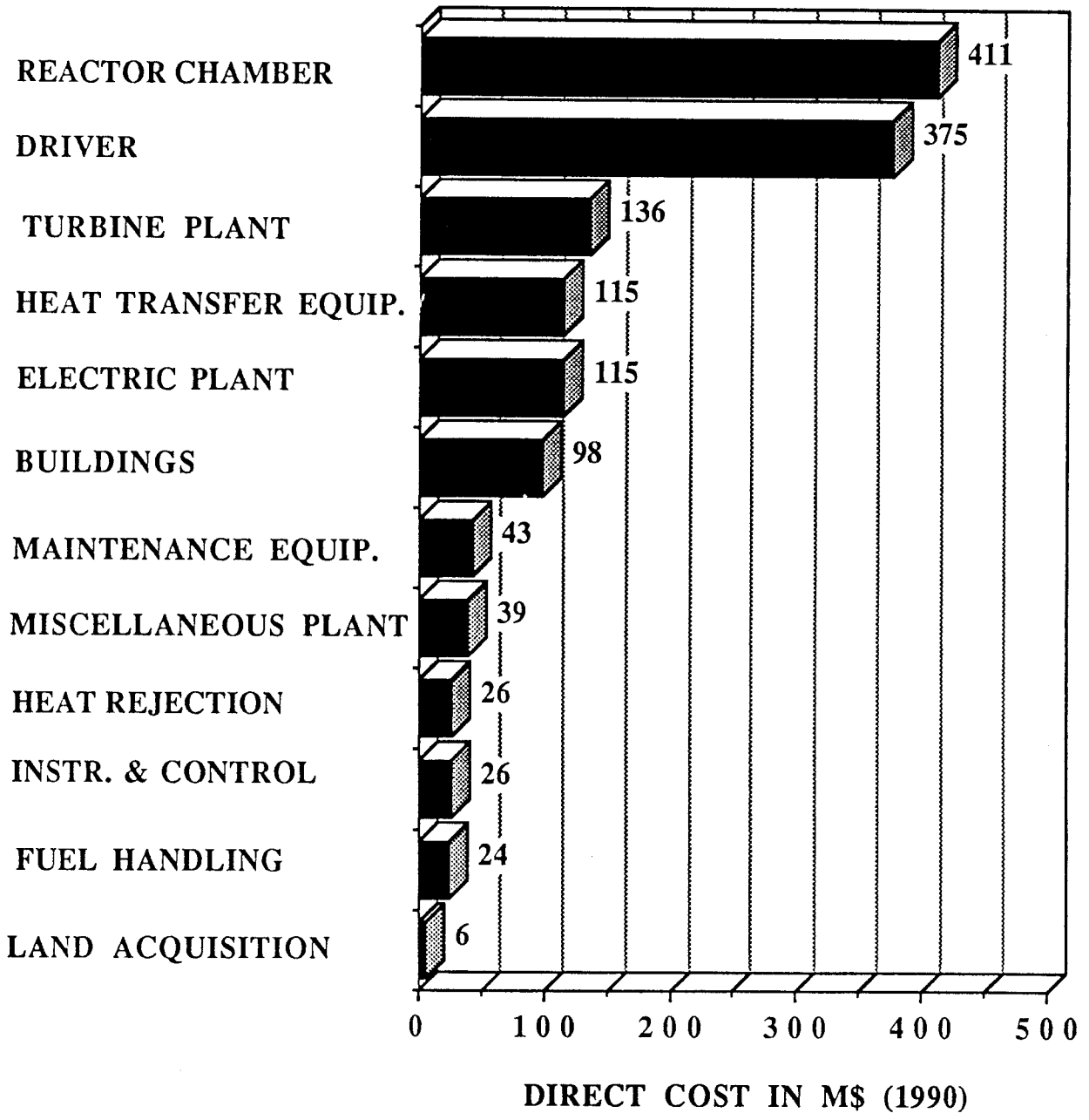

Fig. 1.15. Direct costs of SIRIUS-T are dominated by the reactor chamber and driver.

The total capital costs are 2838 M$ for 5% interest and 3465 M$ for the 10% interest rate. The principal and interest payments are based on a 43 year amortization period. These values give a COT in 1990 dollars of ~9100 $/g for 5% interest and 14,835 $/g for 10% interest.

Figure 1.15 summarizes the direct costs. It shows that the reactor chamber at 411 M$ and the driver at 375 M$ account for over half the SIRIUS-T costs. Unfortunately, these accounts are also the most design dependent and for this reason we have been conservative in estimating them. The next four large accounts all have to do with the balance of plant in which there is a lot of confidence.

Sensitivity analysis shows that the component replacement schedule has a minimal effect on COT. The difference between replacing blanket modules every 2 FPY as compared to 3 FPY increases the COT by ~2%. Varying the target cost from 10¢ to 20¢ per target impacts the COT by 8% and 5% at the 5% and 10% interest rates, respectively. Finally, the driver efficiency has almost no impact on the COT at efficiencies above 5%. Below that, the reactor ceases to be self sufficient with respect to electricity and the COT rises exponentially.

1.9. Conclusions

The SIRIUS-T study, utilizing conservative target performance parameters as well as conservative technical and economic assumptions, can produce tritium at a cost which is very competitive with other tritium production schemes under consideration. However, ICF reactors are advanced systems which will require extensive research and development, as well as time to realize. This design also shows that practical solutions exist for integrating a large number of symmetrically distributed beams in a direct drive ICF reactor configuration.

The critical issues identified are: survival of the final focusing mirrors and the recovery fractions during annealing; survival of the graphite material in the first wall tiles under the synergistic effects of radiation damage, repeated shock loading and cyclic thermal stresses; and finally, the survival of a single shell target with no high Z coating during injection needs investigation.

References for Chapter 1

1. R.C. Davidson et al., "Inertial Confinement Fusion Reactor Design Studies Recommended Guidelines," Sept. 14, 1990.
2. Blanket Comparison and Selection Study - Final Report, Argonne National Lab Report, ANL/FPP-84-1, Sept., 1984.
3. R.R. Peterson, J.J. MacFarlane and G.A. Moses, "CONRAD-A Combined Radiation-Hydrodynamics Vaporization-Condensation Computer Code," University of Wisconsin Fusion Technology Institute Report UWFDM-670, 1988.
4. R.D. O'Dell et al., "User's Manual for ONEDANT: A Code for One Dimensional, Diffusion Accelerated Neutron Particle Transport," LA-9184-M, Los Alamos National Laboratory (1982).
5. M. Birch and J. Brocklehurst, "A Review of the Behaviour of Graphite Under the Conditions Appropriate for Protection of the First Wall of a Fusion Reactor," ND-R-1434(S), UK AEA (Dec. 1987).
6. D.L. Baldwin et al., "Tritium Release from Irradiated Beryllium at Elevated Temperatures," 4th International Conf. on Fusion Reactor Materials, Kyoto, Japan, Dec. 1989. To be published in J. of Nuclear Materials (1990).
7. G.J. DeSalvo and R.W. Gorman, "ANSYS Engineering Analysis System Users Manual," Revision 4.4, Swanson Analysis Systems, Inc. (May 1989).
8. D.N. Braski, ASTM Spec. Tech. Pub., ASTM-STP-1047, p. 161, 1990.
9. B.A. Loomis and D.L. Smith, "Relationship of Microstructure and Tensile Properties for Neutron Irradiated V Alloys," p. 225 in Fusion Reactor Materials, Semi-Annual Progress Report, DOE/ER-0313/8, August, 1990.
10. W.F. Calaway, "Electrochemical Extraction of Hydrogen from Molten LiF-LiCl-LiBr and Its Application to Liquid Lithium Fusion Reactor Blankets," Nuclear Technology, 39, 63 (1978).
11. C. Hsu and Buxbaum, "Palladium Catalyzed Oxidative Diffusion for Tritium Extraction from Breeder Blanket Fluids at Low Concentrations," J. Nuclear Materials, 141-143, 238 (1986).

12. R.A. Causey, M.I. Baskes and K.L. Wilson,"The Retention of Deuterium and Tritium in POCO AXF-SQ-Graphite," J. Vac. Science and Technology, A4, 1189 (1986).

13. J.L. Anderson et al., "Experience of TSTA Milestone Runs with 100 Gram-Level of Tritium," Fusion Technology, 14, 438 (1988).

14. L.J. Porter, "Upgrade of a Fusion Accident Analysis Code," MIT REPORT PFC/RR-89-10 (June 1989).

15. Z. Musicki, "FUSCOST: A PC-Based Menu Driven Program for Economic Analysis of Fusion Facilities," Proc. of 12th Symp. on Fusion Engineering, Vol. 2, pp. 955-958, Monterey, CA, Oct. 1987.

16. T.J. McCarville, W.R. Meier, C.F. Carlson, B.B. Glasgow, "SAFIRE-A System Analysis Code for ICF Reactor Economics," LLNL UCRL 15872, Vol. 1, Jan. 12, 1987.

Figure Captions

Fig. 1.1. Target gain as a function of driver energy.

Fig. 1.2. Overall view of the SIRIUS-T reactor.

Fig. 1.3. Reactor structural frame.

Fig. 1.4. Cross section of a typical hexagonal blanket module.

Fig. 1.5. Coolant distribution in first wall tile metallic backing.

Fig. 1.6(a). Effect of Li enrichment on the TBR.

Fig. 1.6(b). Effect of overall blanket thickness on TBR.

Fig. 1.7. Radial build of SIRIUS-T blanket.

Fig. 1.8. Radial variation of dpa and helium production in vanadium alloy structure.

Fig. 1.9. Cross-section of hexagonal module showing direction of coolant flow.

Fig. 1.10. Reference coolant routing through a blanket module.

Fig. 1.11. Life limiting mechanisms for SIRIUS-T components.

Fig. 1.12. Tritium removal system for the lithium breeder and the helium intermediate heat transfer circuits.

Fig. 1.13. Blanket module showing tile replacement from inside the reactor.

Fig. 1.14. Blanket module replacement from outside the reactor.

Fig. 1.15. Direct costs of SIRIUS-T are dominated by the reactor chamber and driver.

2. INTRODUCTION

Tritium production has been an active part of the nuclear activity within the U.S. national laboratories since the introduction of thermonuclear weapons. For the most part, tritium is currently produced in fission reactors designed for and dedicated to that purpose. By far the major user of tritium is the U.S. government with a miniscule requirement by industry. These ageing production reactors are presently being phased out and need to be replaced. The U.S. Department of Energy has initiated a New Production Reactors Program which will provide for the design, construction and operation of new facilities for the production of tritium and other special nuclear materials. Preliminary requirements are currently being prepared, leading to construction and operation by the year 2000.

The two fission designs currently under investigation utilize thermal neutrons produced in fissile fueled nuclear piles to irradiate ^{6}Li in fertile assemblies. They are the heavy water moderated reactor HWR[1] and the modulated high temperature gas-cooled reactor MHTGR.[1] Aside from tritium production, prime consideration is given to the safety and environmental aspects, both during operation and the eventual decommissioning of the reactors.[2] The commitment by the Secretary of Energy is that these reactors will have a level of safety that is equal to or greater than that of modern commercial nuclear power plants

It has long been known that a nuclear fusion facility is ideally suited for tritium production due to the high number of neutrons it provides relative to the thermal energy of reaction. For example, in the fissioning of ^{235}U, 250 MeV of energy is produced during the production of one triton atom, whereas in a DT reactor, only 27.21 MeV of energy is released. Therefore, a DT reactor can produce 9 times as many tritons as a fission reactor of the same thermal power. The advantage is clear. On the other hand, fission reactors have been in existence for a long time, and for the last several years, new inherently safe reactors are on the drawing board. Fusion reactors have many years before they can be demonstrated as viable producers of energy. Nevertheless, it is interesting to see how such reactors can perform as tritium producers both from the technology and economic standpoints.

Besides being copious producers of tritium, fusion reactors have other advantages. Current fission reactors require batch processing of tritium while fusion reactors can have on-line tritium recovery. Thus, the vulnerable tritium inventory is lower. There are obvious safety advantages in the operation of fusion reactors as compared to fission. Finally, fission reactors have spent fuels which must be processed and the long-lived isotopes disposed of in deep geological repositories. The structure of fusion reactors will also be activated by the 14.5 MeV neutrons. However, with proper design and material selection, these materials can meet Class C waste disposal ratings, which require shallow burial (>5 m) and a much shorter monitoring period.

Over the last five years there have been four studies of fusion tritium production facilities, two in magnetic (MFE)[3,4] and two in inertial (ICF)[5] confinement. One ICF study[5] utilized indirect drive with an unspecified laser driver. The other, the present study, utilizes direct drive symmetric illumination with a 2 MJ KrF laser.

The Fusion Technology Institute (FTI) at the University of Wisconsin, Madison, has been studying symmetric illumination ICF systems since 1983. This work has been performed in collaboration with the University of Rochester's Laboratory of Laser Energetics (LLE) and frequent consultation with the Naval Research Laboratory (NRL). For the past three years, the FTI has been investigating the tritium production facility SIRIUS-T. This is the final report on this study.

In the first year of the study scoping investigations aimed at coming up with a design which maximized T_2 production at the lowest cost and at identifying critical issues were performed. Several breeding concepts were considered and the most promising one selected. The second year was spent developing a self consistent design and performing optimization studies utilizing material fractions obtained from the actual design. At the same time the critical issues were addressed within the limitations of existing data. At the end of the second year, the design was frozen with respect to major parameters. In the final year, detailed analysis was performed and design adjustments made. During this year a detailed costing analysis was performed. Thus far there have been five papers presented at conferences on SIRIUS-T.[6-10] This, the final report on the study does not portray the amount of work performed during the past three years. It does, however, give a

glimpse into where the study ended up and the implications of such an application (i.e. T_2 production) for the current ICF program.

This report is organized to provide the reader with a quick overview up front with details following for those who will make use of them. Chapter 3 describes the overall reactor giving a birds-eye view of the whole system. Chapter 4 briefly discusses target performance and the justification for the selection of target and driver energy. In Chapter 5, a detailed description of the chamber is given. This chapter includes the work done on first wall protection and structural analysis of the first wall tiles and the structural frame. Chapters 6 and 7 give the neutronics analysis and thermal hydraulics respectively. Material lifetimes and justification are given in Chapter 8. Chapter 9, on tritium considerations, covers all areas of tritium except breeding which is covered in Chapter 6. Chapters 10 and 11 give a description of reactor maintenance and system integration, and Chapter 12, the economic evaluation. Chapter 13 makes a comparison of T_2 production in SIRIUS-T with other proposed facilities dedicated for the same purpose. Finally Chapter 14 gives the summary and conclusions.

References for Chapter 2

1. "New Production Reactors Capacity Cost Evaluation," DOE DP-0052, Oak Ridge National Laboratory (1988).
2. K.A. Klein, "New Production Reactor Safety," Trans. Amer. Nucl. Soc., 611, 154 (1990).
3. J.D. Lee, "Economic Analysis of a Magnetic Fusion Production Reactor," J. Fusion Energy, 6, 59 (1987).
4. J.D. Lee, "Tritium Breeding Analysis of a Tokamak Magnetic Fusion Production Reactor," J. Fusion Energy, 8,, 89 (1989).
5. W.R. Meier, et al., "An ICF Tritium Production Reactor," Fusion Technology, 8, 1208 (1985).
6. I.N. Sviatoslavsky, et al., "SIRIUS-T, A Symmetrically Illuminated ICF Tritium Production Facility," Proceedings IEEE 13th Symposium on Fusion Engineering, Knoxville, TN, Vol. II, 1416 (1989).

7. J.J. MacFarlane, et al., "Energy Deposition and First Wall Response in the SIRIUS-T Target Chamber," Proceedings IEEE 13th Symposium on Fusion Engineering, Knoxville, TN, Vol. I, 746 (1989).
8. J. Powers, et al., "SIRIUS-T Structural System Design and Analysis," 9th Topical Meeting on the Technology of Fusion Energy, Oak Brook, IL (1990).
9. I.N. Sviatoslavsky, et al., "SIRIUS-T, An Advanced Tritium Production Facility Utilizing Symmetrically Illuminated Inertial Confinement Fusion," 9th Topical Meeting on the Technology of Fusion Energy, Oak Brook, IL (1990).
10. M. Sawan and E. Mogahed, "Neutronics and Thermal Analyses for the Breeding Blanket of the ICF Tritium Production Reactor SIRIUS-T," 9th Topical Meeting on the Technology of Fusion Energy, Oak Brook, IL (1990).

3. OVERALL REACTOR DESCRIPTION

The SIRIUS-T reactor utilizes a 2 MJ KrF laser to symmetrically illuminate a single shell direct drive target with 92 beams uniformly distributed around a spherical chamber. A very conservative target gain of 50 is used and a repetition rate of 10 Hz giving 1000 MW of fusion power. The effective blanket energy multiplication is equal to 1.41 and thus the thermal power is 1410 MW which when converted at 36% power cycle efficiency yields 507 MWe. This electric power output is adequate to drive the laser even if the laser efficiency is only 5%.

The spherical chamber is supported on a pedestal in the center of a spherical containment building 22 m in radius as shown in Fig. 3.1. The 92 beams originate from a single KrF laser, are then split into two groups of 46 beams which are then routed in such a way that they approach the containment building from opposite sides, all in a horizontal configuration. Mirrors placed outside the building then direct each beam radially through the spherical wall of the containment building.

Each beam as it penetrates the containment building passes through a window which is the vacuum barrier between the containment and the laser beam layout facility. Since the beam at this point is quite large, on the order of 1.2 m in diameter, the energy density in the glass window is very low. After passing through the window the beam is incident onto a turning and focusing mirror. This next to last mirror turns the beam almost 90° and focuses it through an aperture which is 5 cm in diameter. The enclosure which houses the next to last mirror is shielded and the whole concept of the beam crossover through the aperture is designed to minimize the neutron streaming through the beam lines. Indeed, neutronic calculations have shown that the next to last mirror as well as the vacuum barrier window are lifetime reactor components. Once the beam passes through the aperture it expands back to its original size and then is incident onto the final focusing mirror. The distance between the final focusing mirror and the next to last mirror is 4 m. The function of the final focusing mirror located 20 m away from the center of the chamber is to turn the beam another nearly 90° and then focus it down through one of the beam ports in the reactor chamber to a spot directly in the center of the chamber. All 92 beams are focused

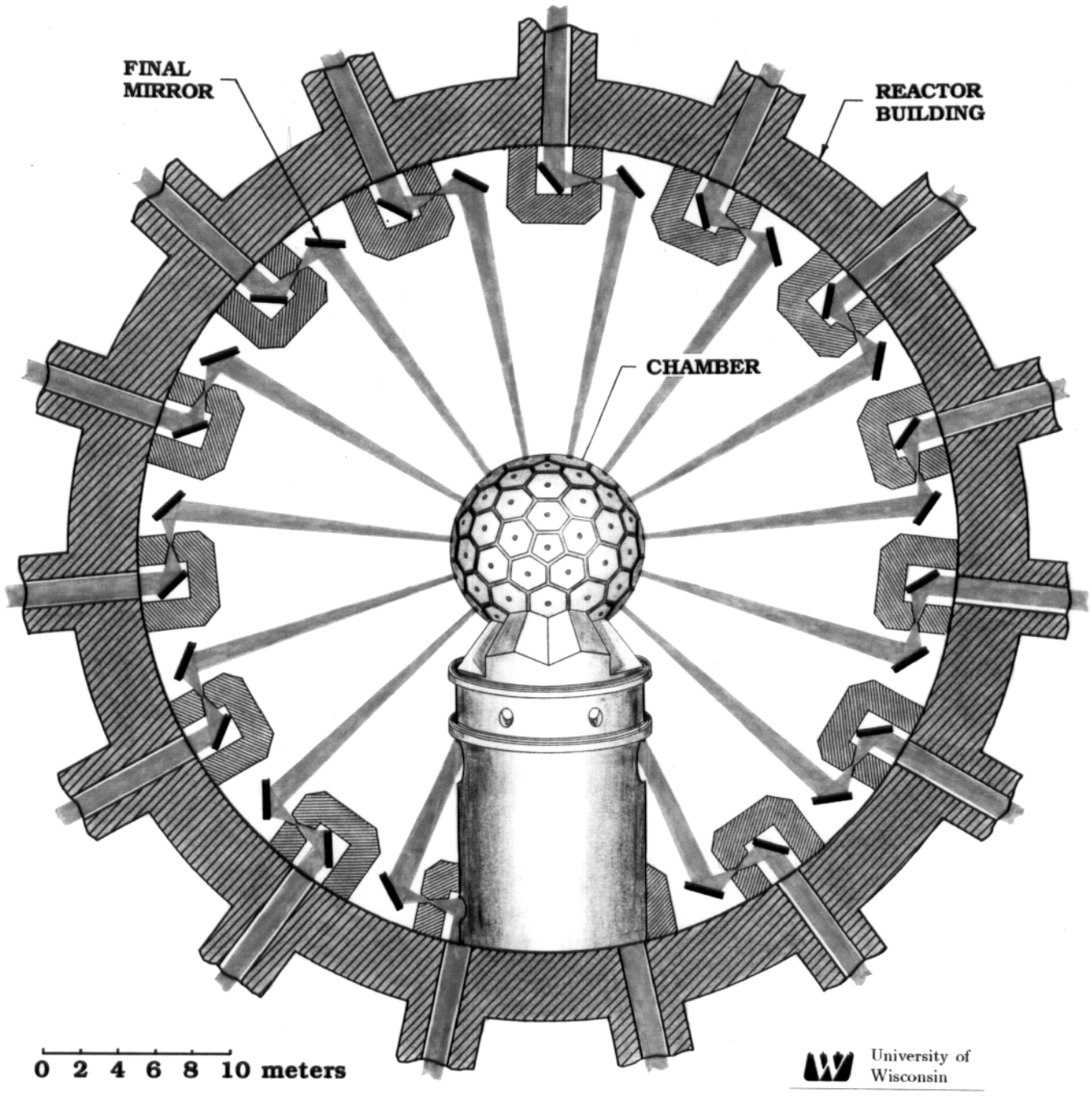

Fig. 3.1. View of the SIRIUS-T reactor shown within a cross section of the containment building.

simultaneously to the same spot converging onto the target which is illuminated in a direct drive mode. The f number of the final focusing mirrors is equal to 17.

Figure 3.1 shows that there are no beam tubes between the reactor chamber and the final focusing mirror. Rather the laser beam travels through empty space between the chamber and the containment building wall. There are several implications to this concept which are:

- The reactor chamber shares the same atmosphere as the containment building.
- Unburned tritium from the target is exhausted into the containment building.
- A steady state vacuum system is used to evacuate the containment building and the reactor chamber.
- The space between the reactor and the containment building wall is not cluttered, making maintenance of the reactor from the outside much easier.
- Maintenance of the final focusing mirrors is much eased.
- It is possible to decouple the chamber and its support from the containment building.

The containment building is spherical, 22 m in diameter and has a reinforced concrete wall 3.2 m thick which limits the biological dose at the outside surface during reactor operation to 2.5 mr/h. Although the reactor containment building is quite large it is dwarfed by such containment buildings as for Super Phénix, the French LMFBR and for ITER as shown in Figs. 3.2 and 3.3. After several conversations with architects and constructors, it appears that a spherical reinforced concrete building would be relatively easy to construct. In any case, it would not be that much more difficult than a cylindrical containment building such as that of Super Phénix and in some ways may be easier. A spherical shape is of course the preferred configuration for a pressure boundary, which in this case is an atmosphere of pressure, since the containment building will have xenon gas at 1 torr. The xenon gas is needed in the cavity as part of the scheme for first wall protection, and it shares the same space as the containment building.

The reactor chamber is spherical with an inner radius of 4 m and an outer radius of 5 m. The chamber configuration is based on the Platonic icosahedron figure which has twenty equilateral triangles joined together. These triangles can be superimposed onto a sphere. The surface of the

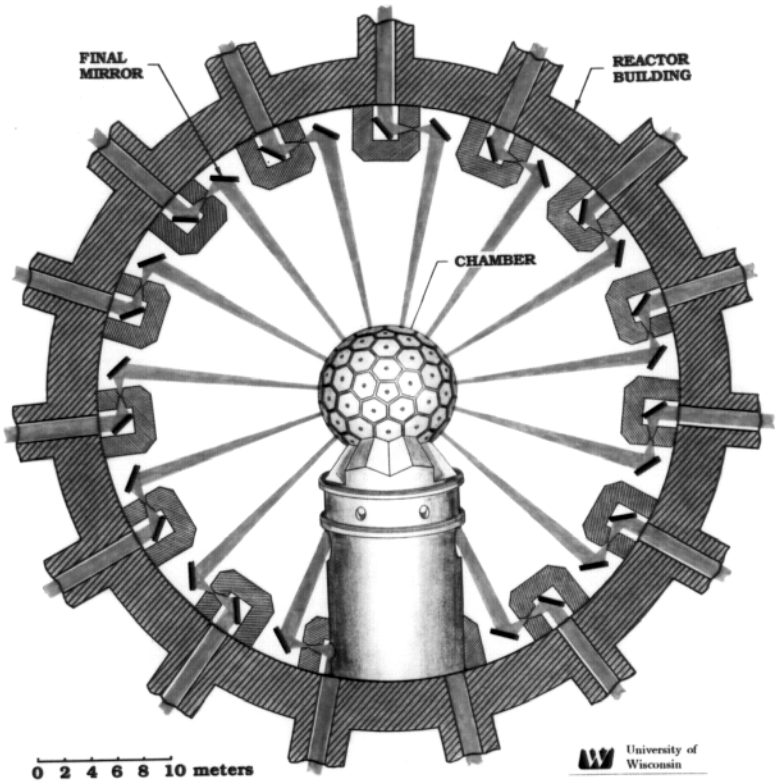

SIRIUS-T

**SYMMETRIC ILLUMINATION ICF
TRITIUM PRODUCTION FACILITY**

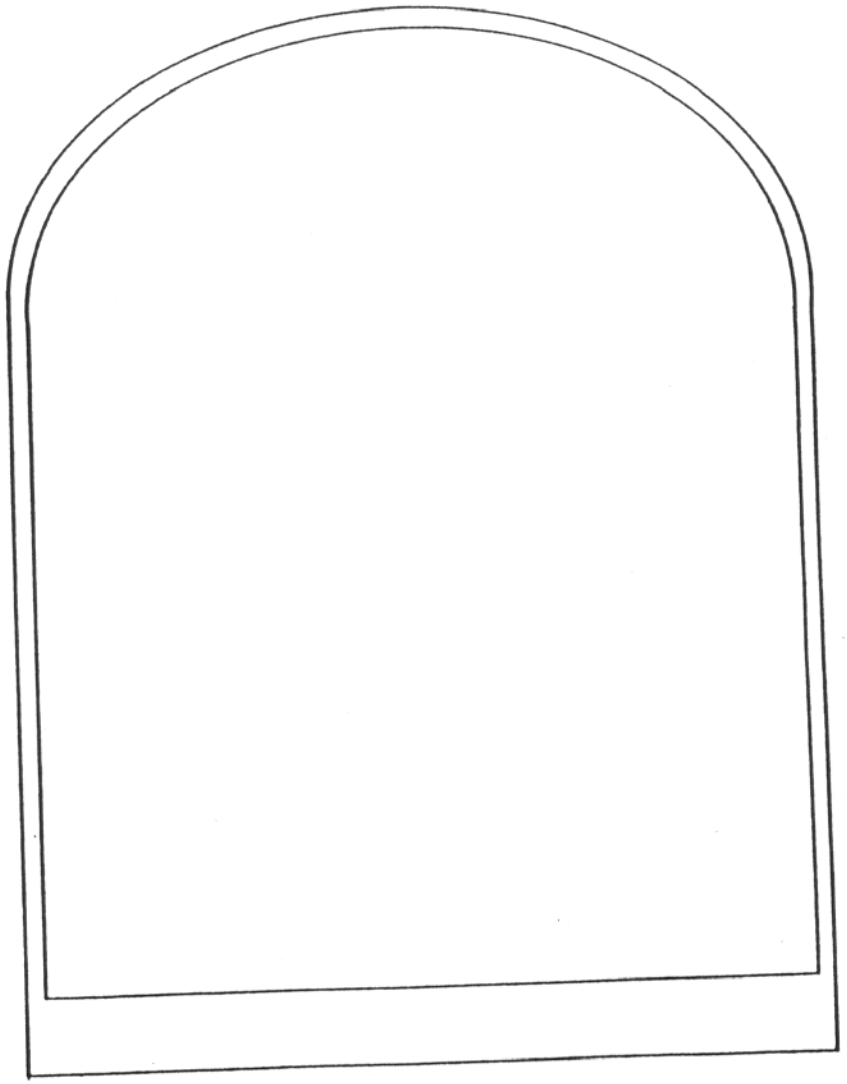

SUPER PHENIX

Fig. 3.2. Comparison of the SIRIUS-T containment building with that of SUPER PHENIX, the French LMFBR.

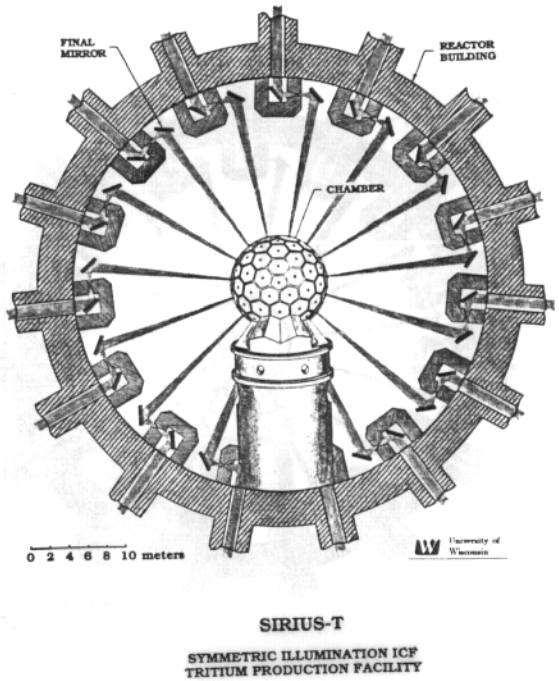

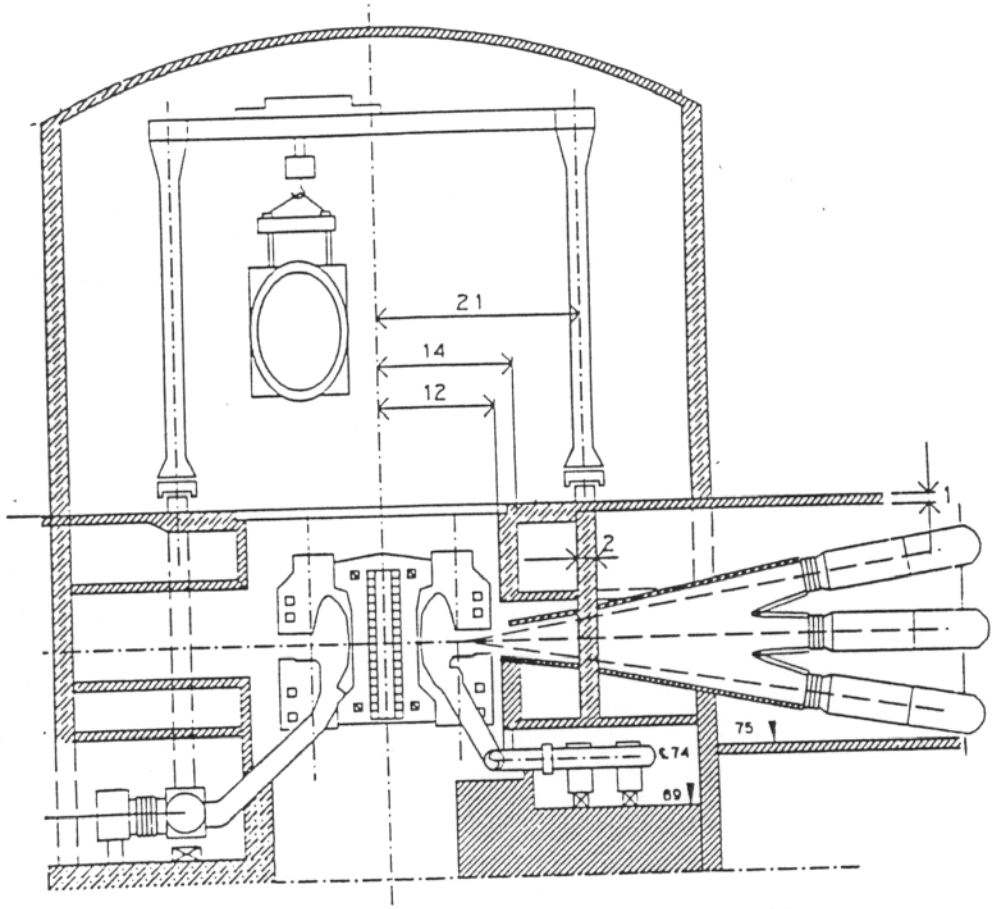

Fig. 3.3. Comparison of the SIRIUS-T containment building with that of ITER, the International Thermonuclear Engineering Reactor.

sphere can be further subdivided into hexagonal and pentagonal shapes in which both hexagons and pentagons share the same side. The pentagonal shapes occur at the confluences of the vertices of the triangles of which there are twelve locations. Thus there are always 12 pentagonal shapes regardless of the number of hexagonal shapes. The most basic subdivision has 42 surface elements, 30 hexagonal and twelve pentagonal and constitutes the familiar soccer ball. The next subdivision produces 92 elements of which 80 are hexagonal and 12 pentagonal. We have selected this configuration for SIRIUS-T. Similar subdivisions of 162, 252, 362, 492, 642 and so on are possible. Figure 3.4 shows the 42, 162 and 642 element versions.

One of the first observations in such a configuration is that the beam ports on the spherical surface are not equidistant. However, this does not necessarily mean that the distribution is not symmetric. A cluster of one pentagonal and five hexagonal shapes when taken by itself does not constitute symmetric illumination, but when all twelve clusters are taken together with the inclusion of the other 20 intervening hexagonal modules, then the coverage becomes symmetric.

An important issue in any ICF design is the protection of the first surface (so called first wall) which faces the target microexplosions. The surface heat load from the x-rays and ion debris is very high; moreover, since the pulse length of this incident energy is so short (several nano-seconds) this power cannot be dissipated by conventional heat transfer mechanisms. Several schemes for mitigating this problem are used: among them is making the chamber large, thus diluting the power by spreading it over a large surface; having a wetted wall and using the latent heat of vaporization to dissipate the power; and finally, using a buffer gas in the chamber. The function of the buffer gas is to stop the x-rays and ion debris, then radiate the energy over a longer time, thus reducing the incident heat flux on the first wall.

Symmetric illumination makes it very difficult if not impossible to have a wetted first wall protection scheme. Making the chamber very large has severe cost implications. We have thus opted for the buffer gas protection scheme for SIRIUS-T.

The first wall is made of tiles consisting of carbon/carbon composite bonded to a vanadium alloy (V-3Ti-1Si) backing which is actively cooled with liquid lithium. The tile configuration

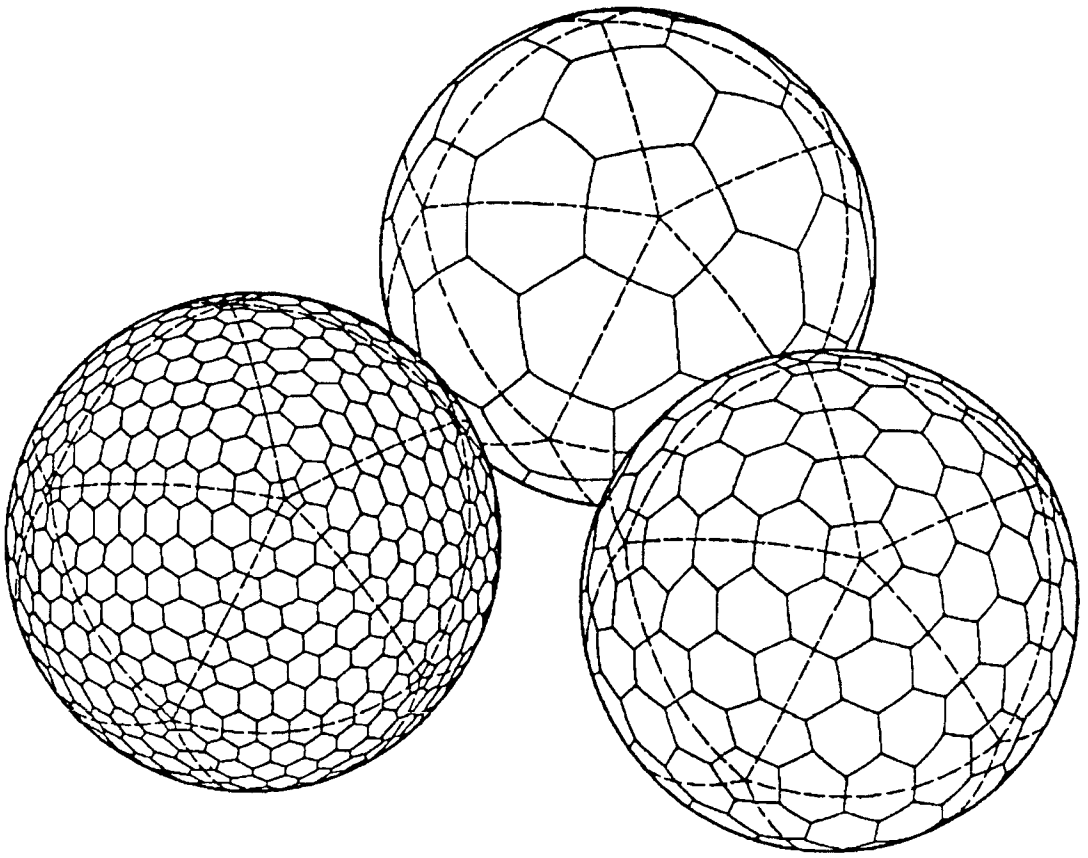

Fig. 3.4. Platonic icosahedron projections on spherical surfaces with 42, 162 and 642 elements.

conforms to the segmentation described earlier, of the 12 pentagonal and 80 hexagonal shapes. Each tile is attached to a module by means of a collar which is also the beam tube.

The blanket is 1.0 m thick and is made of V-3Ti-1Si alloy containers filled with Be plates and cooled with liquid lithium. Each module regardless of whether it is hexagonal or pentagonal, has only a single inlet and a single outlet coolant connection. Internally, some of the coolant is diverted to the tile, and after passing through the tile metallic backing, rejoins the bulk of the lithium from the module itself.

Extensive optimization has been performed with iterations between structural, breeding and multiplier materials, their volumetric fractions and distribution in order to maximize the breeding ratio. This is covered in detail in the neutronics chapter.

The modules in the chamber are held together by means of a homogeneous structural frame also made of V-3Ti-1Si. The frame has tapered honeycomb-like receptacles into which the modules are inserted from the outside. The beams of the frame do not extend all the way to the first wall but stop at a distance of 30 cm from the first wall. There are two reasons for this. The first is that the frame is designed to be a lifetime component and for this reason must be located far enough away from the first wall to make it survive radiation damage for the 30 full power years of operation. The second reason is geometric. We have designed the chamber such that modules, with the first wall tiles still attached to them, can be removed from the outside of the reactor. Thus, the chamber structural frame must be back far enough to allow the outer limit of the tiles to clear it as the module is being withdrawn radially from the frame. The design of the chamber also allows the discrete removal of a first wall tile from inside the reactor, without disturbing the module itself. This will be covered in detail in the maintenance chapter.

The reactor chamber is supported on a pedestal such that it is in the center of the spherical containment building as shown in Fig. 3.1. The pedestal interfaces with the chamber frame along a perimeter composed of six modules, a pentagonal module in the center surrounded by five hexagonal modules. Immediately beyond the interface, the pedestal slopes away from the chamber and connects to a cylindrical support, the base of which is built into the containment building.

Gravity forces are transmitted through the frame to the pedestal and are reacted by the floor of the containment building. The modules trapped within the pedestal can be extracted from inside the cylinder within the space provided by the sloping surfaces. The support cylinder has holes in it at appropriate places to allow laser beams to access the beam ports inside the support cylinder as can be seen in Fig. 3.1.

Cooling/breeding fluid in the form of liquid lithium is supplied to the reactor via supply and return manifolds which circumvent the chamber following the frame network in the horizontal direction. The manifolds are not shown in Fig. 3.1 so as not to obscure the chamber details. Supply and return manifolds alternate at each level to make it possible for each module to have access to both manifolds. In this way, each module has a single supply and a single return coolant connection.

After going through the reactor, the coolant goes to a heat exchanger of a helium intermediate loop while a small side stream goes through a cold oxide trap. After going through the heat exchanger, the lithium is returned to the reactor. A small side stream consisting of only 0.4% is diverted to a T_2 removal system where it mixes with a fused salt. The salt extracts the T_2 from the lithium. After the T_2 is transferred to the salt it is recovered via electrolysis. The hot helium gas then goes through a steam generator which supplies steam to a conventional steam turbine generator. The electricity produced is used to power the laser driver.

The unburned T_2 from the targets as well as the target debris, is exhausted through the beam ports along with some xenon gas into the containment building. A steady state vacuum pumping system consisting of Roots blowers backed up with mechanical pumps then evacuate the effluent gases and send them in a pipe under slight positive pressure to the tritium handling building. Here T_2 is separated and reused in new targets, while the xenon is recycled back into the reactor. Some T_2 remains stuck to the chamber and the building walls. Careful estimates of T_2 inventories and their leakage paths to the environment are covered in the tritium issues chapter.

Extensive neutronic optimization has been performed on the reactor chamber with the final TBR (tritium breeding ratio) being 1.9. The tritium requirement for 1 GWy at 70% availability is 39.2 kg/calendar year. If we assume that a TBR of 1.05 is required to operate the reactor, this means 41.16 kg of T_2 will be needed annually. At a TBR of 1.9, the surplus T_2 will be 33.3 kg/calendar year.

To prevent T_2 diffusion into the steam cycle, a helium gas intermediate loop is used. The intermediate heat exchanger (IHX) has a palladium coating on the outside of the V alloy tubes to insure oxidation of the permeating T_2. The oxidized T_2O is then collected on molecular sieves within the helium loop. With the exit temperature of the Li at 550°C, the steam generated is at 360°C giving a power conversion efficiency of 36%. With these precautions in place, the routine T_2 permeation into the steam cycle is only 4 Ci/day.

Table 3.1 gives the major parameters of the SIRIUS-T reactor.

Table 3.1. Major SIRIUS-T Parameters

Driver Energy	2 MJ
Target Gain	50
Driver Efficiency	5-10%
Repetition Rate	10 Hz
Pulse Length	10 ns
Fusion Power	1000 MW
Thermal Power	1410 MW
Electrical Conversion Efficiency	36%
Capacity Factor	70%
Chamber Inner Radius	4 m
Number of Beams	92
Tile Thickness	2 cm
Gap Between Tile and Blanket	1 cm
Blanket Thickness	97 cm
Structural Material	V-3Ti-1Si
Breeding Material	Li (90% enr. ^{6}Li)
Breeding Ratio	1.9
Blanket Energy Multiplication	1.4
Inlet Li Temperature	350°C
Outlet Li Temperature	550°C
Maximum Blanket Structural Temperature	650°C
Lifetime of Tiles	2 FPY
Lifetime of Modules	3 FPY
Containment Building Radius	22 m
Distance to Final Focusing Mirrors	20 m
Diameter of Final Focusing Mirrors	1.35 m
Lifetime of Final Focusing Mirrors	1 FPY
Containment Wall Thickness	3.2 m
Mass of Graphite in Reactor	3.44 tonnes
Mass of Li Inside Chamber	8.97 tonnes
Mass of Li Outside Chamber	17.94 tonnes
Mass of Vanadium in Reactor	272 tonnes
Mass of Be Purchased (includes 33% extra)	324.9 tonnes
Annual Tritium Production	33.32 kg
Maximum Routine T_2 Release	29 Ci/d
Maximum Accidental T_2 Release	19.9 g
Total Tritium Inventory	183.6 g

4. TARGET PERFORMANCE

The target for the SIRIUS-T study was not designed in detail. Instead the target performance was based upon gain estimates for direct drive targets. The gain of 50 with 2 MJ of KrF laser energy that was chosen for the study is shown in Fig. 4.1 in comparison with the latest gain estimates.[1] It is approximately a factor of two below the optimistic gain curve and very near to the lower conservative gain curve. The SIRIUS-T target performance corresponds to designs that are optimized to reduce the effects of Rayleigh-Taylor unstable growth on capsule performance. This is accomplished by imploding the target along a higher isentrope that might otherwise be used, thus trading some implosion efficiency for improved stability. This conservative design has less restrictive requirements on drive and capsule uniformity than the most optimistic designs.

The critical issue in direct drive target performance is the uniformity of the drive energy deposition around the target and the subsequent uniformity of the ablatively driven implosion. These are a function of a number of parameters, the most important being the number of laser beams and the sphericity and uniformity of the spherical shell target. The target fabrication issues were not addressed in the study. For SIRIUS-T the number of beams was chosen to be 92. This large number of beams adds to the complexity of the design. However, this large number of beams provides the opportunity to create a very uniform irradiation of the target as shown in Fig. 4.2. For 96 beams the uniformity has a broad minimum of about 0.1%. We assume that 92 beams will have equivalent characteristics. This large number of beams also provides an immunity to power imbalances in the beams and beam pointing errors. Figure 4.3 shows that a 5% power imbalance produces a 1% illumination nonuniformity for 60 beams. It is assumed that 92 beams would improve this to less than 1%. Figure 4.4 shows that a beam could be mispointed by 8% of the target radius and still produce only a 1% nonuniformity for 60 beams. Again, it is assumed that 92 beams would improve this. In each of these cases the large number of beams relaxes the laser design constraints, thus allowing a more conservative design.

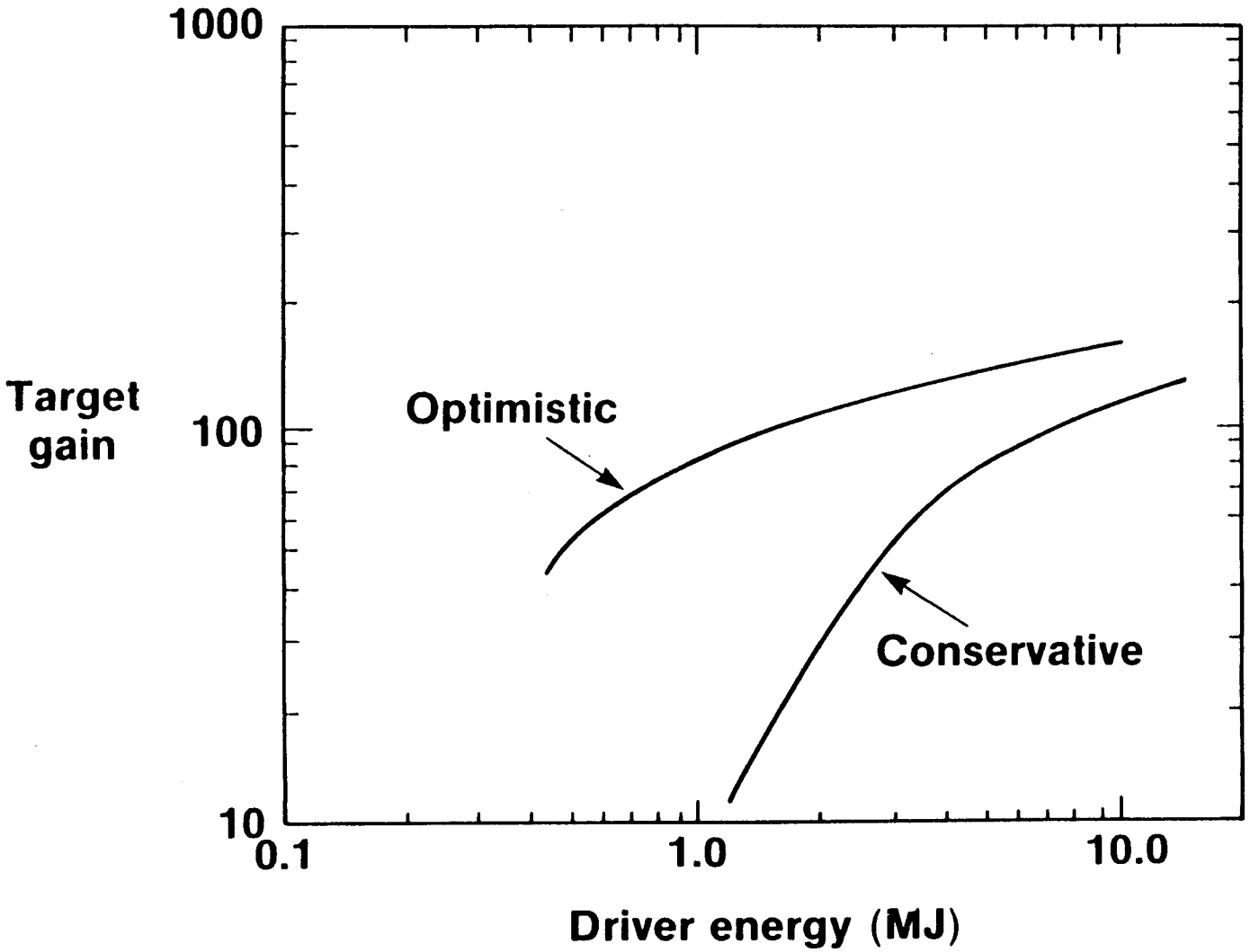

Fig. 4.1. Target gain curves for direct drive laser fusion targets.

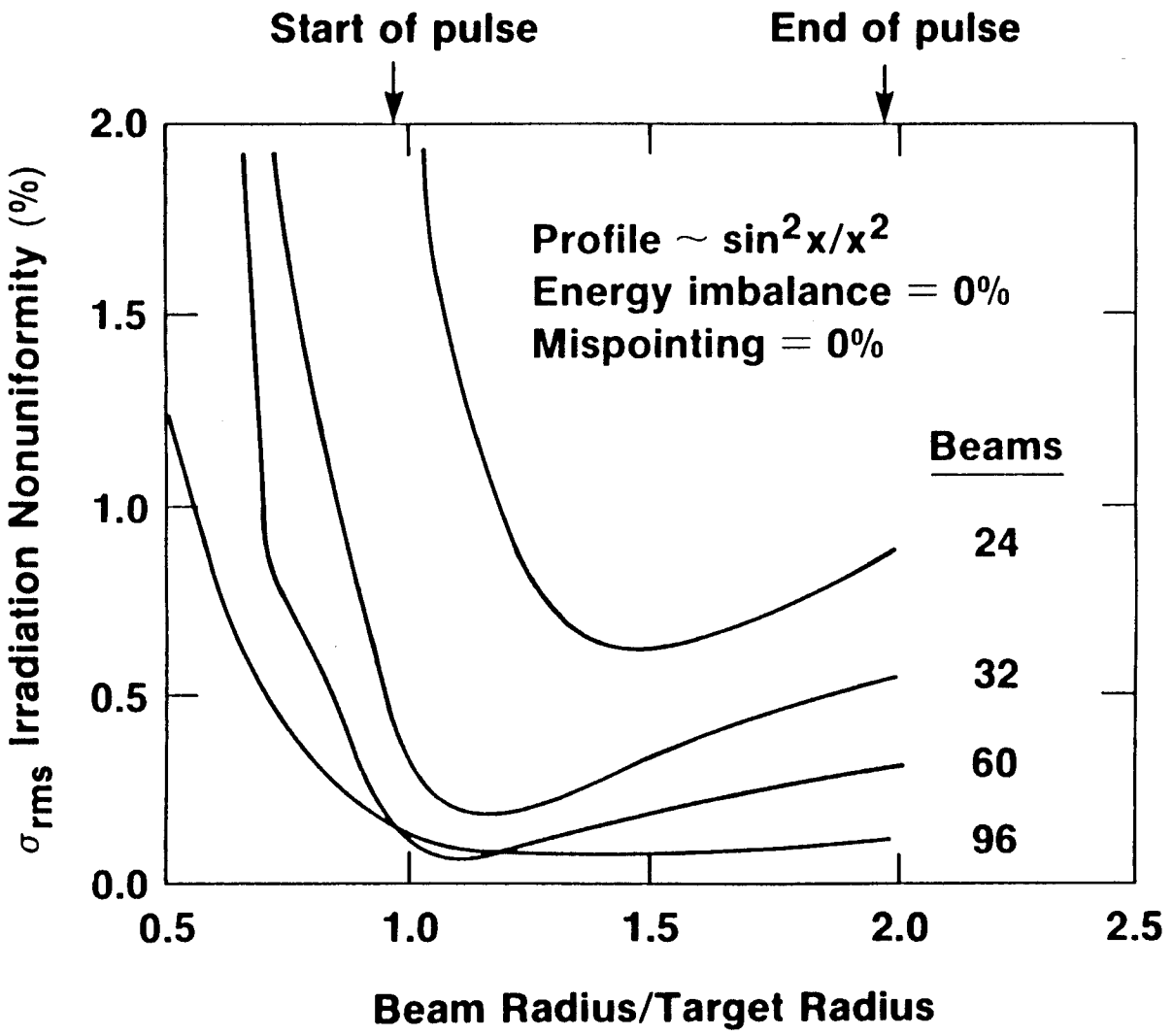

Fig. 4.2. Effects on target irradiation uniformity for different numbers of laser beams.

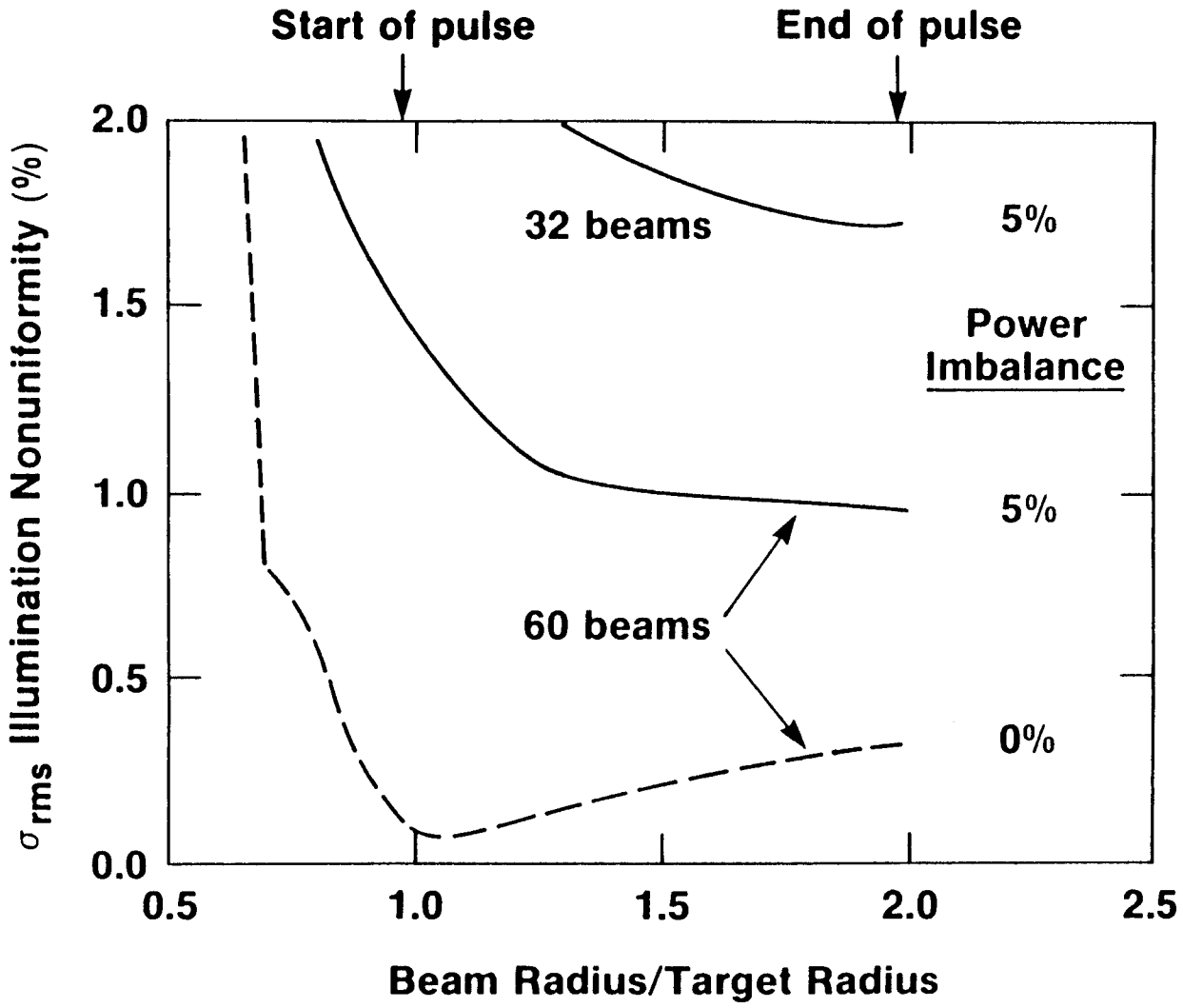

(Assumes: profile ~ $\sin^2 x/x^2$; perfect beam balance)

Fig. 4.3. Effects on target irradiation uniformity by power imbalances between the individual laser beams.

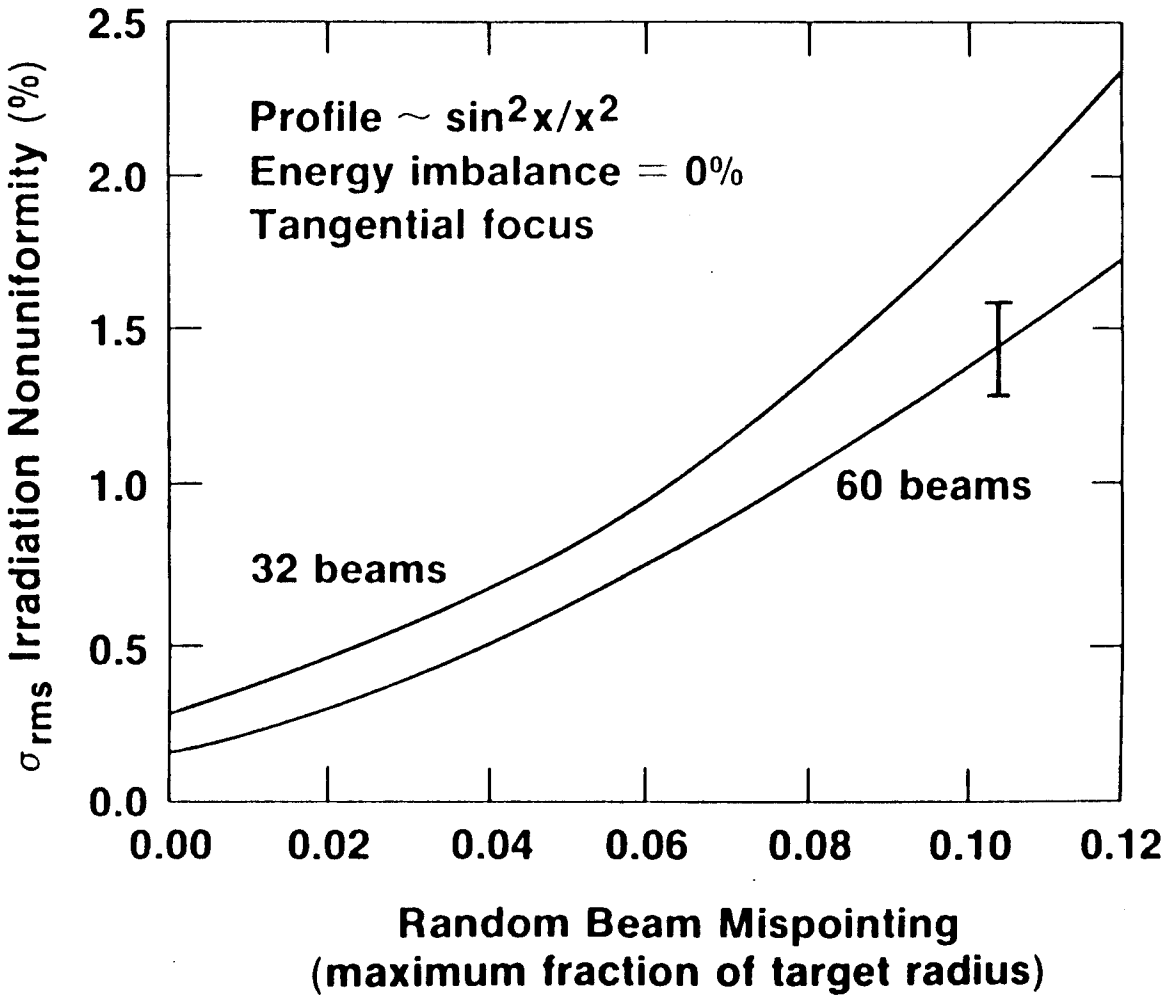

Fig. 4.4. Effects on target irradiation uniformity by pointing errors in the beams.

Reference for Chapter 4

1. R.C. Davidson et al., "Inertial Confinement Fusion Reactor Design Studies Recommended Guidelines," Sept. 14, 1990.

Figure Captions

Fig. 4.1. Target gain curves for direct drive laser fusion targets.

Fig. 4.2. Effects on target irradiation uniformity for different numbers of laser beams.

Fig. 4.3. Effects on target irradiation uniformity by power imbalances between the individual laser beams.

Fig. 4.4. Effects on target irradiation uniformity by pointing errors in the beams.

5. CHAMBER DESIGN

5.1. General Description

A brief description of the chamber has been presented in Chapter 3. In this section, the design will be given in more detail.

Figure 5.1 shows a cross section of the containment building with the reactor chamber supported on a pedestal in the center of the building. The figure only shows those beams that fall along the plane of the cross section cut. Obviously there are many beams within the shown half of the containment building which have been left out so as not to clutter the figure. Those are the beams which fall beyond the plane of the cross-section cut. The coolant manifolds as well as the target injector are the only other reactor components not included in the figure.

The reactor chamber is spherical with a 4 m inner radius and 5 m outer radius. It has 92 symmetrically distributed beams covering 360° of solid angle. Subdivision of the spherical surface is based on the Platonic icosahedron figure which has twenty equilateral triangles joined together along common sides. These triangles are the background against which further subdivisions of the spherical surface can be made. This subdivision consists of clusters of one pentagonal figure surrounded by five hexagonal figures where each hexagonal figure shares one side with the one pentagonal figure. Each pentagonal figure is located at the confluence of the equilateral triangle vertices of which there are twelve locations. Thus there are only 12 pentagonal figures in such subdivisions whereas the number of hexagonal figures can vary from a minimum of 30 to essentially an infinite number when the figures are made very small. For SIRIUS-T we have selected 92 figures, with 12 pentagonal and 80 hexagonal figures. Each figure will have a beam port in the center.

Symmetric illumination does not necessarily imply equidistant beam ports. For example the distance between adjacent beam ports in one pentagonal and a hexagonal shape is different from the distance between two hexagonal shapes. A cluster of one pentagonal and five hexagonal shapes when taken by itself does not constitute symmetric illumination. But when all twelve clusters are

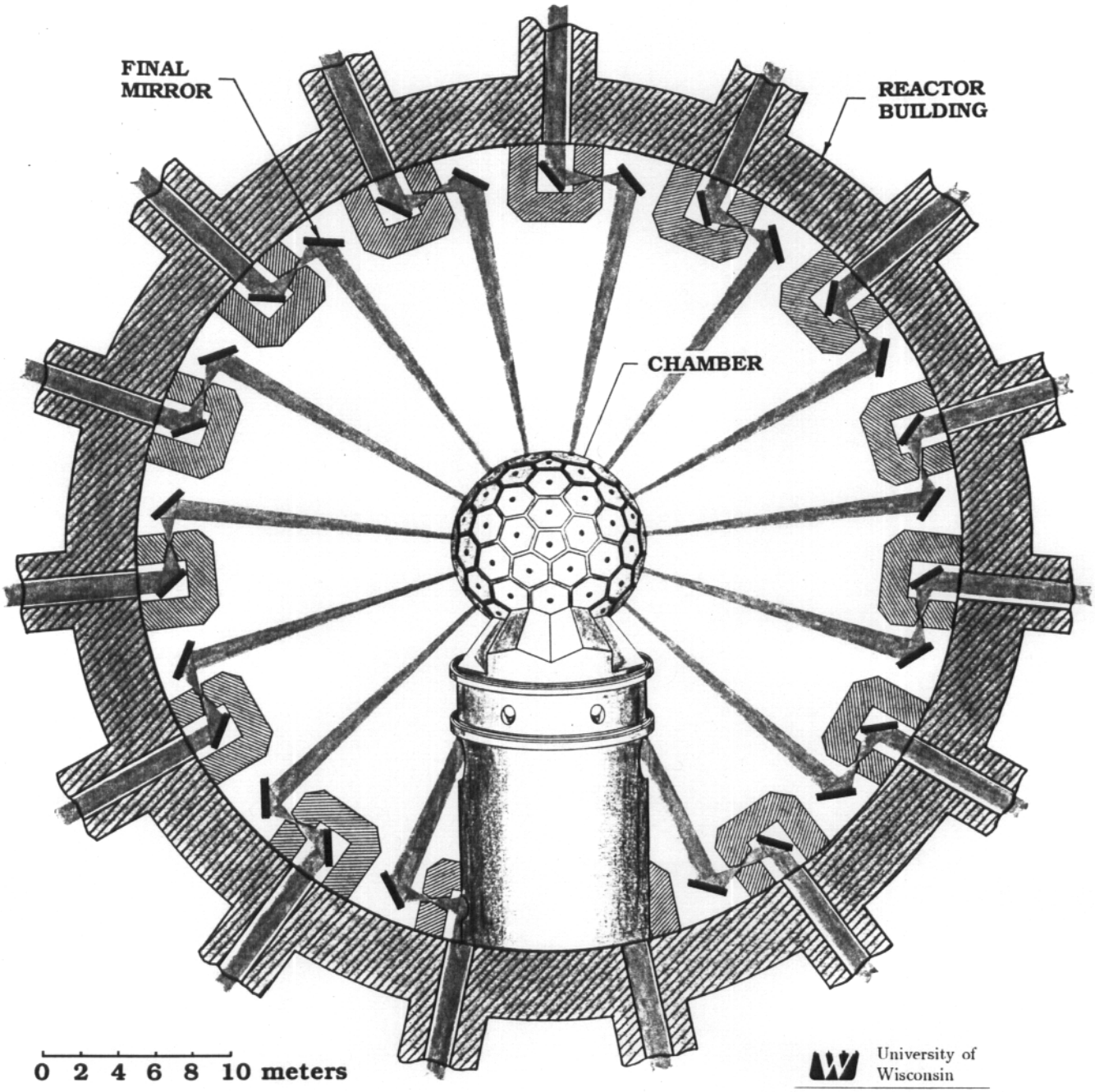

Fig. 5.1. SIRIUS-T, a symmetric illumination ICF tritium production facility.

taken together plus the inclusion of the remaining 20 intervening hexagonal shapes, then the coverage becomes symmetric.

The overall reactor was described in Chapter 3. It was shown that the 92 laser beams are focused into the reactor by 92 final focusing mirrors located on the containment building wall at a distance of 20 m. There are no beam tubes connecting the chamber to the final focusing mirror; rather the laser beams travel through the vacuum space of the containment building on their way to the chamber. The f-number of the final focusing mirror is 17 and thus the beam diameter at the first wall is 23.5 cm, at the entrance to the blanket it is 29.4 cm and at the final focusing mirror it is 117.6 cm. The actual beam port will be somewhat larger to allow for slight misalignments in the location of the module within the structural frame. Alignment of the beam port relative to the laser beam is not critical as long as all the laser beams converge onto the same spot without scraping the walls of the beam ports. It is also critical that the target injector is programmed to know very accurately where this focal spot is located so that the target can arrive at that location at the right time. This implies that the target injector should not be attached to the chamber physically but rather be independently supported on the reactor containment building. The art of tracking a target and aiming the mirrors is still in its infancy but the technology for doing this is already in hand.

The 92 breeding modules are held together in the reactor chamber by means of a homogeneous structural frame made of the vanadium alloy V-3Ti-1Si. A view of this frame is shown in Fig. 5.2. The structural frame consists of a network of pentagonal and hexagonal tapered receptacles into which the blanket modules are inserted from the outside. The inner radius of the structural frame is at 4.3 m, or 30 cm larger than the location of the first wall. This is done for two important reasons:

1. The structural frame is a lifetime component of the reactor and as such must be located far enough from the first wall as to make the accumulated damage in it consistent with 30 full power years.

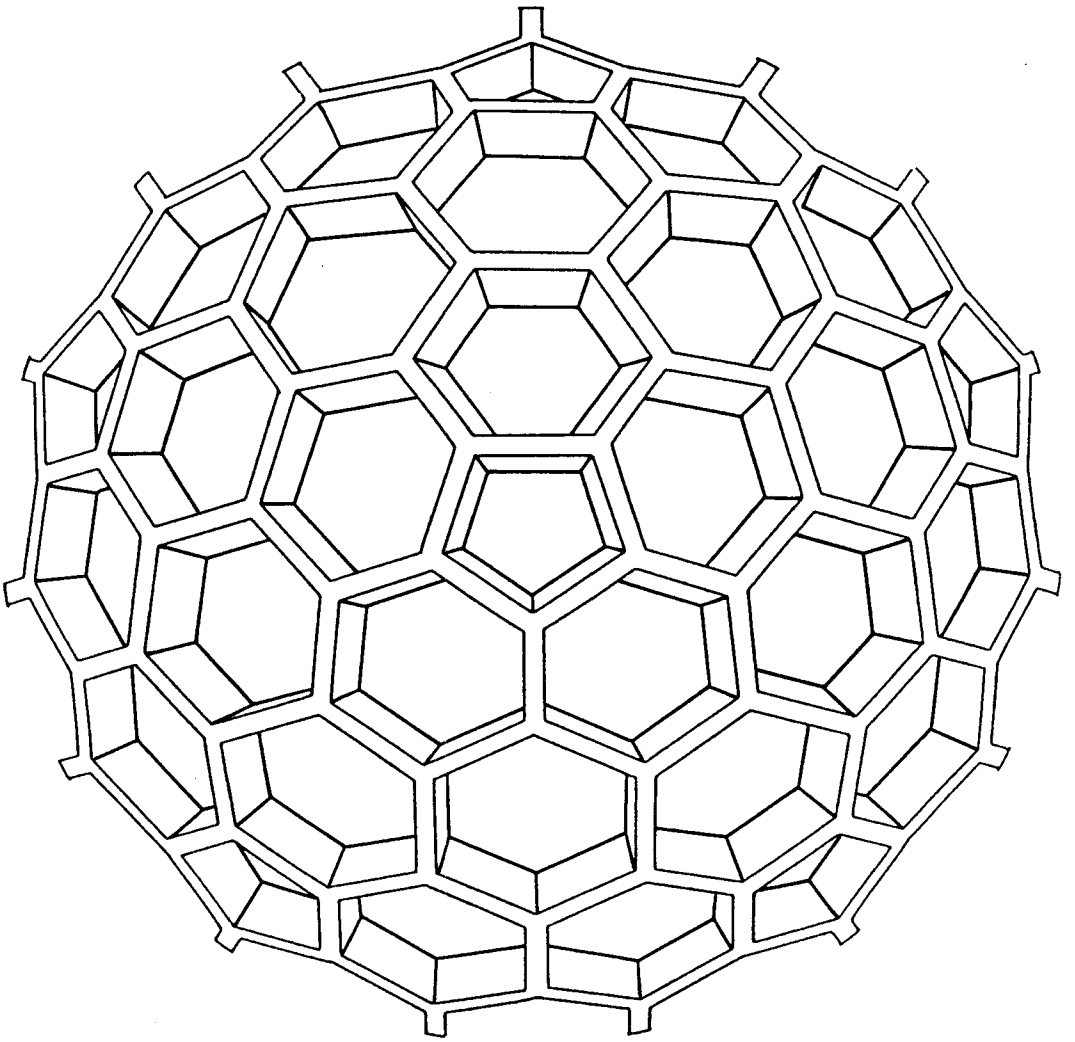

Fig. 5.2. Side view of the SIRIUS-T structural frame.

2. The modules, including the first wall tiles, can be recovered from the outside of the chamber. For this reason the innermost extremity of the structural frame must be far enough from the first wall as to make it possible for the attached tile to clear the frame when the module is being withdrawn.

At 30 cm into the blanket, the displacement damage rate for a 100 MJ yield target at 10 Hz in V-3Ti-1Si is ~5.5 dpa/FPY (full power years) and helium generation is ~8 appm/FPY. After 30 FPY the accumulated damage will be 165 dpa and helium will be 240 appm. Scaling from available data[1] shows that at these damage levels the strength of the alloy goes up to almost σy of 800 MPa while the ductility goes down to ~4%. The maximum stress in the structural frame for a web thickness of 8 cm under the worst conditions is <100 MPa as will be shown in Section 5.3 of this chapter. The maximum swelling at 240 appm is <1%.[1] This appears to satisfy the lifetime component criteria. Further, at a distance of 30 cm into the blanket, the first wall tiles clear the innermost extremity of the structural frame during extraction.

The blanket is the heart of the reactor where nuclear energy is converted to heat and tritium breeding takes place. As mentioned in Chapter 3, we have selected liquid lithium as the breeding/cooling material where the lithium is enriched to 90% ^{6}Li. A large amount of Be is used as a neutron multiplier. The blanket modules are made of V-3Ti-1Si and are filled with Be discs.

Figure 5.3 shows several views of a hexagonal breeding module which has a beam port going down its middle. Note the tapered shape of the module made for easy insertion and removal from the structural frame. The bottom view of the module looks at it from inside the reactor. What is illuminated by the target is the first wall tile which is the innermost hexagon shown in the bottom view. The tile is attached to and a part of the module, and when all the modules are in place within the reactor, the tiles form a continuous smooth spherical surface interrupted only by the outlines of the tile interfaces and by the beam ports.

Figure 5.4 is a cross section of a typical hexagonal module showing the internal details. The module is shown nestled between two webs of the structural frame. The outlines of two first wall tiles can be seen adjacent to the tile (shown in cross section) which is attached to the module.

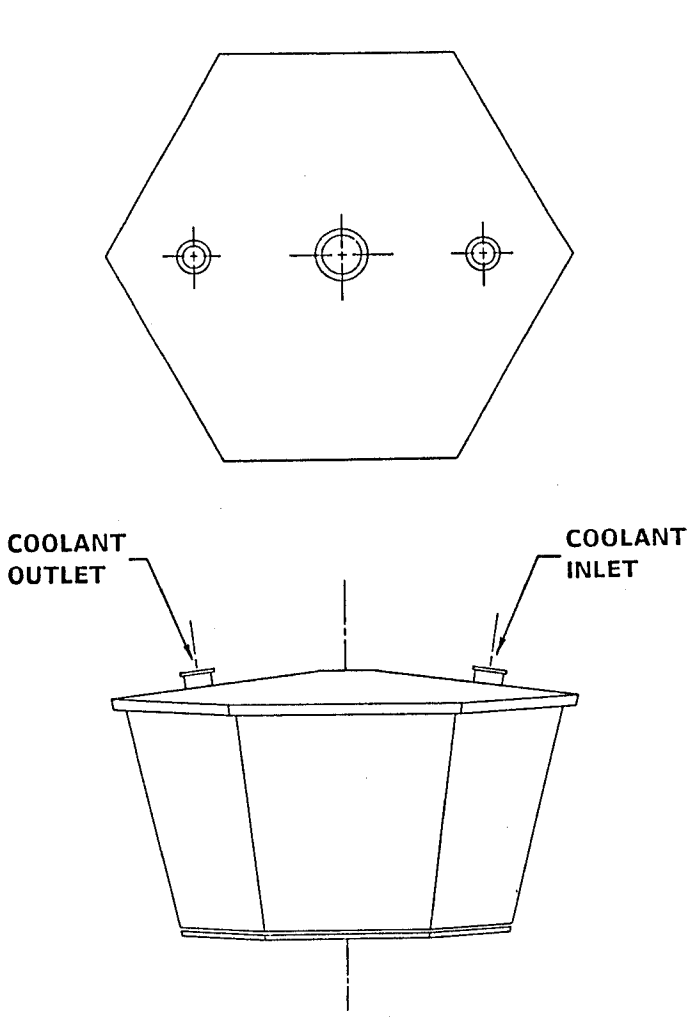

SIDE AND TOP VIEWS OF A HEXAGONAL BREEDING MODULE

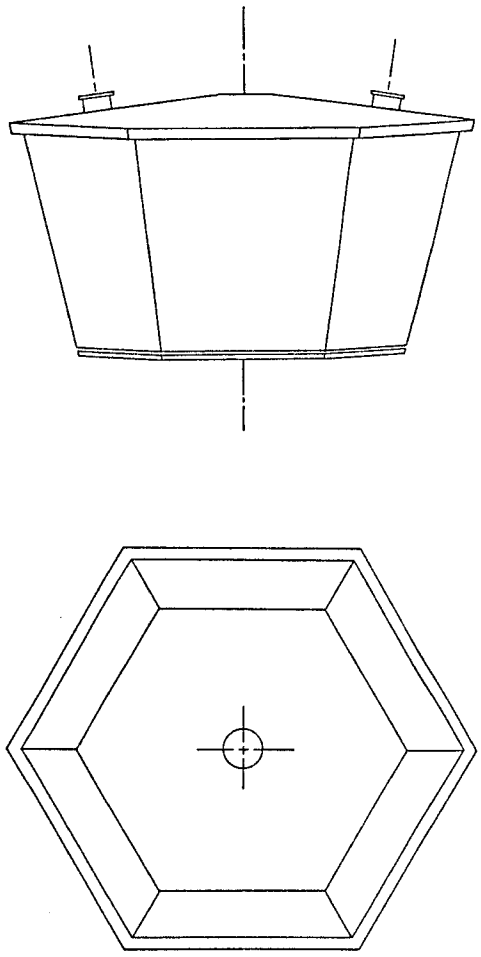

SIDE AND BOTTOM VIEWS OF A HEXAGONAL BREEDING MODULE

Fig. 5.3. Several views of a hexagonal breeding module.

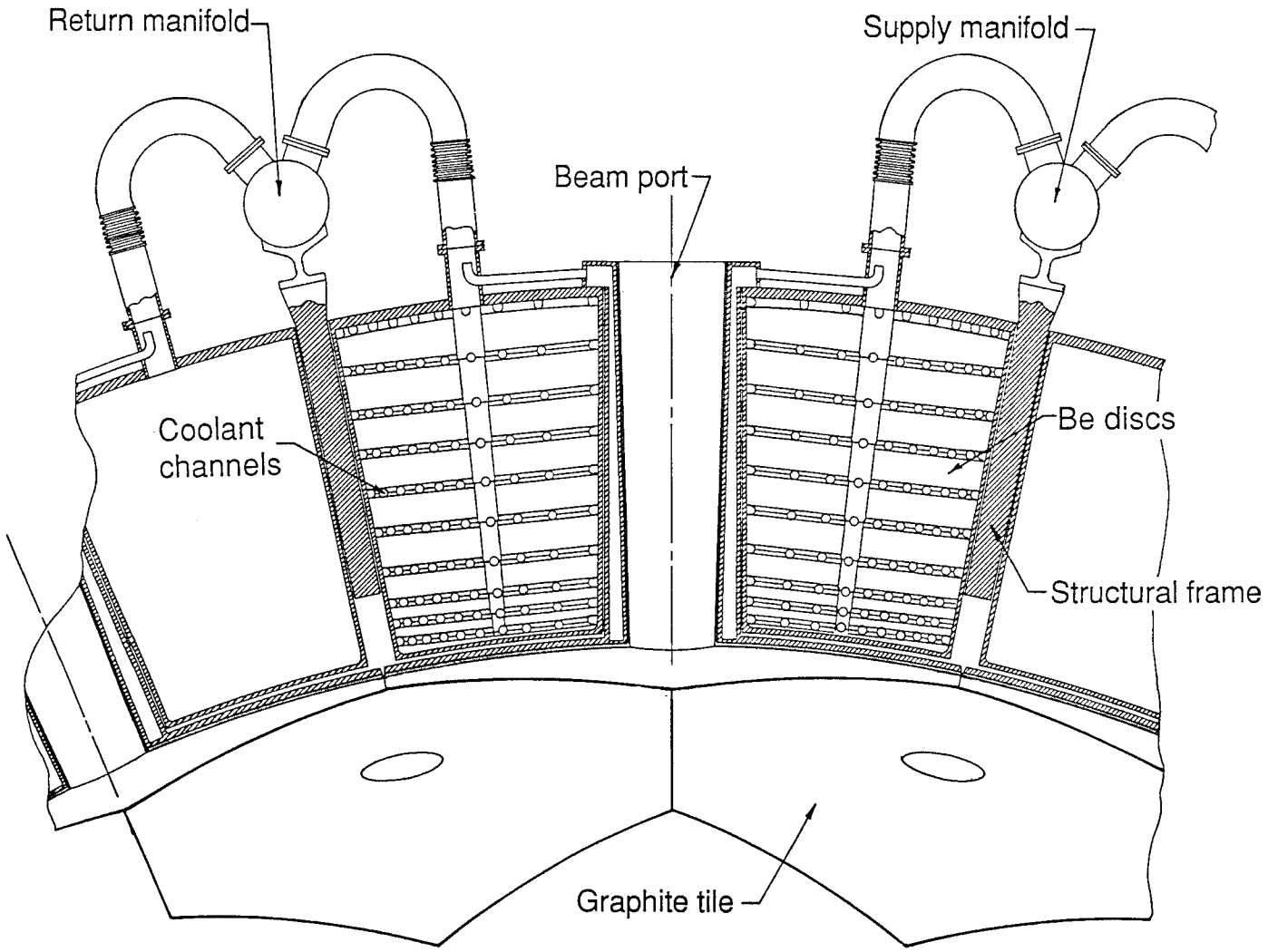

Fig. 5.4. Cross section of a typical hexagonal breeding module.

The tiles are shown flush with each other at the 4 m inner radius of the chamber. Note that the structural frame stops short of the first wall by 30 cm. When the module is extracted radially, the tiles clear the inner edge of the structural frame, and the rear corners of the module clear the supply and return coolant manifolds which are supported on the frame. The structural component of the module which consists entirely of V-3Ti-1Si comprises the six outer sides, the inner and outer closure sides, and a constant diameter tube connecting the inner and outer closure sides which constitutes the receptacle for the actual beam tube which is part of the first wall tile.

The first wall tile is attached to two concentric tubes, one a constant diameter tube which fits within the tube in the module and the other a tapered tube through which one of the laser beams passes on its way to the target in the center of the chamber. The constant diameter tube is needed to make it possible to extract the first wall tile from inside the reactor. The annular space between the two tubes is used to channel liquid lithium coolant to the actively cooled tile. Figure 5.4 shows how some of the main coolant supply is diverted to this annular space, and travels through one half of it to the first wall tile, then after going through the metallic backing of the graphite tile returns through the other half of the annular space, finally rejoining the main coolant in the return manifold. Figure 5.5 shows a layout of the coolant channels in the metallic backing of the first wall tiles. Coolant comes through one half of the annular space, then flows through a channel to one of the corners of the tile from which circumferential channels carry the coolant around the tile, finally connecting to the other half of the annular space. The thickness of the graphite tile is 1.0 cm, with 50% consisting of Li and the rest structure.

Figure 5.4 shows the blanket module as filled with Be discs. A single coolant supply line channels Li down one side of the module with channels radiating from it to the inner and outer perimeters of the module. Circumferential channels then carry the coolant between the Be discs to the other side collecting in a single return line leading to the return manifold. Figure 5.6 shows the radial build through the blanket and Fig. 5.7 shows the coolant path through the Be discs. Numerous iterations were needed between the neutronics analysis and thermal hydraulics to

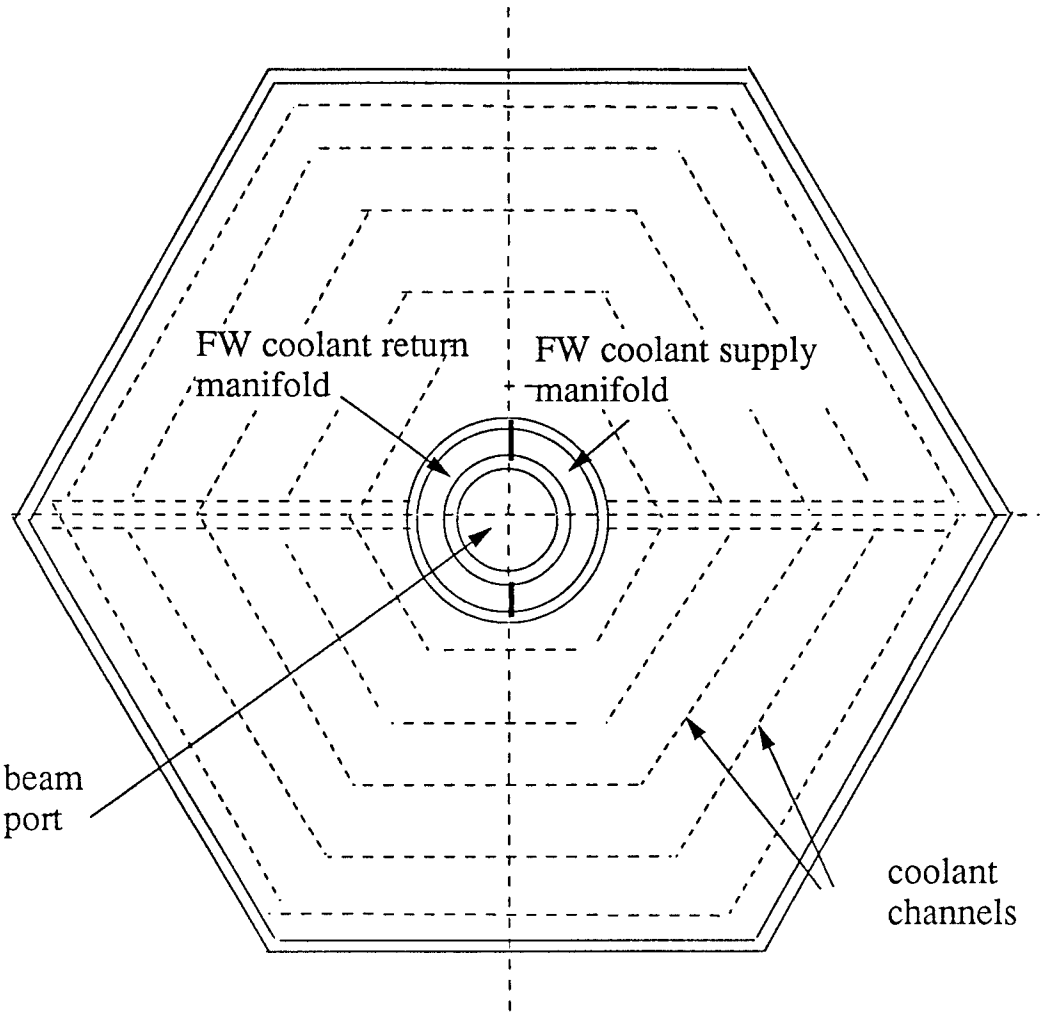

Fig. 5.5. Front view of first wall tile metallic backing showing the coolant channel layout.

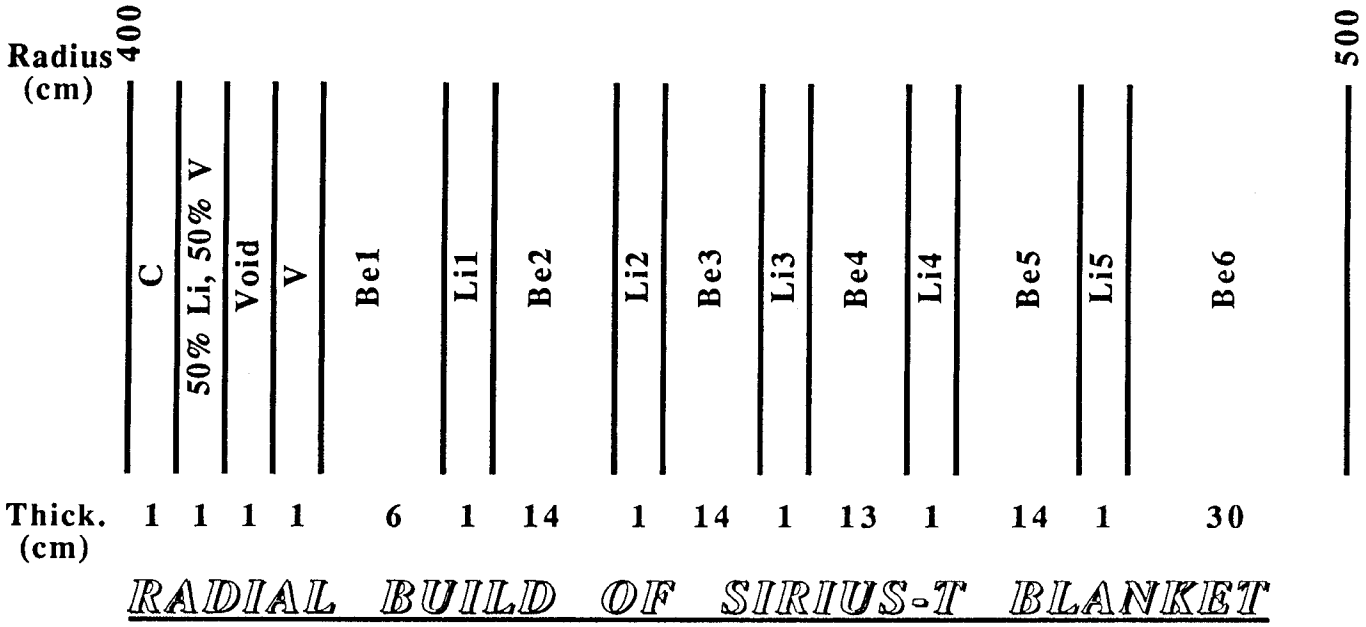

Be zone: 82.96% Be, 2.3% Li, 12.77% V, 1.97% void
Li zone: 85.26% Li, 12.77% V, 1.97% void

Fig. 5.6. Radial build of the SIRIUS-T breeding blanket.

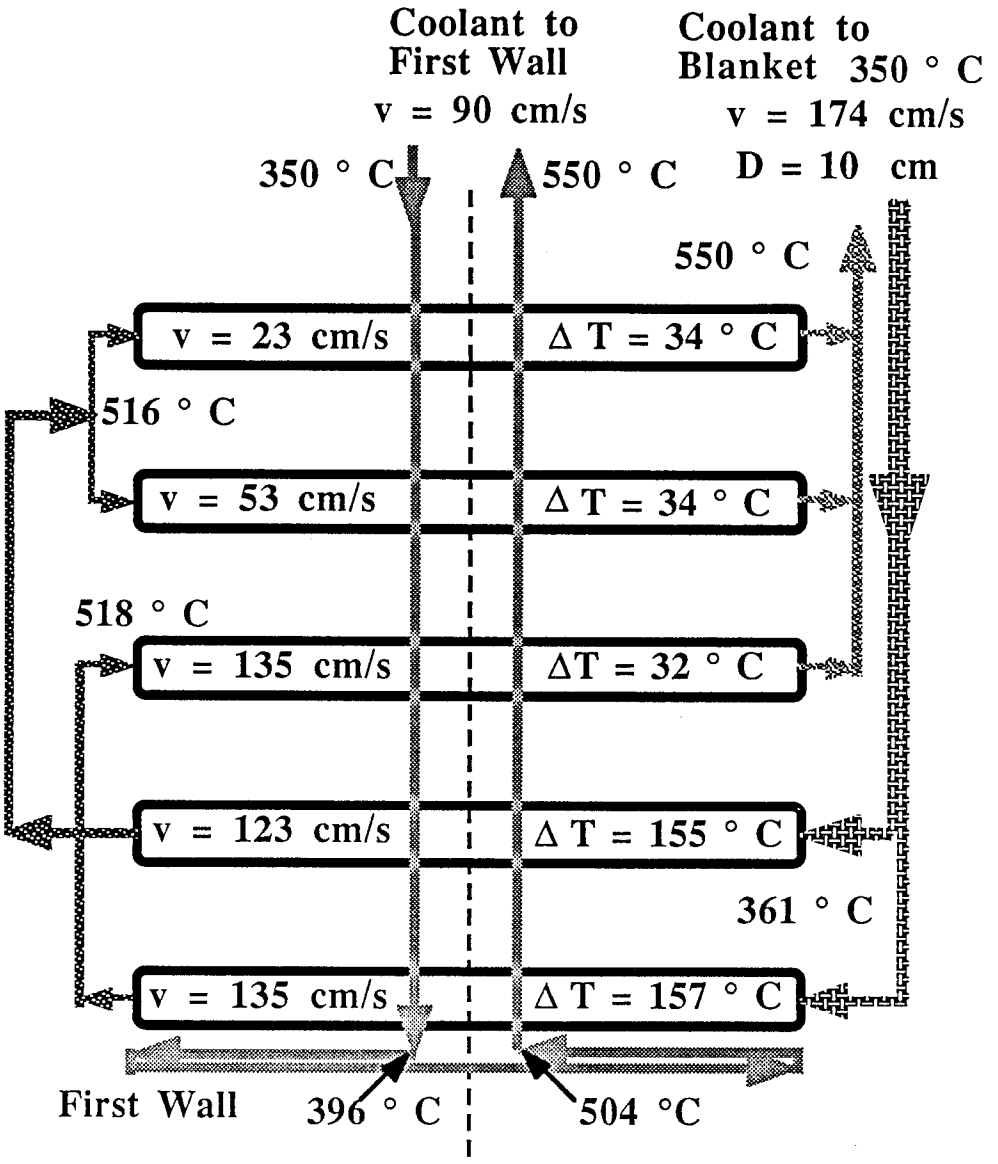

Fig. 5.7. Diagram showing the coolant routing through the Be discs.

maximize T_2 breeding while keeping the maximum structural temperature below 650°C. Chapter 7 gives the detailed thermal hydraulics analysis.

Figure 5.8 shows the conceptual layout of the supply and return manifolds. The figure shows the top view of only one half of the chamber. In actual fact, there is a supply manifold at the equator (not shown) followed by the same distribution on the underside of the reactor culminating with a supply manifold at the south pole. In effect, this means that there is a mirror image of the manifold distribution on the underside of the reactor (the mirror being at the equator) but with the manifolds rotated 180°. One thing that is immediately obvious from this manifold distribution is that 90 of the 92 modules will have a supply and return manifold in close proximity. Two very short connecting tubes will be needed for each module to hook up the coolant as can be seen in Fig. 5.4. The two exceptions are the two pentagonal modules at the north and south poles which will have only supply manifolds surrounding them. In this case, the return lines will have to span across the adjacent modules to hook up with the return manifolds. Supply and return coolant lines leading to the manifolds will come up vertically from the support pedestal. They are not shown in the figure.

Figure 5.9 is a view of the chamber on its support pedestal. Note the convoluted structural surfaces connecting the chamber with the support cylinder. These surfaces interface with the chamber structural frame along a perimeter which surrounds a cluster of one pentagonal module and five hexagonal modules. These modules are effectively trapped within the support cylinder. The convolutions shown in the figure make it possible for these modules to be extracted from the chamber on the inside of the support pedestal. Thus, maintenance of these modules will be performed by remote machines designed to operate within the support pedestal which has an inner diameter of 10 m. Holes in the support pedestal are needed to allow laser beams to reach the beam tubes on the modules trapped within the pedestal. The two rails shown surrounding the cylinder are needed for a remote maintenance machine which can circumnavigate the chamber on 360°. This will be described further in Chapter 10.

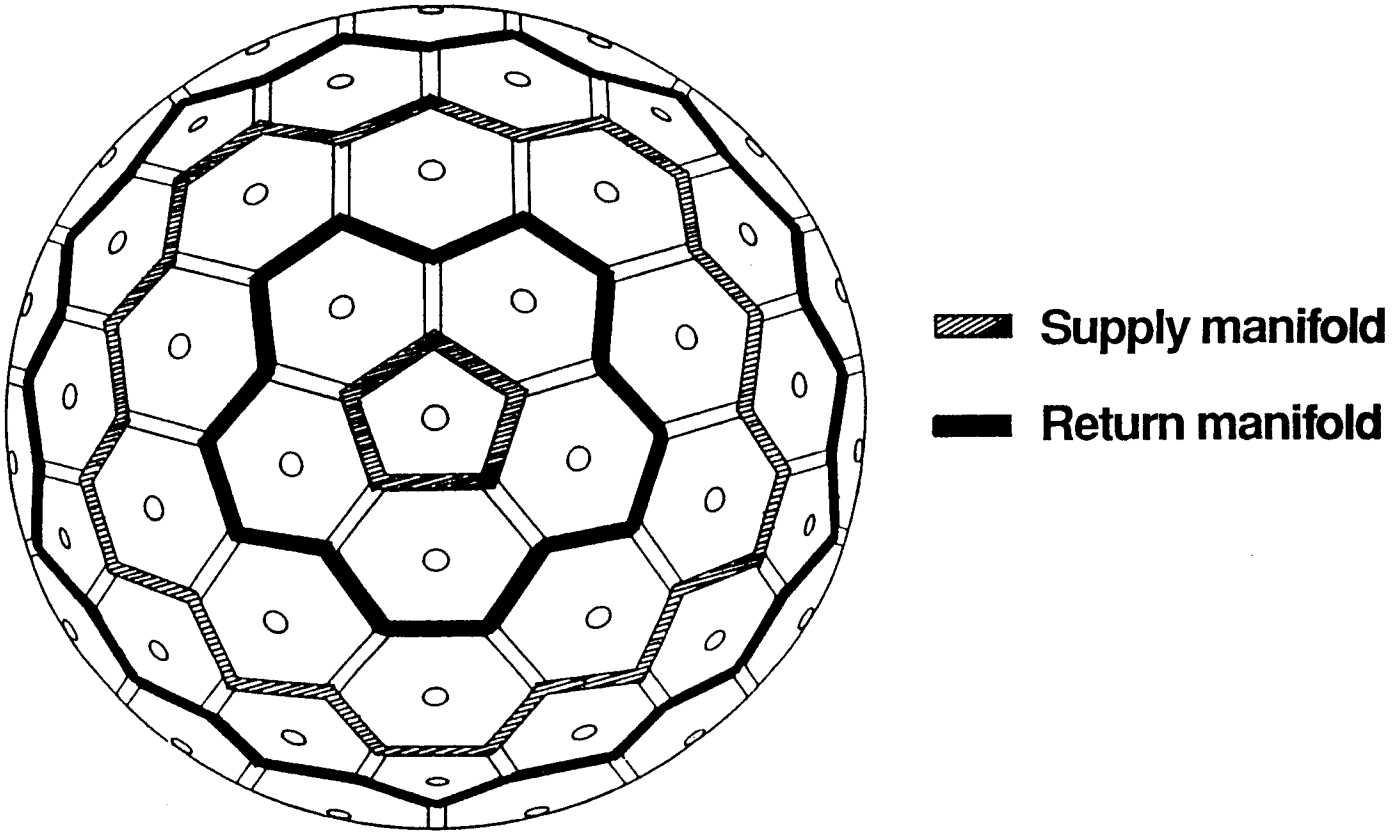

Fig. 5.8. Top view of reactor chamber showing the layout of the supply and return coolant manifolds.

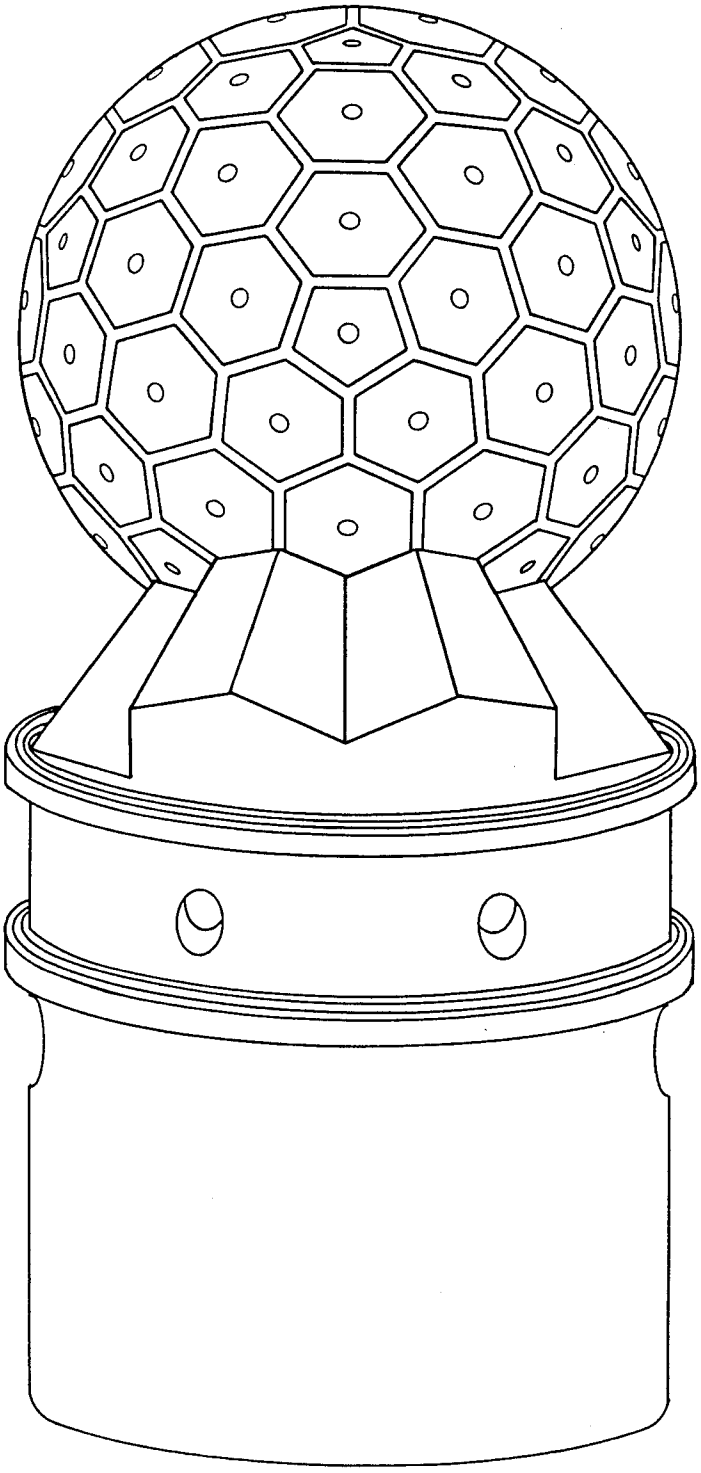

Fig. 5.9. Side view of reactor chamber on the support pedestal.

First wall protection in the chamber is provided by two mechanisms, graphite tiles and a buffer gas of xenon at 1.0 torr. The 4 torr-m of gas in the chamber effectively stops all the x-rays and target ions. The energy is then radiated by the gas over a longer time scale to the graphite tiles of the first wall. The graphite, which is an excellent high temperature material, then conducts the heat to the actively cooled metallic backing. The presence of the gas in the chamber prevents any evaporation of the graphite by limiting its temperature to values below the corresponding vapor pressure. Lifetime of the graphite tile is limited not by evaporation, but by swelling due to radiation damage. Detailed discussions of first wall protection are given in Section 5.2 and of structural analysis in Section 5.3. Material lifetime analysis is given in Chapter 8.

5.2. First Wall Protection

5.2.1. Numerical Simulations of the Target Chamber Plasma

CONRAD Simulations

We have used the CONRAD target chamber physics code to simulate the radiation-hydrodynamic environment for SIRIUS-T. Details of the numerical and physics models used in this code have been presented elsewhere.[2,3,4] A brief review of the major features of the code will be presented here. A schematic illustration of the SIRIUS-T target chamber is shown in Fig. 5.10.

CONRAD is a one-dimensional Lagrangian radiation-hydrodynamics code that simulates the major physical processes that will occur within the target chambers of high-gain ICF facilities. The code simulates time-dependent energy deposition by the target debris ions and x-rays, the expansion of the microfireball and blast wave, radiative emission from the microfireball, and the vaporization of and thermal conduction through the first wall material. The x-rays and debris ions emanate from a point source at the center of the chamber. (Neutrons have much longer mean free paths and usually deposit the bulk of their energy beyond the first wall.) Spherical symmetry is assumed. X-ray energy is deposited in the background gas and first wall using an exponential attenuation model which includes bleaching (electron stripping) effects.[5] Analytical fits are used for the x-ray cross-sections.[6] Debris ion energy deposition is calculated using a time-, charge-,

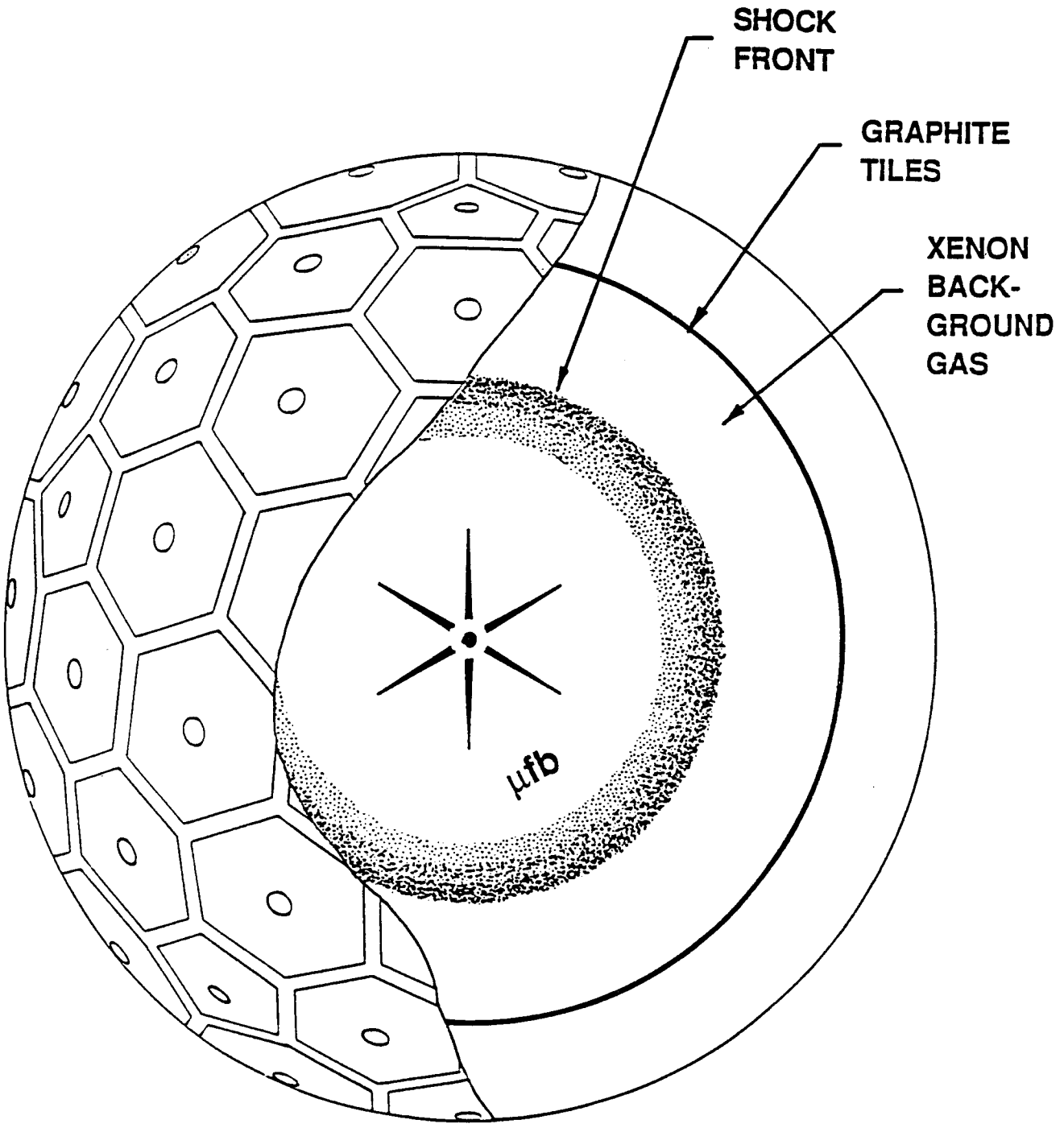

Fig. 5.10. Schematic illustration of the SIRIUS-T target chamber.

energy-dependent stopping power model.[3] Collisional ionization, collisional, radiative, and dielectronic recombination, and charge-exchange reaction rates are evaluated to determine the time-dependence of the debris ions as they travel through the background gas/plasma.

CONRAD transports radiation using a multigroup flux-limited diffusion model. 180 photon energy groups were used in the calculations discussed below. Equation of state and opacity data are computed with the IONMIX code.[7] In this code, steady-state ionization and excitation populations are calculated by balancing collisional ionization and excitation rates with collisional and radiative recombination and deexcitation rates. Hydrogenic ion approximations are used to compute bound-bound, bound-free, and free-free contributions to the opacities. Vaporization in CONRAD is modeled using a combination of energy balance and kinetic theory models.[4]

The chamber and target parameters used in our calculations are summarized in Table 5.1. The target was composed of a thin plastic shell surrounding the DT fuel. The partitioning of the target energy is characteristic of single-shell direct-drive targets, with a relatively high x-ray/debris yield ratio compared with targets with high-Z outer shells. The target x-ray spectrum was determined from target-burn calculations[8] and is shown in Fig. 5.11. The debris ion characteristics are listed in Table 5.2. Each ion species was divided into 10 groups that were emitted from the target over a period of 5 ns. (For computational reasons the D and T species were grouped together.) The ions leave the target fully ionized and pick up electrons as they travel through the Xe background plasma. The Xe density corresponds to a pressure of 1 torr at 0°C.

Table 5.1. Chamber and Target Parameters

Total Target Yield	100.0 MJ
X-ray Yield	6.0 MJ
Debris Ion Yield	20.9 MJ
First Wall Material	Graphite
Background Gas Species	Xenon
Background Gas Density	3.5×10^{16} cm^{-3}

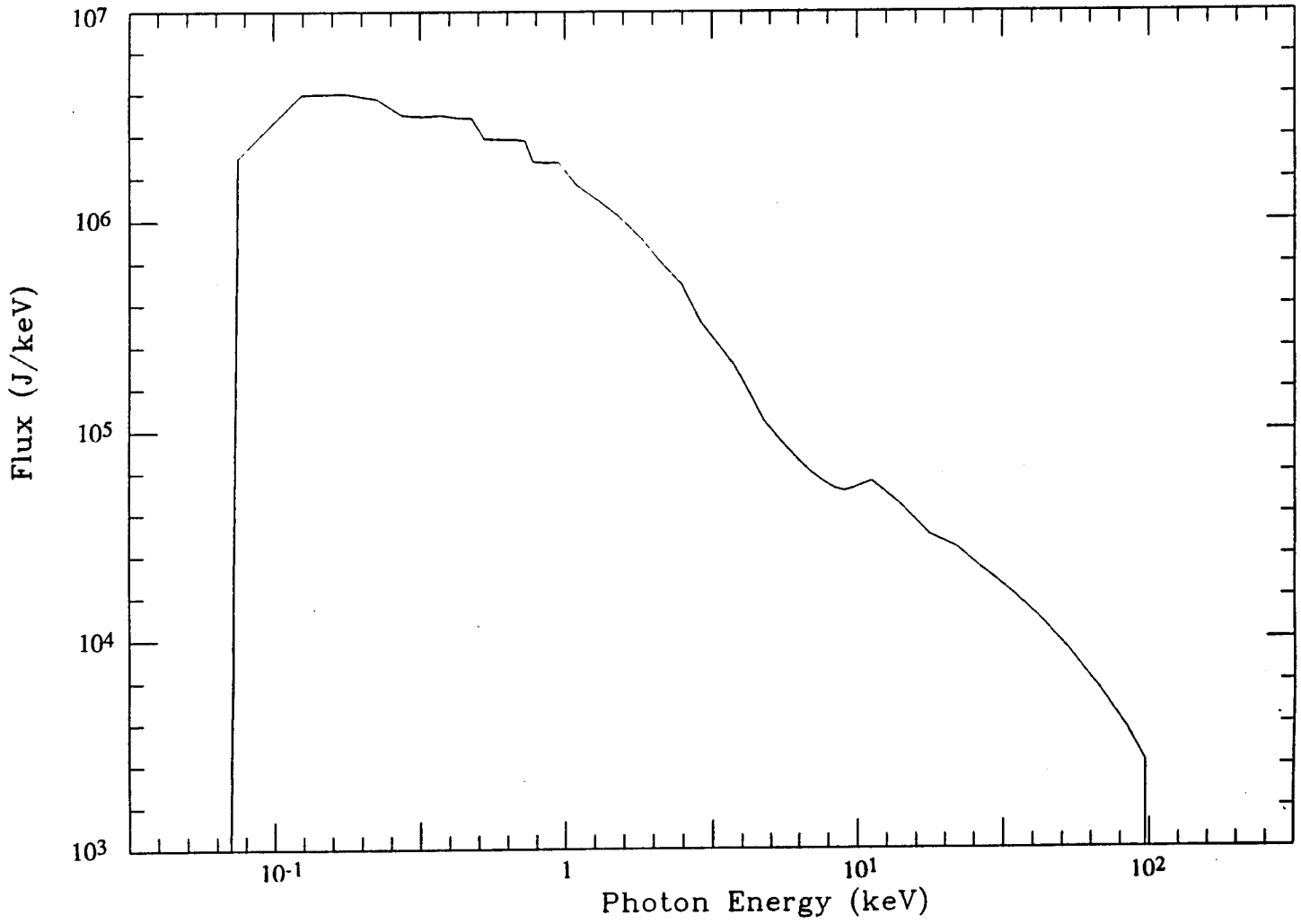

Fig. 5.11. Target x-ray spectrum.

Table 5.2. Debris Ion Properties

Ion	Initial Energy (keV)	Number of Ions	Total Energy (MJ)
H	138	1.05×10^{20}	2.3
D	94	9.70×10^{19}	1.5
T	140	9.70×10^{19}	2.2
He	188	3.73×10^{19}	1.1
C	1650	5.23×10^{19}	13.8

The temperatures within the Xe gas are shown in Fig. 5.12 at several simulation times. At these times, two regions with large temperature gradients are evident at each time. The innermost region corresponds to the outer boundary of the expanding microfireball. The outer region corresponds to the location of the carbon debris ions. By about 1-2 μs, essentially all of the target debris has been stopped in the background gas. A strong shock forms near the outer boundary of the microfireball. However, by the time the shock reaches the first wall, the pressures are quite small (P_{max} ~0.02 MPa = 0.2 bar).

Little radiative energy is absorbed by the graphite tiles before the microfireball has expanded to fill the chamber. This is because radiation emitted by the microfireball is reabsorbed in the relatively cool Xe gas surrounding it. The radiation flux and time-integrated flux at the first wall are shown in Fig. 5.13. By ~10^{-4} s, the microfireball fills the chamber so that the temperatures throughout the chamber cavity are above 1 eV. At this time the radiative flux at the first wall rises dramatically. By 10^{-3} s, most of the energy deposited by the target within the cavity has been radiated to the graphite tiles.

To examine the dependence of our results on the number of photon energy groups in our radiation transport model, we ran a series of calculations and compared the time-dependence of the flux at the first wall. Figure 5.14 shows the time-integrated flux at the graphite tiles as a function

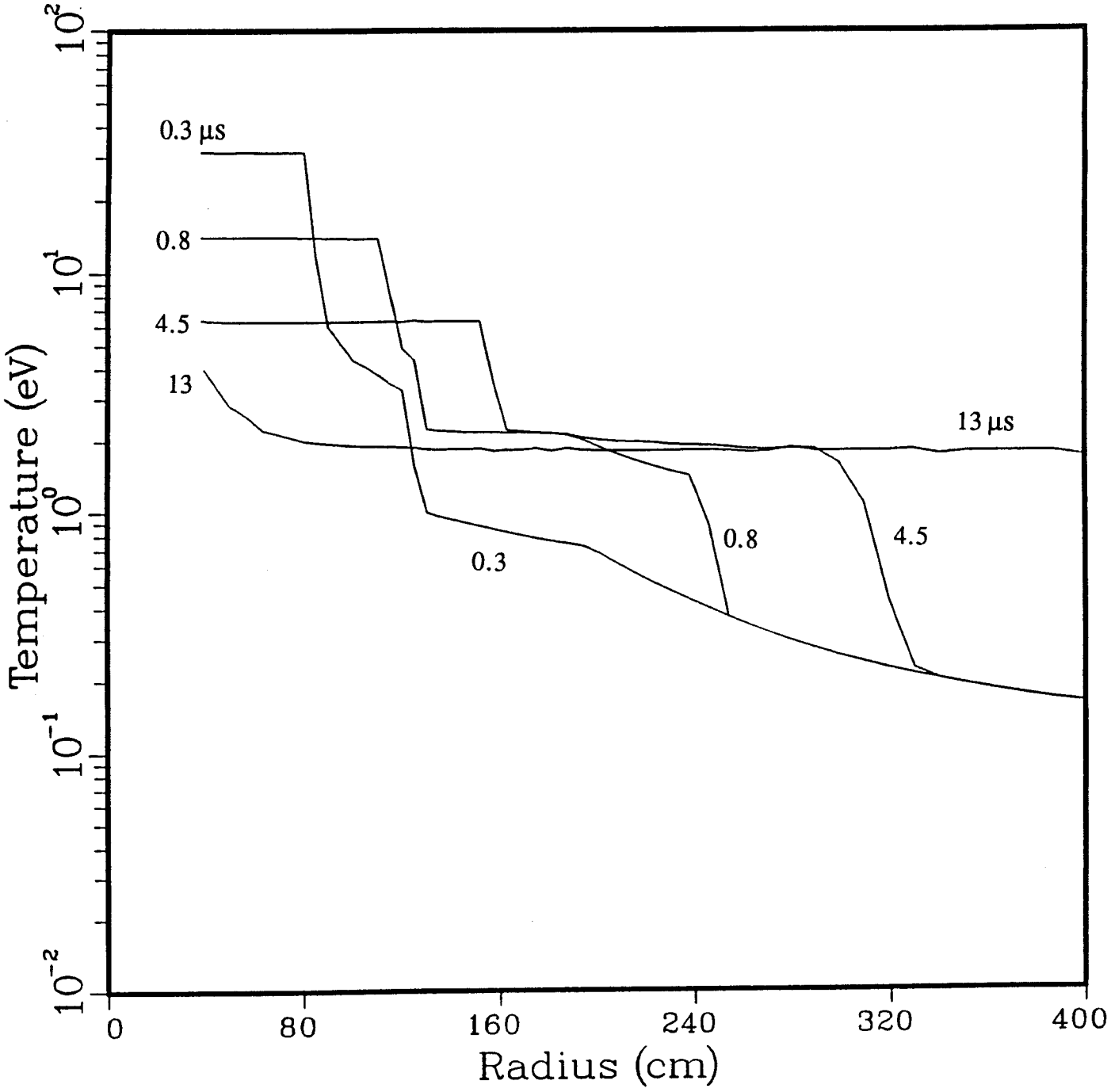

Fig. 5.12. Temperature profiles in the Xe gas at simulation times of 0.28, 0.78, 4.5, and 13 microseconds.

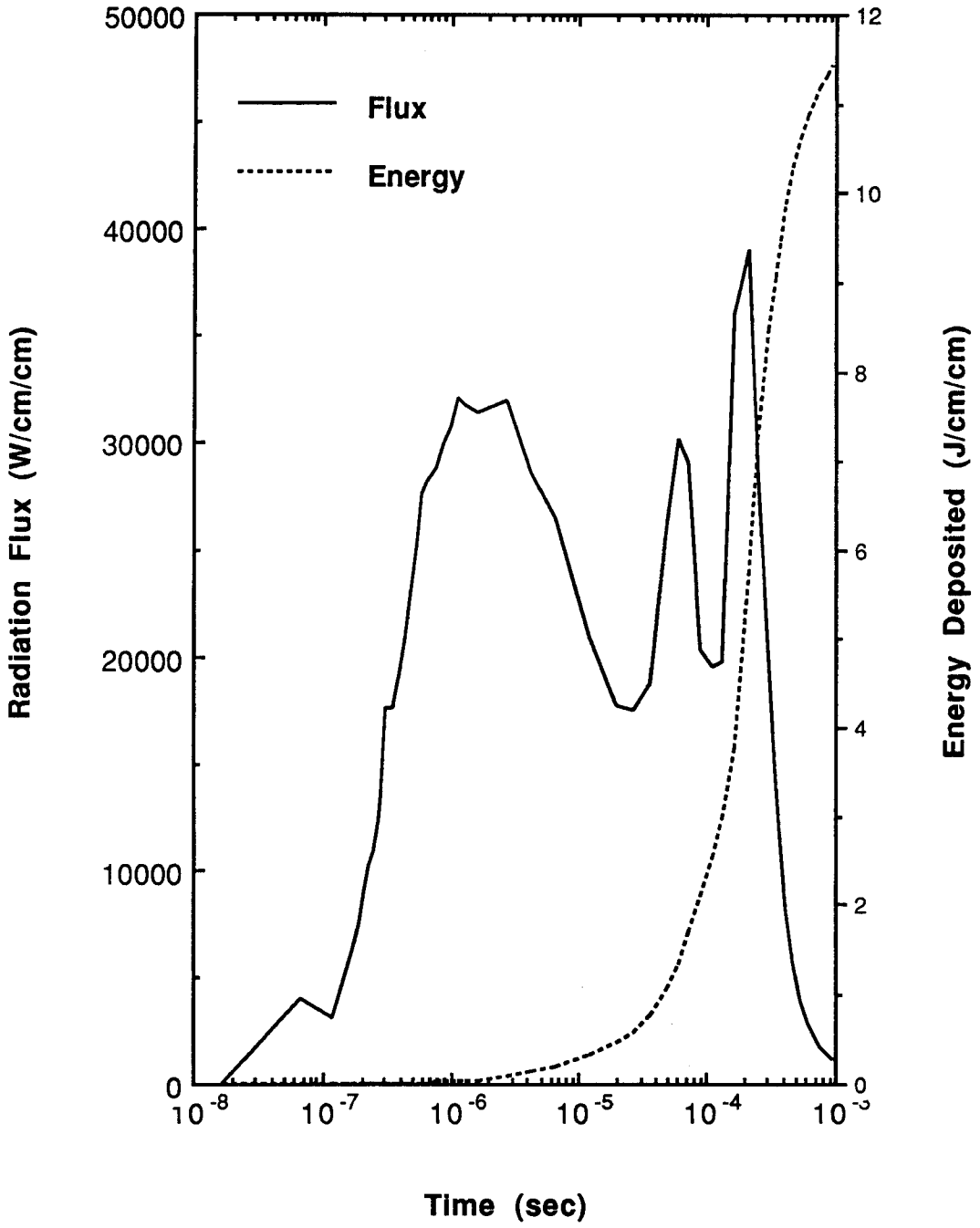

Fig. 5.13. Radiation flux and time-integrated flux at the first wall (180 group case).

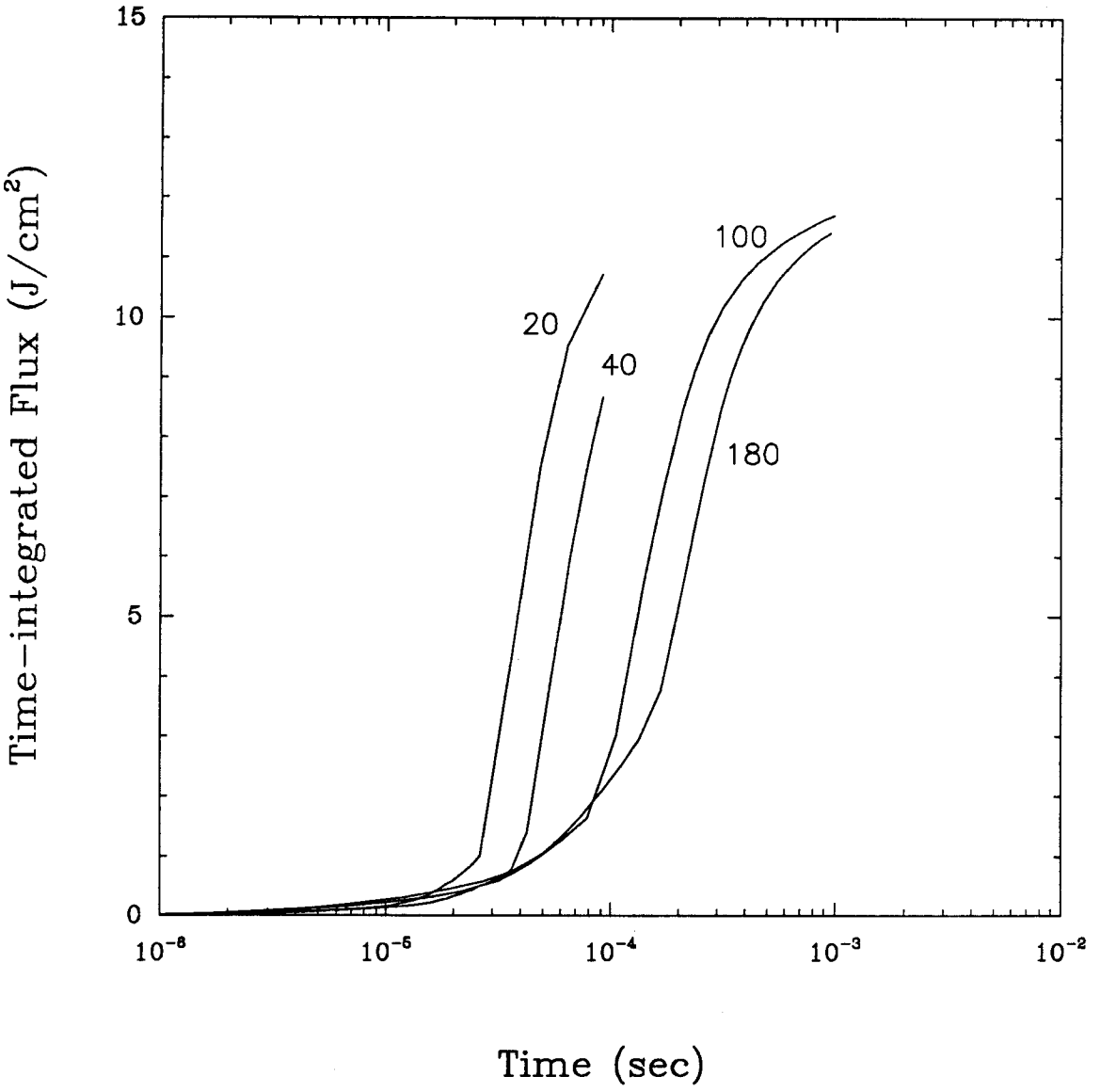

Fig. 5.14. Dependence of time-integrated radiation flux at the graphite tiles on the number of photon energy groups in the radiation diffusion model.

of time for simulations using 20, 40, 100, and 180 photon energy groups. Note that as the number of groups is increased, the time it takes for the microfireball energy to diffuse its way to the wall increases significantly. For example, the time it takes to deposit 10 J/cm^2 in the graphite tiles in the 180 group case is about a factor of 6 longer than in the 20 group case. This occurs because the bound-bound emissivity, which has very narrow line widths, greatly exceeds the continuum emissivity at these densities. A discussion of the implications of the reduced radiation flux on the graphite tiles is presented in Section 5.2.2.

Non-LTE Radiation Transport Simulations

We have recently performed detailed non-LTE radiation transport calculations for SIRIUS-T. Target chamber plasmas created after a high-gain ICF target explosion are very far from local thermodynamic equilibrium. The atomic level populations are *not* well-described by the Saha equation and Boltzmann statistics. The internal energy and opacity at each point in the plasma depend not only on the local temperature and density, but also the radiation field. Also, the radiation flux escaping the plasma is nothing close to that of a blackbody. Target chamber plasmas can be optically thick at some frequencies (e.g., at line centers), while being optically thin in other parts of the spectrum. To better understand these effects, we have developed a non-LTE radiative transfer code[9] and several atomic physics codes.[10]

A collisional-radiative equilibrium (CRE) model is used to compute the ionization and excitation populations. In this model, the density of atoms (or ions) in level **i**, $\mathbf{n_i}$, is obtained by solving a matrix of steady-state rate equations:

$$\frac{dn_i}{dt} = \sum_j n_j (C_{ji} + R_{ji}) - n_i \sum_j (C_{ij} + R_{ij})$$

where $\mathbf{C_{ji}}$ and $\mathbf{R_{ji}}$ are the collisional and radiative transition rates, respectively, from state **j** to **i**. The rates we consider in our model are: collisional excitation and deexcitation, spontaneous decay, photoexcitation and stimulated emission, collisional ionization and recombination, radiative recombination, dielectronic recombination, and photoionization and stimulated recombination. The

major difficulty in solving problems of this type is that the photoexcitation and photoionization rates depend on the radiation field. The radiation field in turn depends on the state (i.e., the opacity) of the plasma. Thus, to properly model target chamber plasmas, the atomic rate equations and radiation field must be solved self-consistently.

To model the transport of radiation in target chamber plasmas, we use an escape probability technique.[11,12] Frequency-averaged escape probabilities for bound-bound (line) photons and bound-free photons are calculated using empirical fits to exact numerical results. Angle-averaged zone-to-zone "coupling coefficients" are calculated to determine the photoexcitation and photoionization rates. This model has previously been shown to be computationally efficient and reasonably accurate.[11,12] Because the model requires relatively little computer time (compared to many other non-LTE radiative transfer codes), it can be coupled with hydrodynamics codes to provide a powerful computational tool for simulating rapidly changing plasma, such as target chamber plasmas.

In our radiative transport model, all levels of an ionization stage are coupled to the ground state of the next higher ionization stage by collisional ionization, photoionization and stimulated recombination, and collisional and radiative recombination. The adjacent ground states are also coupled by dielectronic recombination. The excited levels of a given ion are coupled to other excited levels and the ground state by electron collisional excitation and deexcitation, stimulated absorption and emission, and radiative decay.

In the calculations of atomic energy levels, the interaction between atomic electrons is approximated by an LS-coupling scheme. The energies of the levels and the transition oscillator strengths are generated from Hartree-Fock calculations. The electron collisional excitation rate coefficients employed in this calculation are obtained by two methods. For all electric dipole allowed transitions, the excitation cross sections are calculated by using the semiclassical impact-parameter method.[13] By comparing with available experimental data and other calculated results, we expect that our excitation cross sections are accurate to about a factor of 2. The rate coefficients are obtained by averaging the cross sections over a Maxwellian electron velocity distribution. The

principle of detailed balance is applied to obtain the deexcitation rate coefficients from the excitation rate coefficients.

Electron collisional ionization rate coefficients are calculated using a semi-empirical model,[14] while the electron collisional recombination rate coefficient is obtained by using the principle of detailed balance. Radiative recombination cross sections are obtained from Milne's relation.[15] Photoionization cross sections are generated by using the Hartree-Fock model. Comparison with experimental data[16] shows that Hartree-Fock results are much more accurate than the hydrogenic cross sections. The radiative recombination cross sections are used with the Maxwellian electron distribution to obtain the rate coefficient for radiative recombination to each atomic level. Dielectronic recombination rate coefficients are calculated by using the Burgess-Mertz model.[17]

To gain a better understanding of the radiative properties of target chamber plasmas at the time when the potentially damaging heat flux is highest, we have performed a detailed non-LTE radiation transport calculation using approximately the plasma conditions predicted by CONRAD at 13 μs (see Fig. 5.12). Specifically, we have computed the radiative properties for a spherical 4 meter radius plasma, a uniform temperature of 2 eV, and a uniform density of 3×10^{16} cm^{-3}. We have chosen to use neon as the buffer gas instead of xenon because of the relative complexity of the atomic physics associated with the lower ionizations stages of xenon. The conclusions, however, are unaffected by this choice of buffer gas. For the calculations discussed below, the atomic level structure consists of a modest number of atomic levels (13 levels) distributed over the lowest 3 ionization stages of neon.

Figure 5.15 shows the radiative flux escaping at the boundary of the spherical plasma as a function of photon energy. Several very strong emissions are visible. (In an actual plasma, many more lines would appear. In this calculation, we have considered a rather modest number of levels in our atomic model.) Above the recombination edge at 20 eV the continuum is dominated by bound-free emission, while at lower photon energies, free-free (Bremsstrahlung) emission dominates the continuum. Also shown in Figure 5.15 is the flux emitted by a blackbody with a

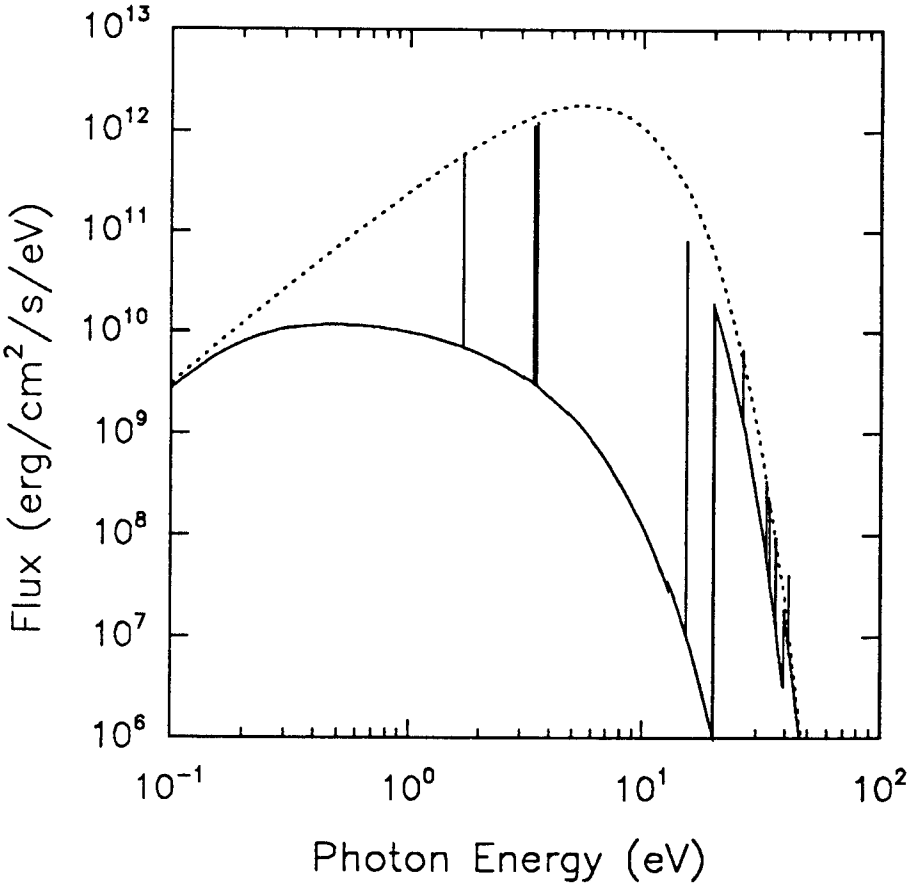

Fig. 5.15. Radiation flux escaping a spherical plasma with T = 2 eV, n = 3 x 10^{16} cm^{-3}, and R = 4 meters. The dashed curve represents the flux from a blackbody.

temperature of 2 eV. It is obvious that the actual spectrum is not at all well approximated by a blackbody spectrum.

The contribution to the total (frequency-integrated) flux is shown in Table 5.3. The fluxes in which radiative transfer effects are included are indicated in the row labelled "optically thick." Note that the lines represent only about 1% of the total flux escaping the plasma. For comparison, we performed calculations for a similar case in which attenuation effects — which influence both the atomic level populations and the flux — were ignored ("optically thin" case). In this case, the total flux is about a factor of 7 higher. Also, the line flux contributes to about 75% of the total flux. Relative to the "thin" case, the optically thick line flux is about 3 orders of magnitude lower. This results from the fact that the absorption cross sections are high at the frequencies where the emissivity is also high. Thus, this self-attenuation of line radiation in target chamber plasmas can dramatically reduce the radiative heat flux at the chamber wall.

Table 5.3. Radiation Fluxes at the Plasma Boundary (units of ergs/cm^2/s)

Case	Bound-Bound	Bound-Free	Free-Free	Total
Optically Thick	5.2×10^8	1.7×10^{10}	3.0×10^{10}	4.7×10^{10}
Optically Thin	4.0 x 10^{11}	1.0×10^{11}	2.5×10^{10}	5.3×10^{11}
20 Group Diffusion				3.4×10^{11}
Blackbody				1.7×10^{13}

A major reason for the difficulty of accurately computing the properties of target chamber plasmas is that the photon mean free paths are extremely small at some frequencies, while being quite large (in fact, larger than the chamber radius) at others. Figure 5.16 shows the optical depth — along a ray from the center of the plasma radially outward to the plasma boundary — as a function of the photon energy. Near the line cores, the optical depth is often quite large; in this case, up to 10^5. On the other hand, at other frequencies the optical depths can be quite small and

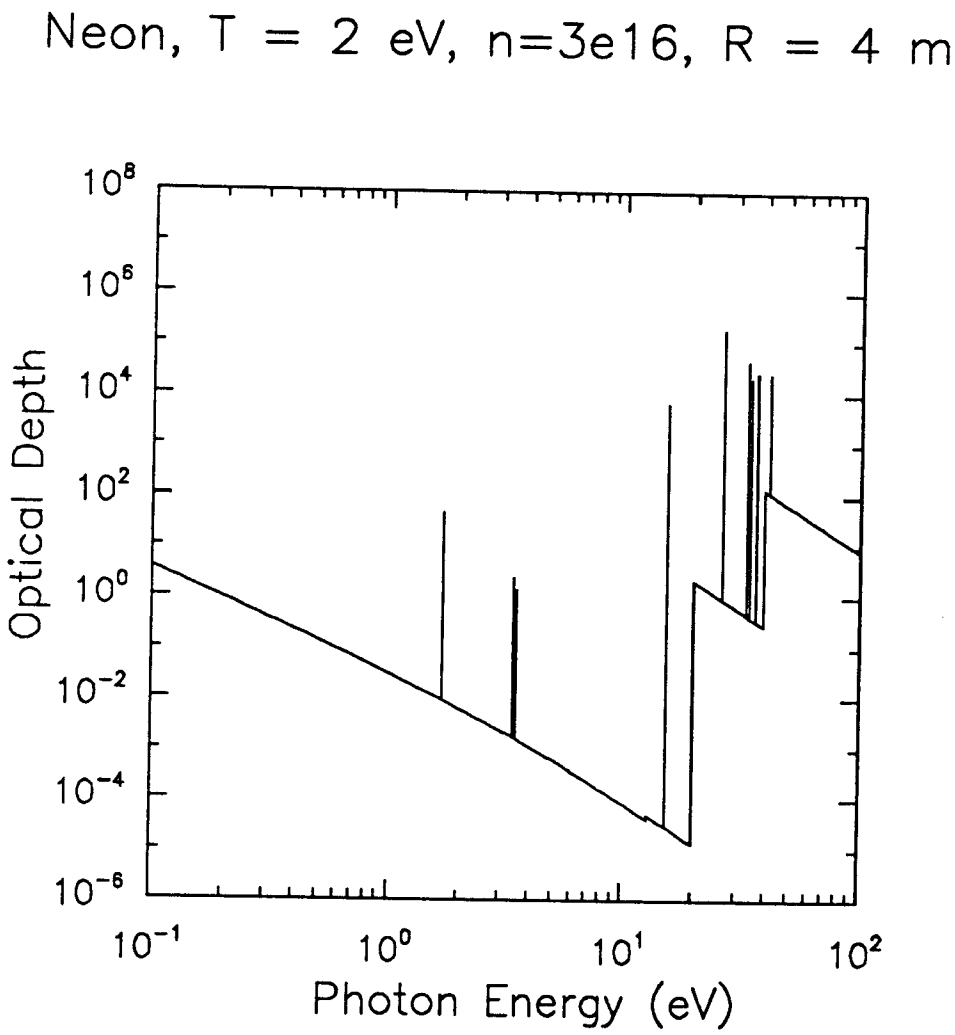

Fig. 5.16. Optical depth from the center of the spherical plasma to the plasma boundary.

the photon mean free paths can be much larger than the target chamber. For example, at energies just below the NeI photoionization edge at 20 eV the optical depth is about 10^{-5}. Because of the wide range of optical depths, computation of the plasma radiative properties requires rather detailed modelling.

We have also compared our results with those obtained using a multigroup radiation diffusion model for a spherical plasma at the same conditions. Diffusion models are often used in radiation-hydrodynamics codes because of their relative ease in programming and computational speed. In the diffusion calculation, 20 groups were used and hydrogenic ion atomic data was supplied by the IONMIX code.[7] A comparison of the spectral fluxes computed using the non-LTE radiative transfer code and the diffusion model is shown in Figure 5.17. Note that there is considerably more detail in the non-LTE model because lines are transported individually. In addition, the level populations are computed self-consistently with the radiation field. The total flux predicted by the diffusion model is about 36% lower than the optically thin case (see Table 5.3), but a factor of about 7 - 8 higher than the optically thick case. Also shown in Table 5.3 is the flux emitted by a blackbody at the same temperature. In short, we find that for typical target chamber plasma conditions, optically thin and 20-group diffusion models can overestimate the flux by about an order of magnitude, while the blackbody flux is about 2 to 3 orders of magnitude too high.

There are several potential sources of error in multigroup diffusion models. For the densities and temperatures of target chamber plasmas, lines are often the dominant contributor to the plasma emissivity and absorption coefficient. These quantities can vary by several orders of magnitude over a very narrow frequency range. This makes the idea of using group-averaged opacities rather suspect because the widths of energy groups are generally orders of magnitude larger than characteristic line widths. Second, diffusion models are based on the assumption that the photon mean free paths are small compared to the size of the plasma. This assumption does not hold at all photon frequencies for target chamber plasmas. And finally, it has been shown[18] that the radiation

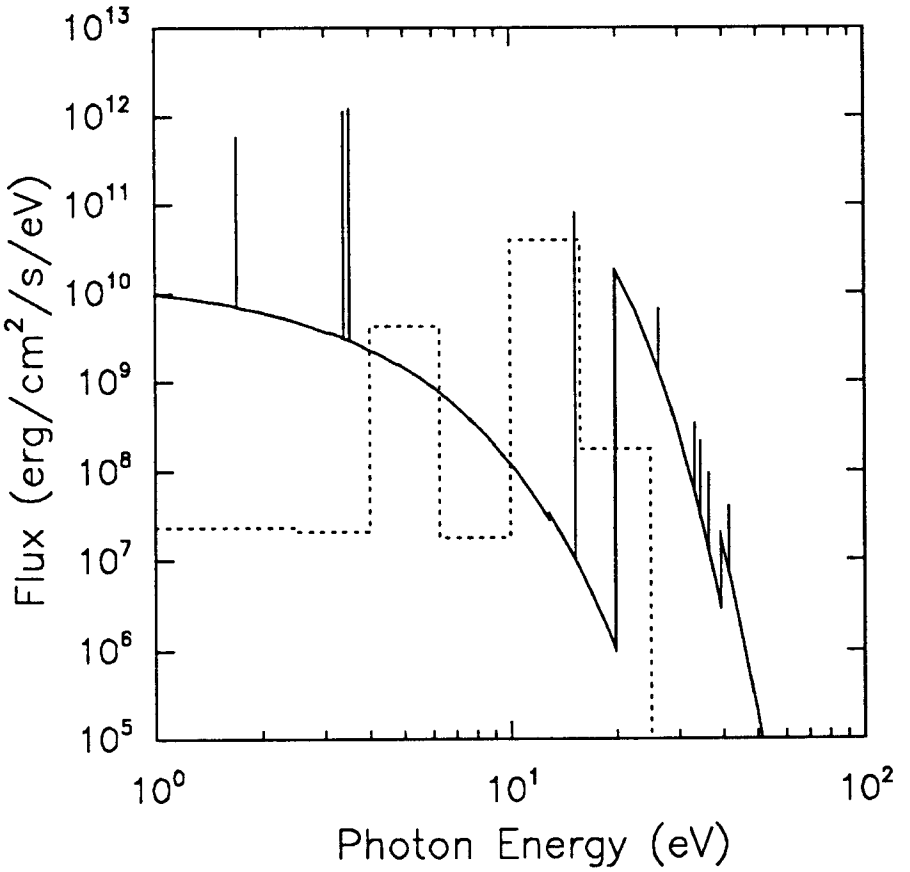

Fig. 5.17. Comparison of fluxes computed using our non-LTE radiative transfer model (solid curve) and a multigroup diffusion model (dotted curve).

field in target chamber plasmas significantly alters the atomic level populations. Thus, opacities depend not only on the local temperature and density, but also on the radiation field.

The lower heat fluxes that result from the self-attenuation of line radiation have important implications for ICF target chamber design. The temperature at the first surface of the target chamber is determined by the competition between the radiative heat flux from the buffer gas and the conductive flux through the first wall. When the radiative flux is reduced, both the temperature and temperature gradients are reduced. Thus, the attenuated fluxes may substantially mitigate some of the problems associated with vaporization and thermal stresses for the first wall. The same conclusions also apply to the use of buffer gases to protect ICF driver components and diagnostic equipment.

5.2.2. Heat Conduction in Tiles

The non-neutronic target energy is stopped in the xenon fill gas and is reradiated to the graphite tiles that line the inner walls of the tritium breeding blanket modules. The tile and blanket module assembly is shown in Fig. 5.3. The thermal heat flux on the tiles has been calculated with the CONRAD computer code as described in Section 5.2.1. The radiant heat flux on the surface of the graphite tiles 4 meters from a 100 MJ target explosion as calculated with CONRAD using 180 energy group radiation diffusion is shown in Fig. 5.18. In this section, we describe computer calculations of the thermal conduction through the tiles and the time-dependent temperature profiles through the graphite. The type of graphite is still an open question and the thermal properties of neutron irradiated graphite change with neutron fluence. Therefore, we present temperature profiles for three sets of graphite thermal properties. These results are used in calculations of the thermal stresses in the tiles, which are discussed in Section 5.3.4.

We have used the WALL computer code in these calculations. WALL is a finite-difference computer code that allows the use of temperature-dependent thermal conductivities and heat capacities. A time-dependent surface heat flux is provided to the code and it is assumed that all of the energy is absorbed in the first finite-difference zone. The shot rate is also an input to WALL and the code assumes that the same time-dependent surface flux is incident on the material every

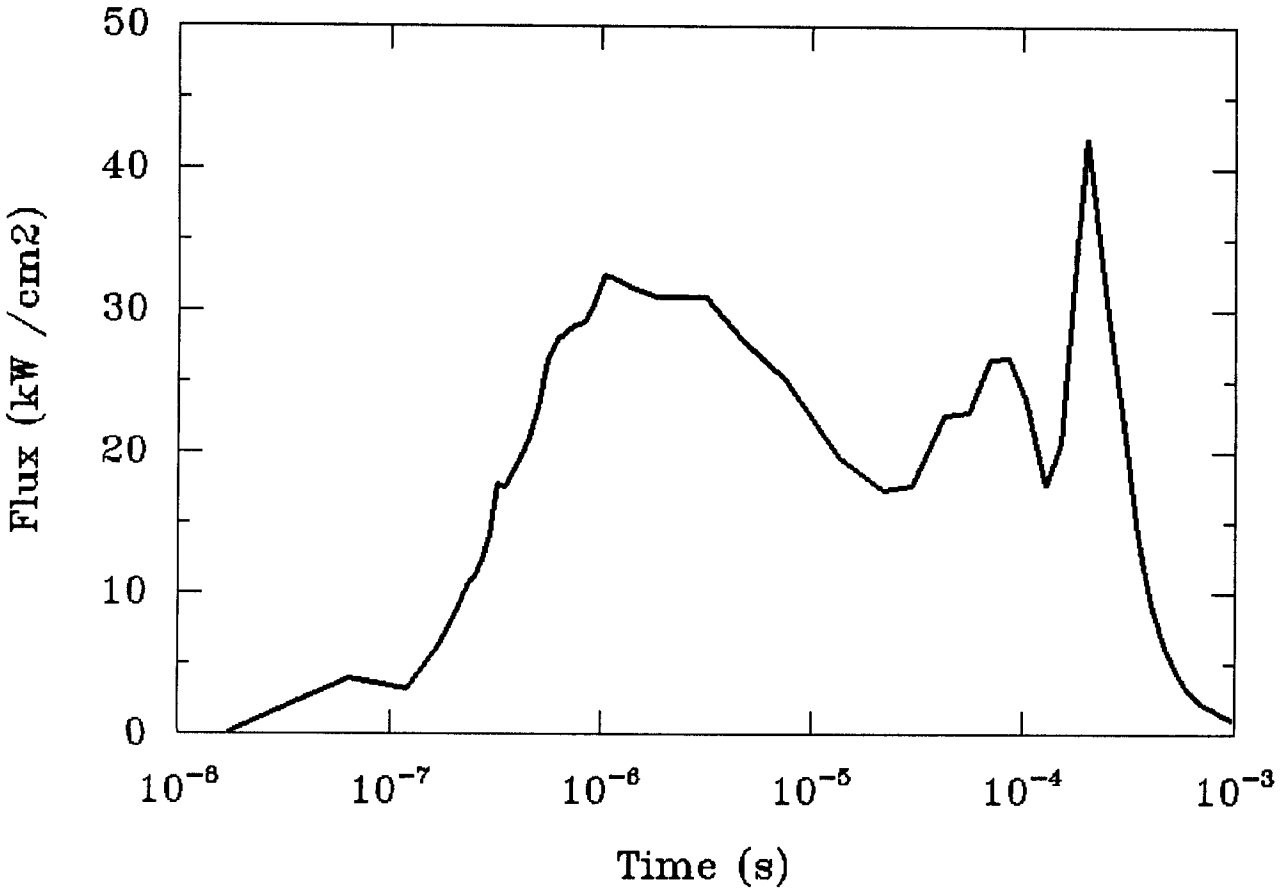

Fig. 5.18. Radiant heat flux on SIRIUS-T graphite tiles. Calculated with CONRAD with 180 energy group radiation diffusion.

shot. An initial temperature profile is provided by the user and, as the material receives each shot, the temperature profile at the same time interval after the start of a shot changes from the profile at the same time during the previous shot. Eventually, the profiles converge to a "cyclic steady state." In this "cyclic steady state," the temperature profiles rise near the front surface at the peak of the surface heat flux and fall again at the end of each pulse, but they follow the same history each shot. The WALL code terminates once the "cyclic steady state has been reached.

We have run three WALL calculations to bound the behavior expected in SIRIUS-T. For all of the calculations we have used the surface heat flux in Fig. 5.18. The shot rate has been held constant at 10 Hz. In all cases, the back surface temperature is held constant at 960 K. This is consistent with the design of the blanket module cooling system described in Section 7. In the analysis of that design, the heat transfer through this tile assembly is calculated for an average heat load of 15 W/cm^2. The tile assembly is shown in Fig. 7.13 with the calculated temperatures at various points in the assembly. The tile assembly is made of three regions: (1) the graphite tile, (2) the vanadium alloy backing plate, and (3) the lithium coolant. The central coolant temperature is taken to be 773 K, leading to a temperature of vanadium/graphite interface of 960 K. We have used three sets of graphite thermal properties: (1) unirradiated H-451, (2) irradiated H-451, and (3) unirradiated FMI 4-directional carbon/carbon composite (c/c). Data is not available for neutron irradiated c/c. The thermal conductivities and heat capacities for the three materials are shown in Figs. 5.19, 5.20 and 5.21, respectively. The irrradiated graphite H-451 has received 10^{22} neutrons/cm^2 with an energy greater than 0.18 MeV. This is equivalent to 10 dpa or 1/3 full power years in SIRIUS-T.

The results of these calculations are depicted in Figs. 5.22 through 5.25. In Fig. 5.22 we show the temperature profiles in unirradiated H-451 at various times. Similarly, we show temperature profiles for neutron irradiated H-451 in Fig. 5.23 for unirradiated c/c in Fig. 5.24. One may note that in all three cases, only a very narrow region of the graphite is heated to a very high temperature. One would expect high compressional thermal stresses only in this narrow layer and rather low tensile stresses in the remainder of the tile. We have not included thermal creep in

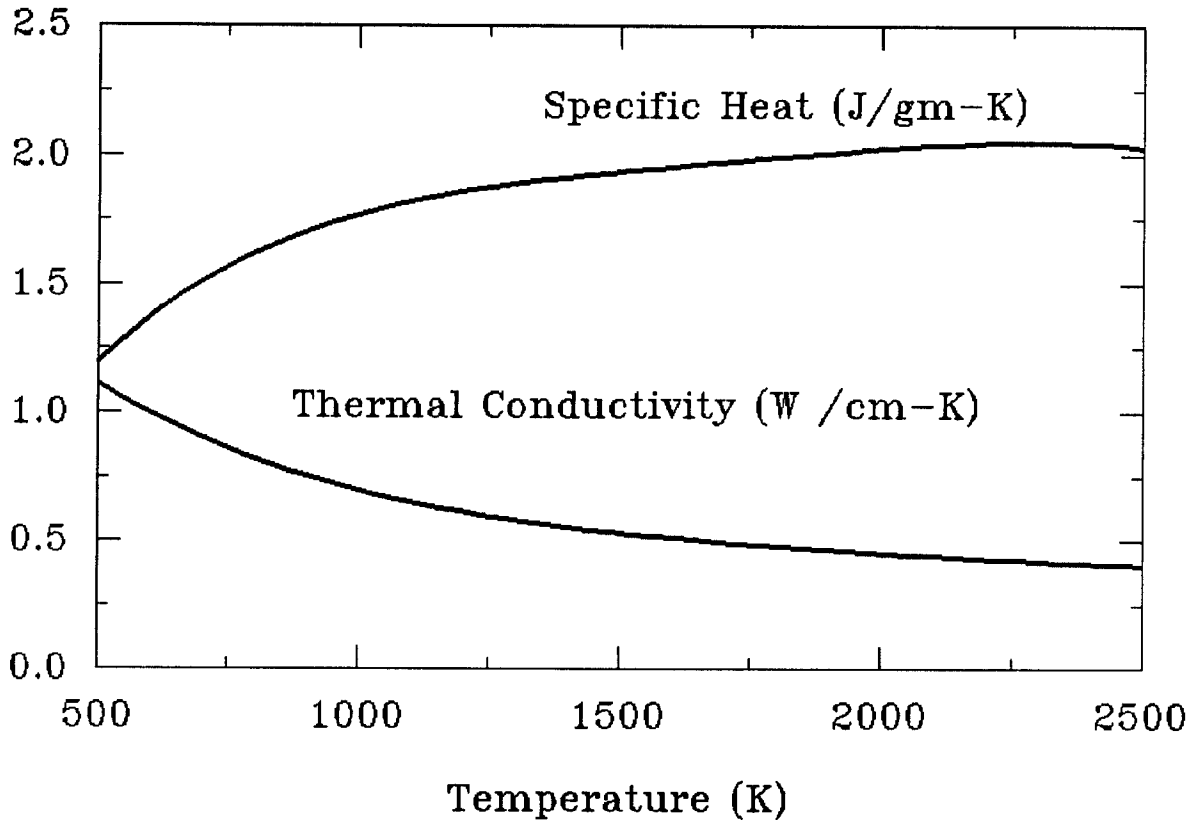

Fig. 5.19. Thermal conductivity and specific heat for unirradiated graphite H-451 versus temperature.

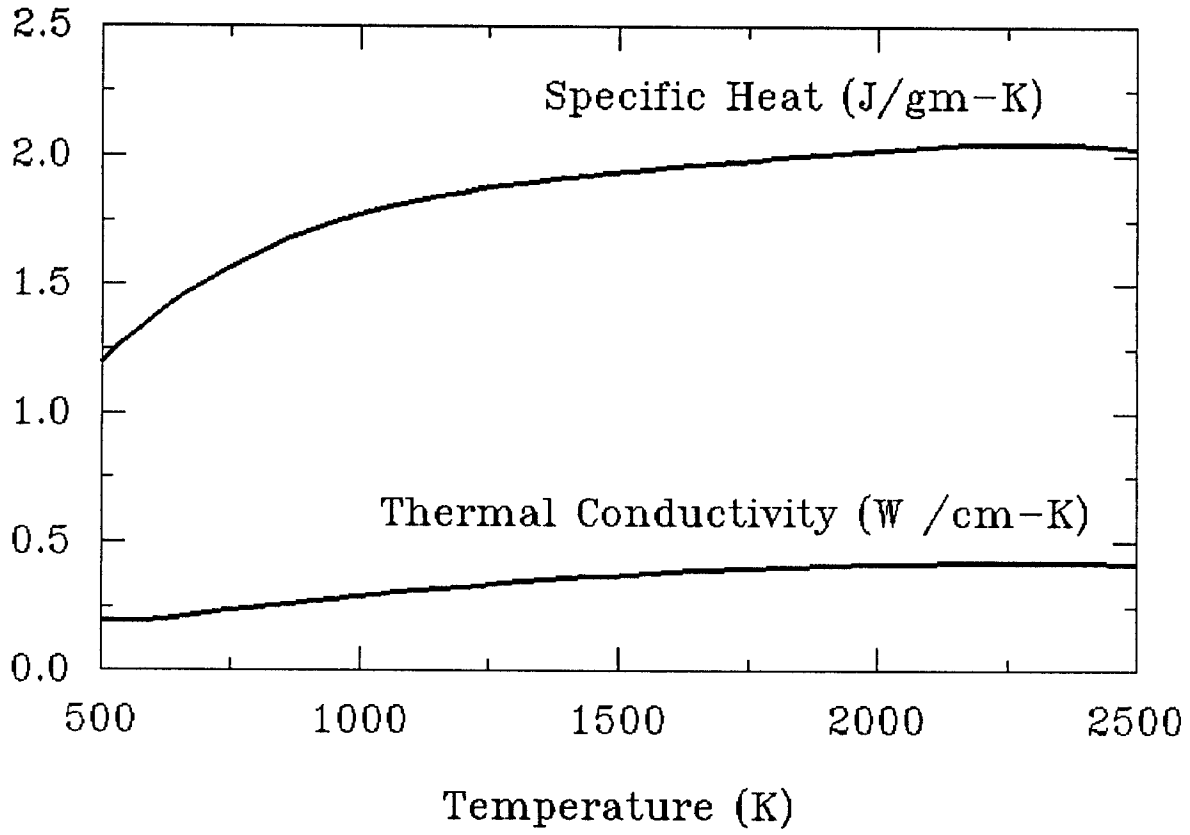

Fig. 5.20. Thermal conductivity and specific heat for irradiated graphite H-451 versus temperature. The graphite is irradiated by 10^{22} neutrons/cm^2 with an energy greater than 0.18 MeV.

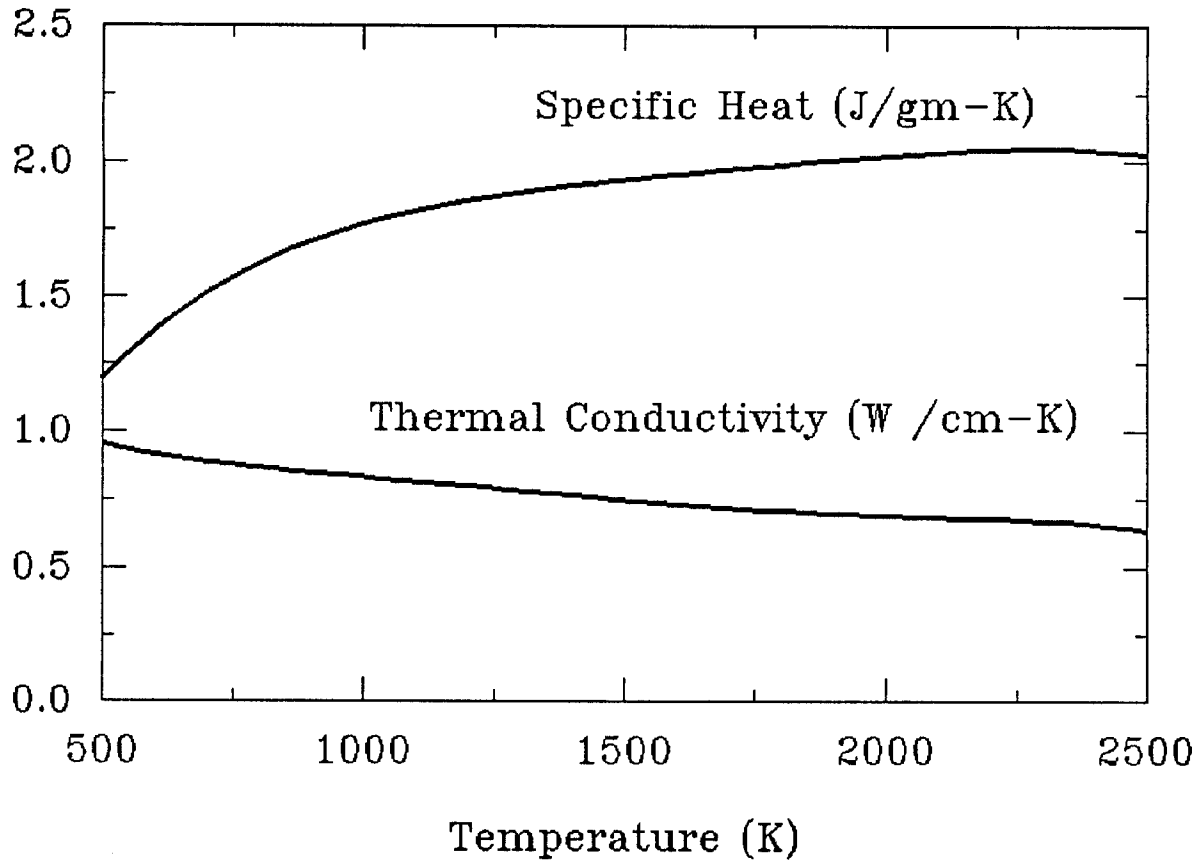

Fig. 5.21. Thermal conductivity and specific heat for unirradiated FMI 4D carbon/carbon composite versus temperature.

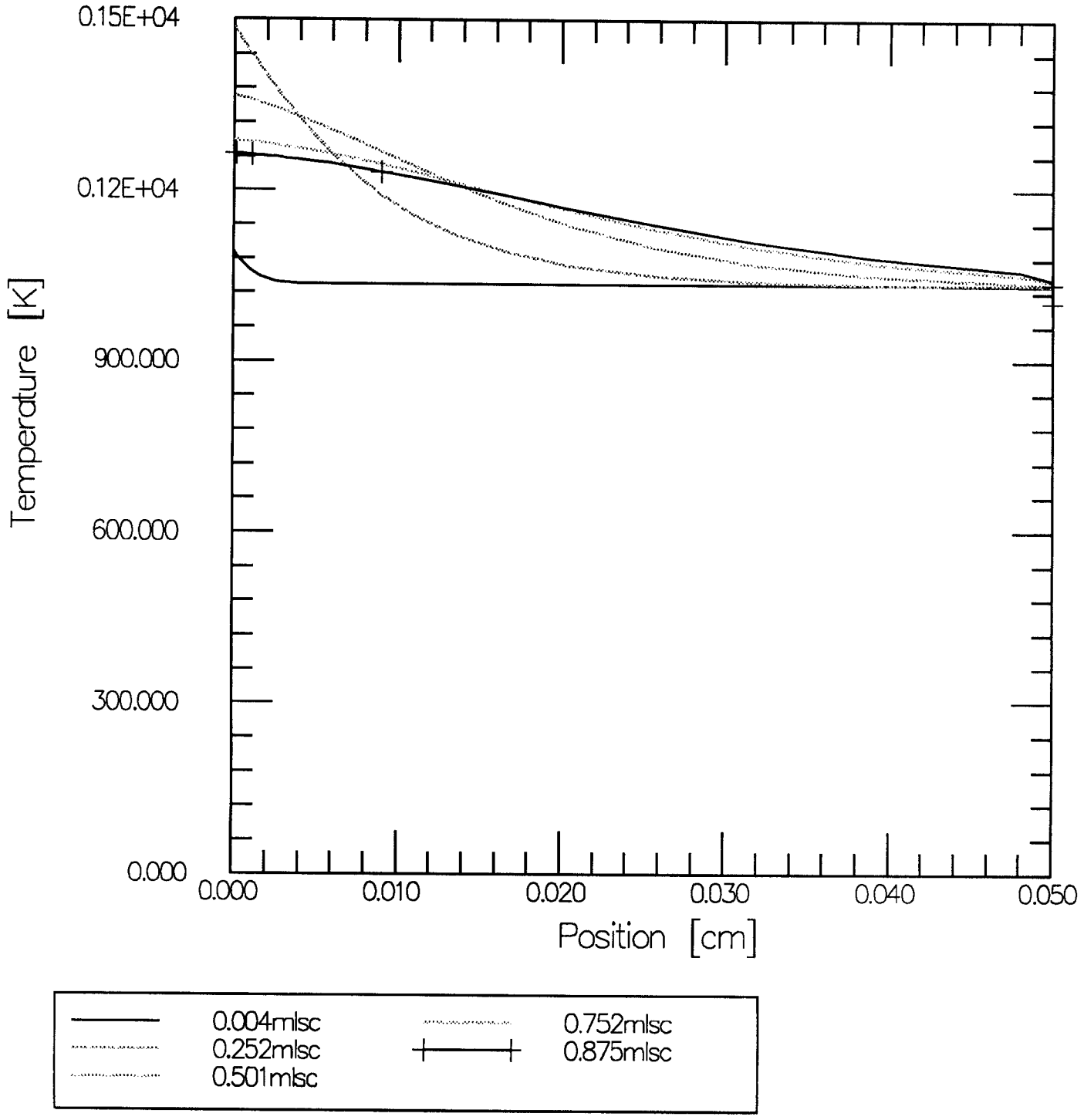

Fig. 5.22. Temperature profiles in unirradiated graphite H-451 SIRIUS-T tiles at various times.

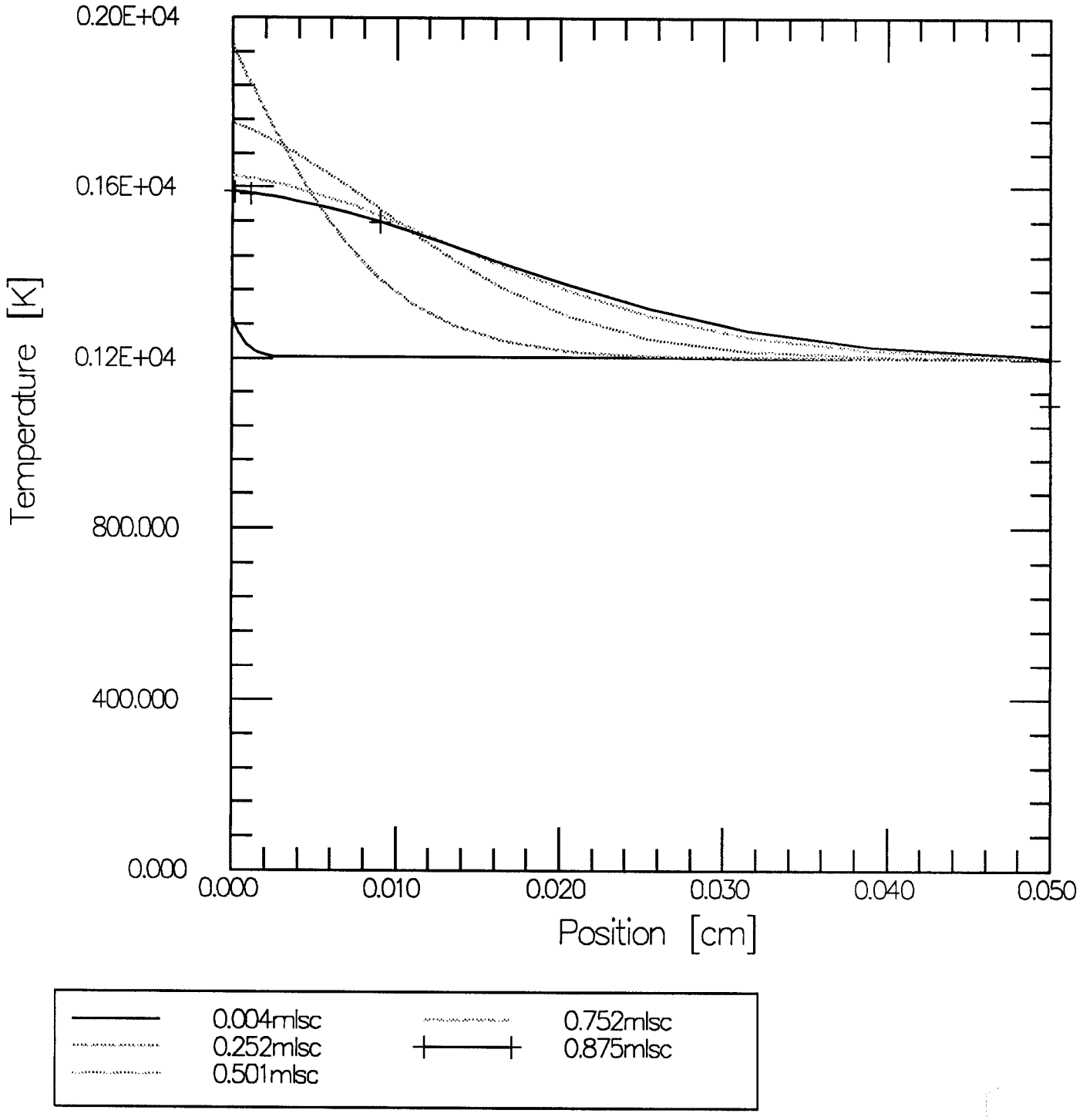

Fig. 5.23. Temperature profiles in irradiated graphite H-451 SIRIUS-T tiles at various times.

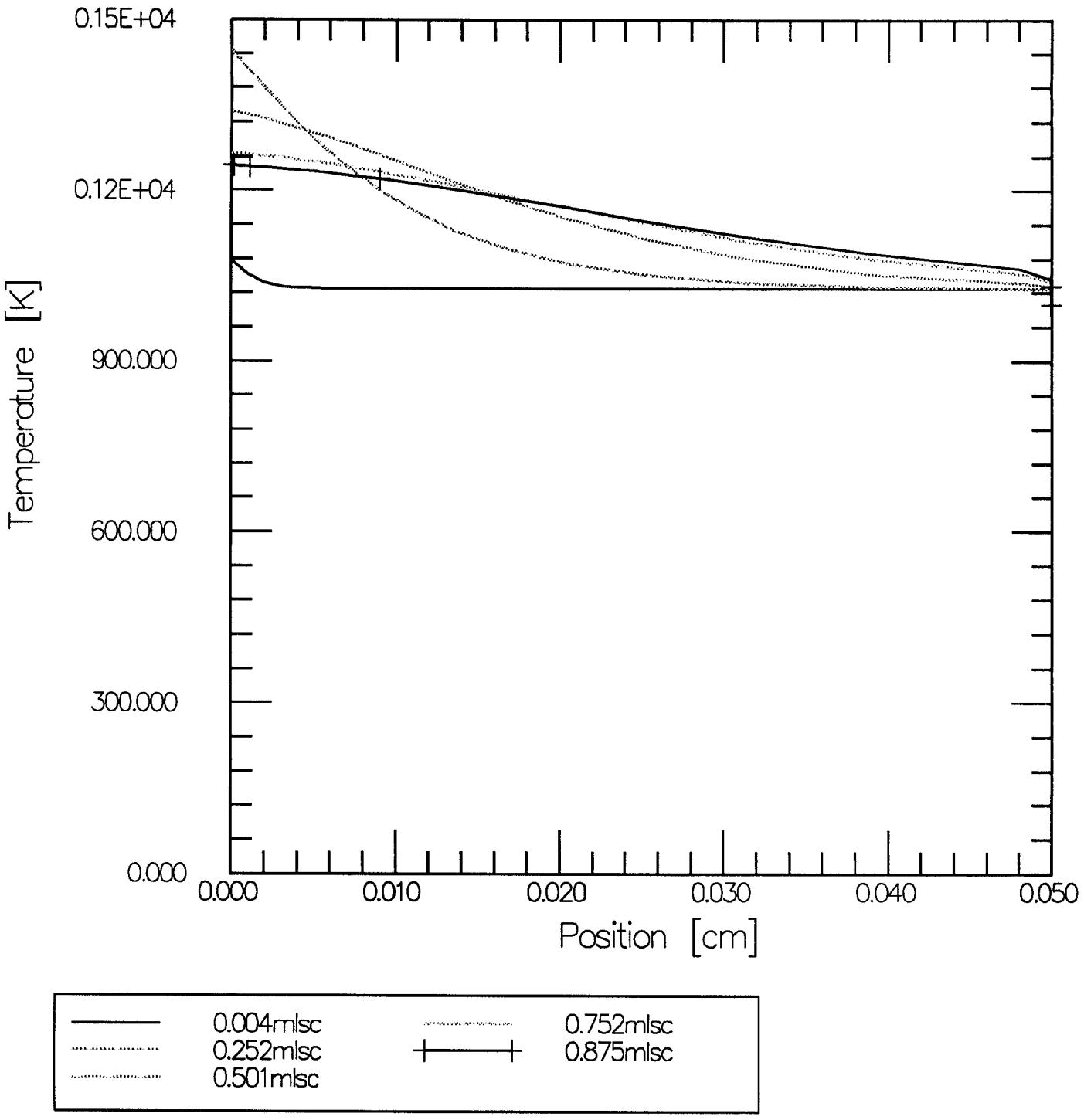

Fig. 5.24. Temperature profiles in unirradiated graphite carbon/carbon composite SIRIUS-T tiles at various times.

the calculations discussed in Section 5.3.4 which could lead to residual tensile stresses in the front surface layer. The front surface temperatures for all three cases are shown as a function of time in Fig. 5.25. Here one sees that there is little difference between unirradiated H-451 and c/c. The temperatures reached in irradiate H-451 are much higher, as one would expect.

5.3. Structural Analysis

5.3.1. Overview

Key structural integrity issues have been addressed for the SIRIUS-T chamber. At critical locations in the reactor chamber's skeletal frame, mechanical stresses and deflections from self-weight loading are evaluated by finite element methods. Thermal stress analyses of the tiles constituting the chamber's first wall include a comparison of the response of carbon/carbon composite and graphite as well as the influence of irradiation. The results substantiate a viable design for the principal aspects of the reactor chamber.

5.3.2. Chamber Description

The chamber configuration originated with the need for a large number of nearly identical geometric units (on the order of 100), to constitute the equivalent of the ideal spherical shape. Each unit corresponds to a blanket module. The design is based upon icosahedron projections. The number of pentagonal modules is 12, which originates with the locations of the 12 vertices of the virtual regular icosahedron inscribed within the spherical surface. Each of the 20 triangular face projections of the icosahedron on the sphere can be uniformly subdivided into unique totals of identical hexagons, e.g., 30, 80, 150, etc. Such divisions are shown in Fig. 5.26.[19] The beam number objective can be satisfied with the 12 pentagonal and 80 hexagonal units. The chamber is comprised of a V-3Ti-1Si vanadium alloy frame in the form of a reticulated shell (Fig. 5.27) and removable tapered blanket modules which occupy the cells. The 92 modules have hexagonal or pentagonal configurations with beam ports running through their centers. The module surface facing the chamber center is covered by a protective graphite tile. Together these form the 4 m radius first surface of the facility. In the work which follows, results are presented for an

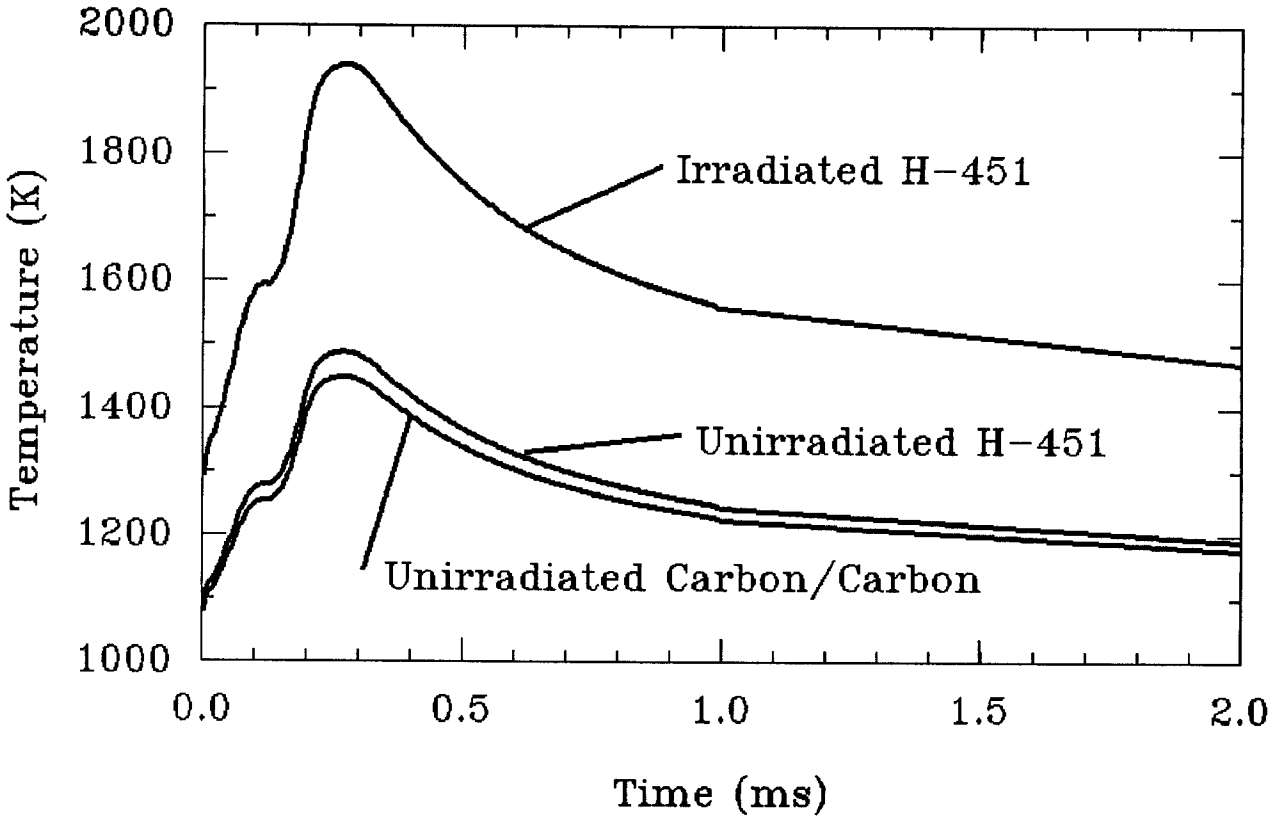

Fig. 5.25. Front surface temperatures of SIRIUS-T graphite tiles versus time. Results are shown for unirradiated H-451, irradiated H-451, and unirradiated carbon/carbon composite.

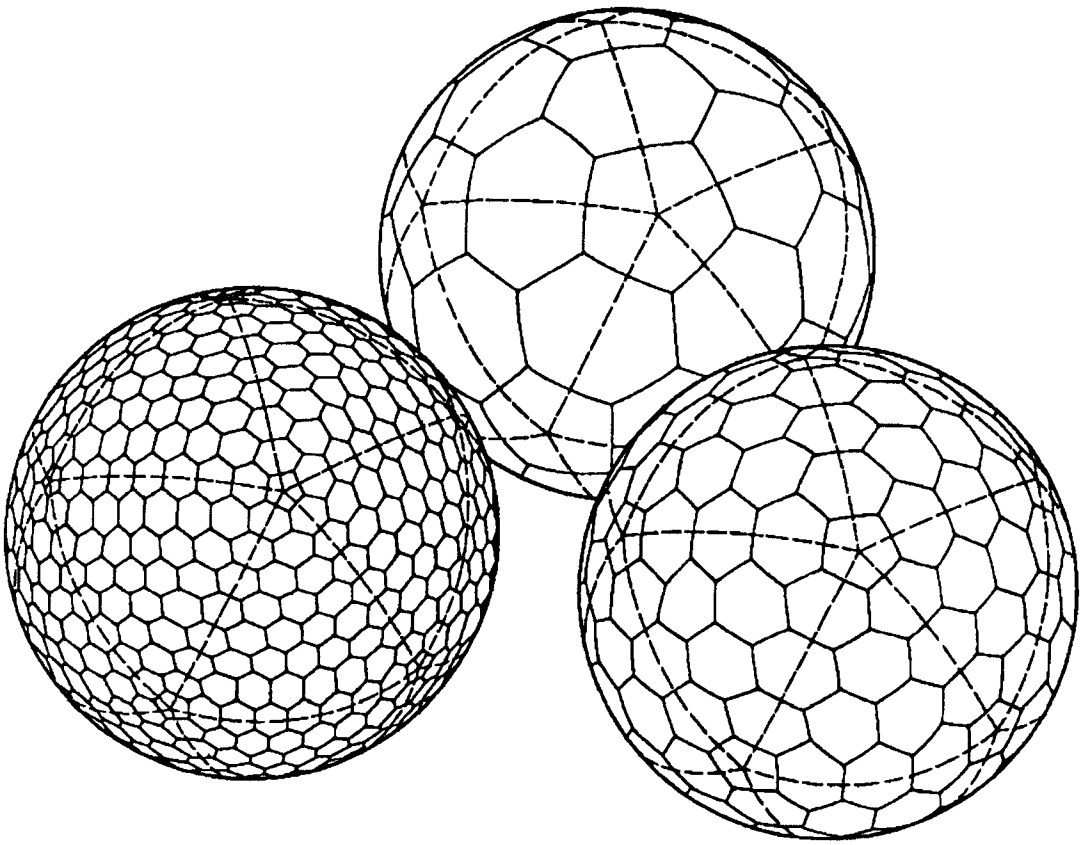

Fig. 5.26. Icosahedron projections on spherical surfaces with different dividing frequencies.

assessment of the structural integrity of the frame. The thermal stress analysis and design of the first surface tiles will also be described.

5.3.3. Frame Structural Analysis

The mechanical loads considered on the structural frame include the dynamic impulsive pressure which follows target implosion and the static dead weight load from the modules, coolant and frame itself. It has been determined that the pressure load resulted in negligible dynamic stresses and displacements of the frame. Typically, stresses did not exceed 10 MPa. Therefore, the investigation focused on evaluating the structural integrity of the frame from dead weight.

A worst case scenario was proposed for the static loading. This consisted of removing the row of modules directly above the support pedestal, with all other modules kept intact. This is depicted in Fig. 5.28, a bottom view in which the pedestal is not shown. Without this row of modules, the exposed supporting webs directly above the pedestal are subjected to the greatest dead weight load. The problem is exacerbated because this location also corresponds to the smallest number of webs to carry the load. At this position, webs are also inclined at the shallowest meridional angle, a geometric disadvantage which generally results in load magnification. A major issue is the determination of whether the webs can provide the necessary margin of strength and stiffness under the most extreme conditions. Stresses should be within the yield strength design limits; stiffness should be sufficient to preclude web buckling as well as limit deflections to tolerances which would facilitate replacement of the modules for maintenance purposes.

To efficiently perform a structural analysis of the supporting frame, the symmetry of the module configuration was exploited. The row of modules removed alternates with "flat hexagonal" and "point hexagonal" cells around the perimeter. As previously mentioned, the dead weight loading on these cells is due to the frame and modules above. These loads are proportioned to the two types of cells in the form of both concentrated loads and distributed loads, as shown in Figs. 5.29-5.31. The distributed loads are from the modules on the layer directly above and represent the actual load on the common web between individual modules and cells. Because the

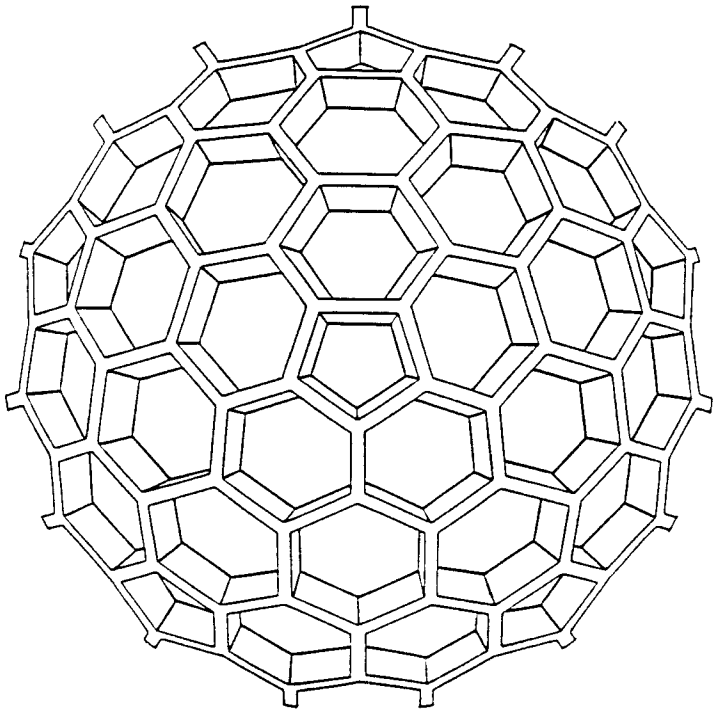

Fig. 5.27. Reactor chamber structural frame.

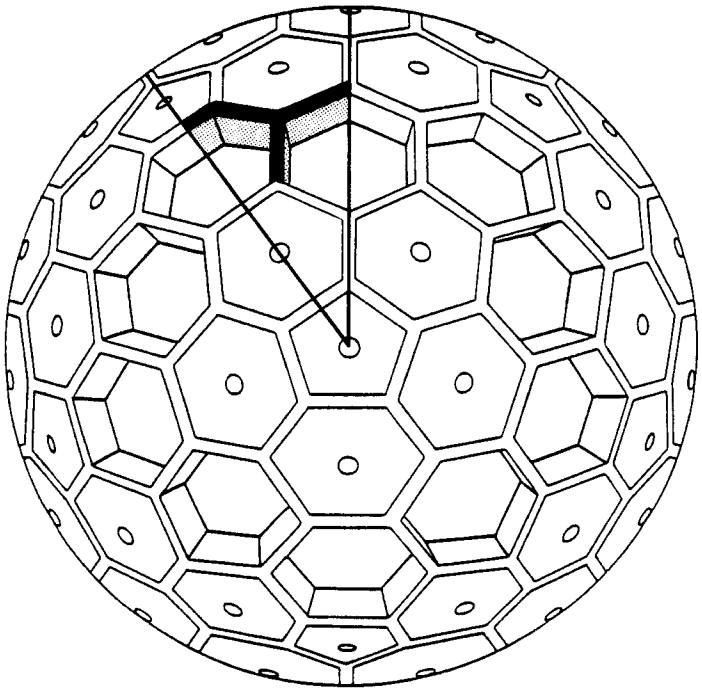

Fig. 5.28. Bottom view of chamber with ten modules removed.

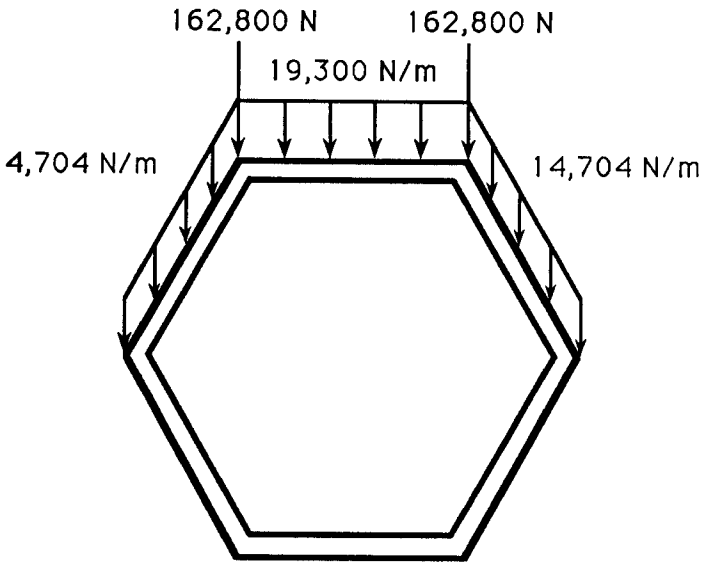

Flat Radial Hexagonal Frame

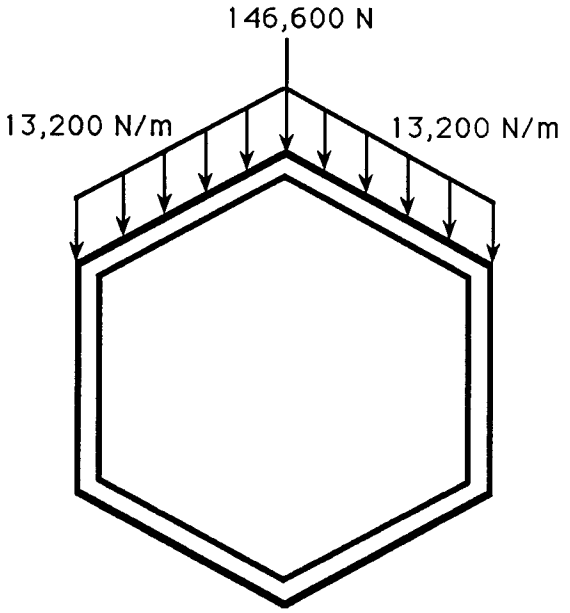

Point Radial Hexagonal Frame

Fig. 5.29. In-plane loading of a cell from dead weight.

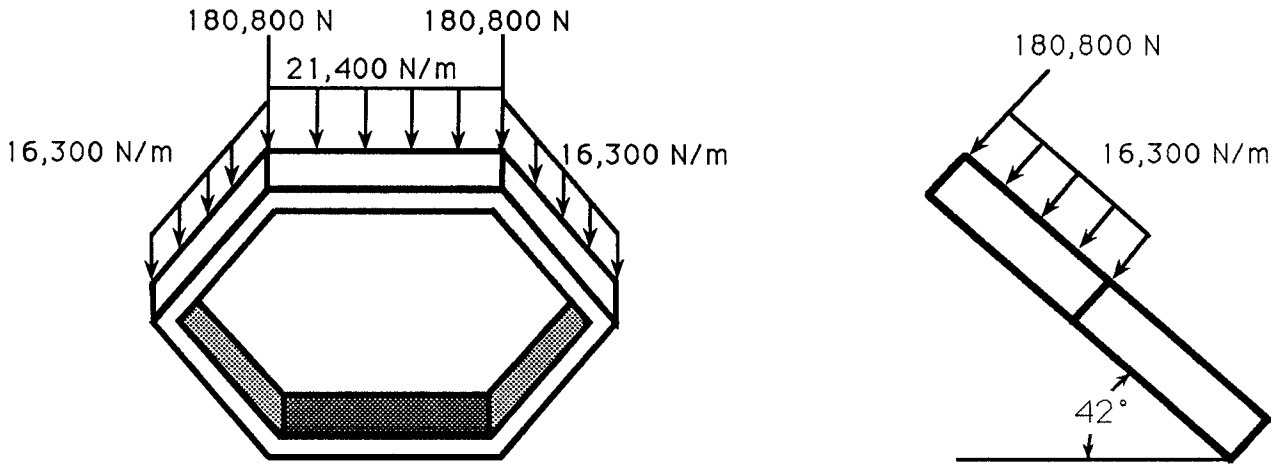

Fig. 5.30. Out-of-plane loading of flat radial cell.

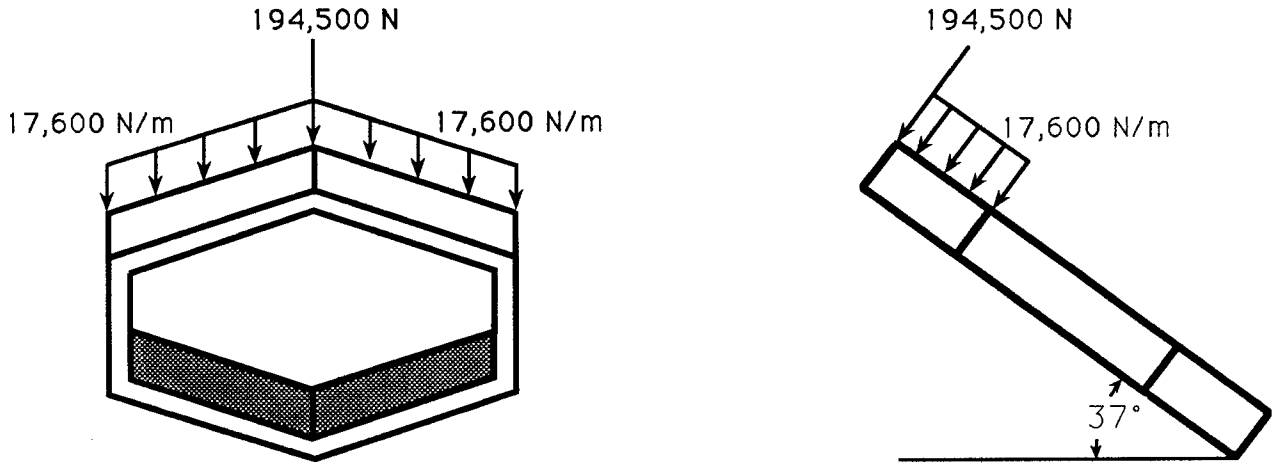

Fig. 5.31. Out-of-plane loading of point radial cell.

orientation of the frame varies at each layer of modules, it is necessary to differentiate the loads as either in-plane (Fig. 5.29) or out-of-plane (Figs. 5.30-5.31). In addition, the two types of cells differ slightly in the angle they make with the horizontal, i.e., 37° versus 42° as shown in Figs. 5.30 and 5.31. With the self-weight loads prescribed, a structural analysis of the exposed webs could be performed.

With the inherent symmetry of this structure, it was only necessary to analyze a representative subsection. The shaded portion of the frame in Fig. 5.28 shows the section that was modeled with finite elements. It should be noted that this subsection consists of half of a "flat hexagonal" cell and half of a "point hexagonal" cell. This portion of the frame replicates itself exactly, or in a mirror image, around the perimeter of the chamber. The corresponding loads (concentrated only) and boundary conditions used for the finite element modeling are shown in Fig. 5.32. By considering the various views of the figure, the exact orientation of the concentrated loads can be visualized, and the same methodology is used to apply the distributed loads. (Key node points are also noted on the structure.) It was assumed that the pedestal would provide essentially infinite rigidity to the lower webs that are in contact with it. Therefore, at node 1 the effective boundary condition is a rigid support with zero displacements and rotations, and there is no further need to consider these lower webs. The other boundary conditions shown in Fig. 5.32 are due to symmetry constraints.

Material properties for unirradiated vanadium were used in the finite element computations, i.e., 124 GPa for the elastic modulus and 0.36 for Poisson's ratio.[1] It was assumed that the static loading for this particular case would take place during shutdown with a frame temperature of 200°C. Additional input data included the web dimensions, which were specified as 87 cm long by 80 cm deep by 8 cm thick. Finally, the commercial code ANSYS was used for all finite element calculations. Fig. 5.33 shows a plot of the structural deflections from the applied loads (all displacements are exaggerated); actual displacement components at the the key node points are given in Table 5.4. With the largest deflection of 1.754 mm at node 5, there should be no difficulty in replacing modules within the tolerance levels provided. Stresses were also well below

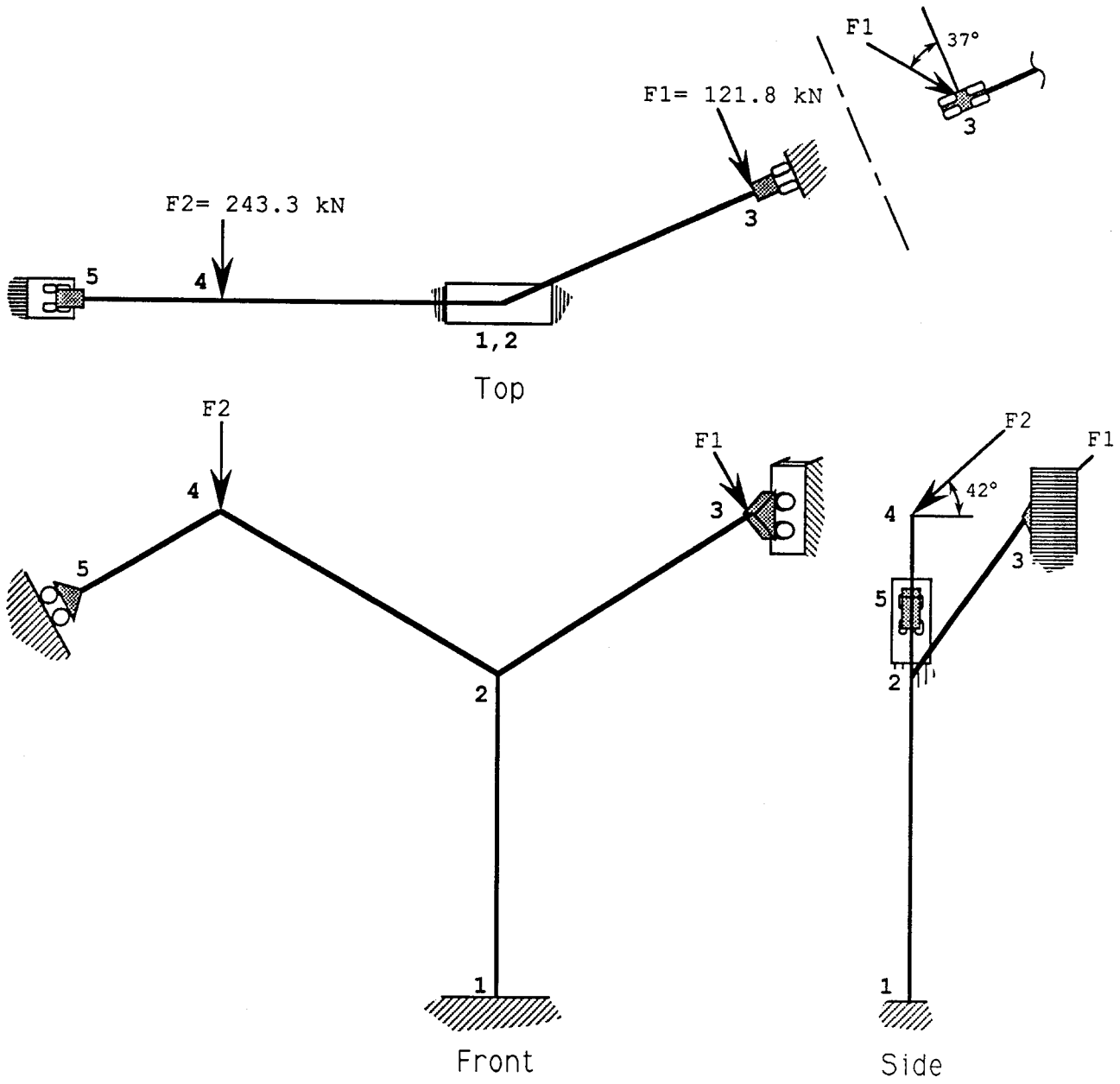

Distributed Loadings Not Shown

Span	Loading (kN/m)	Direction
2-3	21.97	F2
2-4	21.97	F2
4-5	28.84	F1

Fig. 5.32. Loads, geometry and boundary conditions for finite element analysis.

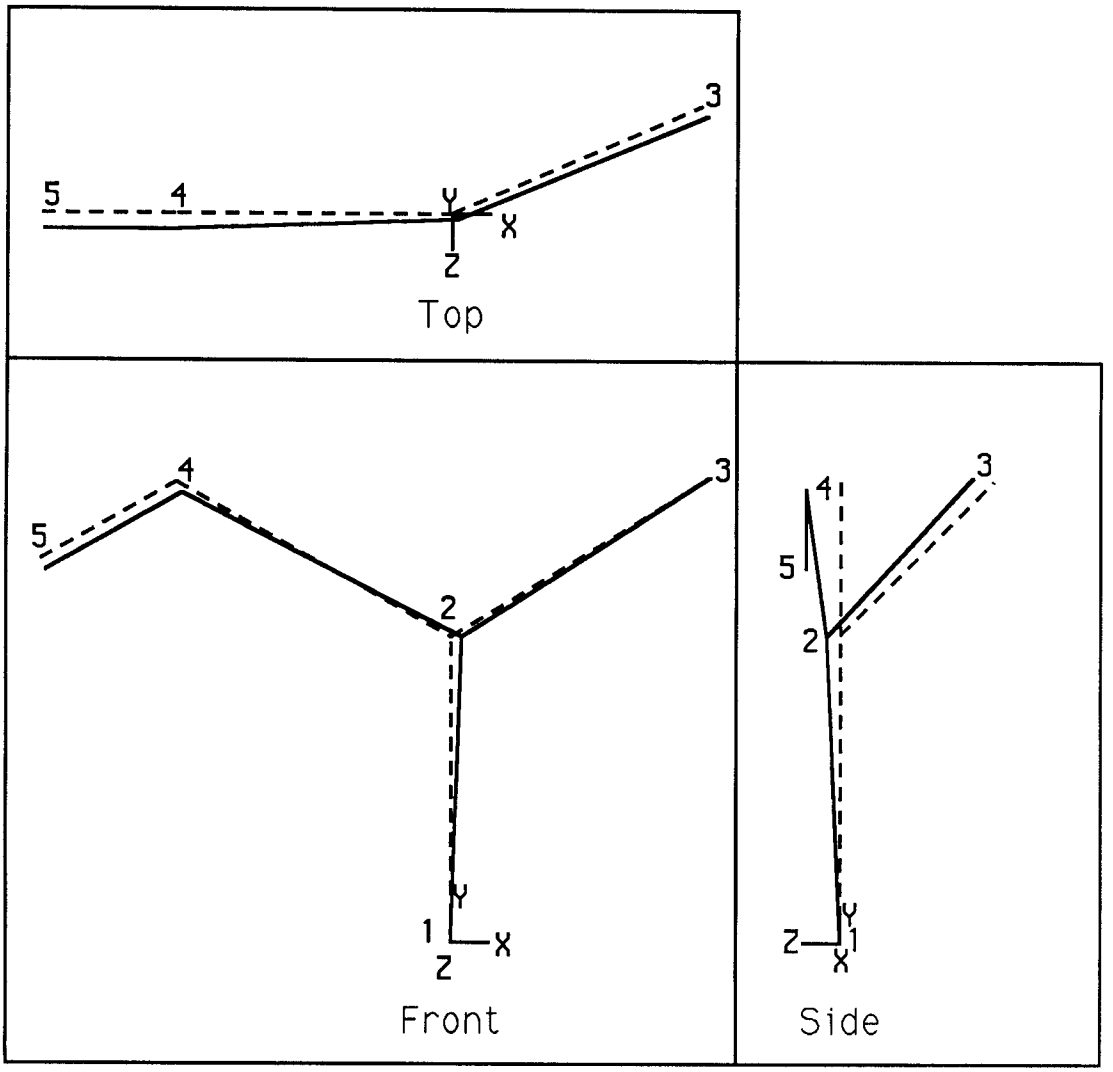

Fig. 5.33. Displaced centerline of replicating unit.

the yield strength of the vanadium, i.e., less than 310 MPa. The location of the maximum tensile and compressive stress was at node 1, where the magnitudes were 70.1 MPa and -75.3 MPa, respectively.

Table 5.4. Displacement Components and Deflections (see Fig. 5.32 for nodal locations)

Node	δX (mm)	δY (mm)	δZ (mm)	Total (mm)
1	0.000	0.000	0.000	0.000
2	0.484	-0.233	0.670	0.859
3	0.450	0.219	1.011	1.128
4	0.255	-0.463	1.622	1.706
5	0.333	-0.576	1.623	1.754

A buckling analysis was also carried out for the structural webs. Results showed that stresses were far below critical values for elastic instability.

5.3.4. First Surface Thermal Stress Analysis

The blanket modules are protected by graphite tiles, which together form the near-spherical first surface of the facility. They operate with the back (blanket) side at a constant temperature of 960°K and receive intense short duration energy pulses on the front (cavity) side. With the tile thickness at 1 cm, deposition layers typically on the order of microns are essentially self-constrained from thermal expansion. Following target microexplosion, the temperature histories of the tiles are found from the CONRAD[2] and WALL computer codes, with the effects of temperature-dependent conductivity included. This is input for a third code which numerically determines thermal stress, modeling the state as biaxial, isotropic and assessing the temperature dependence of the modulus, Poisson's ratio and the coefficient of thermal expansion.

The first tile material considered was a 4-D carbon/carbon composite developed by Fiber Materials, Inc.[a] Under intense thermal loads, such composites have shown higher resistance to crack growth than unreinforced graphite. The composites also have a natural porosity which enhances the material's capacity to accommodate thermal expansion. The temperature history for the unirradiated material is shown in Fig. 5.34, with a maximum of 1449°K. The corresponding stress response of Fig. 5.35 has a peak of 26.2 MPa, allowing for a safety factor of 2.1 when compared with strength at the corresponding temperature.

For comparison purposes, calculations were also made for H-451 graphite. This is a near isotropic, coarse-grained, extruded nuclear graphite developed for HTGRs. It was also selected because material properties are documented quite well.[20] For unirradiated material, the temperature and thermal stress histories of Figs. 5.36 and 5.37 have maxima of 1488°K and 26.47 MPa, respectively. This corresponds to a strength safety factor of 2.5 at this temperature. Irradiation to 10^{26} n/m^2 decreases the thermal conductivity at lower temperatures but does not appreciably change conductivity at temperatures from 1800 to 2300°K. The coefficient of thermal expansion is reduced, particularly at higher temperatures, while compressive strength and the modulus of elasticity increase after irradiation. In this case the maximum surface temperature rise is 1940°K and the thermal stress is higher as well at 49.6 MPa as indicated in Figs. 5.38 and 5.39. However, the compressive strength is 94.4 MPa at this temperature and thus the safety factor is 1.9, not significantly different than the preceding cases. Irradiated strength rises with increasing temperature to a maximum at about 1300°K and then begins to fall off. This causes the dip in the strength curve shown in Fig. 5.39. In addition, representative temperature profiles for unirradiated graphite are shown in Fig. 5.40. Curves (a) through (c) show the increasing gradient, reaching 1488°K at 0.252 ms. It can also be seen that the thickness of the heated/stressed layer is extremely small, typical for these cases.

---

[a] FMI, Biddeford Industrial Park, Biddeford, ME, 04005

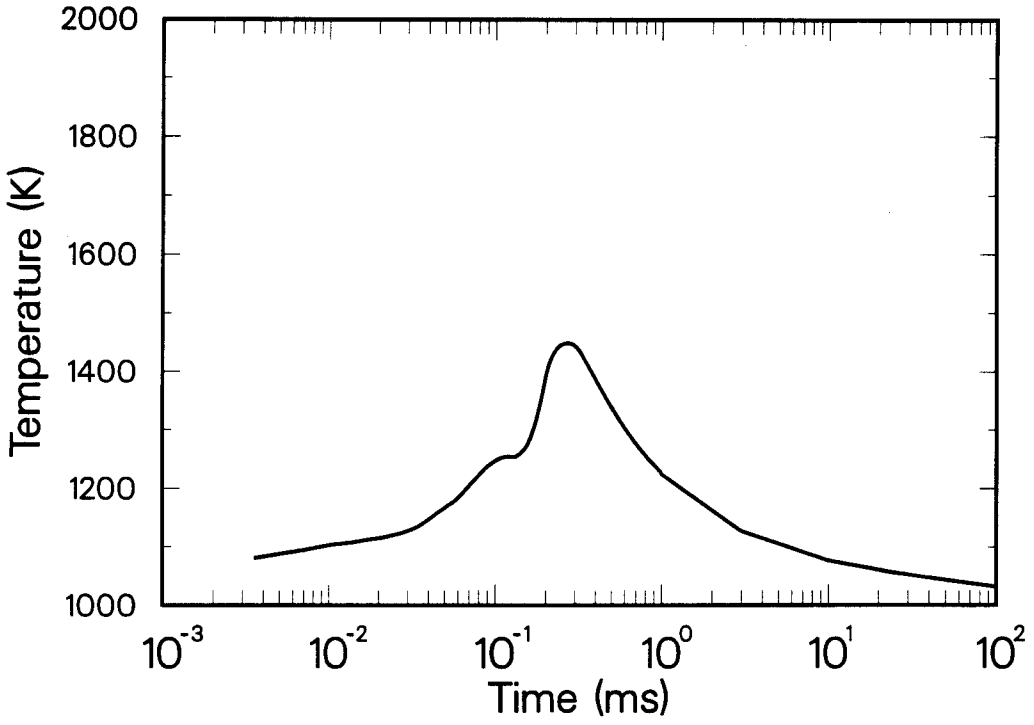

Fig. 5.34. First surface temperature for unirradiated FMI carbon/carbon composite.

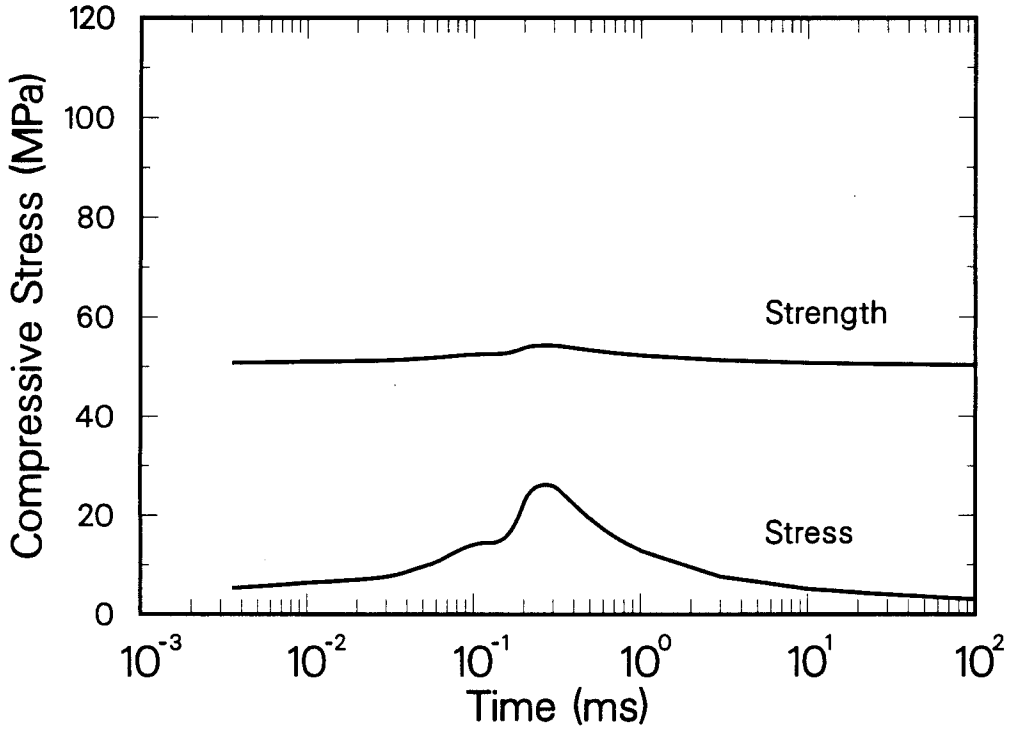

Fig. 5.35. Thermal stress and strength for FMI composite tile.

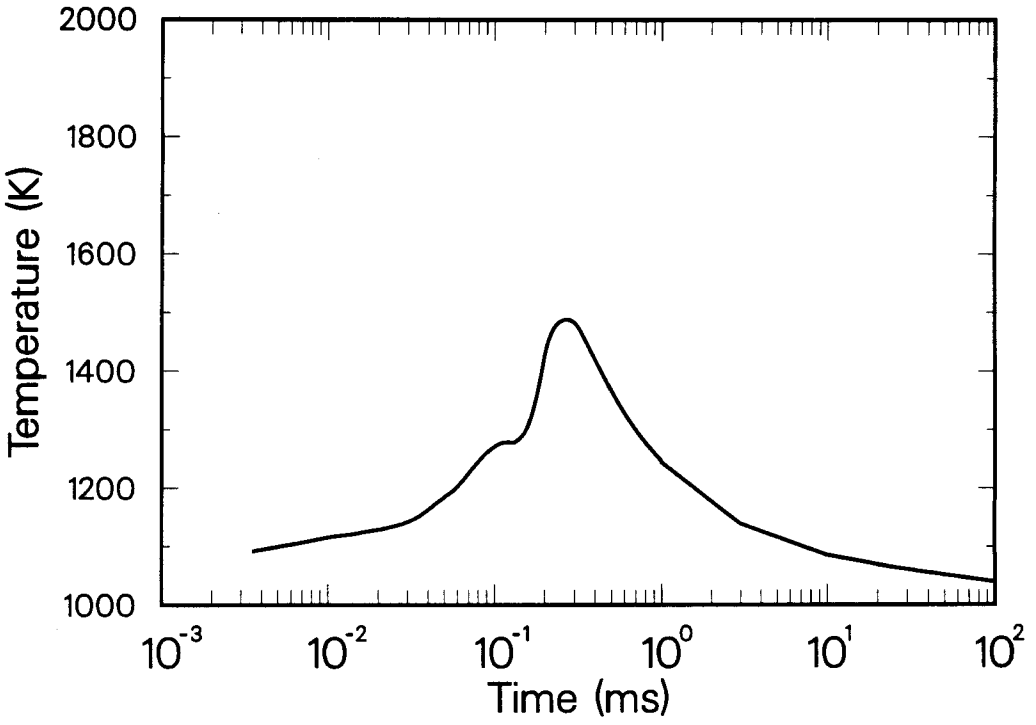

Fig. 5.36. First surface temperature for unirradiated H-451 graphite.

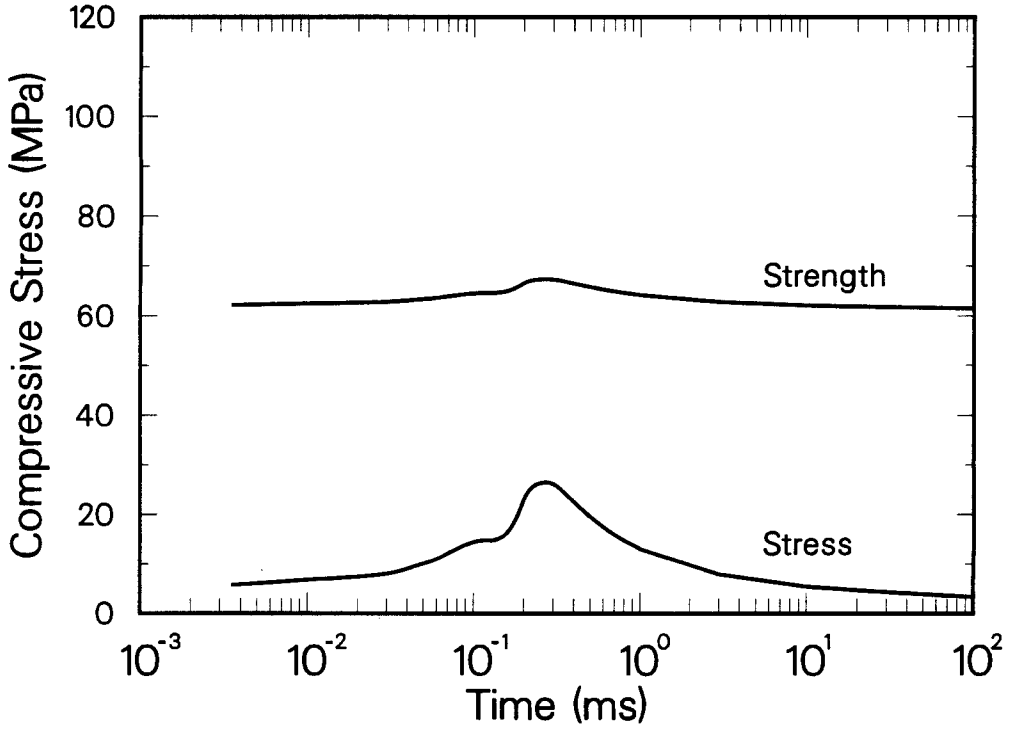

Fig. 5.37. Thermal stress and strength for unirradiated H-451.

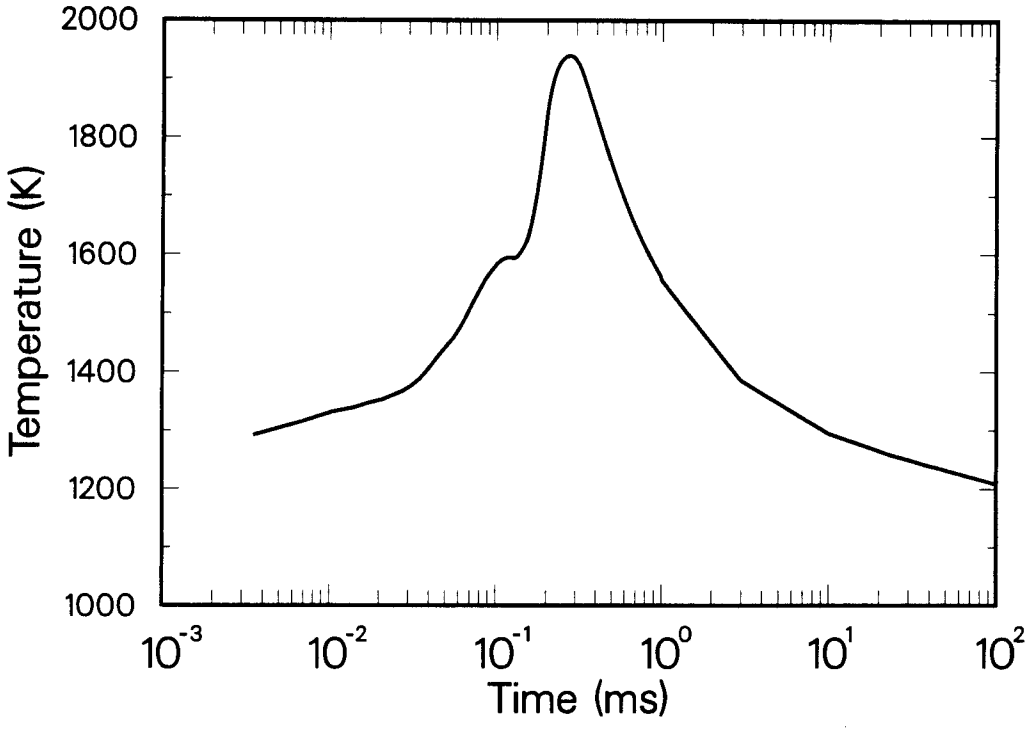

Fig. 5.38. First surface temperature for irradiated H-451.

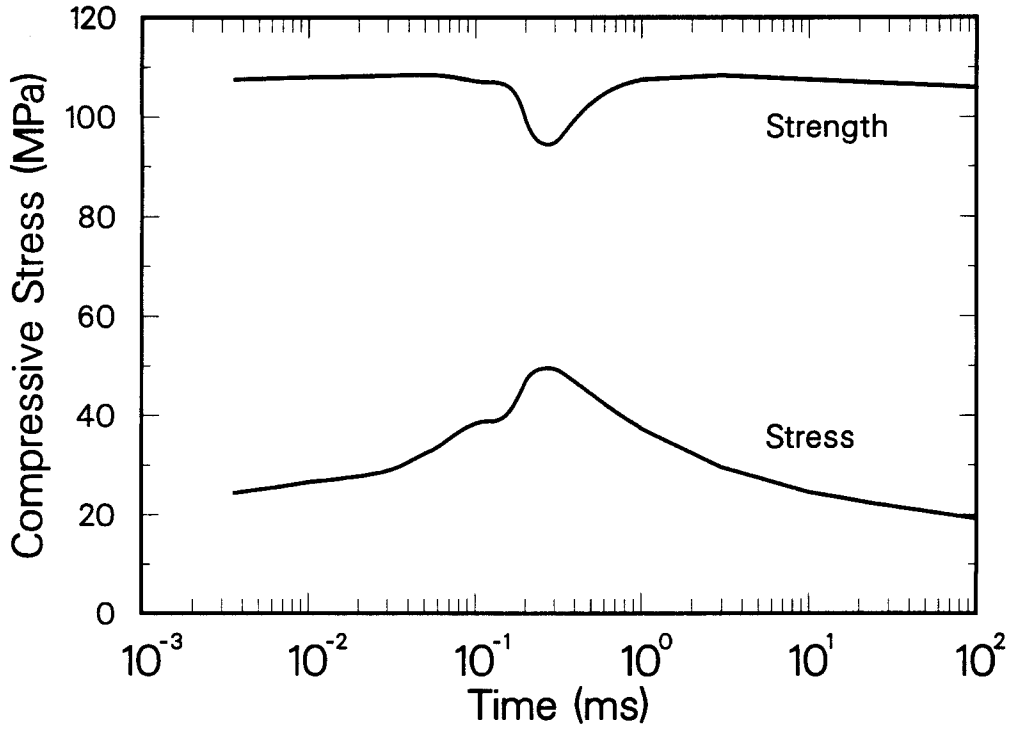

Fig. 5.39. Thermal stress and strength for irradiated H-451.

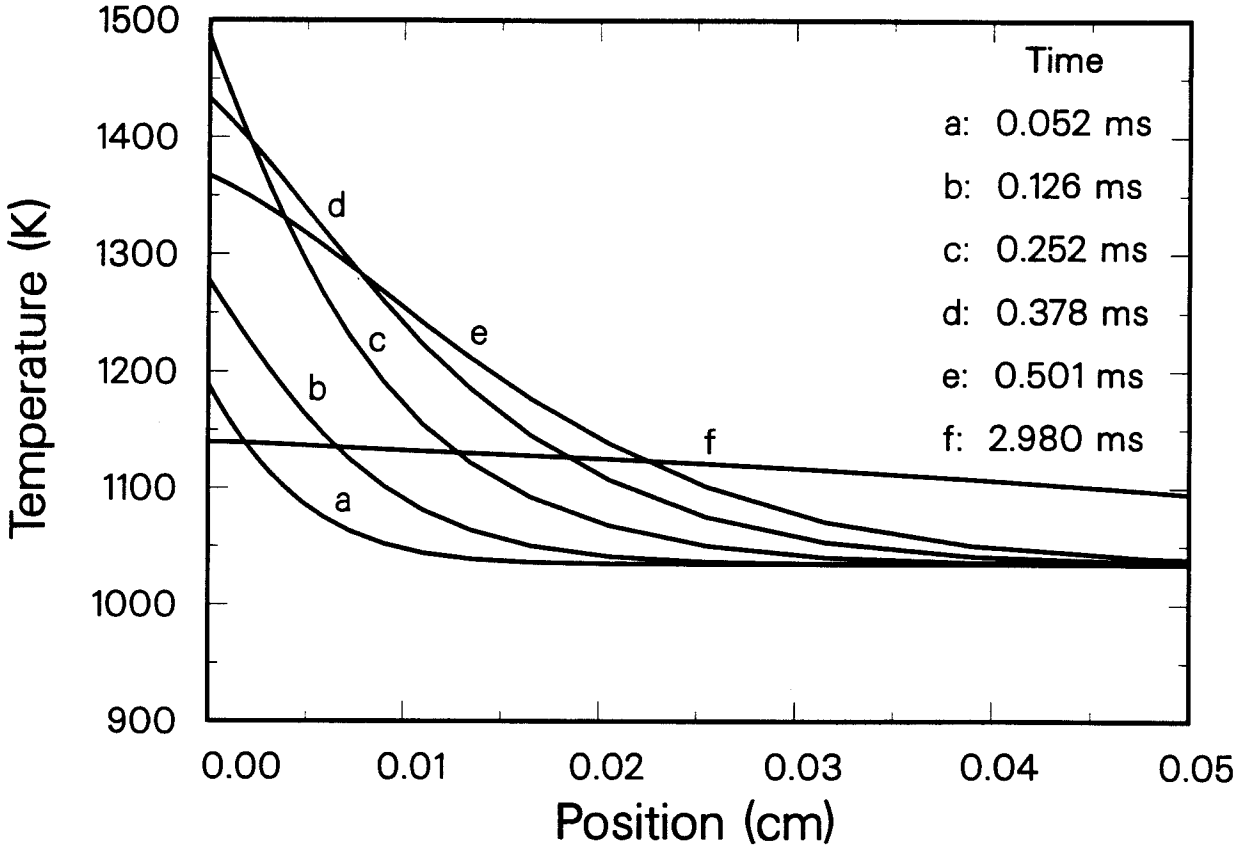

Fig. 5.40. Temperature profiles in tiles of irradiated H-451.

5.3.5 Summary

Results have been obtained for stress and stiffness analyses of the structural frame of the SIRIUS-T reactor chamber. Computations were made by finite element methods for regions which are most highly loaded by dead weight of the frame, modules and liquid metal. Stresses were well below yield limits for the vanadium alloy V-3Ti-1Si. The frame is quite robust, resulting in high mechanical stiffness. Deflections of individual frame cells were sufficiently small to accommodate module removal and replacement without difficulty.

A comparison was made of the temperature and thermal stress response of first wall tiles of carbon/carbon composite, unirradiated and irradiated graphite. Variations in temperature-dependent and irradiation-dependent properties tended to be self-cancelling and resulted in peak thermal stresses that had practically the same margin of safety based upon mechanical strength.

The results substantiate the credibility of the structural design of the SIRIUS-T reactor chamber.

References for Section 5

1. D.N. Braski, "The Post-Irradiated Tensile Properties and Microstructure of Several Vanadium Alloys," ASTM-STP-1047 (1990).
2. R.R. Peterson, J.J. MacFarlane, and G.A. Moses, "CONRAD -- A Combined Radiation-Hydrodynamics Vaporization-Condensation Computer Code," University of Wisconsin Fusion Technology Institute Report UWFDM-670 (1988).
3. J.J. MacFarlane, G.A. Moses, R.R. Peterson, "Energy Deposition and Shock Wave Evolution in Laser-Generated Plasma Expansions," Phys. Fluids B 1, 635 (1989).
4. J.J. MacFarlane, R.R. Peterson, and G.A. Moses, "Analysis of Physical Processes in ICF Target Chambers: Application to the Laboratory Microfusion Facility," Fusion Technology 15, 557 (1989).
5. T.J. McCarville, G.A. Moses, and G.L. Kulcinski, "A Model for Depositing Inertial Confinement Fusion X-rays and Pellet Debris into a Cavity Gas," University of Wisconsin Fusion Technology Institute Report UWFDM-406 (1981).
6. K.G. Adams and F. Biggs, "Efficient Computer Access to Sandia Photon Cross Sections II," SC-RR-71-0507, Sandia National Laboratories, Albuquerque, NM, December 1971.
7. J.J. MacFarlane, "IONMIX -- A Code for Computing the Equation of State and Radiative Properties of LTE and Non-LTE Plasmas," Comput. Phys. Commun., 56, 259 (1989).
8. C. Verdon, R. McCrory, P. McKenty, and S. Skupsky, "Target Design Considerations for SIRIUS-M," University of Rochester, Laboratory for Laser Energetics (1986).
9. J.J. MacFARLANE, P. WANG, and G.A. MOSES, "A Model for Computing Radiation Transport in Moderate Density Plasmas," University of Wisconsin Fusion Technology Institute Report UWFDM-822 (1990).
10. P. Wang, Ph.D. Dissertation, University of Wisconsin, in preparation.
11. J.P. Apruzese, J. Davis, D. Duston, and K.G. Whitney, J. Quant. Spectrosc. Radiat. Transfer, 23, 479 (1980).

12. J.P. Apruzese, J. Quant. Spectrosc. Radiat. Transfer, 25, 419 (1981).

13. A. Burgessand H.P. Summer, Mon. Not. R. Astr. Soc., 174, 345 (1976).

14. A. Burgessand M.C. Chidichimo, Mon. Not. R. Astr. Soc., 203, 1269 (1983).

15. I.I. Sobelman, L.A. Vainshtein, and E.A. Yukov, Excitation of Atoms and Broadening of Spectral Lines, Springer-Verlag, New York.(1981)

16. G.V. Marrand, J.B. West, At. Data Nucl. Data Tables, 18, 497 (1976).

17. D.E. Post, R.V. Jensen, C.B. Tarter, W.H. Grasberger, and W.A. Lokke, At. Data Nucl. Data Tables, 20, 397 (1977).

18. J.J. MacFarlane, P. Wang, and G.A. Moses, "Non-LTE Radiation Transport in Moderate Density Plasmas," submitted to Lasers and Particle Beams (1990).

19. R. Doernach, "Sphärische Raumfachwerke," Der Stahlbau, 29, 97 (1960).

20. G.R. Hopkins et al., "Carbon and Silicon Carbide as First Wall Materials in Inertial Confinement Fusion Reactors," GA-A14894, General Atomic Co. Report (1978).

Figure Captions

Fig. 5.10. Schematic illustration of the SIRIUS-T target chamber.

Fig. 5.11. Target x-ray spectrum.

Fig. 5.12. Temperature profiles in the Xe gas at simulation times of (a) 0.28, (b) 0.78, (c) 4.5, and (d) 13 seconds.

Fig. 5.13. Radiation flux and time-integrated flux at the first wall (180 group case).

Fig. 5.14. Dependence of time-integrated radiation flux at the graphite tiles on the number of photon energy groups in the radiation diffusion model.

Fig. 5.15. Radiation flux escaping a spherical plasma with T = 2 eV, $n = 3 \times 10^{16}$ cm^{-3}, and R = 4 meters. The dashed curve represents the flux from a blackbody.

Fig. 5.16. Optical depth from the center of the spherical plasma to the plasma boundary.

Fig. 5.17. Comparison of fluxes computed using our non-LTE radiative transfer model (solid curve) and a multigroup diffusion model (dotted curve).

Fig. 5.18. Radiant heat flux on SIRIUS-T graphite tiles. Calculated with CONRAD with 180 energy group radiation diffusion.

Fig. 5.19. Thermal conductivity and heat capacity for unirradiated graphite H-451 versus temperature.

Fig. 5.20. Thermal conductivity and heat capcity for irradiated graphite H-451 versus temperature. The graphite is irradiated by 10^{22} neutrons/cm^2 with an energy greater than 0.18 MeV.

Fig. 5.21. Thermal conductivity and heat capacity for unirradiated FMI 4D carbon/carbon composite versus temperature.

Fig. 5.22. Temperature profiles in unirradiated graphite H-451 SIRIUS-T tiles at various times.

Fig. 5.23. Temperature profiles in irradiated graphite H-451 SIRIUS-T tiles at various times.

Fig. 5.24. Temperature profiles in unirradiated graphite carbon/carbon composite SIRIUS-T tiles at various times.

Fig. 5.25. Front surface temperatures of SIRIUS-T graphite tiles versus time. Results are shown for unirradiated H-451, irradiated H-451, and unirradiated carbon/carbon composite.

Fig. 5.26. Icosahedron projections on spherical surfaces with different dividing frequencies.

Fig. 5.27. Reactor chamber structural frame.

Fig. 5.28. Bottom view of chamber with ten modules removed.

Fig. 5.29. In-plane loading of a cell from dead weight.

6. NEUTRONICS ANALYSIS

6.1. Introduction

In order to minimize the production cost of tritium, the neutronics analysis aimed at optimizing the blanket design to maximize the achievable tritium breeding ratio (TBR). We have selected liquid lithium in vanadium structure as the primary breeding concept. This was the number one recommendation of the Blanket Comparison and Selection Study (BCSS).[1] The use of beryllium as a neutron multiplier is required to maximize the TBR.

In this section, the neutronics optimization leading to the reference blanket design is given. The spatial variation of nuclear heating generated in the blanket will be determined and used as input to the thermal hydraulics analysis. In addition, the profiles of the radiation damage produced in the vanadium alloy structural material and graphite tiles will be determined. This information is essential for determining the lifetime of these components. Furthermore, the tritium production rate in the different beryllium zones will be determined and the tritium inventory in the beryllium calculated.

6.2. Calculational Model

The neutronics analysis performed for SIRIUS-T is aimed primarily at optimizing the blanket design to maximize the TBR. A self-cooled liquid lithium blanket with the vanadium alloy V-3Ti-1Si structure and beryllium neutron multiplier is utilized in SIRIUS-T. The Be is assumed to have a 0.9 density factor. Each blanket module is composed of several layers of beryllium tiles shaped to conform to the structural frame and the central beam port. The lithium coolant is radially fed to five coolant layers between the Be layers. 1 cm thick graphite tiles, followed by 1 cm thick back structure that has 50% Li coolant, are used in front of the blanket. The blanket has a 1 cm thick front wall that is separated from the tile back structure by a 1 cm thick void region. The total tile and blanket thickness is 1 m. Based on the mechanical design and structural analysis for the blanket support frame, the webs of the frame and the blanket module side walls were determined to occupy 12.77% of the volume in the blanket region. In addition, the beam penetrations correspond

to 1.97% of the blanket volume. The lithium in the radial tubes feeding the coolant layers amounts to 2.3% of the blanket volume.

The neutronics calculations have been performed using the one-dimensional discrete ordinates code ONEDANT[2] with cross section data based on the ENDF/B-V[3] evaluation and the P_3-S_8 approximation. The 4 m inner radius spherical chamber is modeled in spherical geometry with the target at the center emitting neutrons with energy distribution given by the SIRIUS target spectrum. As a result of neutron target interactions the source spectrum has only 78% of the neutrons at 14.1 MeV, 21% in the range 3.5-14.1 MeV, and 1% in the range 1.5-3.5 MeV. Two approaches were considered to calculate the overall TBR. One approach is based on performing the neutronics calculations using the local blanket composition excluding the structural support webs and beam penetrations. The results are then modified to account for the reduced blanket coverage. The other approach uses a homogenized composition for each blanket layer taking into account the beam penetrations and structural frame. The second approach yields conservative estimates for the overall TBR and is utilized here. In the neutronics calculations, each Li layer is considered to consist of 85.26% Li, 12.77% V, and 1.97% void. On the other hand, each Be layer has 82.96% Be, 2.3% Li, 12.77% V, and 1.97% void.

6.3. Blanket Design Optimization

Preliminary blanket optimization has been performed based on treating the blanket as a single homogeneous region. Figure 6.1 shows the effect of the lithium content in the blanket on the TBR. The effect of replacing the 20 cm thick back layer of the 1 m thick blanket by a graphite reflector is also shown. This results in reducing the TBR with the reduced cost of Be being more than offset by the loss in the value of produced tritium. Hence, no graphite reflector is used at the back of the SIRIUS-T blanket. The effect of the outer radius of the blanket on the TBR is shown in Fig. 6.2. It was found that the increase in produced tritium resulting from increasing the tile/blanket thickness beyond 1 m will be negated by the increased chamber cost. Hence, the total tile and blanket thickness is taken to be 1 m. Based on this preliminary optimization analysis, the

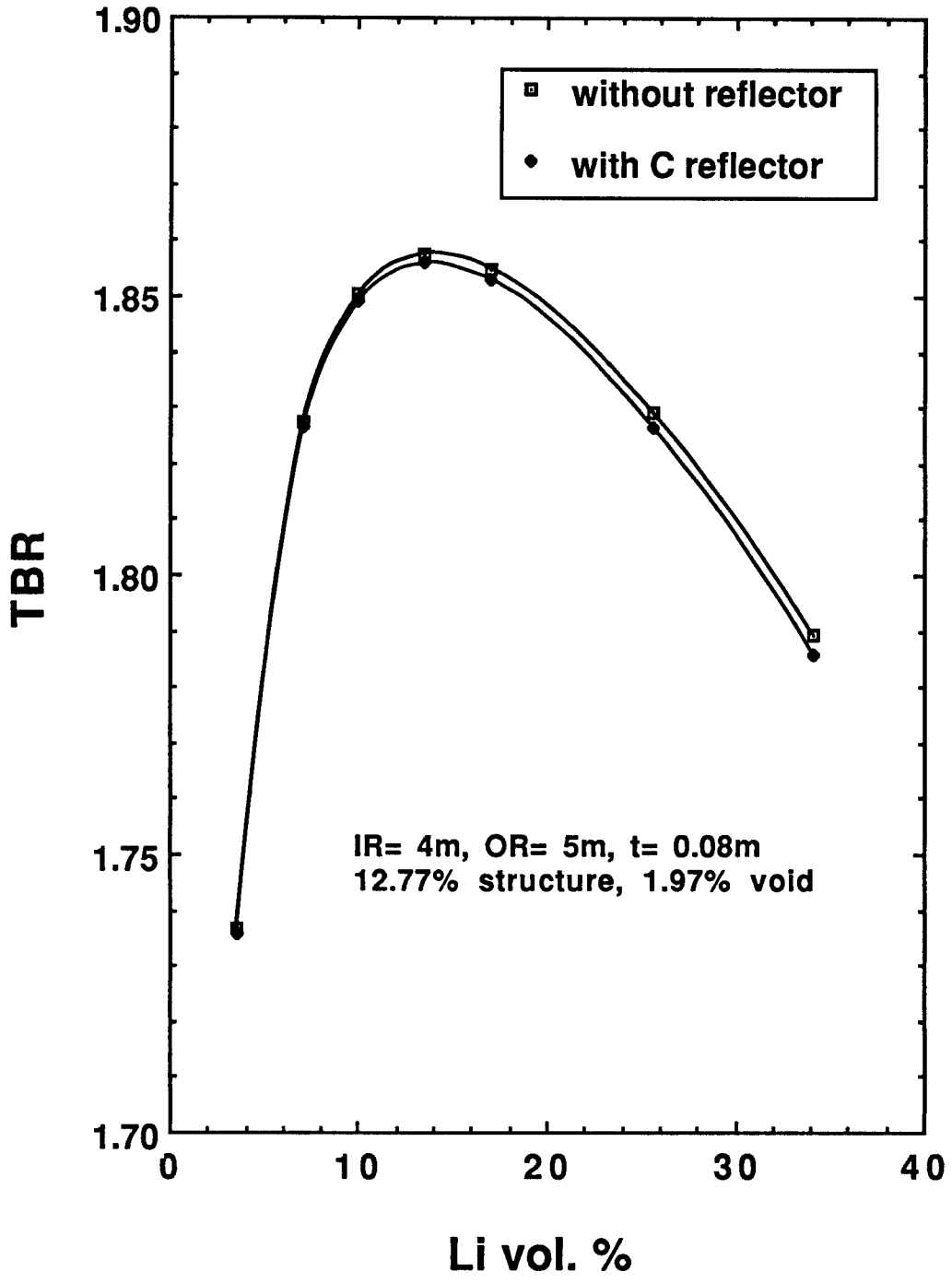

Fig. 6.1. Effect of lithium content in a homogeneous blanket model on the TBR.

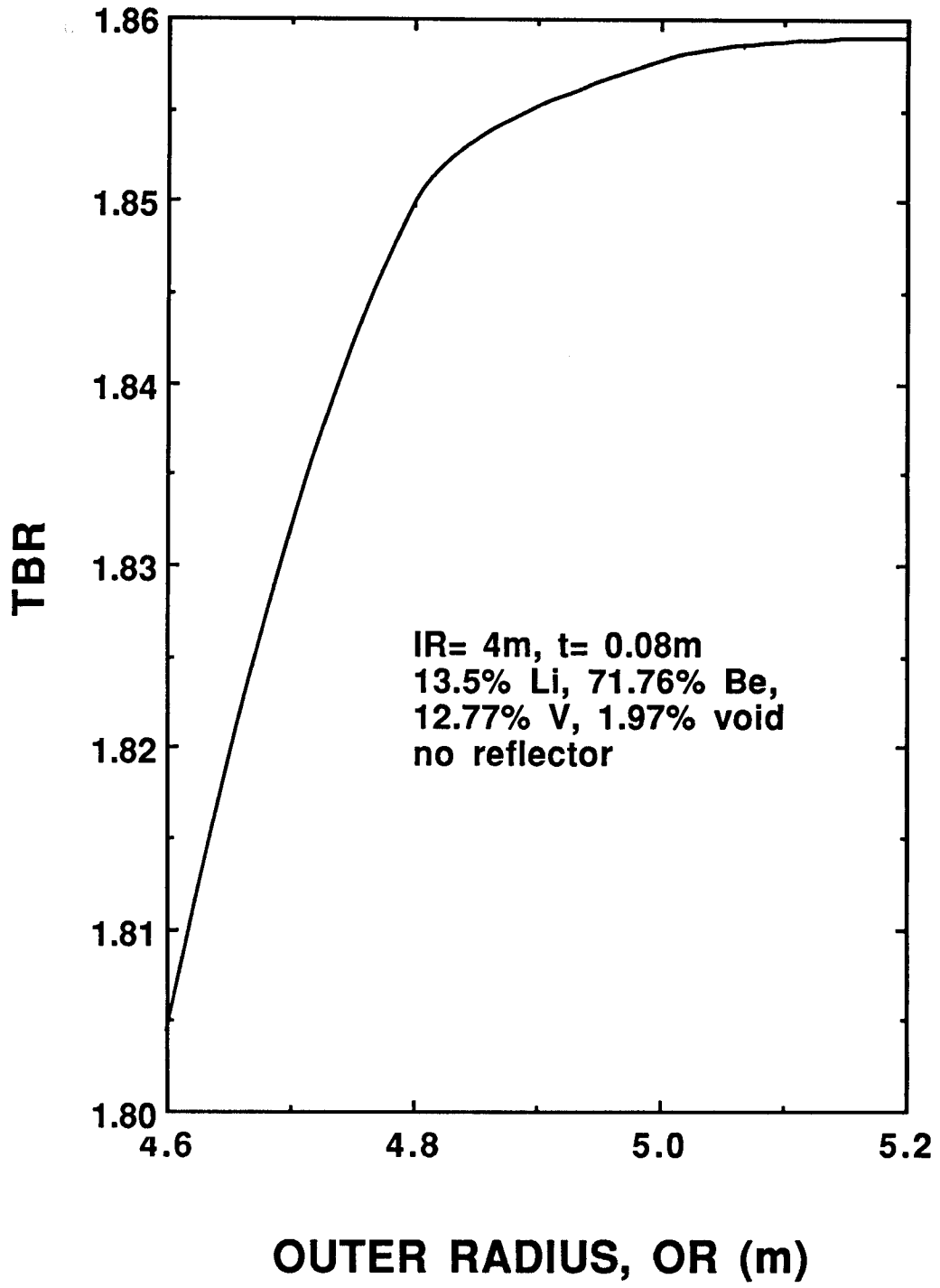

Fig. 6.2. Effect of the homogeneous blanket thickness on the TBR.

TBR maximizes at a lithium enrichment of 20% ^{6}Li and a Li volume fraction of 13.5%. The corresponding TBR value is 1.8577.

Starting from this optimum homogeneous composition, the Li and Be have been arranged in alternating layers with the overall Li volume fraction being preserved. The neutronics calculations have been performed for the layered configuration to maximize the TBR by varying the Li enrichment and the thicknesses of the alternating layers. Varying the Li enrichment for the layered configuration indicated that the TBR maximizes at a Li enrichment of 70% ^{6}Li as shown in Fig. 6.3. The thicknesses of the different Li and Be layers were then varied one at a time to determine the optimum configuration. In general, the results indicate that thinner Li layers and thicker Be layers yield higher values for the TBR. However, thermal hydraulics requirements constrained the Li coolant layers not to be thinner than 1 cm. In addition, for the structure temperature not to exceed 650°C the front Be zone thickness is limited to 5 cm. The lithium volume content in the optimum layered blanket configuration is only 6.6%, which is about half the optimum Li content based on treating the blanket as a single homogeneous region.

Varying the Li enrichment for the optimum layered configuration, the TBR was found to increase as the enrichment increases as shown in Fig. 6.4. Although the TBR enhancement appears to be small, the cost impact will be significant since an enhancement of 0.001 in the TBR results in an additional 1.65 kg of tritium produced over the 30 FPY reactor life for the 100 MJ yield and 10 Hz repetition rate. At a tritium cost of $10,000/g, this translates into $16.5 M enhancement in the value of tritium produced. A simple cost tradeoff analysis has been performed to assess the economic impact of increasing the Li enrichment. In this analysis, the cost of Be is taken to be $450/kg and the increment in cost of Li per 10% increment in enrichment is considered to be $150/kg. The lithium volume outside the blanket is assumed to be twice the volume in the blanket. The analysis indicates that using 90% ^{6}Li results in a net economic gain in spite of the increased Li cost as shown in Table 6.1. The effect of varying the total tile and blanket thickness is shown in Figure 6.5. The cost tradeoff analysis indicated that increasing the thickness to 1.1 m leads to a net economic loss with the increase in tritium produced for the thicker blanket being

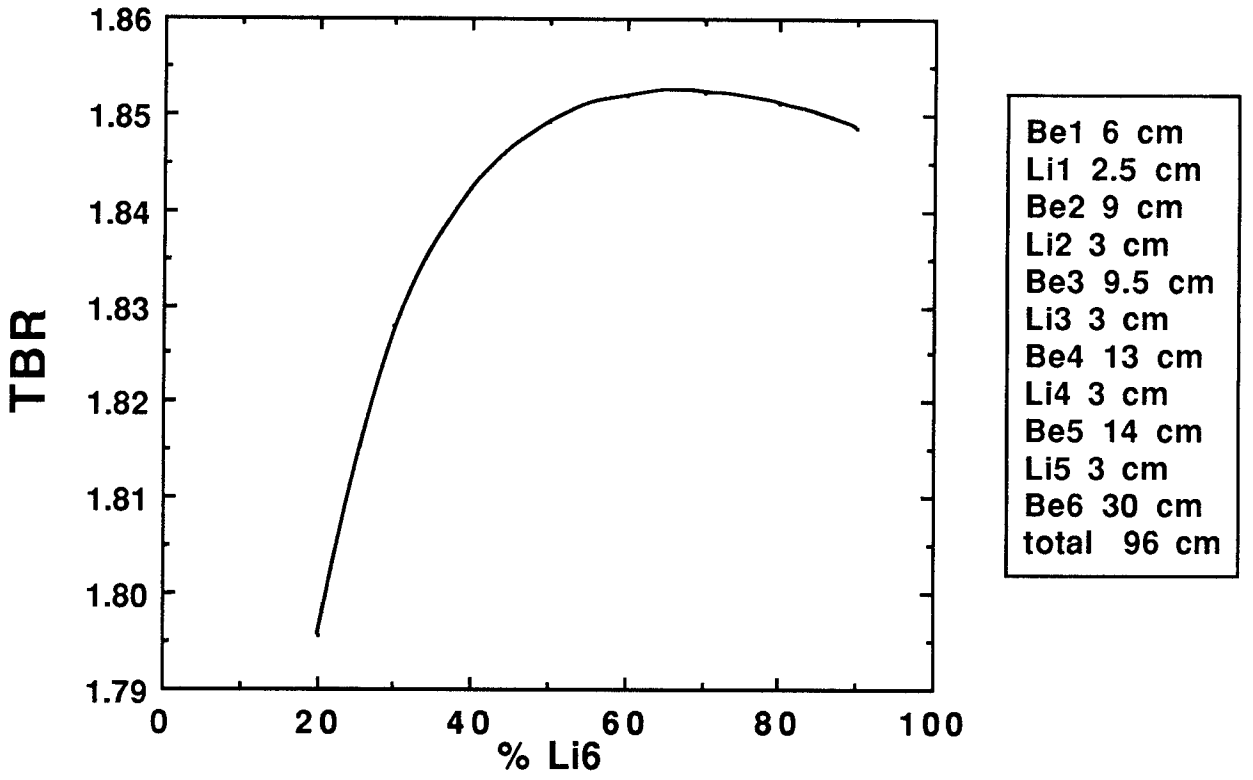

Fig. 6.3. Effect of lithium enrichment on the TBR for the layered blanket configuration that preserves the overall Li content determined for the homogeneous blanket.

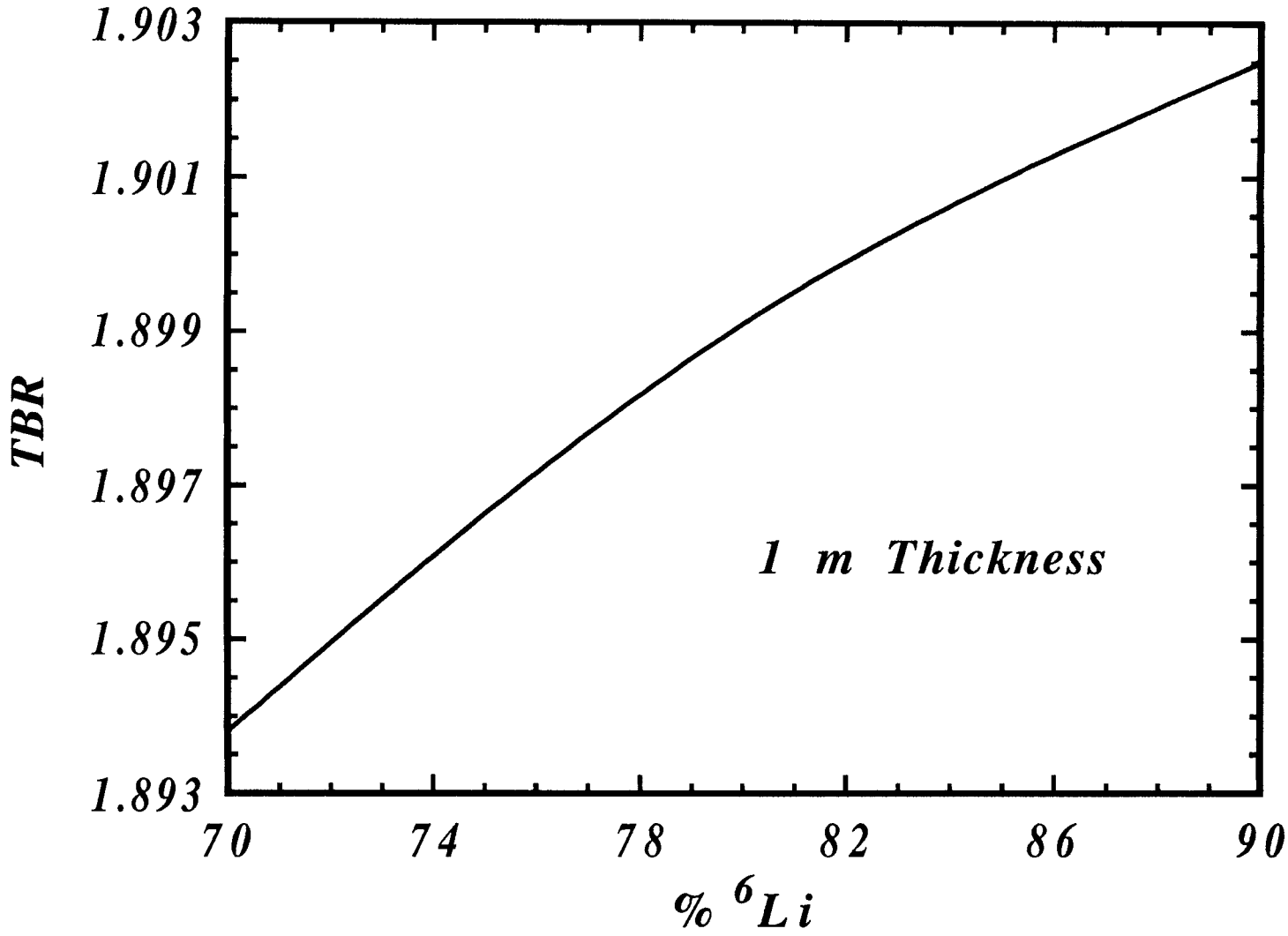

Fig. 6.4. Effect of Li enrichment on the TBR for the optimized layered configuration of the blanket.

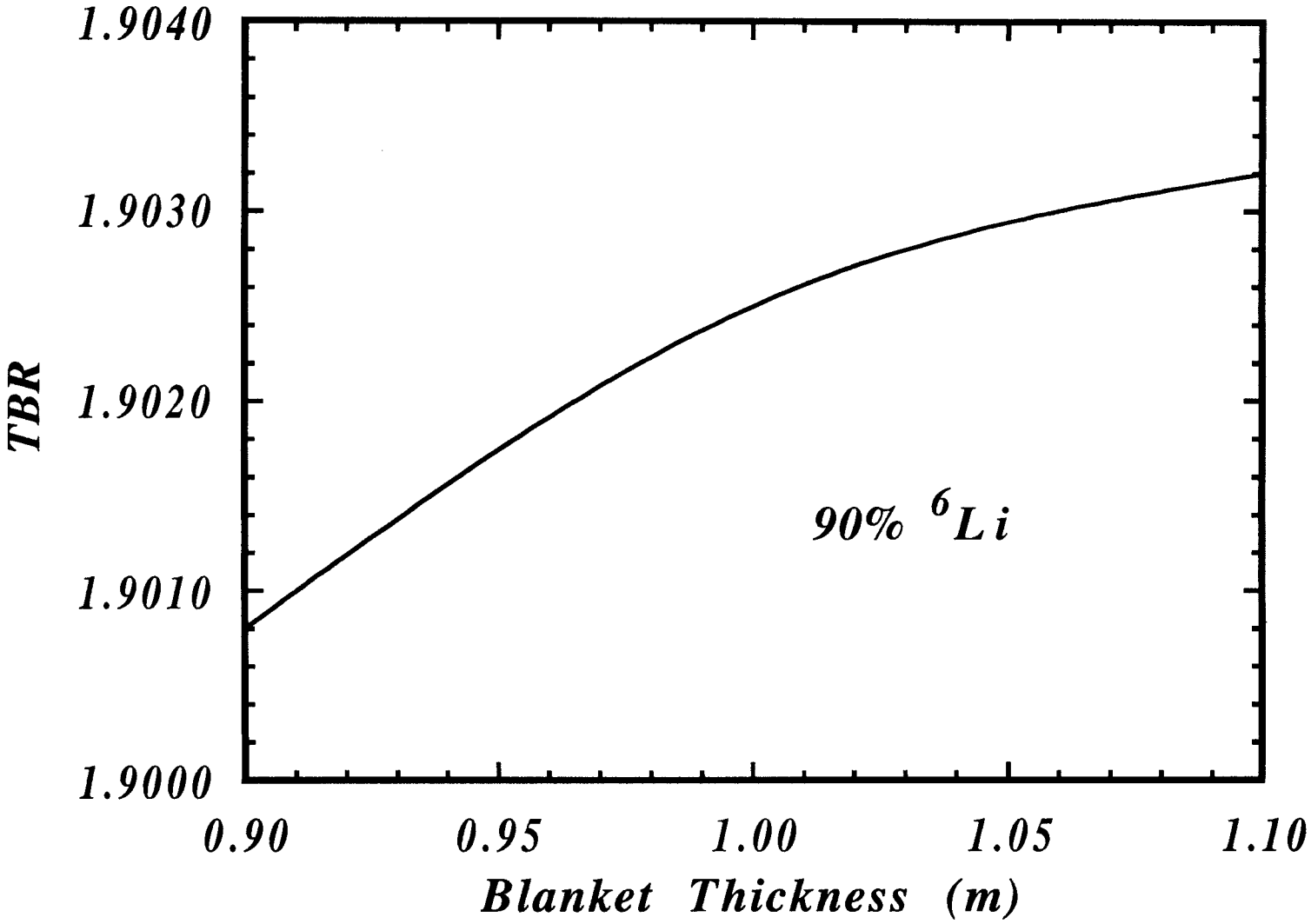

Fig. 6.5. Effect of blanket thickness on the TBR for the optimized layered configuration of the blanket.

negated by the increased chamber cost. Furthermore, reducing the thickness to 0.9 m is not economically attractive with the reduced chamber cost being more than offset by the loss in the value of produced tritium. Therefore, a 1 m thick blanket is chosen for SIRIUS-T with the radial build given in Figure 6.6 and the Li enriched to 90% ^{6}Li.

Table 6.1. Cost Impact of Key Blanket Design Parameters

Thickness (m)	% ^{6}Li	TBR	Increase in Tritium Value (M$)	Chamber Cost Savings (M$)	Net Gain (M$)
1	90%	1.9025	0.0	0.0	0.0
1	80%	1.8991	-56	4	-52
1	70%	1.8938	-144	8	-136
1.1	90%	1.9031	12	-20	-8
0.9	90%	1.9008	-28	19	-9

6.4. Neutronics Performance of the Reference SIRIUS-T Blanket

6.4.1. Tritium Breeding

The overall TBR for the reference SIRIUS-T blanket design is 1.9025. Because of the relatively high lithium enrichment and the large amount of Be used in the blanket, only 0.17% of the tritium is produced by the high energy ^{7}Li (n,n'α)t reaction with the rest being produced via the ^{6}Li (n,α)t reaction.

6.4.2. Nuclear Heating

The total nuclear heating in the blanket amounts to 19.36 MeV per incident source neutron with 16.08 MeV contributed by neutron heating and the rest (3.28 MeV) resulting from gamma photon heating. The average energy of the source neutron incident on the blanket from the target is

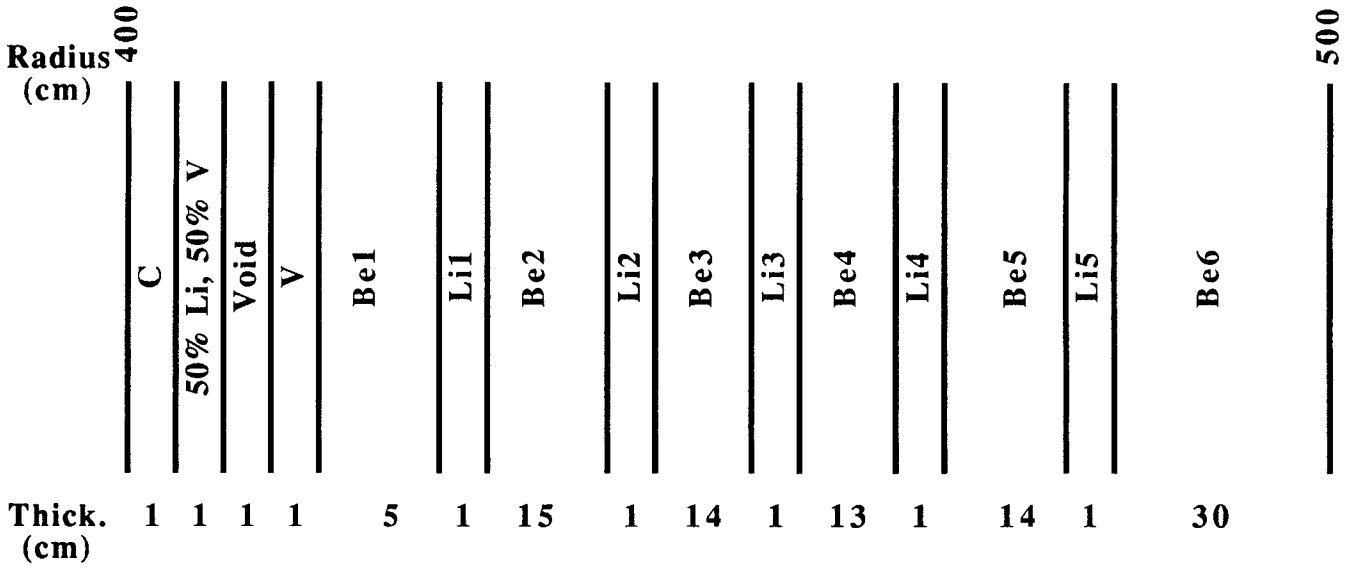

REFERENCE RADIAL BUILD OF SIRIUS-T BLANKET

Be zone: 82.96% Be, 2.3% Li, 12.77% V, 1.97% void
Li zone: 85.26% Li, 12.77% V, 1.97% void

Fig. 6.6. Reference radial build of SIRIUS-T blanket.

12.48 MeV. This implies that the nuclear energy multiplication of the blanket is 1.55. For a target yield of 100 MJ and a repetition rate of 10 Hz, the target yields a power of 1000 MW. Out of this power, 746 MW is carried by neutrons and 254 MW is carried by the x-rays and debris. The total nuclear heating in the blanket, therefore, corresponds to a power of 1156 MW. Adding the energy deposited by x-rays and debris at the inner surface of the blanket, the total thermal power is 1410 MW and the overall energy multiplication defined as the ratio of the thermal power to the target DT fusion power is 1.41. The radial variation of the nuclear heating in the different blanket layers is shown in Fig. 6.7. The results of Fig. 6.7 have been used as input for the blanket thermal hydraulics analysis.

6.4.3. Radiation Damage

The radial variation of dpa and helium production rates in the vanadium alloy structure is shown in Fig. 6.8. The results indicate that the peak dpa and helium production rates in the V back structure of the tiles are 30 dpa/FPY and 94 appm/FPY, respectively. The peak dpa rate in the front wall of the blanket module is 24 dpa/FPY and the helium production rate is 70 appm/FPY. Detailed lifetime analysis for the V-3Ti-1Si alloy that takes into account swelling and radiation embrittlement indicated that the vanadium alloy lifetime in the SIRIUS-T blanket is expected to be ~4 FPY. The structural frame, which is also made of V-3Ti-1Si, starts at a point 35 cm behind the FW where the damage level is 3.5 dpa/FPY and 5 appm of He/FPY. Under these conditions we project that the frame will be a lifetime component. The peak dpa rate in the graphite tiles is 18 dpa/FPY. The lifetime of graphite is determined by the damage level at which the graphite passes through the shrinkage phase and crosses the zero dimensional change axis on the way to runaway swelling. Data on irradiation of several forms of graphite show that the useful life in SIRIUS-T is 2 FPY. Detailed lifetime analysis is given in Section 8.

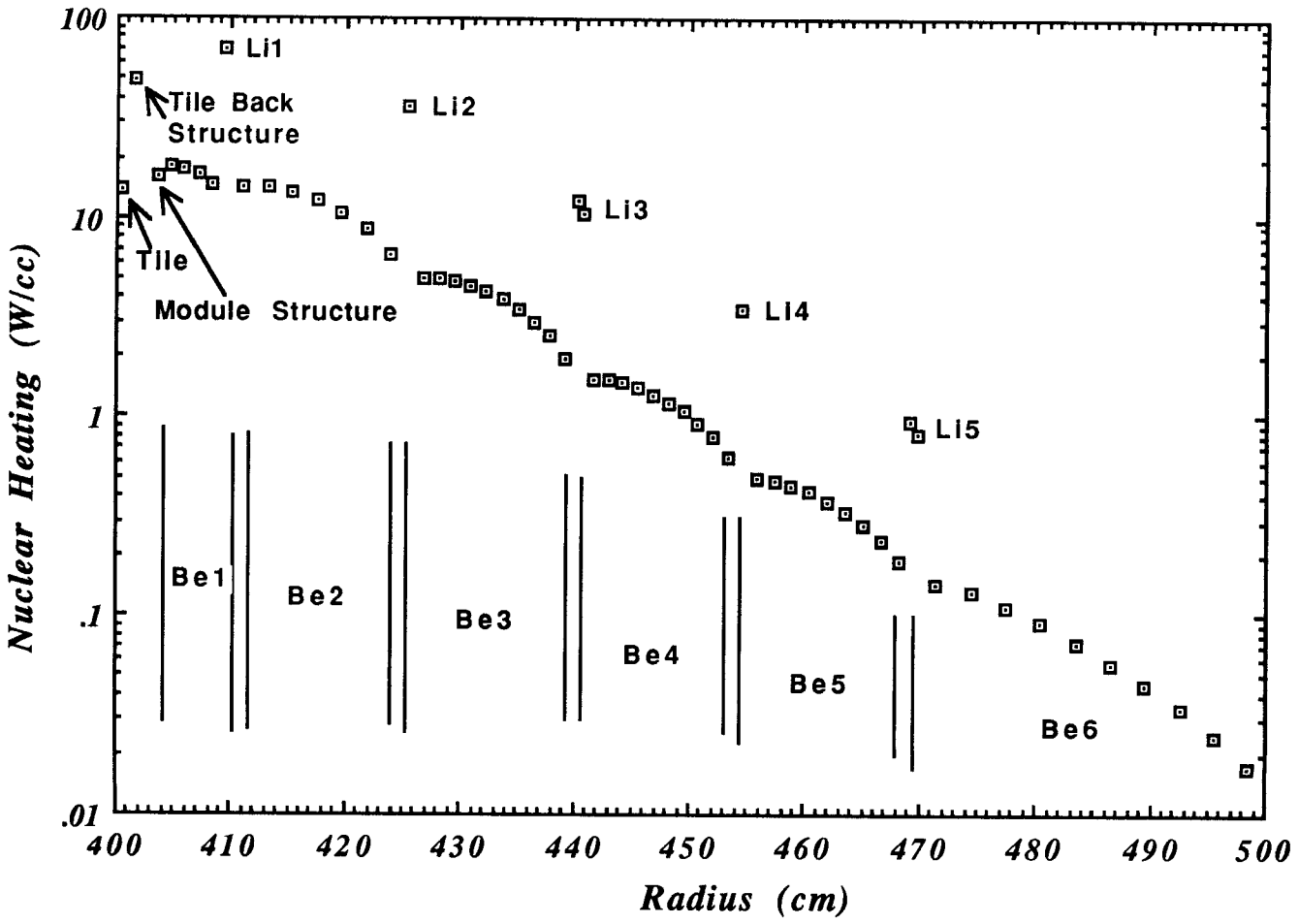

Fig. 6.7. Spatial distribution of nuclear heating in the blanket.

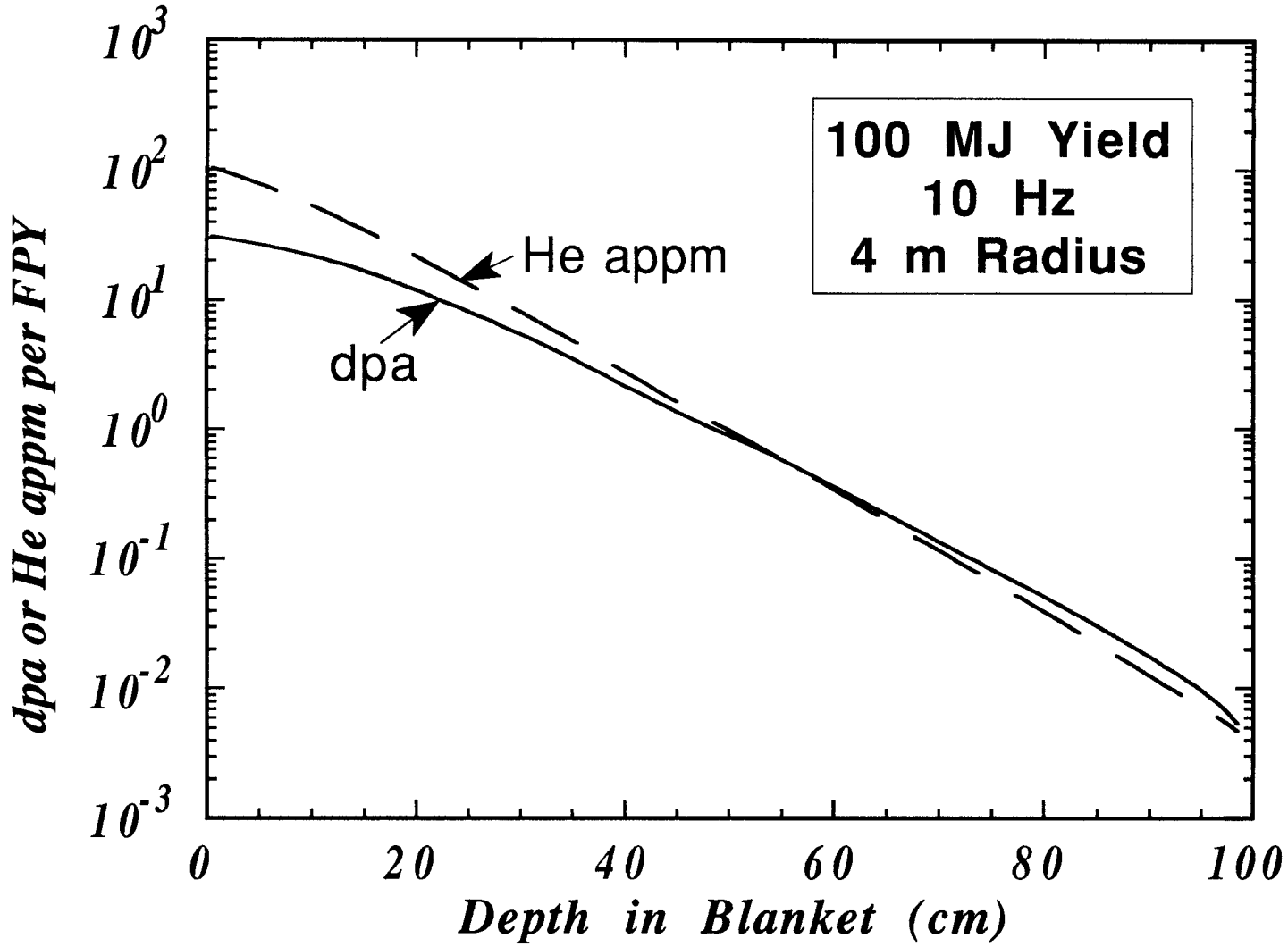

Fig. 6.8. Helium and dpa production rates in V structure.

6.4.4. Tritium Production in Beryllium

Neutron irradiation of beryllium in fusion reactors results in the production of tritium. The tritium inventory in the Be depends on the rate of tritium production and the retention and transport characteristics of tritium in Be. The limited data available on tritium retention in Be show that the retention rate drops as the temperature increases.[4] The tritium production rate determined from the neutronics calculations along with the calculated temperature distribution have been used to determine the tritium inventory in the different Be layers of the blanket at the end of the blanket lifetime. The results given in Fig. 6.9 assume that the Be is annealed to 650°C every 2 months. At this temperature only 2% of the tritium produced is retained in the Be. The total tritium inventory in the Be used in the SIRIUS-T blanket is 19 g.

6.5. Summary

Table 6.2 gives the major neutronics parameters for the reference SIRIUS-T blanket.

Table 6.2. Neutronics Parameters for the Reference SIRIUS-T Blanket Design.

Tritium breeding ratio:	T6	1.8993
	T7	0.0032
	Total	1.9025
Nuclear heating (MeV/fusion):	Neutron	16.88
	Gamma	3.44
	Total	20.32
Nuclear energy multiplication	1.55	
Overall energy multiplication	1.41	
Peak dpa rate in graphite tiles	18 dpa/FPY	
Peak He production rate in graphite	4420 appm/FPY	
Peak dpa rate in V alloy	30 dpa/FPY	
Peak He production rate in V alloy	94 appm/FPY	
Total tritium inventory in Be	19 g	

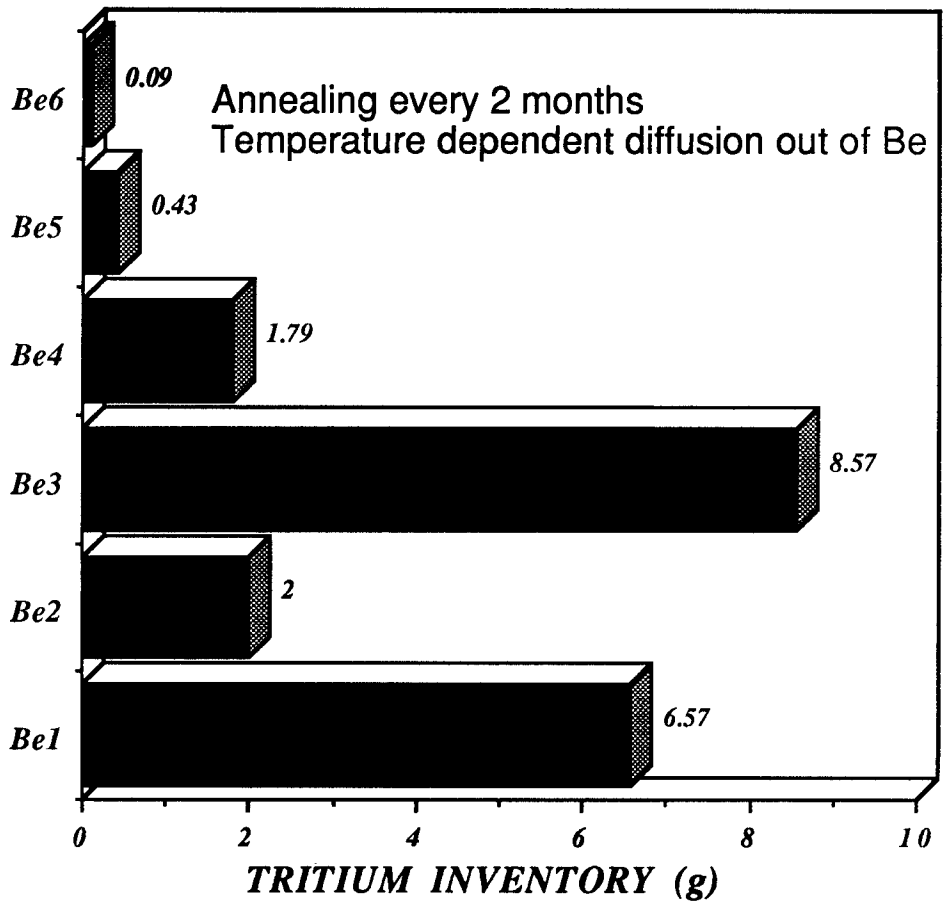

Fig. 6.9. Tritium inventory in the different Be zones.

References for Section 6

1. D.L. SMITH et al., "Blanket Comparison and Selection Study," ANL/FPP84-1, Argonne National Laboratory (1984).
2. R.D. O'DELL et al., "User's Manual for ONEDANT: A Code for One Dimensional, Diffusion Accelerated Neutron Particle Transport," LA-9184-M, Los Alamos National Laboratory (1982).
3. D. Garber, "ENDF/B-V," BNL-17541 (ENDF-201), National Nuclear Data Center, Brookhaven National Laboratory (1975).
4. D.L. BALDWIN et al., "Tritium Release from Irradiated Beryllium at Elevated Temperatures," 4th International Conf. on Fusion Reactor Materials, Kyoto, Japan, Dec. 1989. To be published in J. of Nuclear Materials (1990).

Figure Captions for Section 6

Fig. 6.1. Effect of lithium content in a homogeneous blanket model on the TBR.

Fig. 6.2. Effect of the homogeneous blanket thickness on the TBR.

Fig. 6.3. Effect of lithium enrichment on the TBR for the layered blanket configuration that preserves the overall Li content determined for the homogeneous blanket.

Fig. 6.4. Effect of Li enrichment on the TBR for the optimized layered configuration of the blanket.

Fig. 6.5. Effect of blanket thickness on the TBR for the optimized layered configuration of the blanket.

Fig. 6.6. Reference radial build of SIRIUS-T blanket.

Fig. 6.7. Spatial distribution of nuclear heating in the blanket.

Fig. 6.8. Helium and dpa production rates in V structure.

Fig. 6.9. Tritium inventory in the different Be zones.

7. THERMAL-HYDRAULICS ANALYSIS

7.1. Introduction

The configuration and parameters of the coolant system must be optimized simultaneously with the neutronics and thermal stress calculations to achieve the maximum possible TBR, while satisfying the engineering constraints imposed on the design. Iterations are needed to determine the optimum configuration of Li coolant and Be multilayer in the SIRIUS-T layout. The neutronics results have been used in the blanket thermal-hydraulics analysis.

A description of the SIRIUS-T chamber is given in great detail in Sections 2, 3 and 5 in this report. Here, for the sake of completeness, a brief introduction will be given. The SIRIUS-T chamber is spherical and has 92 beams symmetrically distributed around it. Each beam is located in the center of a blanket module of which there are 80 hexagonally and 12 pentagonally shaped. All modules are fitted into the structural support frame. Each blanket module consists of a 1 cm thick vanadium topless box with a hexagonal/pentagonal cross section. The box contains several layers of beryllium multiplier disks stacked on top of each other. The disks are shaped to conform to the interior of the vanadium container at their perimeters and the beam port tube at their centers. Coolant channels are engraved in the beryllium disks at 5 different levels. At each level 5 concentric coolant paths are utilized. The positions of these levels have been optimized to insure maximum TBR keeping the maximum temperature of structural material at 650°C. The liquid lithium, coolant and breeder, enters each module from a single supply manifold at the top down a radially (towards chamber center) tapered hole in the Be disks to feed the coolant at the different cooling levels. Figure 7.1 shows a detailed cross section of a typical blanket module. The coolant traverses each channel to the other side where it finds its way up and out through the return manifold. Figure 7.2 is a schematic of the coolant channels at one of the coolant layers. The first wall is composed of graphite tile on Li cooled vanadium structure. Cooling the first wall is achieved by feeding the coolant down an annulus around the beam port to the coolant channels which have the same geometrical configuration as the blanket coolant channels. The annulus is divided into two separate channels, one for supply and the other for return.

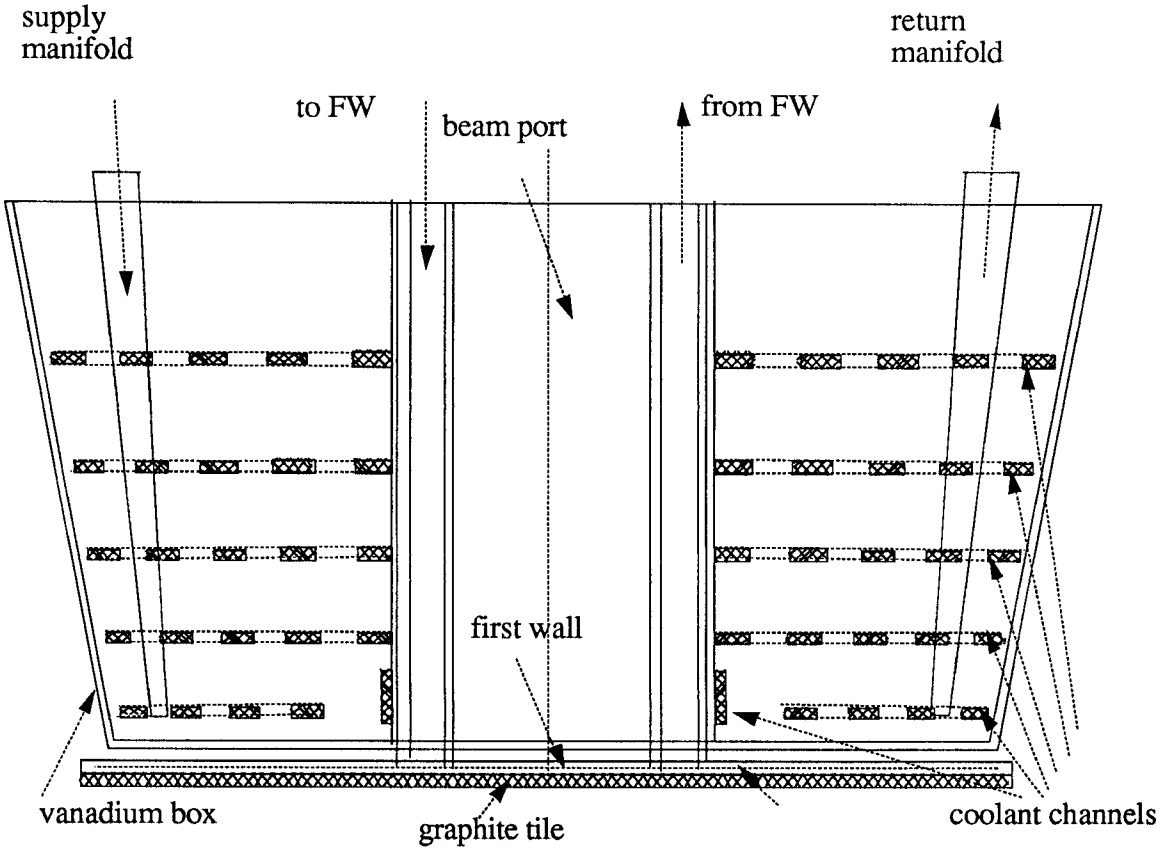

Fig. 7.1. Detailed cross section of a hexagonal blanket module with first wall.

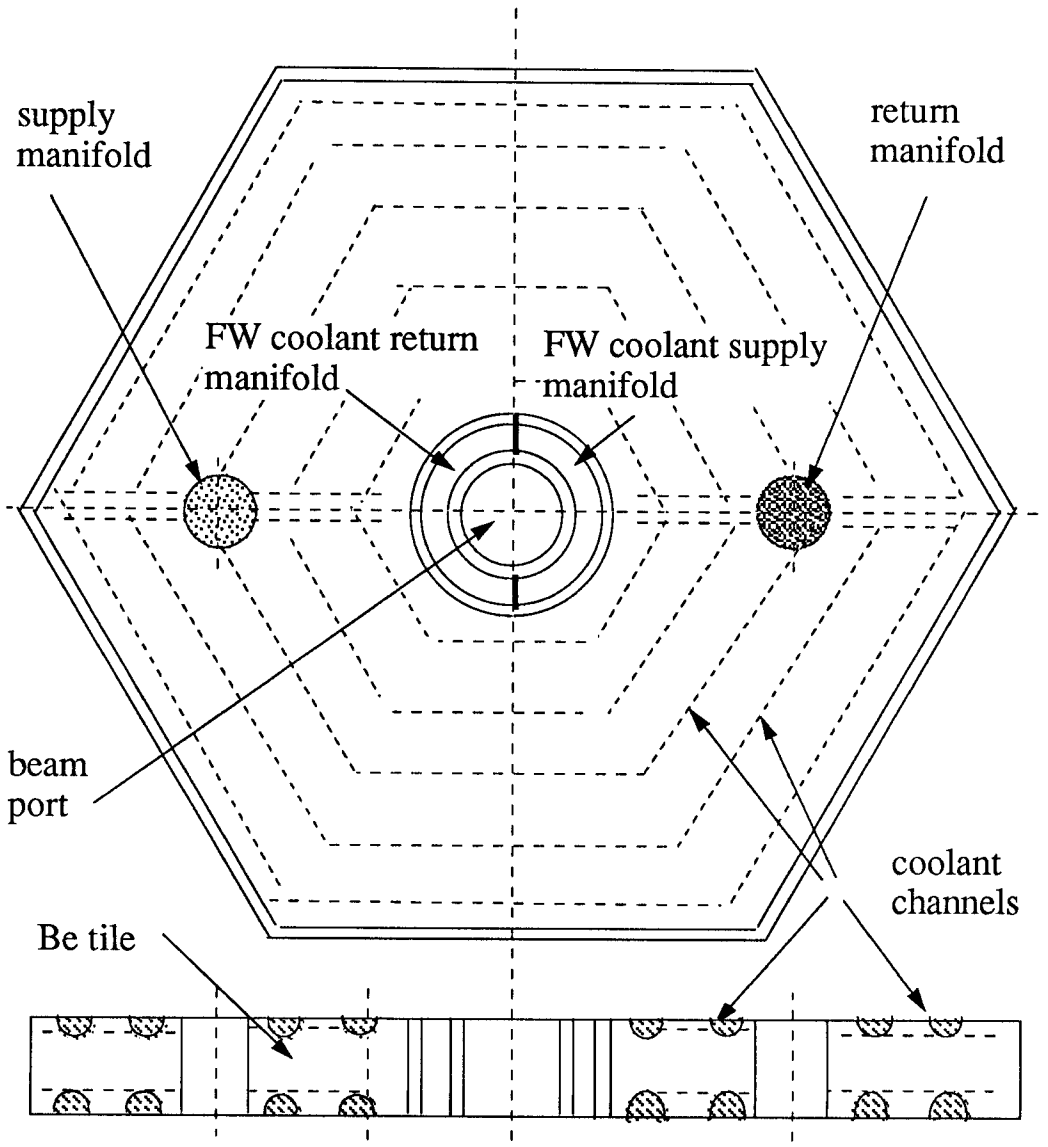

Fig. 7.2. A schematic of the coolant channels at one of the coolant layers.

7.2. Thermal-Hydraulics Calculations

A two-dimensional finite-element thermal model has been generated for use with the ANSYS code,[1] to examine the thermal performance of the proposed configuration utilizing the nuclear heating results obtained from the neutronics analysis (Section 6 in this report). It is assumed that the liquid lithium enters at a temperature of 350°C and exits at 550°C. The temperature of the vanadium structure should be in the range between 350°C and 650°C. The lower limit is needed to eliminate any concern about DBTT and the upper limit is required to avoid helium induced degradation in ductility. In the meantime, the temperature of the beryllium should be kept as high as possible to allow tritium to diffuse out of it and hence reduce the tritium inventory. Several approaches for blanket coolant, in connection with FW coolant, have been examined. When the inlet of blanket coolant is on the same side as the inlet of FW coolant, this side will be cold while the other side will be hot enough to exceed the recommended temperature for the structural material. Figure 7.3 gives the reference coolant routing for the blanket and FW. Included also in the figure are the parameters of the coolant as it traverses the coolant channels in the blanket and FW.

The two-dimensional thermal model uses the temperature dependent thermal properties for the different materials used. Moreover, it allows heat to be radiated between the blanket and FW. The two sides of the model have been modeled separately. Different boundary conditions are imposed on each side during the calculations since the thermal model handles each module side separately. Each side is thermally independent since the two sides are separated with the laser beam port. In relatively early stages of the thermal design, the optimum neutronics calculations required that the first Be layer would be 6 cm in width. In this case the resulting temperature distribution in both sides is shown in Figs. 7.4 and 7.5. As one can see the maximum temperature in the structural material exceeds the recommended value of 650°C. Different coolant routes have been utilized in order to satisfy the temperature requirements. The finite element model and the resulting temperature distributions are shown for both the right and the left sides in Figs. 7.6, 7.7, 7.8 and 7.9. One can see that the maximum Be temperature is 718°C in the middle of the first Be

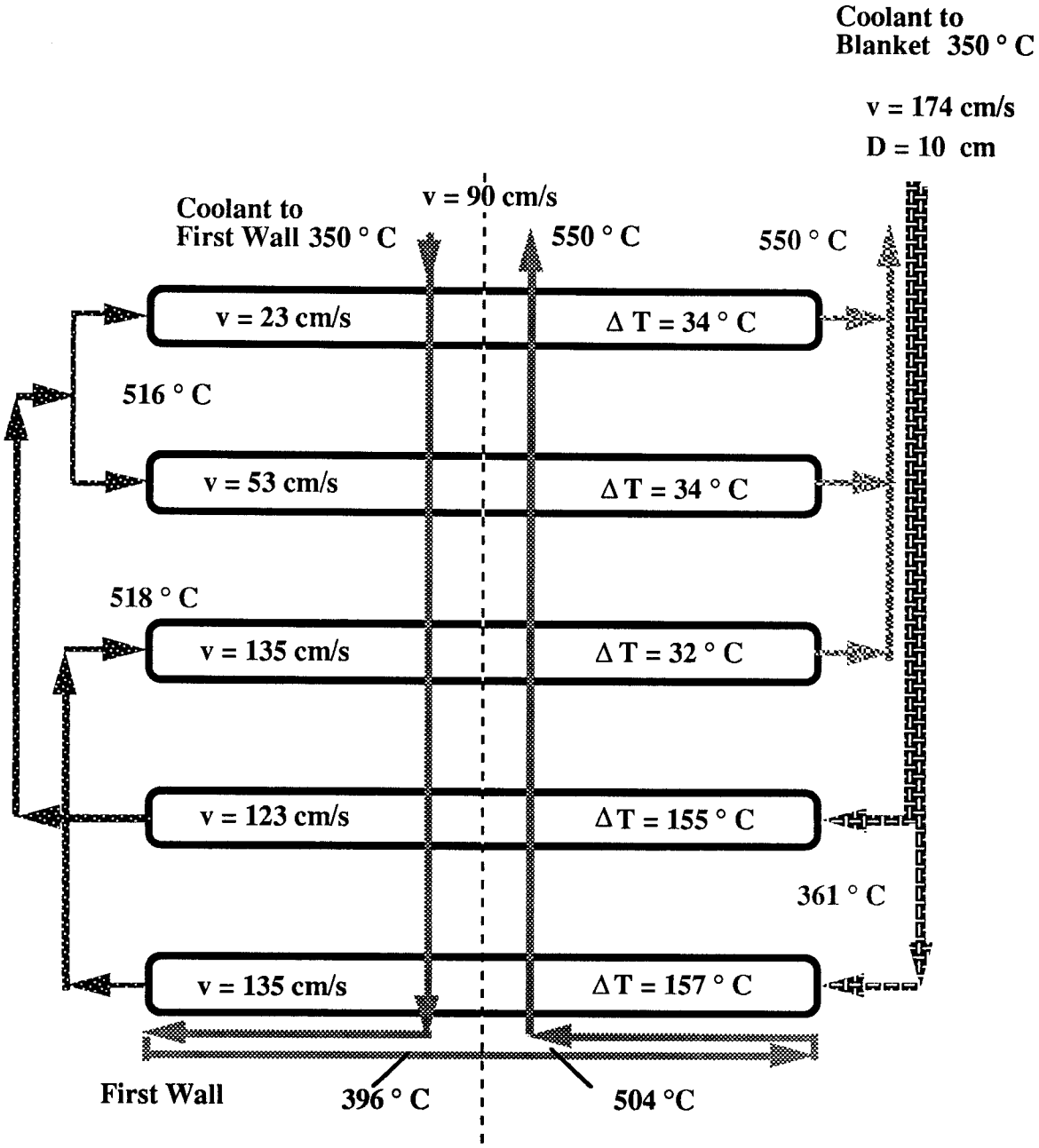

Fig. 7.3. The reference coolant layout to the blanket and first wall.

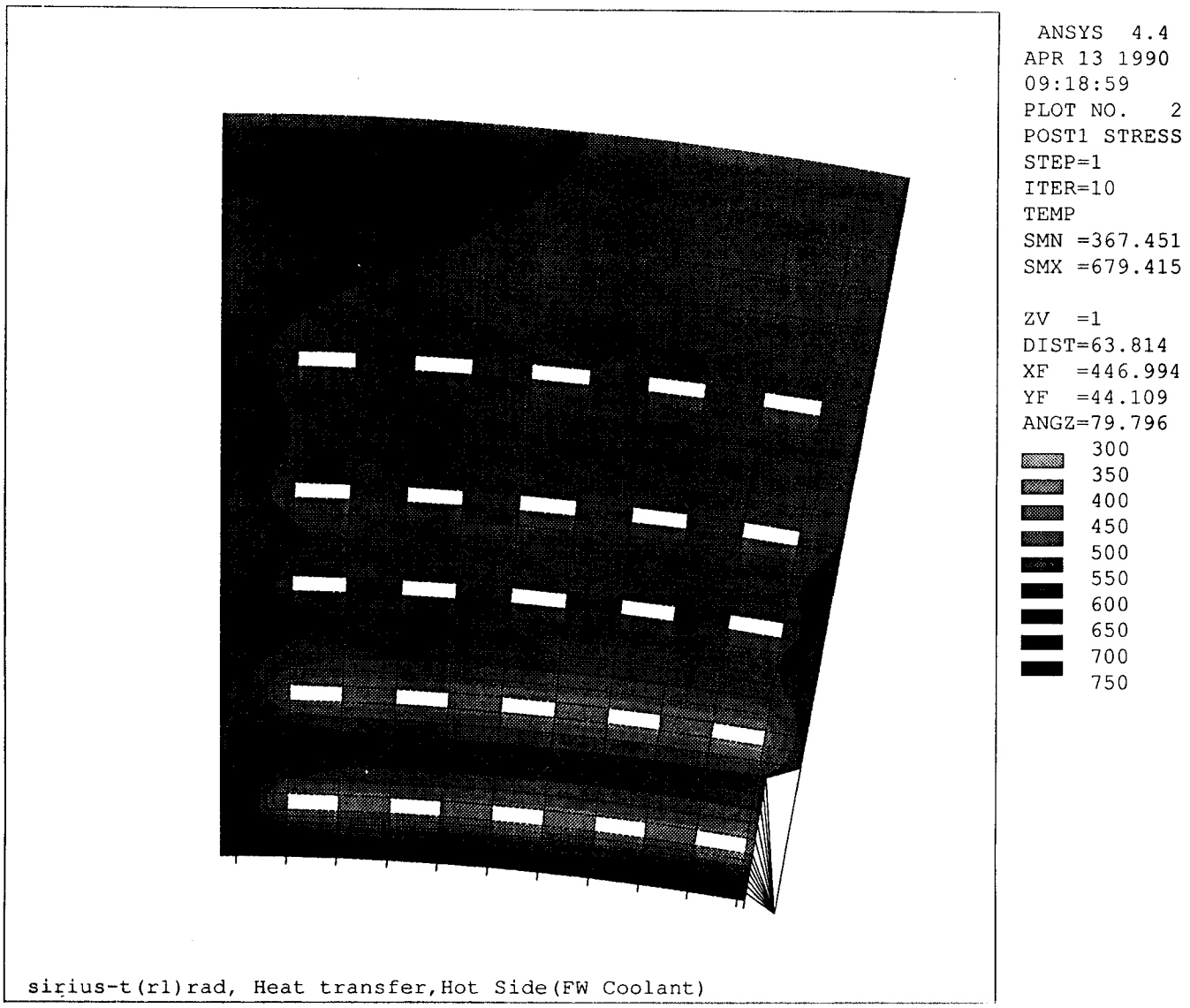

Fig. 7.4. Temperature distribution for the right side.

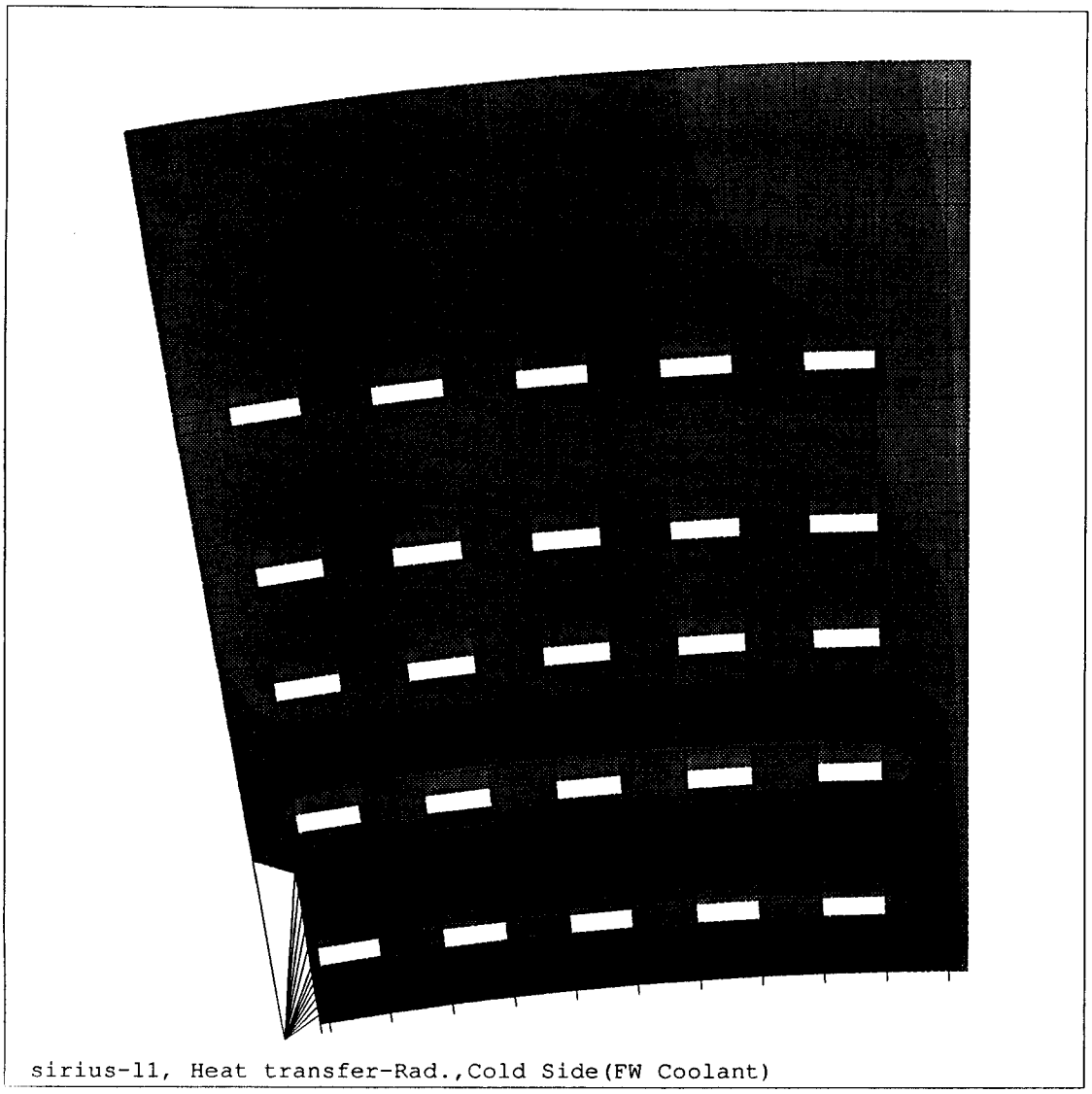

Fig. 7.5. Temperature distribution for the left side.

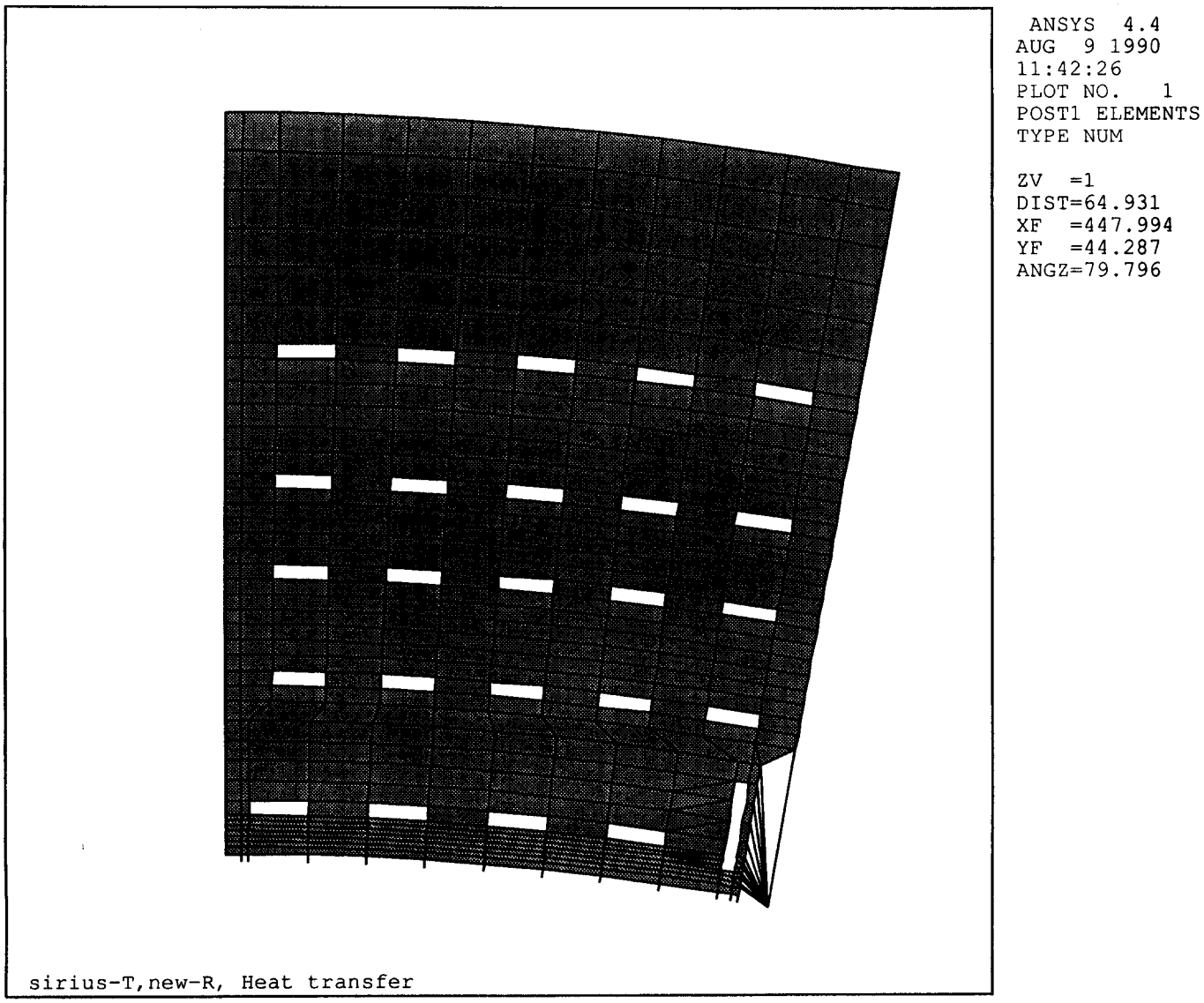

Fig. 7.6. Finite element model for the right side (reference case).

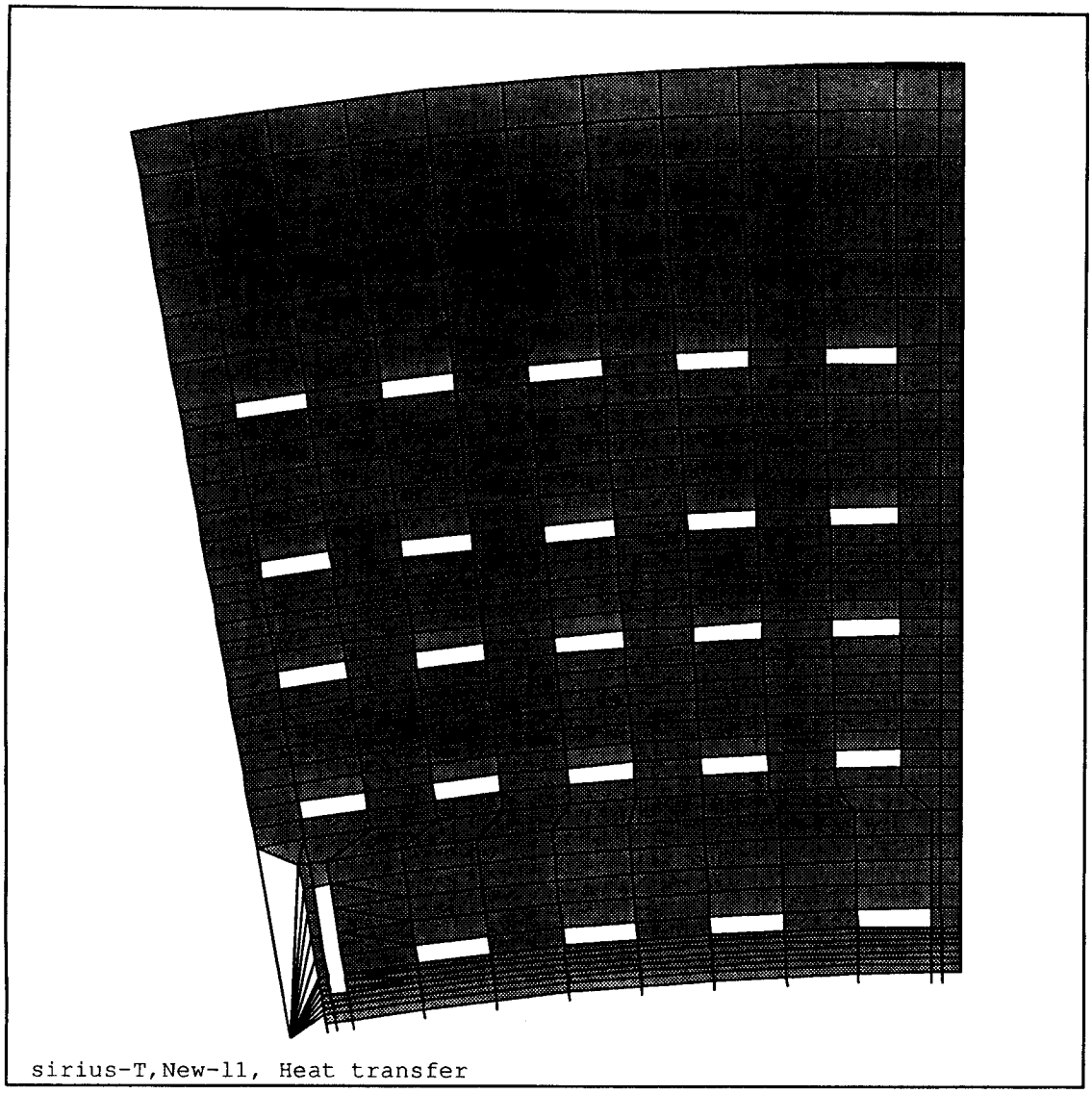

Fig. 7.7. Finite element model for the left side (reference case).

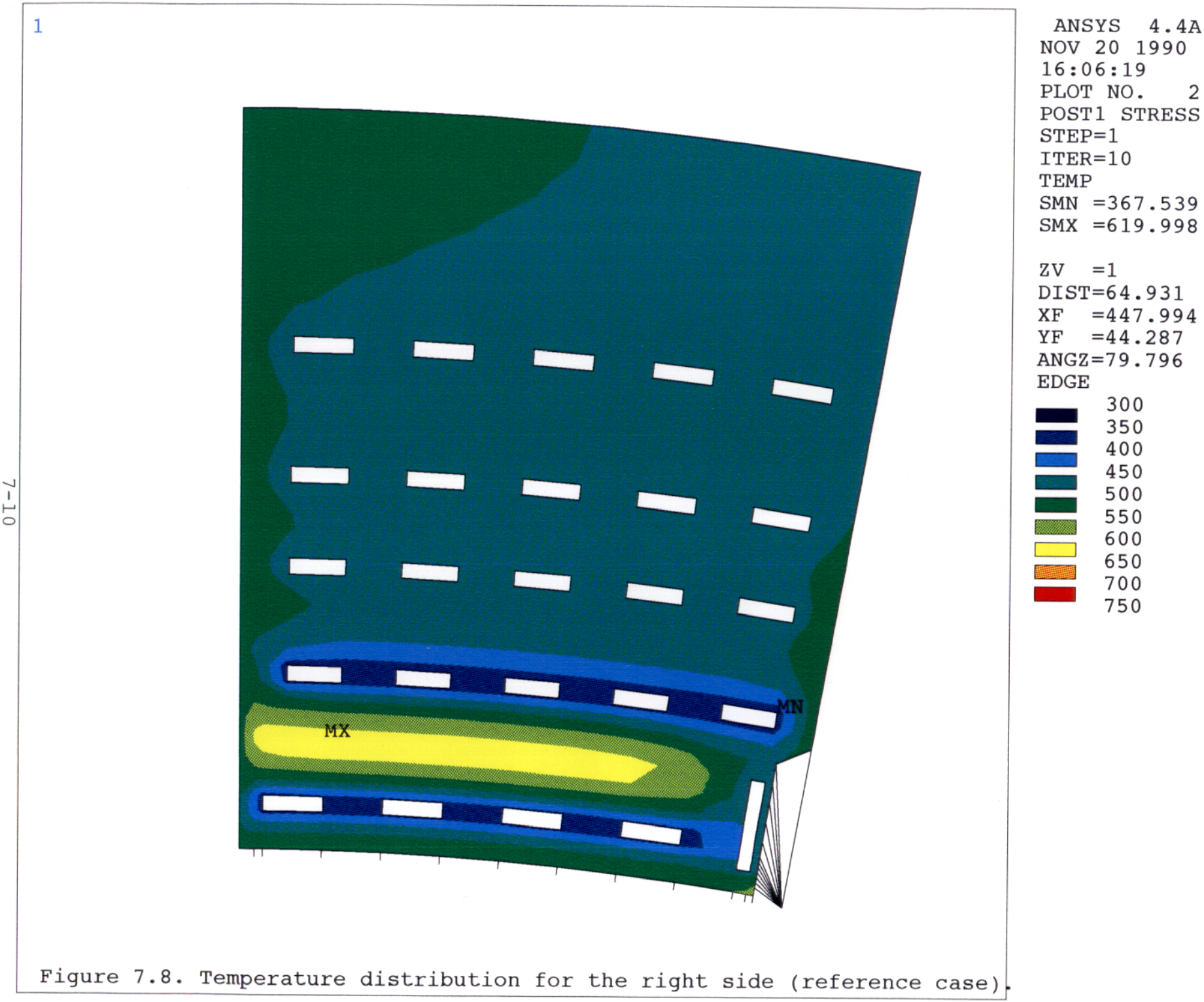

Figure 7.8. Temperature distribution for the right side (reference case).

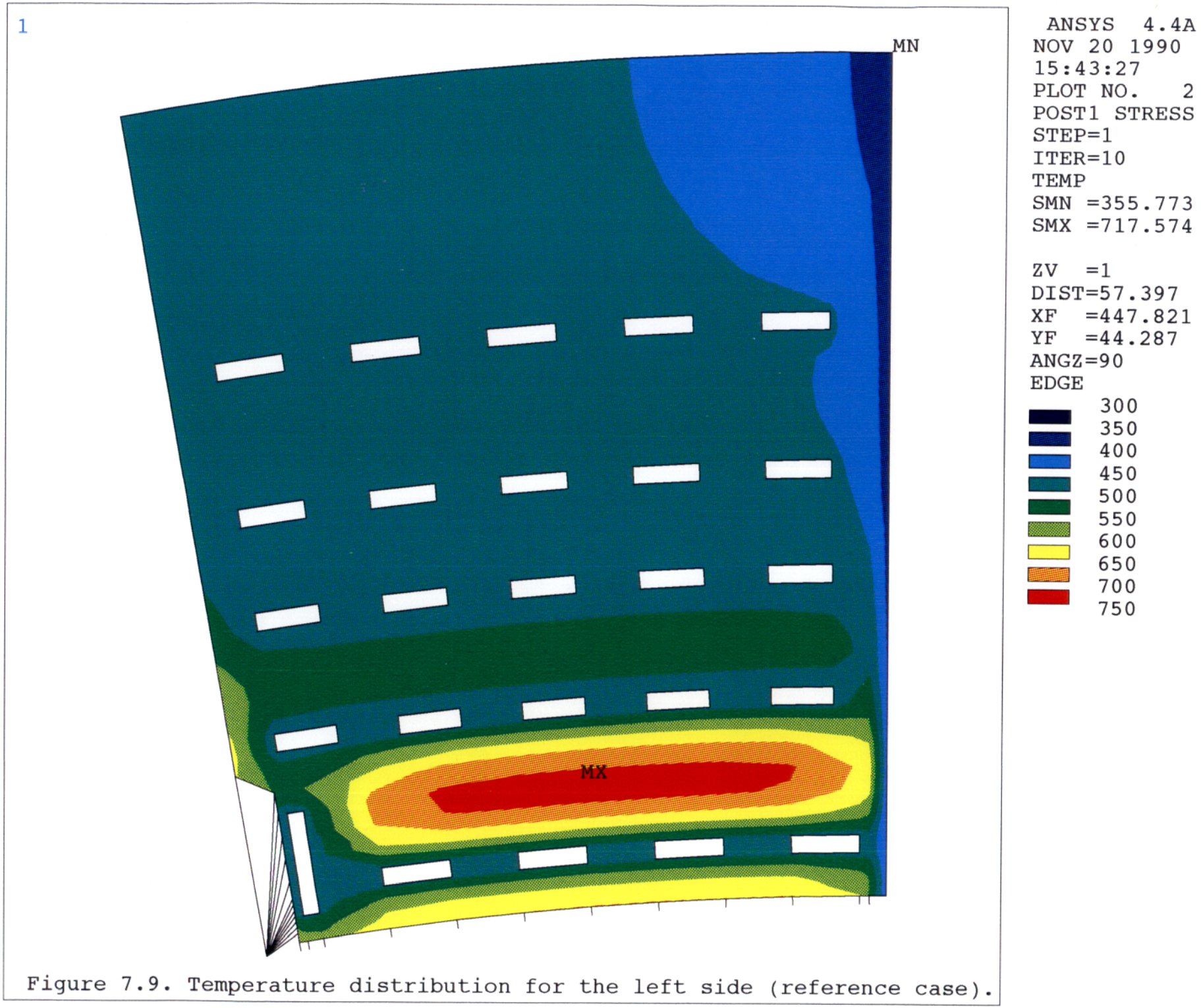

Figure 7.9. Temperature distribution for the left side (reference case).

layer while the maximum vanadium temperature is 650°C at the front surface of the module. Figure 7.10 shows the volume fraction of structural material temperature while Fig. 7.11 shows a histogram of the percent volume-temperature relationship for the structural material temperature in a typical module.

Figure 7.12(a) and (b) shows a schematic of the coolant route for a typical first wall. The 1-D steady state temperature distribution of the first wall has been calculated. The maximum temperature of the graphite surface equals 834°C, while the temperature difference across the vanadium is 163°C. These temperature distributions are needed for stress analysis calculations (Section 5.3 in this report). Fig. 7.13 shows the steady state temperature distribution in the first wall.

Reference for Chapter 7

1. Gabriel J. DeSalvo and Robert W. Gorman, "ANSYS Engineering Analysis System Users Manual," Revision 4.4, May 1989, Swanson Analysis Systems, Inc.

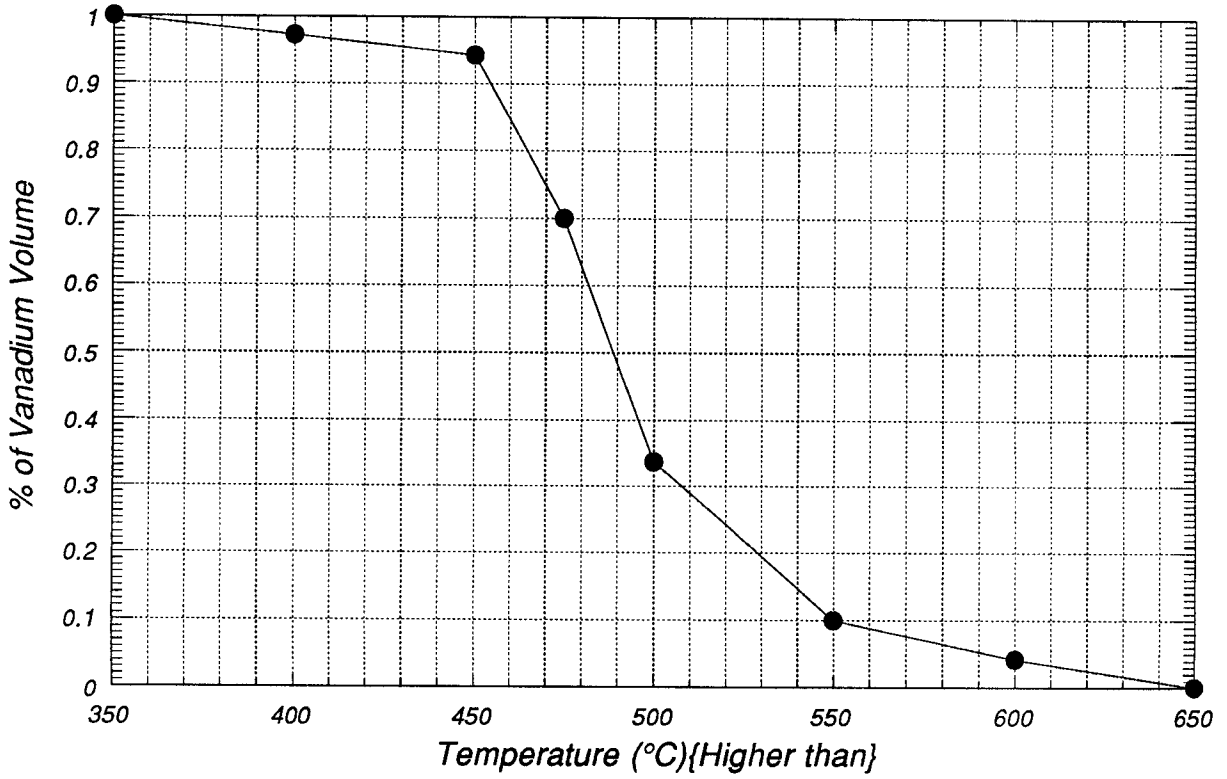

Fig. 7.10. Percent volume-temperature relationship for the vanadium.

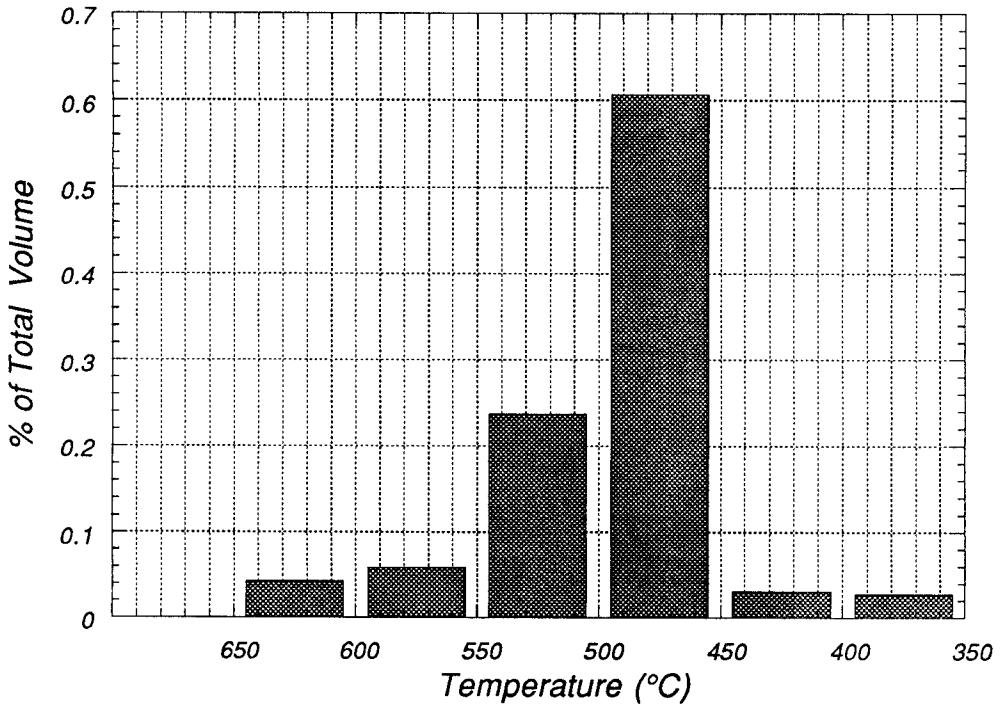

Fig. 7.11. Histogram of percent volume-temperature relationship for the vanadium.

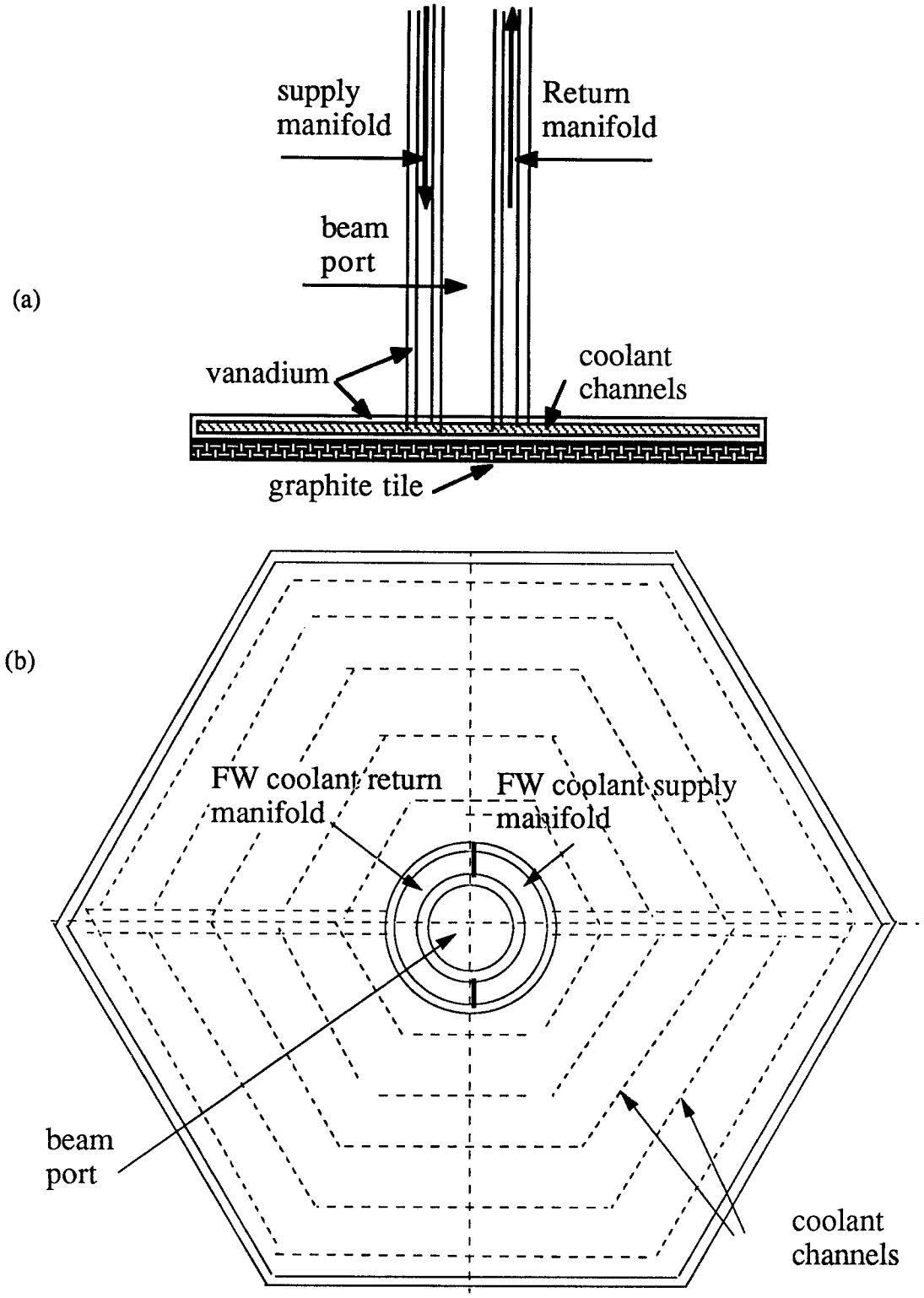

Fig. 7.12. (a) A schematic of the coolant route in the vertical direction for a typical first wall. (b) A plane view of the coolant channels for a typical first wall.

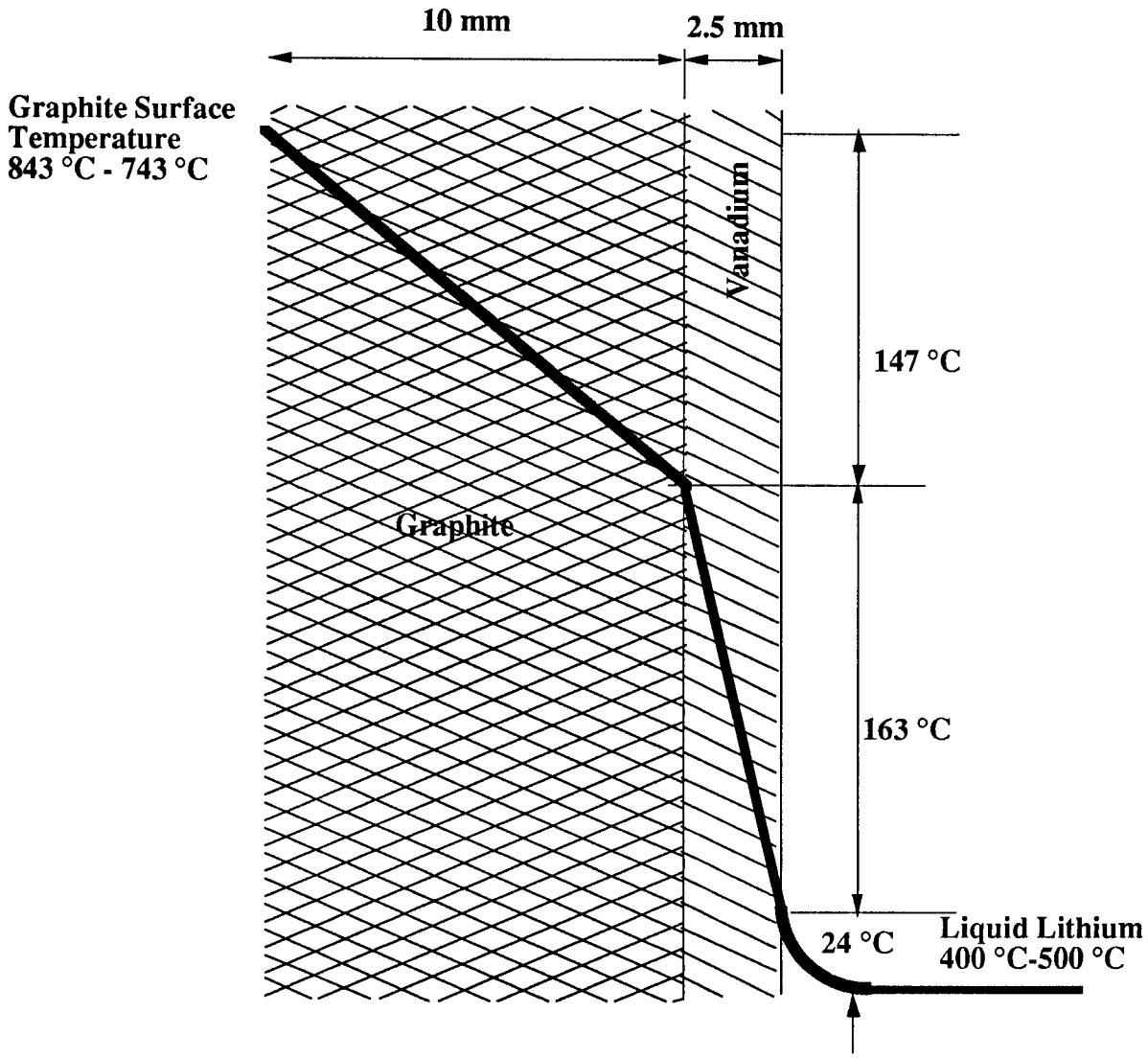

Fig. 7.13. Steady-state temperature distribution in the first wall.

Figure Captions for Section 7

Fig. 7.1. Detailed cross section of a hexagonal blanket module with first wall.

Fig. 7.2. A schematic of the coolant channels at one of the coolant layers.

Fig. 7.3. The reference coolant layout to the blanket and first wall

Fig. 7.4. Temperature distribution for the right side .

Fig. 7.5. Temperature distribution for the left side.

Fig. 7.6. Finite element model for the right side (reference case).

Fig. 7.7. Finite element model for the left side (reference case).

Fig. 7.8. Temperature distribution for the right side (reference case).

Fig. 7.9. Temperature distribution for the left side (reference case).

Fig. 7.10. Percent volume-temperature relationship for the vanadium.

Fig. 7.11. Histogram of percent volume-temperature relationship for the vanadium.

Fig. 7.12(a). A schematic of the coolant route in the vertical direction for a typical first wall.

Fig. 7.12(b). A plane view of the coolant channels for a typical first wall.

Fig. 7.13. Steady-state temperature distribution in the first wall.

8. MATERIALS/LIFETIME ANALYSIS

There are four major subsystems in SIRIUS-T that require an analysis of their useful lifetime in the reactor:

1. Graphite tiles facing the exploding target,
2. Vanadium structure,
3. Be neutron multiplier, and
4. Final focusing mirrors.

Other materials such as thermocouples, shielding, and chamber diagnostics will not be covered in this limited study.

8.1. Graphite Tiles

The main problem for the graphite is the dimensional stability of the tiles operating at 700-800°C in a neutron environment for long periods of time. Typical behavior of graphite under irradiation is shown in Fig. 8.1. During high temperature irradiation, the graphite first shrinks and then expands at a very rapid rate. A useful lifetime is usually determined when the dimensional change reverses and crosses the $\Delta V = 0$ line. In Fig. 8.1,[1] the useful life of isotropic graphite is ≈49 dpa (3×10^{22} n/cm^2) at 400°C. This lifetime gets shorter as the temperature increases, dropping to ≈18 dpa at 800°C and to ≈10 dpa at 1000°C. At temperatures higher than 1000°C, the lifetime increases with increasing temperatures as the defects anneal out. Since the damage level in SIRIUS-T is ≈18 dpa/FPY, we might expect a useful life of only 1 FPY from isotropic graphite.

Fortunately, there are other forms of graphite more resistant to radiation damage. Birch and Brocklehurst[2] have reported data on three forms of graphite and show that Graphnol-N3M would not reach the zero swelling point until ≈1.5 FPY's in SIRIUS-T at 700°C (see Fig. 8.2). Since the graphites tested thus far have not been optimized for the fusion environment, and because SIRIUS-T is a device that would not operate for at least 10 years, we feel comfortable in projecting the Graphnol-N3M data by 33%, to 2 useful FPY's.

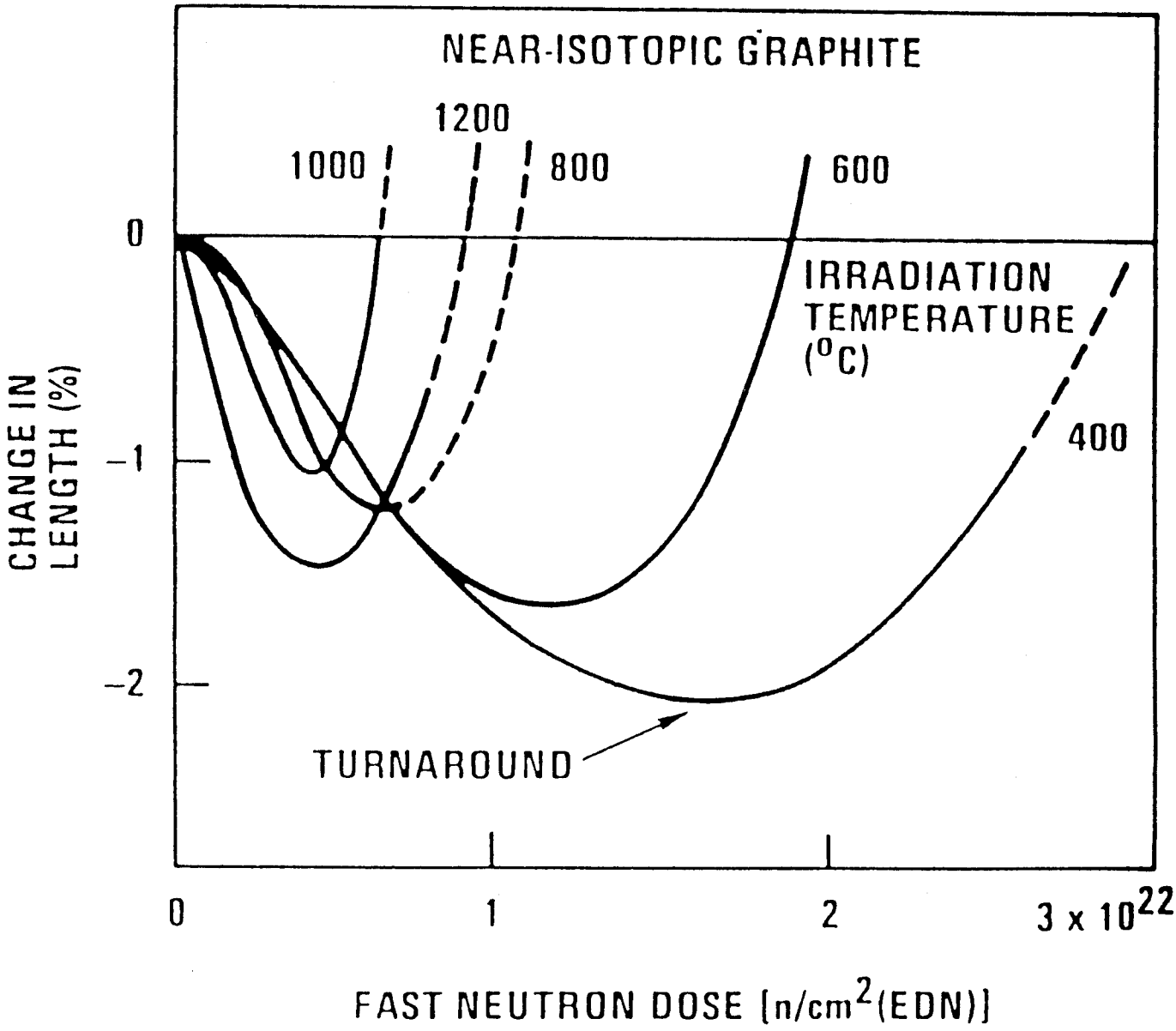

Fig. 8.1. Typical dimensional change in neutron irradiated graphite.[1]

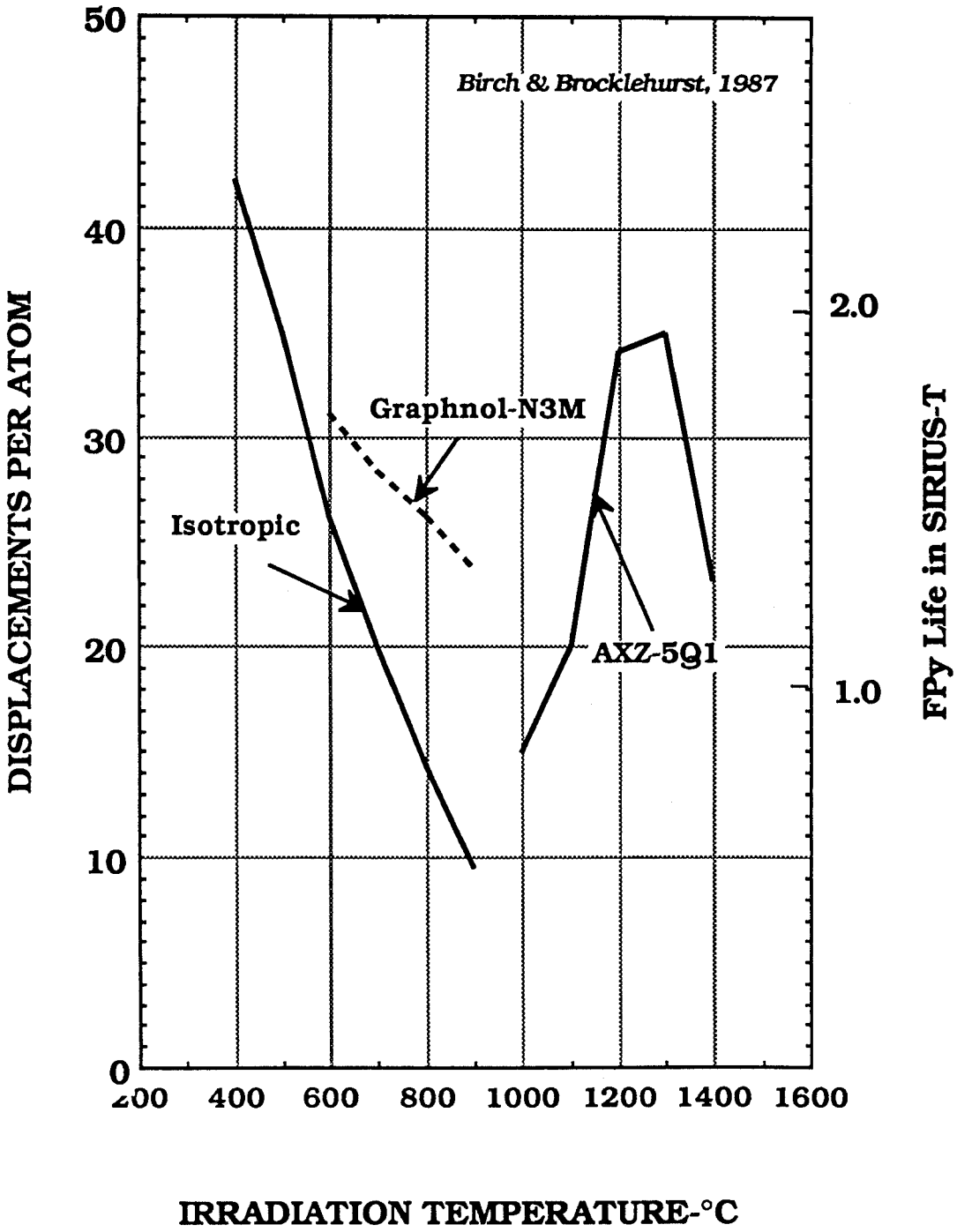

Fig. 8.2. Useful lifetimes of graphite as determined by the point at which the graphite reaches its original volume.[2]

8.2. Vanadium Blanket Structure

There are usually 3 key indicators of the useful lifetime of metallic structural members in a fusion reactor; swelling, embrittlement, and corrosion. The two parameters that have the most impact on the first 2 properties are the dpa level and the amount of He generated at high temperatures in the alloy. For SIRIUS-T, the maximum conditions at the first wall just behind the graphite are:

- 30 dpa/FPY
- 100 appm He/FPY
- T = 750°C.

8.2.1. Swelling in V Alloys

Unfortunately there is relatively little information on neutron damage in V alloys at fusion reactor conditions. Braski,[3] as well as Loomis and Smith[4] have studied the V-3Ti-1Si alloy after irradiation in the fission spectrum of a fast breeder reactor. The irradiation temperatures were lower (420 to 600°C) than the maximum (687°C) anticipated in SIRIUS-T and the He production rate was only ≈0.05 appm He/dpa compared to ≈3 appm/dpa in SIRIUS-T. Nevertheless, reference 3 showed that at low He contents, the swelling at damage levels equivalent to 2.7 FPY's in SIRIUS-T is slightly over 0.2% at 420°C and reference 4 showed 0.5 to 4.3% swelling at 600°C (see Fig. 8.3). When 20 appm He is preinjected into the samples before a 420°C irradiation, the level of swelling is tripled, and by the equivalent 2.7 FPY's of He generation had been preinjected, swelling had reached ≈1.2% (see Fig. 8.4). It is felt that swelling on the order of a few percent can be tolerated. Without further high temperature data, we will assume that irradiation at 687°C will not increase the swelling by more than a factor of 2-3 over the 420°C results (with preinjected He) or by more than a factor of 1 to 3 times over the 600°C results with low He contents. This would indicate that a useful lifetime would be conservatively on the order of 3 FPY's from a dimensional stability standpoint.

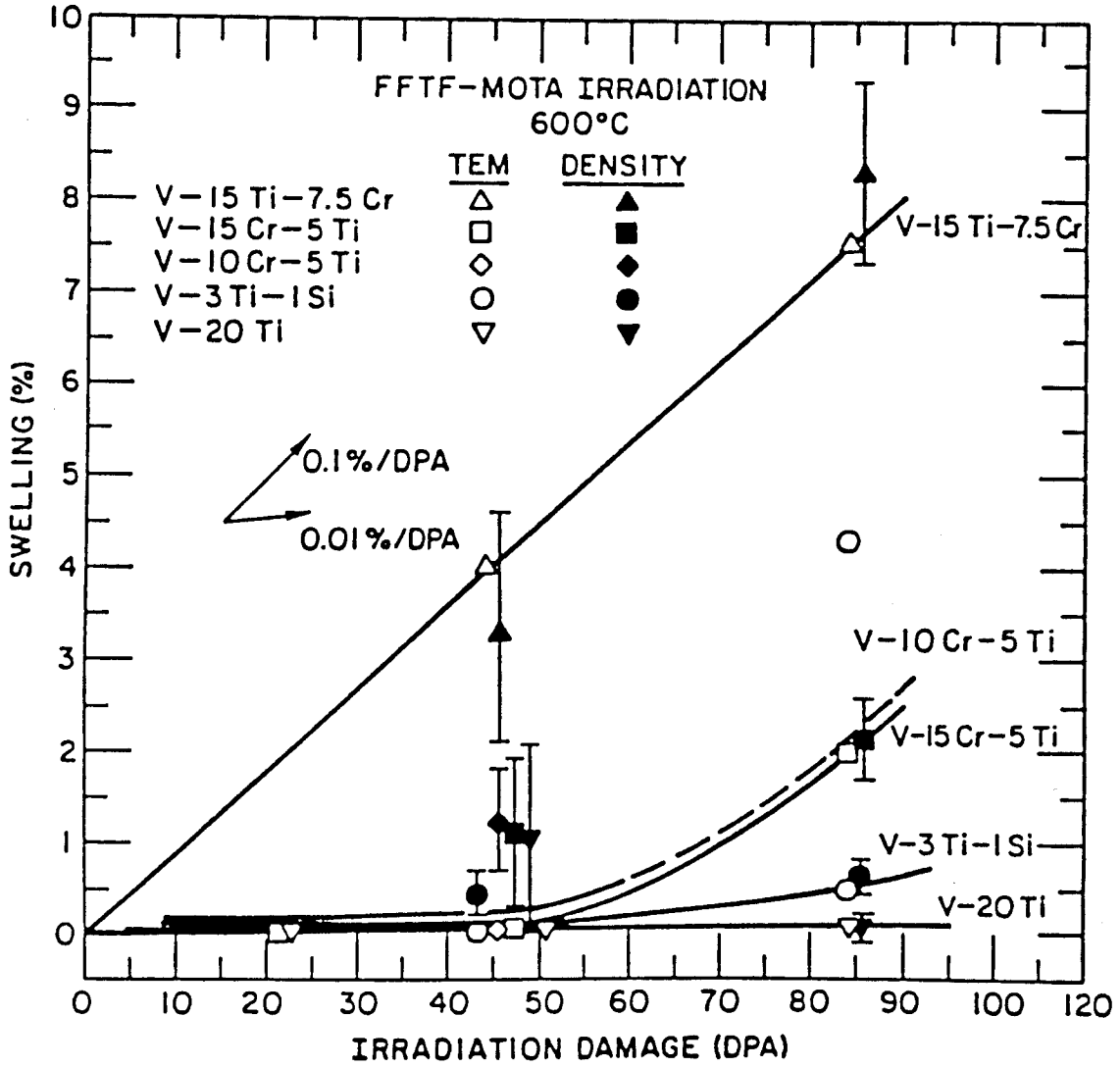

Fig. 8.3. Dependence of swelling of vanadium alloys at 600°C on irradiation damage.[4]

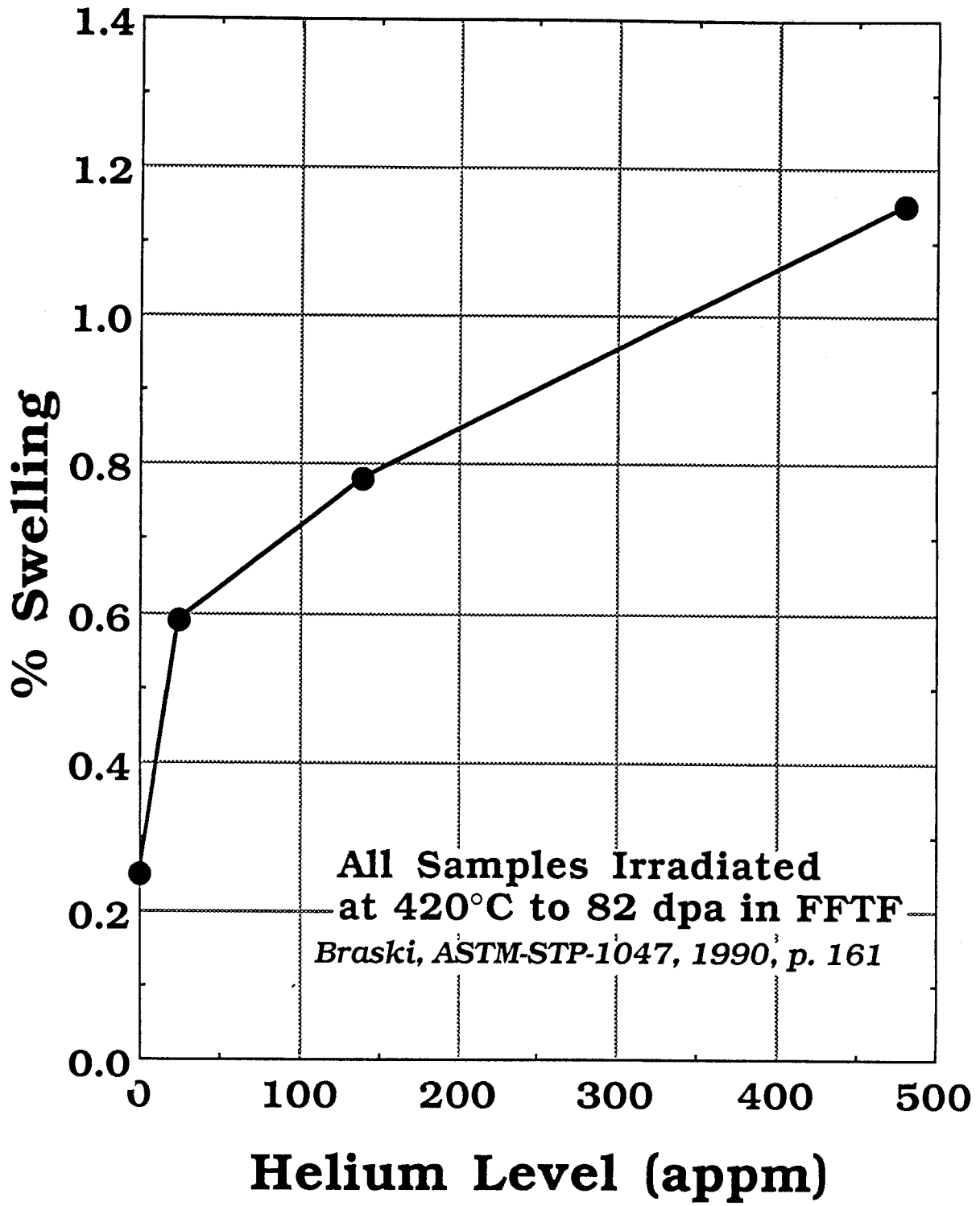

Fig. 8.4. Swelling in V-3Ti-1Si increases with preinjected helium.[3]

8.2.2. Embrittlement

Irradiation of a V-3Ti-1Si alloy at 420°C, with low He content (4 appm), makes this alloy stronger and less ductile (see Fig. 8.5). The ductility drops rapidly within the first 5 dpa (≈4 full power months in SIRIUS-T) and after that, the total elongation at failure remains relatively constant at ≈5%. However, the low He content does not properly simulate the fusion conditions and adding more He before irradiation causes the total elongation to drop even further to ≈2% at dpa levels equivalent to 2.7 FPY's (see Fig. 8.6).[3] One might expect that irradiation at higher temperatures would aggravate this effect but data obtained by Braski[3] shows that preinjected He contents equivalent to 10 full power months does not cause further degradation at higher temperatures (see Fig. 8.7)

With the above limited information in hand and using a 1 to 2% total elongation as a limit, we estimate that the useful life due to a loss of ductility is ≈4 FPY's for the V alloy.

8.2.3. Corrosion

The corrosion data for the Li/V alloy system is even more limited than for irradiated material. However, early work (1961) by Pratt-Whitney,[5] ORNL,[6] and ANL[7] is reviewed in the Blanket Comparison and Selection Study Report published in 1984.[8] From that information, a corrosion rate curve was constructed (see Fig. 8.8). At a 750°C maximum temperature (note that this temperature is achieved well away from the first wall at a lower neutron fluence), the predicted corrosion rate is ≈10 microns/year. This would indicate that, for no more than a 100 micron (0.1 mm) loss, the useful life would be ≈10 FPY's, or essentially 1/3 the full reactor life.

8.3. Beryllium

The use of Be for neutron multiplication is highly beneficial for SIRIUS-T. However, the irradiation of this material has been known to produce large amounts of helium gas and cause swelling of the solid Be. The maximum temperature of the Be is ≈750°C and the dpa rate is ≤20/FPY. The corresponding He production rate is ≈8000 appm/FPY. Normally, a porosity of ≈10-15% can be fabricated into the Be and this would then predict the useful life of the Be to be when the swelling reaches 15%. While there is no fusion spectrum data to relate to at this time,

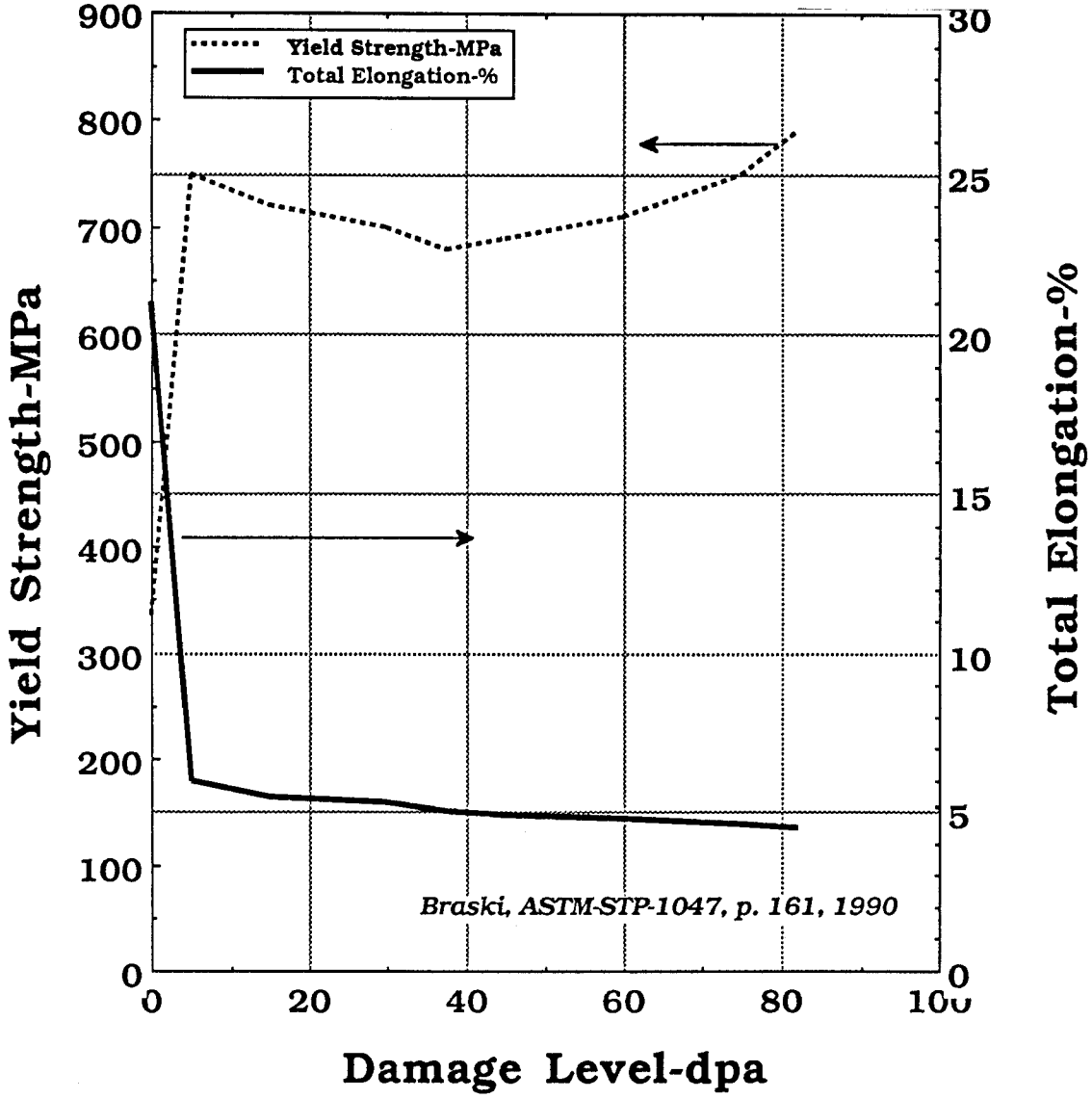

Fig. 8.5. Irradiation of V-3Ti-1Si at 420°C (with <4 appm He) makes this alloy stronger and less ductile.[3]

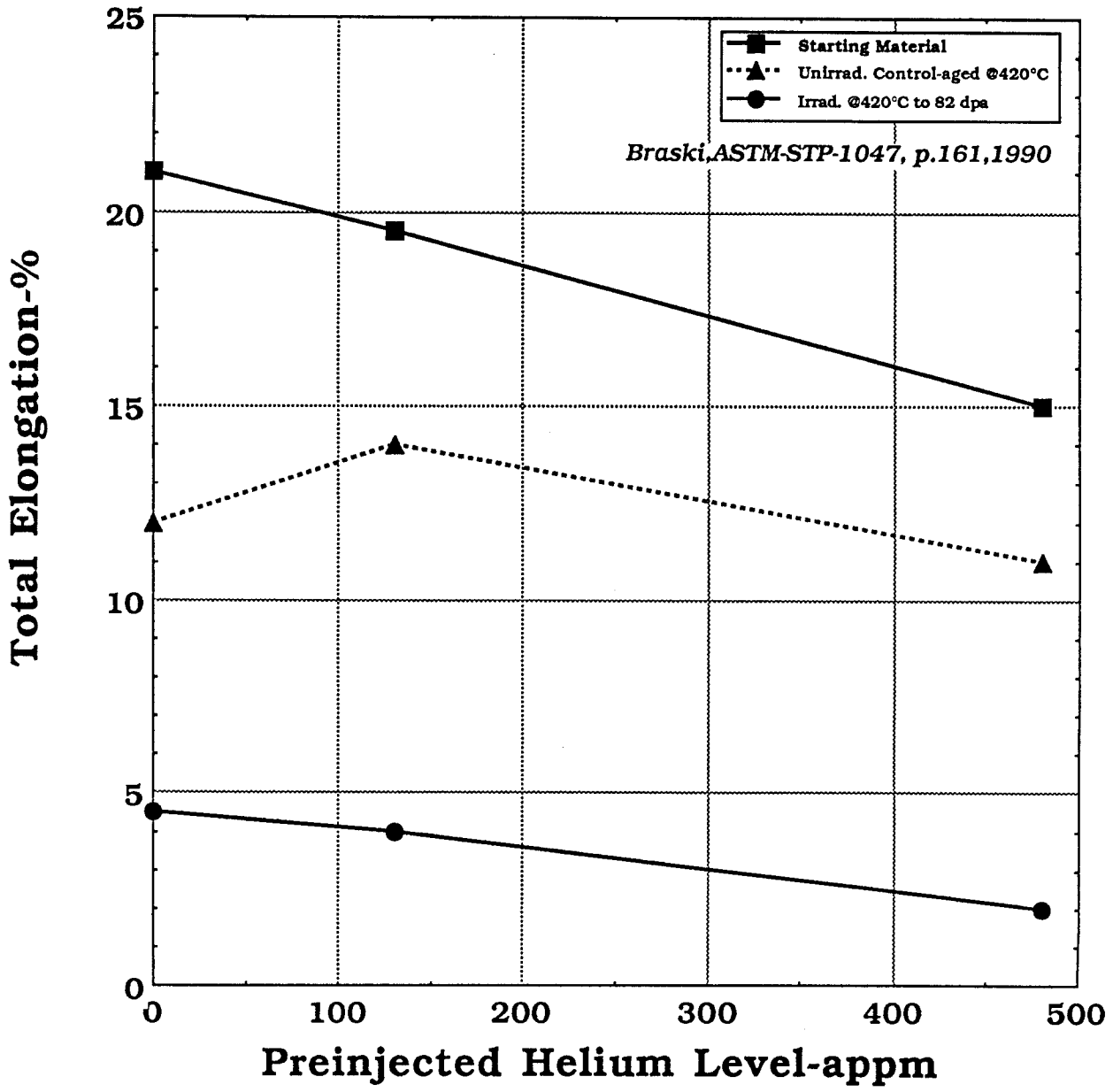

Fig. 8.6. Preinjection of V-3Ti-1Si alloys with helium before irradiation @ 420°C to 82 dpa makes the alloy more brittle.[3]

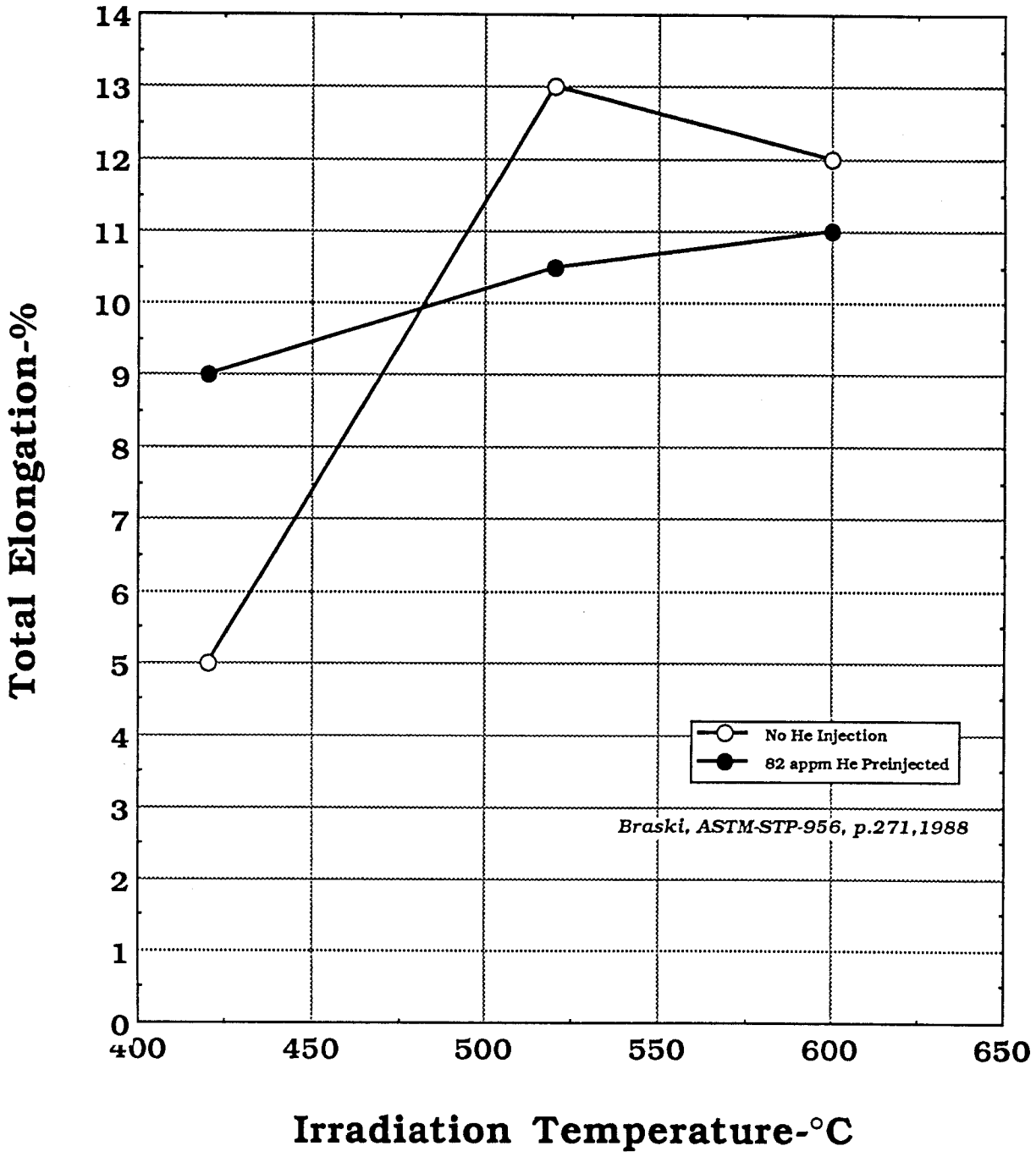

Fig. 8.7. Temperature effect on ductility of V-3Ti-1Si is not severe @ 40 dpa and <1 MW-y/m^2 equivalent of preinjected helium.[3]

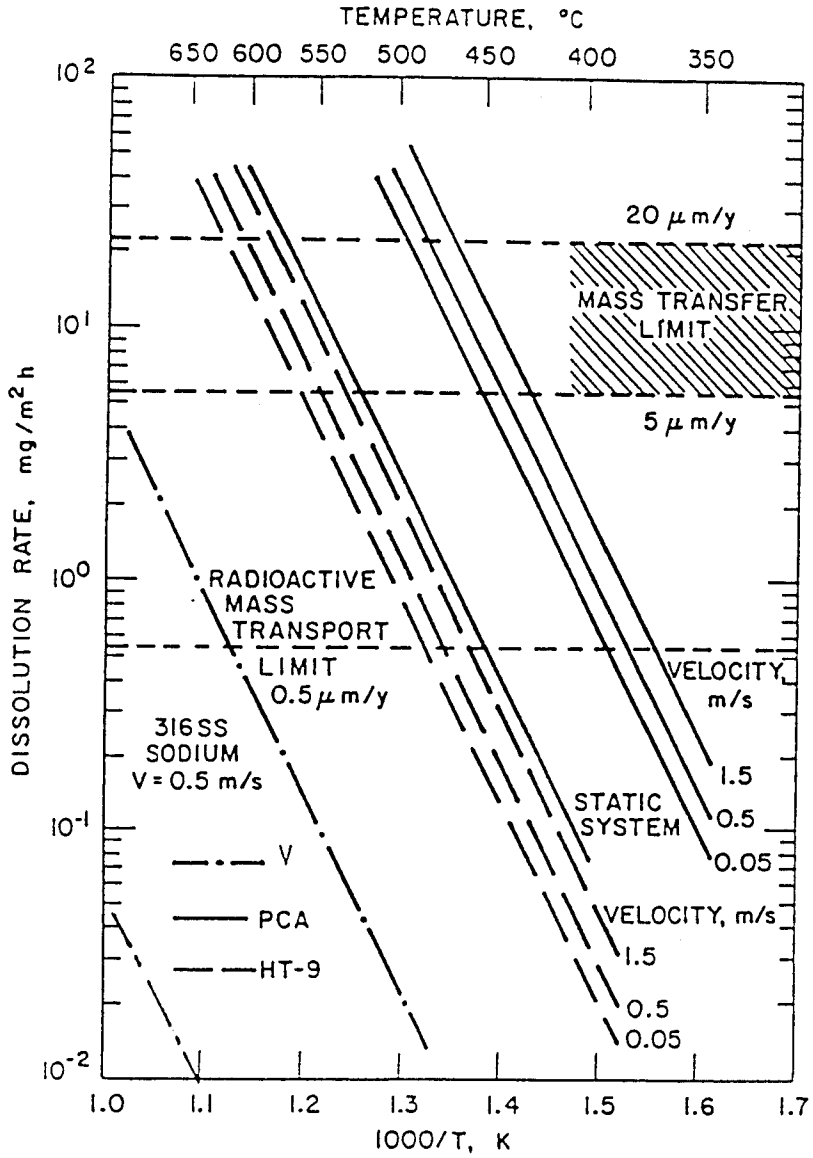

Fig. 8.8. Effect of temperature on the corrosion rate of PCA, HT-9, and V alloy in flowing lithium.[8]

irradiation at T ≥ 650°C causes He gas bubbles to migrate to grain boundaries causing considerable volume change. An analysis by Wolfer and McCarville,[9] shown in Fig. 8.9, predicts that 15% swelling would be reached at 750°C when ≈25,000 appm He was generated. This corresponds to ≈3 FPY's in SIRIUS-T.

8.4. Lifetime of Final Focusing Mirrors

The useful lifetime of the final focusing mirrors is determined by the degradation of the reflective properties of the laser mirror coating. We have used the criterion that no more than 10^{11} rads to the mirror coating is desirable. Assuming that some of the damage can be annealed by high temperature treatments, one can determine the lifetime if the minimum time between anneals, Δt_{min}, and the fraction (r) of damage annealed out in each anneal is known. Figure 8.10 shows, graphically, the level of radiation damage remaining in a coating as a function of time. The damage increases, over the time period Δt_1, to the limit set by the loss of reflectivity. An anneal then takes place which recovers "r" of the damage. The reactor is then operated for another time period, $r\Delta t_1$, after which another anneal is performed. The next operating period is $r^2 \Delta t_1$, etc. The total life is then

$$t_l = \Delta t_1 + r\,\Delta t_1 + r^2\,\Delta t_1 + \cdots + r^{n-1}\,\Delta t_1$$

where $\Delta t_{min} = r^{n-1}\Delta t_1$.

The relationship between the recovery fraction, the minimum time between anneals, the time for the first anneal, and the desired lifetime is shown in Fig. 8.11.

The damage rate at the final optics (20 m from the target) in SIRIUS-T is 5×10^{11} rads/FPY. This means that the first anneal must be conducted after 0.2 of a FPY (2.4 full power months, or 3.4 calendar months at 70% availability). If we assume that the minimum time between anneals is 1 calendar month at 70% availability (0.0583 FPY), then the lifetime can be expressed as a function of recovery fraction (see Fig. 8.12). This analysis reveals that if we wish to have a 1 FPY life for the mirrors, the recovery fraction needs to be ≥85% per anneal.

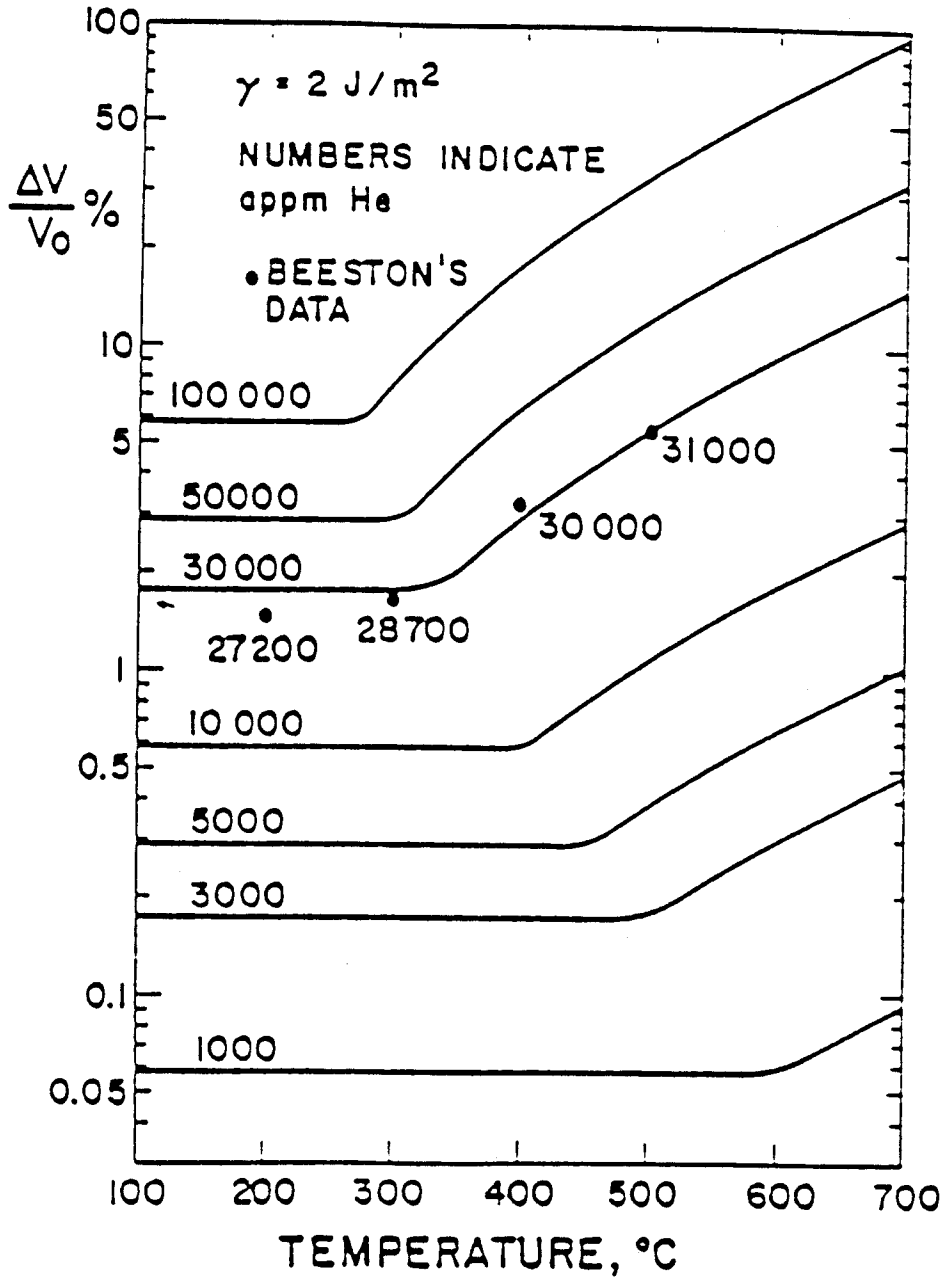

Fig. 8.9. Helium bubble swelling in neutron irradiated and post-irradiation annealed Be.[9]

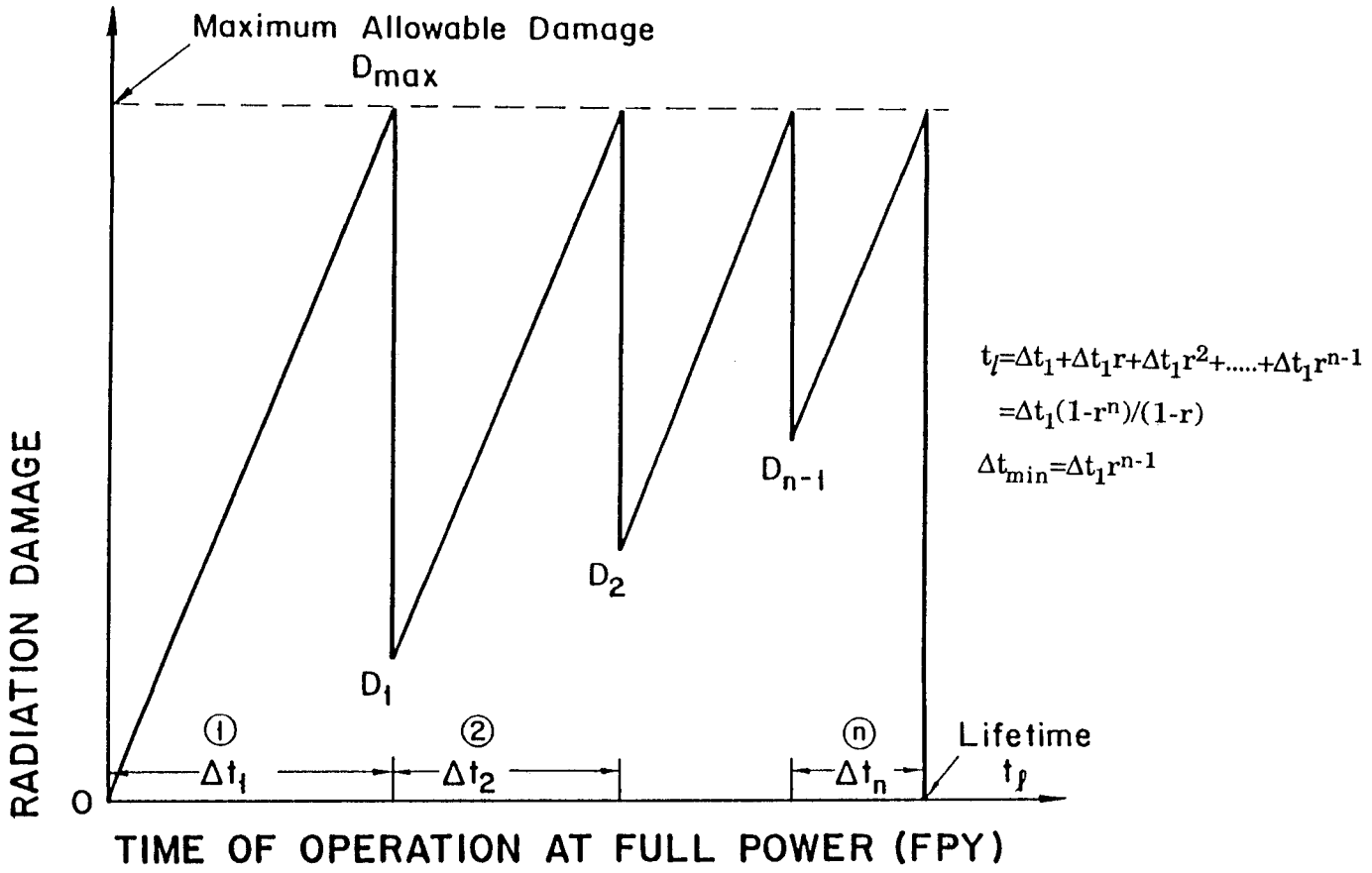

Fig. 8.10. Schematic of radiation damage level in coating of final focusing mirror.

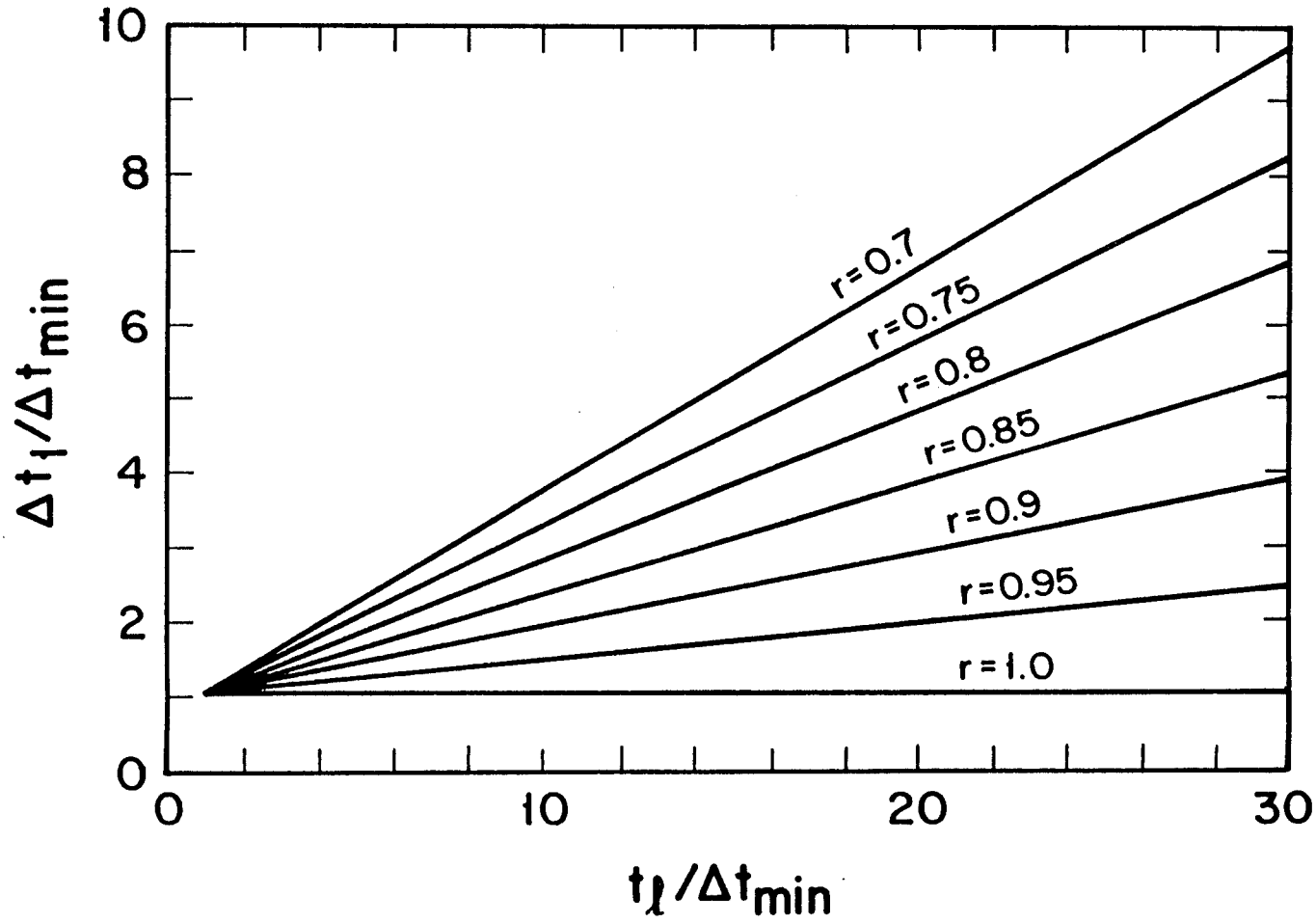

Fig. 8.11. Relationship of the final life, minimum annealing time, and annealing fraction in damaged mirrors.

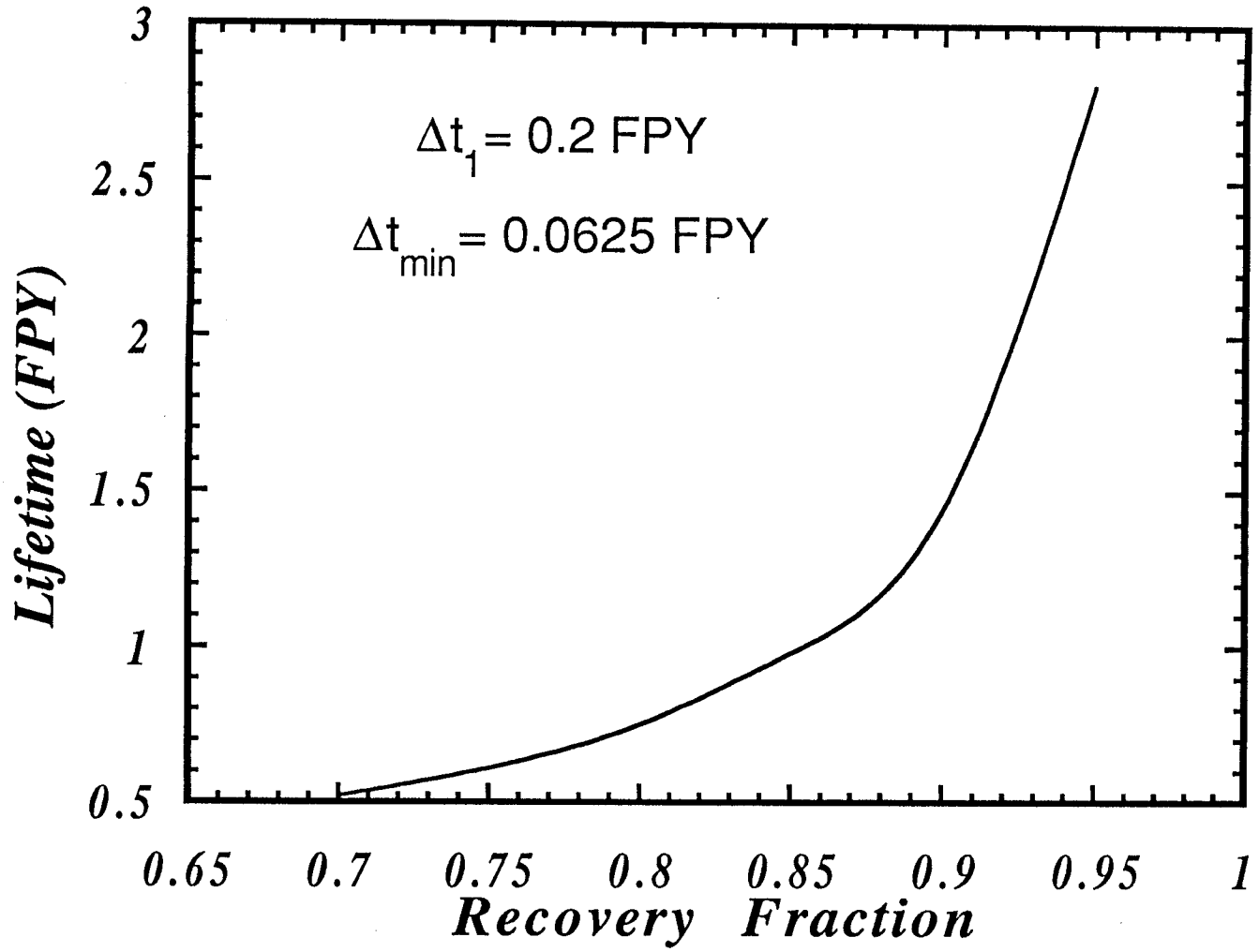

Fig. 8.12. Effect of annealing recovery fraction on final focusing mirror lifetime.

8.5. Summary

Figure 8.13 summarizes the critical lifetime components in SIRIUS-T. It can be seen that the most limiting materials are the mirrors at 1 FPY and the graphite tiles at 2 FPY's. These are followed by the Be neutron multiplier and by radiation damage to the V alloy structure at 3 FPY's. Finally, the corrosion of the V alloy does not pose significant problems in availability for the SIRIUS-T reactor.

References for Chapter 8

1. S. Sharafat, "Promising First Wall Materials For ARIES-III," Presented at Rensselaer Polytechnical Inst., July 12, 1990.
2. M. Birch and J.E. Brocklehurst, "A Review of the Behavior of Graphite Under the Conditions Appropriate for Protection of the First Wall of a Fusion Reactor," Springfield Nuclear Power Development Lab., ND-R-1434 (S), Dec. 1987.
3. D.N. Braski, ASTM Spec. Tech. Pub., ASTM-STP-1047, p. 161, 1990.
4. B.A. Loomis and D.L. Smith, "Relationship of Microstructure and Tensile Properties for Neutron Irradiated V Alloys," p. 225 in Fusion Reactor Materials, Semi Annual Progress Report, DOE/ER-0313/8, August, 1990.
5. M.S. Freed and K.J. Kelly, Pratt and Whitney Report PWAC-355 (1961).
6. J.R. DiStefano, Oak Ridge National Laboratory Report ORNL-3551 (1964).
7. D.L. Smith, R.H. Lee, and R.M. Yonco, Proc. 2nd Intern. Conf. Liquid Metal Technology in Energy Production, Richland, WA, April 20, 1980, p.2.
8. Blanket Comparison and Selection Study - Final Report, Argonne National Lab Report, ANL/FPP-84-1, Sept., 1984.
9. W.G Wolfer and T.J. McCarville, "An Assessment of Radiation Effects in Beryllium," University of Wisconsin Fusion Technology Institute Report UWFDM-632, Feb. 1985.

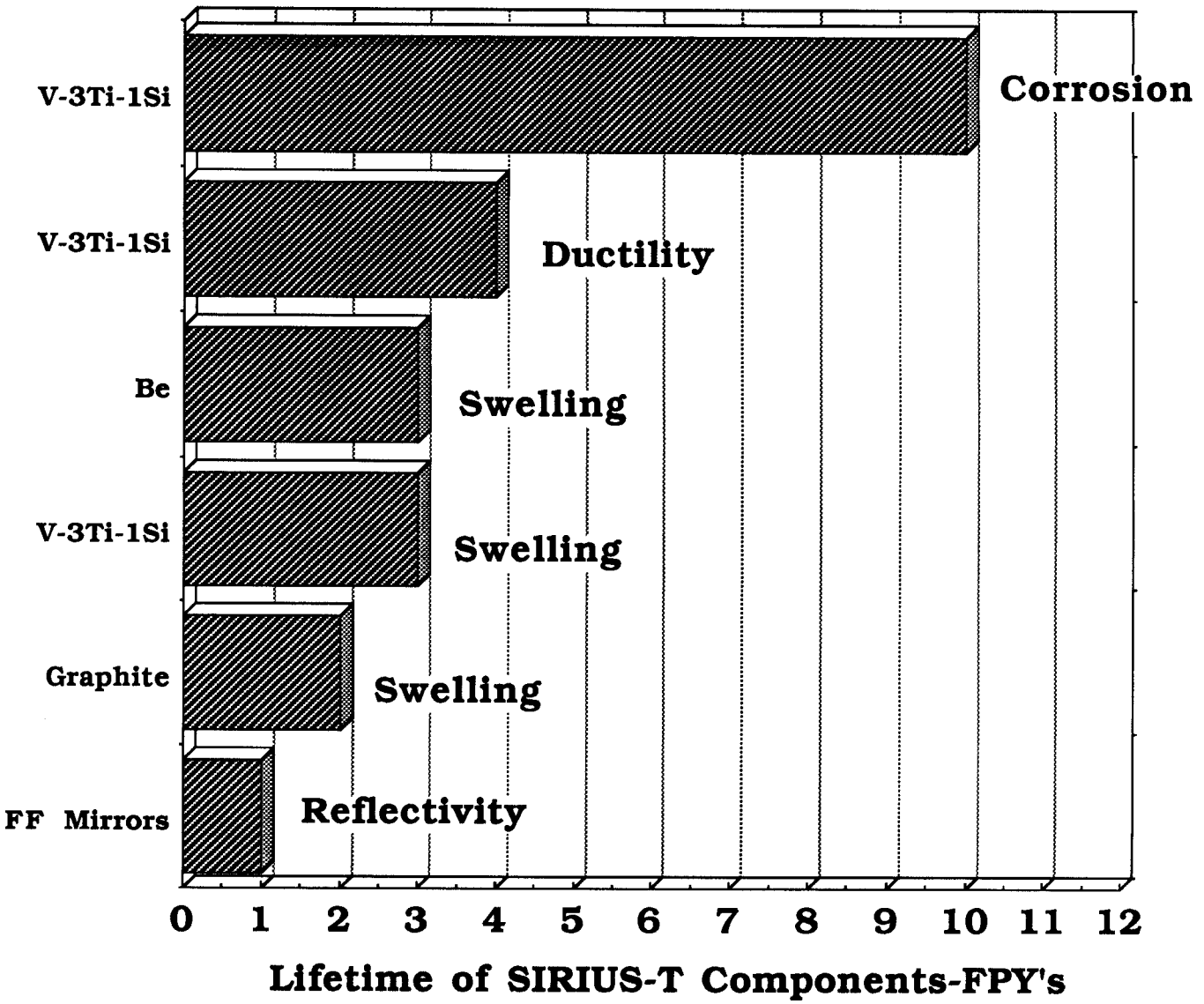

Fig. 8.13. Radiation induced growth in graphite and damage to final focusing mirrors are the life limiting factors in SIRIUS-T.

Figure Captions for Chapter 8

Fig. 8.1. Typical dimensional change in neutron irradiated graphite.[1]

Fig. 8.2. Useful lifetimes of graphite as determined by the point at which the graphite reaches its original volume.[2]

Fig. 8.3. Dependence of swelling of vanadium alloys at 600°C on irradiation damage.[4]

Fig. 8.4. Swelling in V-3Ti-1Si increases with preinjected helium.[3]

Fig. 8.5. Irradiation of V-3Ti-1Si at 420°C (with <4 appm He) makes this alloy stronger and less ductile.[3]

Fig. 8.6. Preinjected of V-3Ti-1Si alloys with helium before irradiation @ 420°C to 82 dpa makes the alloy more brittle.[3]

Fig. 8.7. Temperature effect on ductility of V-3Ti-1Si is not severe @ 40 dpa and <1 MW-y/m^2 equivalent of preinjected helium.[3]

Fig. 8.8. Effect of temperature on the corrosion rate of PCA, HT-9, and V alloy in flowing lithium.[8]

Fig. 8.9. Helium bubble swelling in neutron irradiated and post-irradiation annealed Be.[9]

Fig. 8.10. Schematic of radiation damage level in coating of final focusing mirror.

Fig. 8.11. Relationship of the final life, minimum annealing time, and annealing fraction in damaged mirrors.

Fig. 8.12. Effect of annealing recovery fraction on final focusing mirror lifetime.

Fig. 8.13. Radiation induced growth in graphite and damage to final focusing mirrors are the life limiting factors in SIRIUS-T.

9. TRITIUM CONSIDERATIONS

Tritium management and control are important considerations in the safety and environmental impact of a tritium production facility, as it is with all D-T fueled fusion systems. Although the produced tritium has a monetary value in the production facility, the safe containment of the tritium is of paramount importance, even though it may increase the cost of tritium. In order to assess the safety and environmental impact of the tritium during normal and off-normal operations of the facility, the inventories of tritium in the various components of the reactor must be determined and the potential for tritium leakage from these components to the environment must be evaluated.

The tritium is located within three principal systems within the SIRIUS-T facility; namely, (1) the tritium breeder blanket and the structure of the reactor cavity, (2) the heat transfer and tritium breeder system, and (3) the fuel target delivery system and the exhaust gases from the containment building. Each of these systems will be described and their tritium inventories determined.

9.1. Tritium Breeding in the Reactor Cavity

As described in Chapter 5 the reactor cavity is constructed of a vanadium alloy and liquid lithium is utilized as both the tritium breeder and the heat transfer fluid. In addition, the reactor cavity structure contains beryllium as a neutron multiplier. Because of neutronic reactions with Be and Li, both of these components produce tritium which dissolves in these metals. Although neutronic reactions do not produce tritium in the vanadium alloy, it will absorb tritium by contact with the Be and Li.

The concentration of the tritium in the liquid Li is determined by the operation of the Tritium Removal System, Fig. 9.1, which is located external to the reactor cavity. As the Li flows from the reactor cavity to the heat exchanger a portion of the liquid is diverted to the Tritium Removal System (TRS) which removes tritium at the rate it is generated in the reactor blanket. By the use of the TRS, the concentration of T in the Li is maintained at 1 wppm. With ~9 tonnes of Li in the reactor chamber and ~18 tonnes is the remainder of the Li circuit, the total tritium inventory in the Li is 27 g (9 g in the reactor chamber and 18 g in the external circuit).

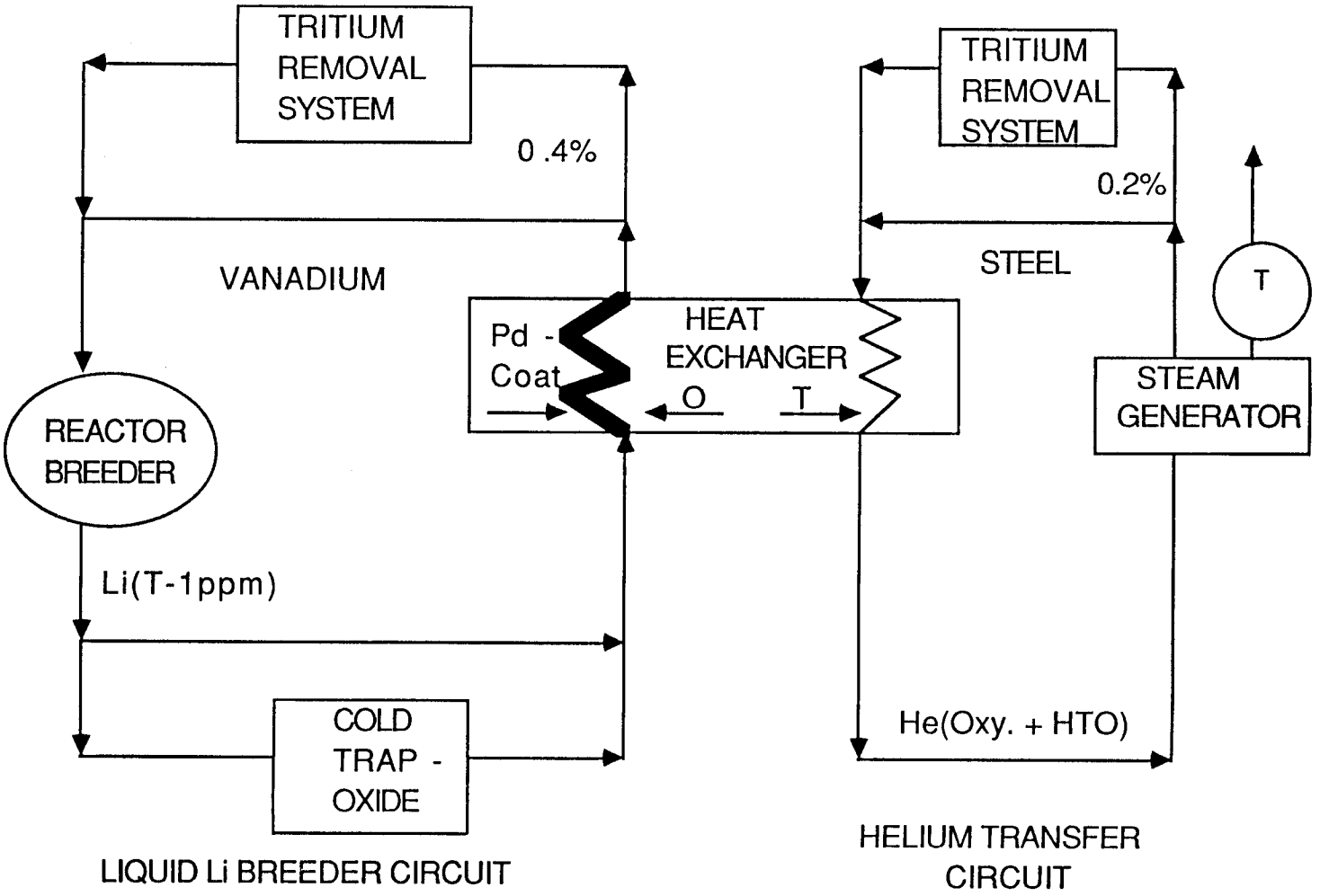

Fig. 9.1. Tritium removal systems for the lithium breeder and the helium intermediate heat transfer circuits operated in series.

The vanadium alloy which forms the shell of each module and also the structure of the reactor cavity, absorbs tritium from the Li coolant. The solubility of T_2 in vanadium is a function of the T_2 pressure and the structure temperature, and is given by the relationship,

$$S = \frac{0.116 \text{ wppm}}{Pa^{1/2}} \exp(0.34 \text{ eV/kT}) .$$

The pressure of T_2 in the liquid Li at 1 wppm is ~10^{-7} Pa. At a temperature of 600°C, the solubility of T in V is 3.3×10^{-3} wppm. For the entire vanadium in the modules and the structure, 370 tonnes, the total tritium inventory is 1.2 g.

Beryllium is an additional constituent of the tritium breeder module. Neutronics calculations indicate that the production of tritium in the first two layers facing the center of the reactor is particularly high, 0.88 and 0.84 kg per 3 FPY, the designed lifetime of the module. The retained inventory of tritium in the Be during this time is difficult to assess because of sparse and conflicting experimental data, Fig. 9.2. The initial experimental study by Jones and Gibson indicated that the diffusion of T atoms in Be was abnormally low when compared to other hexagonal close-packed metals (αTi and αZr). The samples used in these experiments were discs prepared from arc-cast Be which were soaked with T_2 at relatively high temperatures and relatively high pressure (2000 Pa). The tritium recovery was performed by step-wise annealing of the samples between 300-900°C in a vacuum with a stream of H_2 used to enhance tritium release. The results of this study indicated that the retained fraction of T was much greater at temperatures <600°C than the solubility determined at higher temperatures. This increased retention was attributed to chemical trapping and could be caused by a BeO coating on the discs. The samples had not been irradiated which would promote trapping.

In an additional experiment by Wampler, Be samples were bombarded by deuterium beams, and then the samples were annealed to release the D_2. This treatment resulted in a lower amount of D_2 retained in the Be sample as the temperature was increased. The ion-implantation experiments

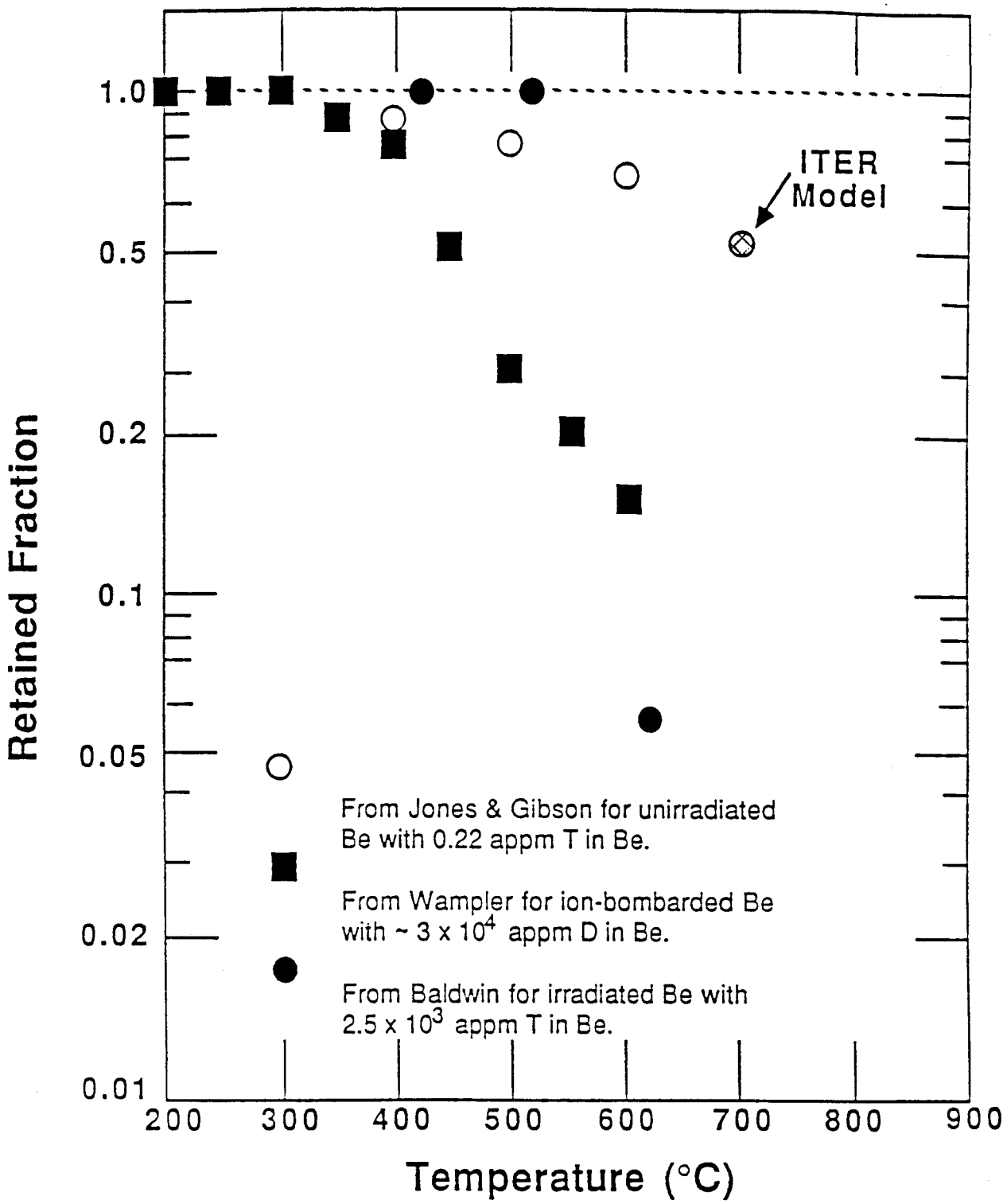

Fig. 9.2. Fraction of "trapped" hydrogen isotope remaining in Be as a function of annealing temperature for 25-100 hour anneals of unirradiated Be soaked with tritium (Jones and Gibson), 10 minute anneals of deuterium-ion-implanted Be (Wampler) and Be coupons sectioned from ATR irradiated material (Baldwin).

however, represent a very high surface concentration of D (~3×10^4 appm) in a narrow surface layer (~6×10^{-2} μm).

In a recent experiment, Baldwin utilized Be specimens which had been irradiated in the ATR test reactor to a fast neutron fluence of 5×10^{22} n/cm^2. This sample, which contained 2500 appm tritium and 30,000 appm He, was annealed step-wise at various temperatures and the release of T_2 was determined. The data, Fig. 9.2, indicates that up to ~520°C tritium retention was nearly 100% but at ~620°C only 6% of the tritium was retained. Apparently, when the thermal energy exceeds the chemical or irradiation trap energies tritium outgassing of the Be proceeds rapidly.

In order to determine the T inventory in the Be, the amount of trapped tritium was calculated by the use of Baldwin's data based upon the temperature profile in the breeder module and the mass of Be as a function of temperature. For the two front layers of Be, the amount of tritium retained during operation at temperatures from 500 to 650°C is approximately 10% of the tritium generation in these sections. Additional tritium can be removed, subsequently, during production shutdown when the entire module is evacuated and annealed at >600°C. If this annealing operation is repeated every 2 calendar months, then the entire tritium inventory is calculated to be only 18 g, as shown in the neutronics section, Chapter 6.

9.2. The Heat Transfer and Tritium Breeding System

The use of liquid Li as the tritium breeder provides the opportunity to use it as a good high temperature heat transfer fluid; however, care must be exercised in the design and operation of the system to prevent the escape of tritium from the heat transfer fluid to the environment through the steam generator system during normal or abnormal operations. In order to prevent this potential escape of tritium, two heat transfer systems are utilized in series, Fig. 9.1. The first heat transfer fluid, lithium, absorbs heat and generates tritium by nuclear reactions during its transit of the reactor cavity. This thermal energy is transferred to the secondary helium circuit via the intermediate heat exchanger (IHX). The construction of the IHX is important because the liquid Li must pass through the inside of the vanadium alloy tubes. Consequently, the transfer of metallic elements and interstitial impurities between two different alloys, via the lithium circuit, cannot occur. On the other

hand, the shell of the IHX and the remainder of the helium circuit is constructed of steel, which is compatible with the steam generator circuit. Both the steam generator and the helium circuit are at higher pressures than the Li circuit; consequently, if a leak occurred in the IHX, He would be injected into the Li, which would not develop into a serious accident. Conversely, if a leak occurred in the HX steam generator, steam would enter the He circuit which would not cause an immediate problem with the steel piping if the system could be shut down before the steam reacted with the IHX and entered the Li circuit.

Although the tritium pressure in the Li is very low, 10^{-7} Pa, some tritium, ~17 g/day (2×10^{-4} g(T)/s) would permeate through the IHX into the He circuit and continue to accumulate; consequently, a tritium removal system (TRS) is installed in the He circuit. This TRS removes tritiated water (HTO) by adsorption on a desiccant bed which yields a dew point of -60°C and a HTO pressure of ~1.33 Pa. In order to ensure the oxidation of the tritium, the exterior surface of the vanadium tubes in the IHX is coated with a thin, ~7-10 μm layer of Pd, as described by Hsu and Buxbaum.[1] Sufficient O_2 pressure is maintained in the He so that the Pd is saturated with oxygen; consequently, as the tritium atoms permeate through this Pd coating they are oxidized when they desorb into the gaseous stream. Based upon the parameters of the He circuit, the tritiated water pressure is maintained at ~2.6 Pa when 0.3 m^3/s of the He flow is directed to the TRS. As a result the entire He circuit contains only 2 g of tritium and only ~4 Ci/d of tritium permeates into the steam generator. The desiccant beds are recycled every 4 hours so that they contain only 3 g of tritium.

The principal extraction of tritium occurs in the tritium removal system (TRS) attached to the lithium circuit. This system, which has been experimentally demonstrated,[2] initially mixes a portion of the Li containing tritium with a second liquid phase of a fused salt composed of LiF-LiCl-LiBr. During this contact, the LiT present transfers from the liquid metal to the molten salt phase. The Li is returned to the reactor and the tritium is released as gaseous T_2 from the molten salt during electrolysis. This system has demonstrated approximately 50% efficiency for the extraction of T from Li at a T concentration of 1 wppm. In order to remove T at the rate it is produced in the Li

breeder, 3.37×10^{-3} g(T)/s, approximately 1.35×10^{-2} m^3/s of Li must be sent to the TRS which is only 0.4% of the Li stream circulating at 3.24 m^3/s. The recycle time for the Li is ~17 s for thermal extraction, but the mean residence time for a T atom in the Li is ~134 min. The recovered T_2 is sent to the Target Fabrication Facility.

9.3. Tritium Inventory in the Containment Building

The outer spherical structure will serve as the containment building for the site. This building will have thick, cast concrete walls which should be able to withstand any large missiles accidentally released within the building. However, this structure must have 92 penetrations for the laser beams which enter the building through large windows so that the photon flux per area of the window is low. These windows will be protected on the interior-side of the building by concrete structures which support the large turning mirrors. On the exterior-side of these windows an emergency ventilation system will be in place to capture gases exiting through a shattered window. If such an active emergency system failed to operate, then the contaminated atmosphere within the building might be released to the environment. For this reason, therefore, the potential tritium inventory within the containment building must be assessed. The sources of tritium and other radioactive materials reside in several systems; namely, the reactor cavity, the building atmosphere and the exposed surfaces within the building.

The tritium residing in materials within the reactor cavity has been assessed in the previous section. The probability is low, however, that this tritium might be released through a shattered window.

The atmosphere within the containment structure contains xenon at a pressure of 1 torr (133 Pa) and the unburned fuel from the exploded fuel targets which exit from the reactor cavity through the open penetrations provided for the laser beams. At this time, it is assumed that Xe is continually admitted into the reactor cavity at a rate so that the cavity gas is replenished once per second requiring 14.4 moles of Xe/s. This Xe contains, therefore, the target debris for one second (10 targets) which includes 1.4×10^{-3} moles of DT (1×10^{-4} mole fraction DT/Xe). The entire

building contains 2.4×10^3 moles of Xe, and consequently 0.24 moles of (DT) equivalent to 0.75 g of tritium. The processing of this exhaust gas is described later.

The interior of the concrete containment building will be covered with thin stainless steel plates so that tritium does not penetrate into the walls and to prevent a chemical reaction between any accidentally released molten lithium and the concrete. This steel surface, which can be easily decontaminated following an accident, will adsorb some of the gaseous atmosphere in the building. It has been demonstrated[3] that if a gaseous atmosphere does not contain water vapor the adsorption of gaseous tritium molecules is very small, and follows the relationship,

$y = 2.54\ x^{1.03}$ where y = atmospheric DT concentration, mCi/m^3

x = disintegrations per min $\times 10^{-3}/100\ cm^2$.

Based upon the concentration of DT in Xe (1×10^{-4} mol fraction DT/Xe) and the density of the Xe gas @ 1 torr (5.4×10^{-2} mole Xe/m^3), the concentration of the DT is 161 mCi/m^3. By the use of the above relationship the adsorbed DT for the entire steel surface ($6 \times 10^7\ cm^2$) is only 1×10^{-8} g of tritium.

When the DTO species is present its adsorption increases, significantly, following the relationship,

$y = 1.11 \exp(4.6\ x)$,

where y = surface contamination, disintegrations per min. $\times 10^{-3}/100\ cm^2$

x = atmospheric HTO concentration, mCi/m^3.

Oxygen is not normally present in the containment building; however, it is used in the processing of the exhaust stream. Consequently, DTO must be efficiently stripped from the Xe processing stream. The final removal of tritiated water will be accomplished in the Xe distillation column operating at 166 K (-107°C). At this temperature the vapor pressure of the DTO is $\sim 10^{-2}$ Pa but it is in contact with Xe at $\sim 10^5$ Pa (1 atm) so that the concentration of DTO is 10^{-7} mol fraction DTO/Xe. Upon entry into the reactor chamber that Xe pressure is reduced to 1 torr (133 Pa) so that the DTO pressure is reduced to 1×10^{-5} Pa, which yields a tritium concentration in the

containment building of 0.16 mCi/m^3. By use of the above relationship, one can calculate a total surface concentration of 6×10^{-8} g of tritium as HTO for the entire building.

An additional surface within the containment hold which will absorb tritium is the graphite tiles which protect the interior of the reactor cavity. Because of the Xe gas shield, the tritium ions do not reach these tiles as an ionic beam; however, the molecular reformed DT does have a solubility in graphite, which is expressed by the relationship,

$$\text{solubility H/C} = \frac{4 \times 10^{-4} \text{ atoms H/atm C}}{\text{atm}^{1/2}} .$$

This relationship indicates a solubility of only 3 mg of tritium in all the graphite (3.4 tonnes). On the other hand, it has been noted[4] that hydrogen saturates in the grain boundaries of graphite to a concentration of 5 ppm atoms H/atoms C. This relationship indicates that all the graphite tiles may retain up to 4.3 g of tritium.

An additional source of tritium is contained in the fuel target injector which must reside within the containment building (at a location which has not been defined at this time). The injector will contain a supply of cryogenically-cooled targets which are prepared in the Target Fabrication Facility. The targets are injected at 10 Hz delivering 6 mg/s of tritium. A 30 min supply of targets would contain 10.8 g(T) (18 g of DT).

9.4. Gas Handling and Processing System

A conceptual design of a simple gas handling system is presented (Fig. 9.3) which processes the exhaust gases from the containment building, prepares decontaminated xenon gas for reinsertion into the reactor cavity, and recovers, purifies, and isotopically-separates DT for the preparation of new target fuel. This processing must be accomplished with low loss and minimal inventories of xenon and tritium because of the high cost of Xe and tritium and the potential radiological hazard caused if tritium escaped to inhabited areas.

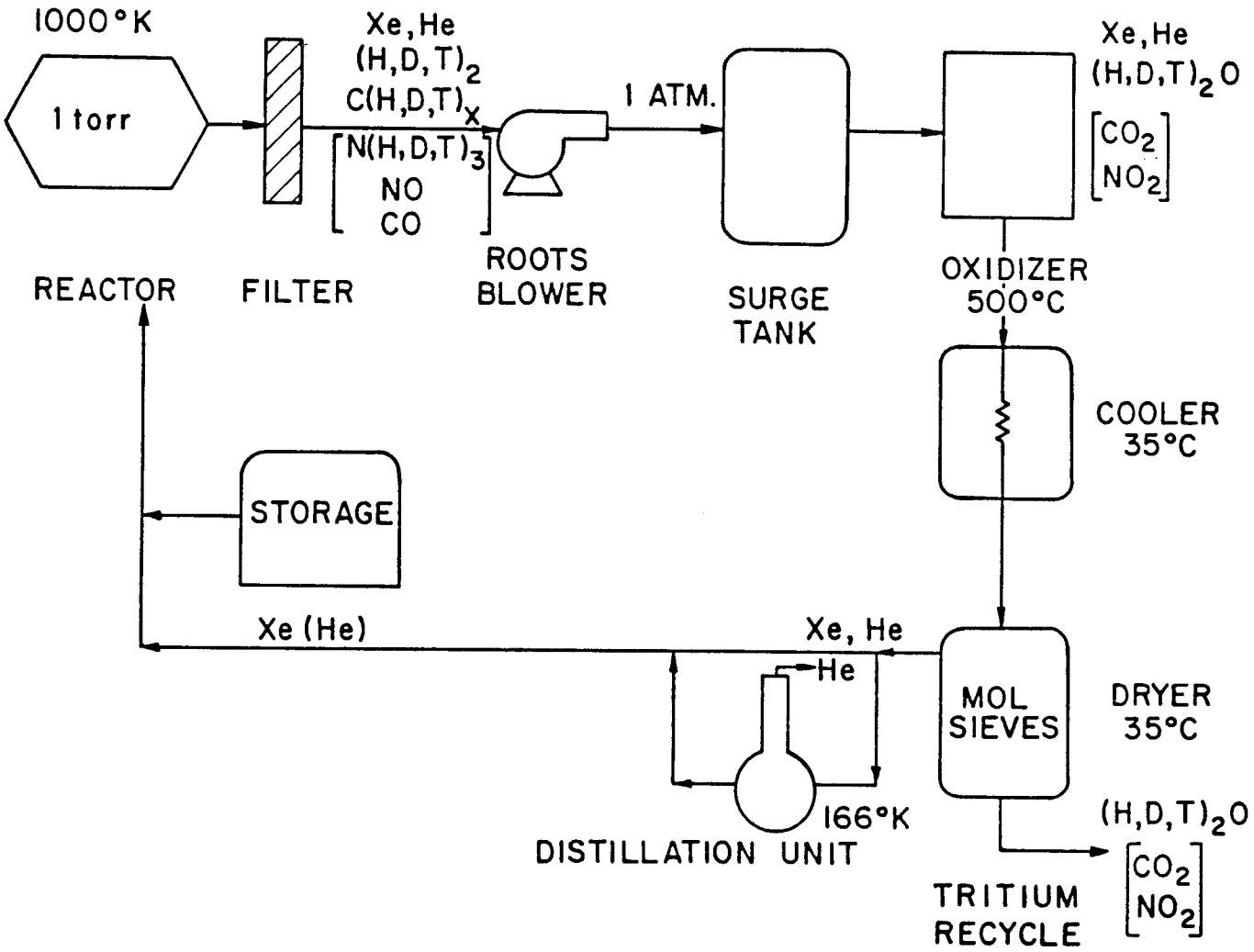

Fig. 9.3. Exhaust gas recycle system for recovery of xenon and tritium from containment building atmosphere.[8]

The required flow rate of Xe through the reactor cavity would be determined normally by the allowable impurities in the gas which may degrade either the focus or the flux of the laser beams. Such impurity levels have not been determined at this time; therefore, a one second residence time for Xe and the target debris particles in the cavity was assumed. The gas processing scheme therefore requires the purification of 323 liters (STP)/s Xe with small quantities (Table 9.1) of unburned fuel (DT), He ash, target shell debris $(CH_2)_x$ and some methane and acetylene (containing H, D and T) formed by reaction of the hydrogen isotopes with the hot graphite first wall. At the high temperature of the graphite first wall, >1000 K, a large fraction of the tritium may be chemically bound in the hydrocarbon gases.

Table 9.1. Chemical Composition of Containment Building Exhaust/s

	m mole	ppm (volume)
Xe	14,400	10^6
DT	1.4	100
He	0.59	41
$(CH_2)_x$-shell debris	1.31	91
$CH_4 + C_2H_2$	(unknown - formed at expense of D, T, H molecules)	

Briefly, the purification technique proposed (see Fig. 9.3) considers the oxidation of all the reactor exhaust to form water (containing H, D and T) and carbon dioxide in the Xe carrier gas. Spectrographic analysis of Xe and hydrogen mixtures at high temperatures have reported the formation of xenon hydride; however, the oxidation of all the gases should destroy such a compound. The oxidized gases are next absorbed on molecular sieve desiccant beds at ambient temperature, ~25°C. The desiccants are selected for preferential adsorption of water and CO_2. Finally, the He is removed from the Xe by cryogenic distillation.

Specific features of the reprocessing scheme are described, as follows:

a) A gas compressor, such as a Roots-blower, is used to exhaust the reactor cavity operating at 1 torr (133 Pa) and boost the gas pressure to nearly one atmosphere. This compression will decrease the volumes of the pipes and tanks needed. Nearly all of the processing system will be doubly contained so that any leaking Xe or tritium can be detected and will be captured.

b) The oxidation process will require the addition of oxygen to the gas stream ahead of the precious metal catalysis operating at 500°C. The "cracking" of the methane, acetylene and other hydrocarbons is usually difficult. It may be necessary to recycle the gases through the oxidizer several times in order to destroy these hydrocarbons. Also, oxidation in the presence of Xe may be very inefficient because of poor mixing. The excess oxygen can be removed after the desiccant beds.

c) The desiccant beds are recycled approximately every 2 hours. Tritiated water is released and collected when the desiccant bed off-line is heated to 300°C. The tritium and other hydrogenic isotopes are reclaimed from this water by a technique which initially electrolyzes the water. Then, the hydrogen isotopes are sent to a cryogenic distillation column which produces a stream of pure DT (very low in protium) and a protium stream (very low in tritium). The protium stream can be vented after suitable tritium decontamination.

d) The Xe distillation apparatus can be a simple liquefaction system to cool gas to -107°C (the boiling point at 1 atm) at the rate of 14.4 moles/s, forming 536 cm^3/s of liquid. This liquefaction would freeze any traces of DTO on the condenser plates. Also, any He or O_2 remaining in the Xe would evaporate due to their lower condensing temperatures. Such a distillation apparatus requires development but a continuous inventory of ~100 cm^3 of liquid Xe appears reasonable. The distillation system for the hydrogenic isotope separation is based upon a tested design.[5]

The inventories of Xe and tritium in the various processing equipment have been estimated, Table 9.2. The total tritium inventory is only 56 g and is isolated from any accidents in the reactor cavity.

Table 9.2. Inventory of Xenon and Tritium in Gas Handling System

	Xe (l)	Tritium (g)
Containment building	5.4×10^4	0.75
Surge tank (10 s)	3.2×10^3	4.3×10^{-2}
Oxidizer (1 s)	320	4.3×10^{-3}
Cooler (3 s)	960	1.3×10^{-2}
Dryer beds (2 hr recycle)	640	31
Pipes (10 s)	3.2×10^3	4.3×10^{-2}
Distillation column (100 cm^3 liquid Xe)	61	---
Xe storage (10 s)	3.2×10^3	---
DT-isotope purification	---	24
Total Inventory	65,600	56

9.5. Tritium Inventory and Potential Off-Site Releases

The inventories of tritium in the various locations and components are summarized in Table 9.3. Review of this table indicates that the majority of the tritium exists in the Exhaust Recycle System which is located in a basement below the reactor cavity but would share the single containment structure. Because this is a tritium production reactor, the tritium produced would be packaged for storage in the facility near the Tritium Removal System for the Li coolant. When they are securely sealed, the tritium containers would be transported to a separate storage vault away from the reactor. It is postulated that this storage vault would contain no more than one-month's production, ~2.8 kg of tritium.

Table 9.3. Tritium Inventory and Potential Off-Site Release

Location	Components	Inventory Tritium, g	Tritium Release Routine Ci/d	Tritium Release Accidental g
Containment building	Fuel injector	11	-	11
	Atmosphere	0.8	2	0.8
	Surfaces	<0.1	-	-
Reactor cavity	Beryllium	18	-	18
	Vanadium	1.2	-	1.2
	Graphite	4.3	-	4.3
Coolant circuits	Lithium	27	-	27
	Li-TRS	0.03	-	0.03
	Helium	2	4	2
	He-TRS	3	6	3
	Steam generator	-	4	-
Exhaust recycle	Desiccant beds	16	-	16
	Isotopic separator	24	-	24
	Other	1	2	1
Vault storage		2800	-	-
		2909	18	109

The routine release of tritium from the containment building via a stack of 100 m high is very low because most of the equipment is within double or triple containment structures. Experience at the Tritium System Test Assembly (TSTA)[6] has shown that these multiple containment structures release very small amounts of tritium off-site.

The quantity of tritium which would be released following an accident within the containment building would require an assessment of potential accident scenarios, which was not undertaken. A very conservative assumption would be that all the tritium in all the components might be released to the atmosphere. In such a case, up to 109 g of tritium would become airborne. Based upon the FUSECRAC model,[7] which is currently being used in the USA for fusion reactor studies, the radiation dose to the most exposed individual at the 1 km site boundary would be only 1 rem. A comprehensive accidental safety analysis would also consider other radioactive isotopes which might be released with the tritium, such as the vanadium structure. Fortunately, vanadium is a low activation material and would contribute only a small additional hazard off-site. This brief review suggests that the dose to the most exposed individual off-site can be kept below 25 rem, which is the guideline requiring evacuation of the neighborhood.

The Target Fabrication Facility has not been included in this analysis since targets will be purchased from a vendor. The vendor's facility will require its own safety assessment.

References for Section 9

1. C. Hsu and R.E. Buxbaum, "Palladium Catalyzed Oxidative Diffusion for Tritium Extraction from Breeder Blanket Fluids at Low Concentration," J. Nuclear Materials, 141-143, 238 (1986).
2. W.F. Calaway, "Electrochemical Extraction of Hydrogen from Molten LiF-LiCl-LiBr and Its Application to Liquid Lithium Fusion Reactor Blankets," Nuclear Technology, 39, 63 (1978).
3. C.J. Sienkiewicz, "Tritium Surface Contamination," Fusion Technology, 8, 2444 (1985).

4. R.A. Causey, M.I. Baskes and K.L. Wilson, "The Retention of Deuterium and Tritium in POCO AXF-5Q-Graphite," J. Vac. Sci. Technology, A4, 1189 (1986).

5. R.H. Sherman, "Cryogenic Hydrogen Isotope Distillation for the Fusion Cycle," Fusion Technology, 8, 2175 (1985).

6. J.L. Anderson et al., "Experience of TSTA Milestone Runs with 100 Gram-Level of Tritium," Fusion Technology, 14, 438 (1988).

7. L.J. Porter, "Upgrade of a Fusion Accident Analysis Code," MIT Report PFC/RR-89-10 (June 1989).

8. B. Badger et al., "SIRIUS-M: A Symmetric Illumination, Inertially Confined Direct Drive Materials Test Facility," University of Wisconsin Fusion Technology Institute Report UWFDM-651, Sept. 1985, p. II-73.

Figure Captions for Section 9

Fig. 9.1. Tritium removal systems for the lithium breeder and the helium intermediate heat transfer circuits operated in series.

Fig. 9.2. Fraction of "trapped" hydrogen isotope remaining in Be as a function of annealing temperature for 25-100 hour anneals of unirradiated Be soaked with tritium (Jones and Gibson), 10 minute anneals of deuterium-ion-implanted Be (Wampler) and Be coupons sectioned from ATR irradiated material (Baldwin).

Fig. 9.3. Exhaust gas recycle system for recovery of xenon and tritium from containment building atmosphere.[8]

10. MAINTENANCE

Reactor maintenance is an important function and must be considered from the earliest stages of the design. In SIRIUS-T, there are three primary components that have to be routinely maintained throughout the lifetime of the reactor. They are:

1. First wall tiles
2. Blanket modules
3. Final focusing mirrors

Each of these components will be discussed separately.

10.1. First Wall Tiles

The first wall tiles are the closest components of the reactor to the incident neutrons and are thus subjected to the most severe radiation damage. It has already been established in Section 5.2 that there will be no evaporation of the graphite. The criterion for their replacement is radiation damage. Graphite lifetime is determined by the damage level at which the graphite passes through the shrinkage phase and crosses the zero dimensional change axis on the way to "runaway" swelling. The peak damage level in the FW graphite is 18 dpa/FPY at an average equilibrated temperature of ~727°C. As the graphite is irradiated its thermal conductivity degrades and the average equilibrated temperature creeps up to 800°C. Swelling due to radiation damage varies dramatically for different graphites. Some graphites cross the zero dimensional change axis at ~30 dpa at 800°C (see Chapter 8). Based on this, a projected lifetime for the first wall tiles of 2 FPY has been made.

The first wall tiles have been described in detail in Chapter 5. They consist of a 1 cm thick graphite composite brazed to a V-3Ti-1Si metallic backing also 1 cm thick. The metallic backing has channels machined in it to allow the circulation of liquid lithium as an active coolant. This metallic backing is welded to two concentric tubes, the outer one a constant diameter tube and the inner one, a tapered tube. The annular space between the tubing is used to duct coolant to and from the tile. The outer constant diameter tube fits within the hole in the module provided by a constant diameter tube joining the inner and outer closure sides of the modules.

The first wall tiles are designed to be removed in two ways. They can be removed separately from the inside of the chamber, or they can be removed along with the whole module from the outside of the chamber. Figure 10.1 shows a cross section of a typical module with the first wall tile in place and Fig. 10.2 is the same cross section showing the tile being removed from inside the chamber. To disconnect the tile from the module the flange which makes up the rear of the coolant distribution header must be machined off as shown in Fig. 10.2. Further, the weld that seals the constant diameter tube connected to the tile, to the constant diameter tube connected to the module must be machined off. The tile can then be withdrawn radially into the chamber. The procedure is reversed when a new tile is inserted. After insertion, the two constant diameter tubes are welded together to provide the seal which prevents coolant from leaking in between them into the chamber. A new rear flange is then welded to provide closure for the coolant distribution header.

A question arises as to how all this can be accomplished. This question has been addressed in a very general way. For having such a maintenance capability, the following features must be provided:

1. Access into the chamber must be provided through two adjacent module receptacles, the pentagonal module at the south pole and one of the adjacent hexagonal modules in that cluster which is located within the support pedestal.
2. A special purpose remote handling machine is inserted into the pentagonal receptacle while the pentagonal port is reserved for bringing in and taking out tiles and other necessary components.
3. The remote handling machine will be capable of indexing on any tile within the chamber and clamping on to the beam port.
4. Machining and welding instruments can then be inserted through the clamp for accessing the rear header flange.
5. Some participation from the external remote handling machine may be needed.

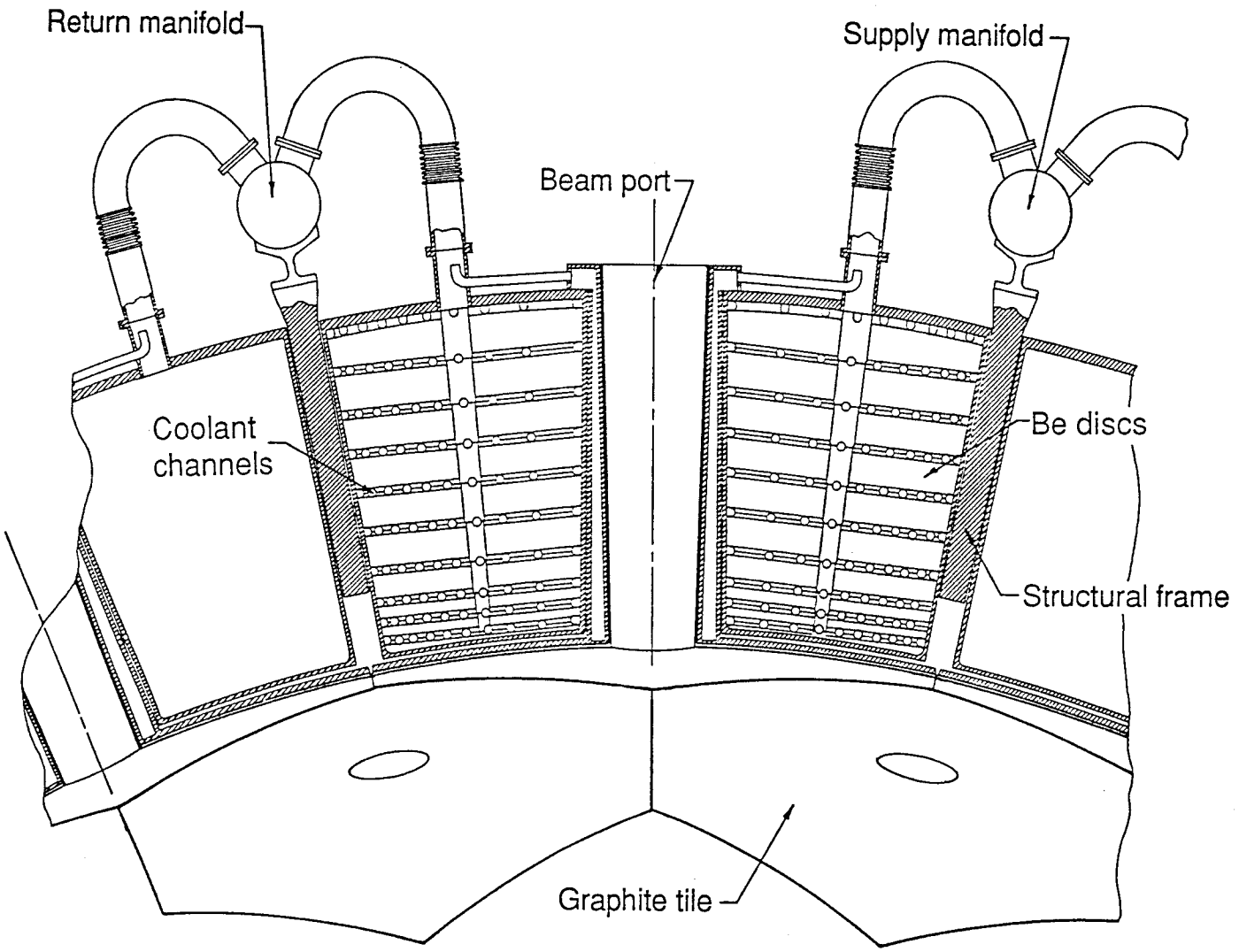

Fig. 10.1. Cross section of a typical hexagonal breeding module.

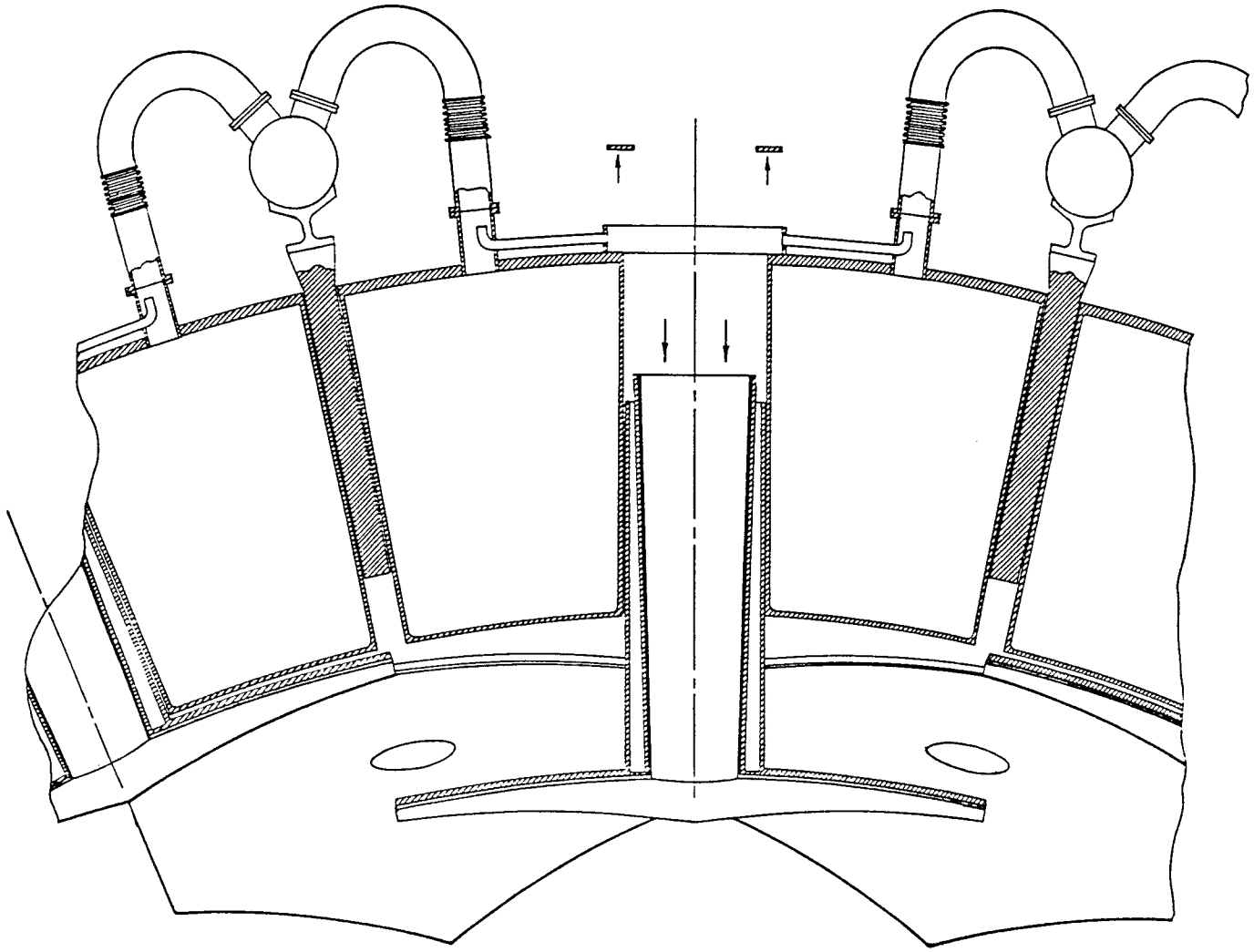

Fig. 10.2. Drawing showing the removal of a first wall tile from inside the chamber.

10.2. Blanket Modules

The blanket modules are made of the vanadium alloy V-3Ti-1Si and for them the need for replacement also comes due to swelling (see Chapter 8). A lifetime of 3-4 FPY is projected for the blanket modules. A 4 FPY lifetime would be very desirable since it is a multiple of the 2 FPY life projected for the tiles and would make scheduling replacement easier.

A blanket module replacement has to be performed from the outside of the chamber. Figure 10.3 shows a blanket module being extracted from the chamber. Note that the first wall tile is still attached and clears the structural frame. Two functions have to be performed before the module can be extracted. The inlet and outlet coolant lines have to be disconnected and the clamps (not shown in the drawing) which hold the module within the structural frame have to be unfastened. These functions are performed from the outside of the reactor by a remote maintenance machine which rides on a set of rails provided on the support pedestal as shown in Fig. 10.4. During reactor operation the machine is parked alongside the support pedestal out of the way of the beams. When needed, the machine is activated with controls built into the rails. The machine will be capable of circumnavigating the chamber on 360° and will be capable of reaching all of the 86 modules outside the support pedestal. Obviously, the remaining 6 modules trapped within the support pedestal will be maintained separately.

Figure 10.4 shows that the support pedestal has been designed to permit maintenance of the 6 modules trapped within it. The convoluted conical surfaces interface with the chamber along the support frame which defines the perimeter of the 6 module cluster. These surfaces provide the needed clearance for the modules to be extracted radially outward within the support pedestal. Another remote maintenance machine which will ride on a set of rails inside the support pedestal will be needed to provide this service.

10.3. Final Focusing Mirrors

The final focusing mirrors are exposed to direct incident neutrons and thus will suffer radiation damage. Their lifetime is determined by damage to the color centers of the mirror coating. The recommended dose upon which the color centers are damaged is $\sim 10^{11}$ rads. Partial

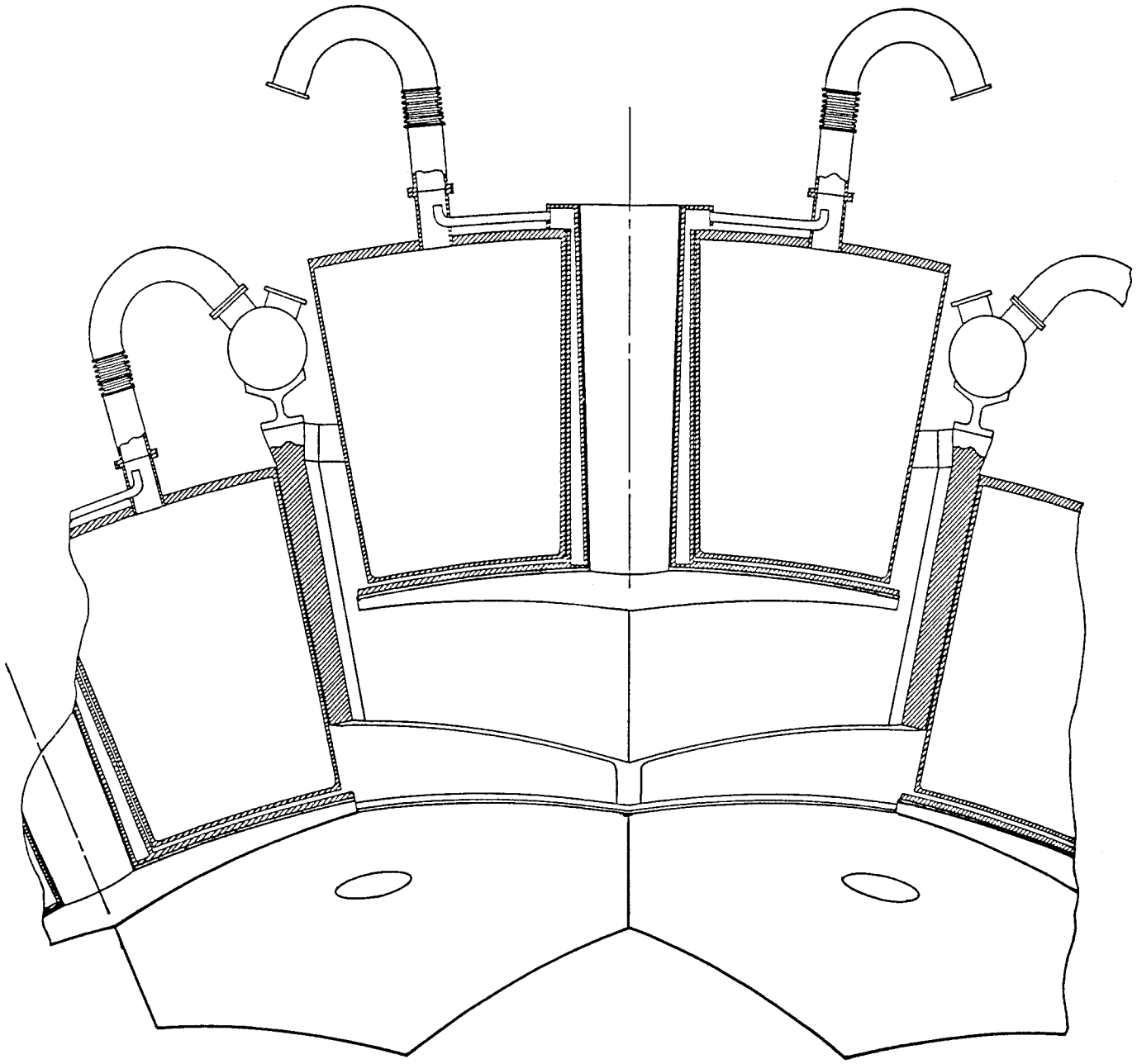

Fig. 10.3. Drawing showing the removal of a first wall tile from inside the chamber.

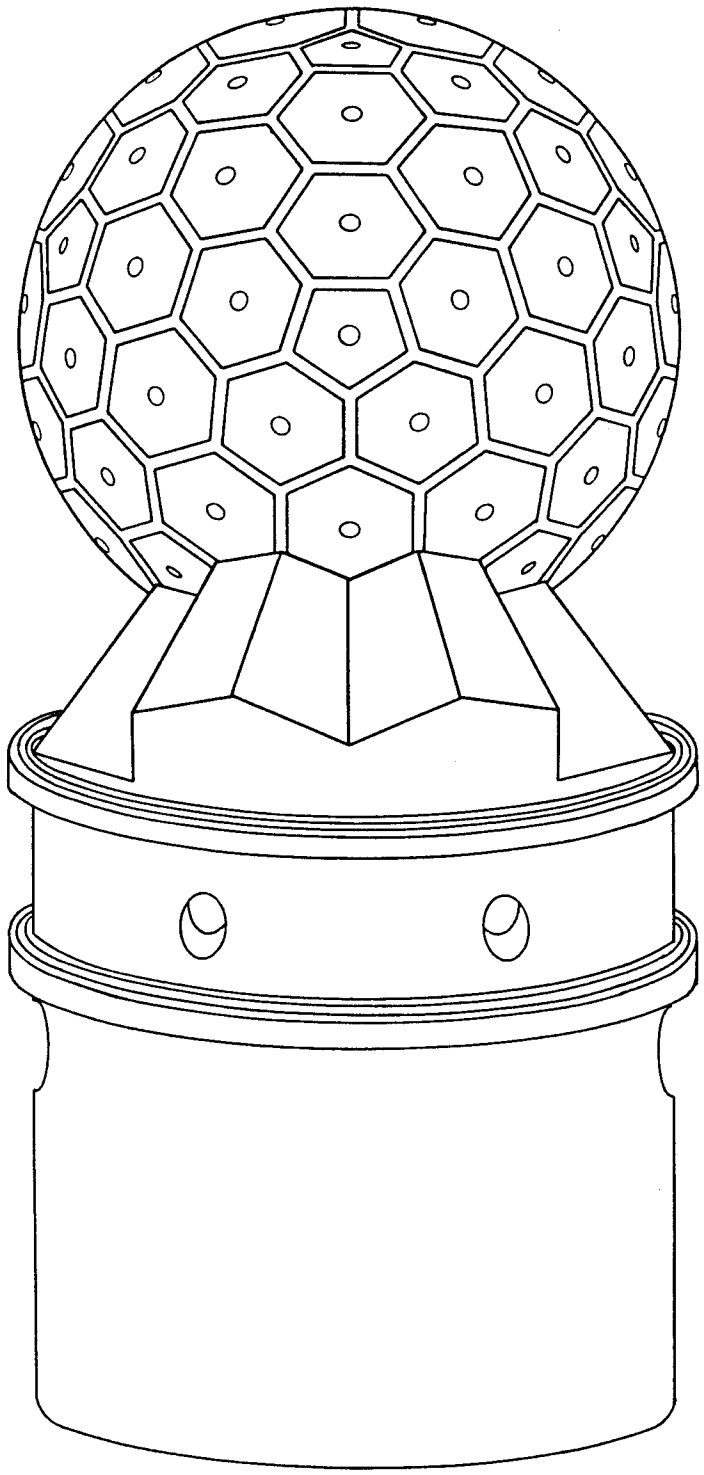

Fig. 10.4. Side view of the reactor chamber on the pedestal support.

recovery of the damage can be achieved by annealing, but the degree of recovery has not yet been established. At 20 m distance from the target, the dose rate for the final focusing mirrors is 5×10^{11} rads/FPY. This means the first annealing will be needed in 0.2 FPY. If we postulate an 85% recovery of the damage, then a 1 FPY lifetime can be projected if the time between anneals is at least one calendar month. Annealing the mirrors can be performed in situ by means of resistive elements built into the bodies of the mirrors.

Replacing the final focusing mirrors will be performed on an 8.5 calendar month schedule when one half (46) of the mirrors will be replaced. Several special purpose remote maintenance machines will operate simultaneously aided by the main machine riding on the pedestal tracks. The special purpose machines will index onto a turning mirror shield module and attach themselves to it. From that perch, they can reach a cluster of mirrors, one at a time. The spent mirrors will be unfastened from this support and handed to the main machine which will deposit them into a retrieval hatch. New mirrors are taken from a supply hatch and handed to the special purpose machine which then fastens it in place. These operations will be fairly repetitive and automatic. Recognition of the station being serviced will automatically program the location, distance and orientation needed for the main machine to handle the mirrors.

Two machines operating simultaneously can replace all 46 mirrors in a 48 hour period, allowing on the average, two hours per mirror. This seems to be a reasonable time for such an operation. The impact on availability is <1%. Further, this maintenance can be performed in parallel with routine maintenance of the power generating equipment.

11. SYSTEM INTEGRATION

The system integration chapter is usually intended to put whatever loose ends together to show a design which is homogeneous and which, so to say, "hangs together." For the reactor itself, this has already been accomplished in Chapter 3, "Overall Reactor" and in Section 5.1, "Chamber Design General Description." There are, however, several loose ends which should be elaborated on. They are the beam line layout and the power cycle.

11.1. Beam Line Layout

Up to now we have described the laser beams as penetrating a spherical containment building radially through glass windows. These windows constitute the vacuum barrier between the containment building and the laser beam layout facility or the laser building. In this section we address beam layout external to the containment building.

A detailed layout of the 92 beams from the laser to the turning mirror which directs the beams radially into the containment building has not been made. This is a major undertaking, given the complexity of modern lasers. Because light travels at 30 cm/ns and the total laser pulse is on the order of 5-10 ns, it is important to insure that each of the 92 beams travels the same distance from the laser to the final focusing mirror within some small tolerance. For symmetrically illuminated direct drive targets this is particularly difficult, because of the large number of beams uniformly distributed around the reactor chamber.

This problem has been worked on at the University of Rochester's Laboratory of Laser Energetics, albeit with only 60 beams. Figure 11.1 shows how they plan to accomplish this task with the OMEGA upgrade laser system. The driver lines are located in the center of the laser bay. The beams are split into two groups of 30 beams each at the stage C-D split area and thereon travel separately. Each group of beams then is directed back horizontally to the target bay area where they are incident onto the distribution mirror structure. From here the beams travel to the last mirrors which direct them radially toward the target chamber.

A similar beam layout can be envisaged for the SIRIUS-T reactor. The difference would be in the number of beams, 46 per group instead of 30 and the final mirrors in the OMEGA upgrade

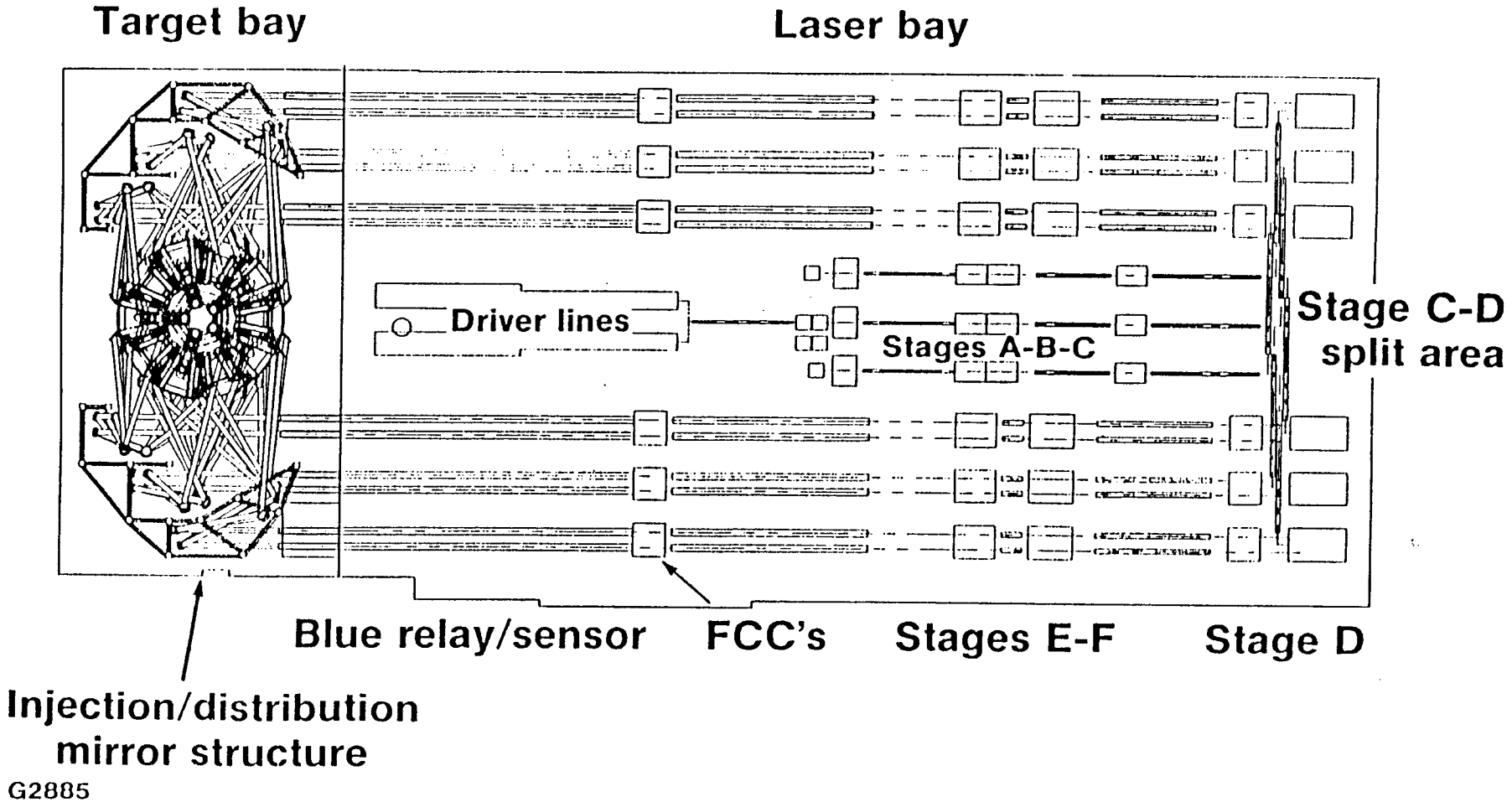

Fig. 11.1. Layout of the OMEGA upgrade laser system beam lines. Courtesy of the University of Rochester's Laboratory for Laser Energetics.

system would be those mounted on the outside of the containment building. From there, the beams must go through the glass windows, make a right turn, are focused through a crossover point and are finally turned another right turn and focused onto the target in the center of the chamber. Thus there are two additional mirrors which will be needed per beam, the shielded, full lifetime next-to-last mirror and the final focusing mirror. From the mirror mounted outside the containment building to the target, the distance is the same for all the beams. Thus the burden falls on the beam layout outside the containment building to insure that that distance is the same for all the beams. This is precisely what the UR-LLE system for OMEGA-upgrade accomplishes.

11.2. Power Cycle

For SIRIUS-T to be self sufficient with respect to electric power needed to drive the laser, it must have a power conversion system. The power required depends on the efficiency of the laser.

SIRIUS-T generates 1410 MW of thermal power consisting of liquid lithium at 550°C. With an intermediate helium gas loop this is expected to produce saturated steam at ~360°C which in a conventional PWR cycle will provide a thermal conversion efficiency of at least 36%. Thus the gross electric power generated will be 507 MWe.

We have assumed the KrF laser efficiency to be 5-10%. A 2 MJ laser at 10 Hz and 5% efficiency will require 400 MWe of power, while at 10%, it will require 200 MWe. Even at 5% laser efficiency, the system provides adequate power to drive the laser and another ~100 MWe for auxiliary power. This makes the system self sufficient.

The question still arises as to how the system can be started. Typical time constants for reaching operating temperatures are usually on the order of 5-10 minutes. This means that power generation and self sufficiency can be established in that order of time. Where is this power going to be supplied from? There are two possibilities. A large amount of very short term power can be purchased from a utility. The cost of this power will be $1500-$3000/startup. The other possibility is to have at hand a power storage unit of 15-30 MWh. This could be in the form of a superconducting solenoidal energy storage unit costing 50-75 M$ in direct costs. Such a unit

should only be used if there is no possibility of purchasing short term electric power. It would be far more advantageous to construct a facility such as SIRIUS-T at a site where 200-500 MWe can be purchased for short periods of time during startup.

12. ECONOMIC EVALUATION

There are two major criteria most people consider in evaluating a new advanced system; 1 - technical feasibility and 2 - cost. The technical feasibility has been addressed in the previous chapters. We should reiterate that wherever possible we have always taken the conservative approach. In this chapter we describe how we arrive at the bottom line, which is the cost of tritium (COT) production.

The methods and procedures for economic evaluation of conceptual fusion systems have come a long way since the start of this activity in the early 1970s. Although there will always be skeptics, most concede that present day costing is much more believable today than it was then. As is the case in technical feasibility, in SIRIUS-T costing we have always tried to err whenever possible on the conservative side. In the next section we will describe the assumptions, the code and other relevant information in the costing of tritium production in SIRIUS-T. A comparison between tritium production in SIRIUS-T and other proposed production reactors is given in Chapter 13.

12.1. Description of Costing Code

The cost code used in the economic analysis is "FUSCOST",[1] a PC-based menu driven program for economic analysis of fusion facilities. The code can do both MFE and ICF analysis, and in the ICF area is capable of costing KrF lasers, heavy ion beams and light ion beams. The algorithm and scaling laws for the drivers are the latest available with input from the national laboratories and industry. Cost algorithms and scaling laws for other items including balance of plant are taken from Scott Thompson[2] and the "SAFIRE"[3] code, which depend heavily on industrial experience in fission power plants.

12.2. Basic Assumptions

Although it can be generally assumed that a facility such as SIRIUS-T will be government owned and operated, we have costed it as a privately owned operation. Thus, the land must be purchased with no infrastructure available on it; further, 100% of the capital must be borrowed.

Table 12.1 lists the economic assumptions made for determining the cost of T_2 in SIRIUS-T. Once the total direct costs are determined, indirect costs are charged at 15% each for construction factor, home office factor and field office factor, while the owners cost factor is 5%. A 10% project contingency is then charged on the sum of direct costs and the construction, home and field factor. Thus the indirect costs amount to 65% of the direct costs. The total direct plus indirect costs are sometimes referred to as the total overnight costs, since they do not include interest during construction.

Table 12.1. Assumptions Used in T_2 Cost Determination

Plant availability (%)	70
Operation and maintenance (% of TOC*)	3
Construction time (years)	8
Plant amortization period (years)	30
Construction factor (%)	15
Home office factor (%)	15
Field office factor (%)	15
Owners cost factor (%)	5
Project contingency (%)	10
Fraction of capital borrowed (%)	100
Interest rate (%)	5-10
Levelized annual interim replacement cost fraction (% of TDC**)	1
Reference year costs	1986
(4.2 % interest rate used from 1986-1990)	

*TOC = Total overnight costs or total direct + indirect costs

**TDC = Total direct costs

Total capital costs depend on the number of years of construction and the interest on capital. We have used an interest range of 5-10%.

The cost of tritium production depends on the total capital cost, plant amortization years, interest on capital, operation and maintenance cost, interim component replacement cost, fuel cost and plant availability. We have assumed that the plant is amortized over 30 calendar years. Operation and maintenance is charged as 3% of total direct and indirect costs (or total overnight costs). A levelized interim replacement cost consisting of the cost of new final focusing mirrors, blanket modules and tiles as well as 1% of all other balance of plant components direct costs is used annually. This will be covered in a future section. Fuel cost, which in this case is the cost of targets, is varied between 10-20¢/target. Finally the plant availability is assumed to be 70%.

The "FUSCOST" code uses 1986 as the reference year but provides for escalation and inflation capability to any year. The costs for SIRIUS-T are inflated at an average consumer price index between 1986-1990 of 4.2%. Thus all the costs related to the reactor are quoted in 1990 dollars.

12.3. Driver Costs

Figure 12.1 gives the total cost of a KrF laser driver as a function of driver energy. The three curves are for TITAN related experience with a 0.9 scaling exponent, 85% learning curve cost with 0.7 scaling exponent and a 77% learning curve cost with 0.63 scaling exponent, all given in 1989 dollars.[4] These curves were taken from the "KrF Laser Driven Laboratory Microfusion Facility" design concept review, LANL, January 17, 1990. Figure 12.2 has the first two curves shown in Fig. 12.1 and in addition has a KrF driver cost curve taken from LANL in 1987 dollars[5] as well as the KrF driver cost scaling used in "FUSCOST." The indicated SIRIUS-T point at 2 MJ shows the conservative approach we have taken for costing this reactor. Since this would be a relatively near term facility, we opted not to take advantage of the learning curves given in these figures. The cost of the 2 MJ KrF laser is 375 M$.

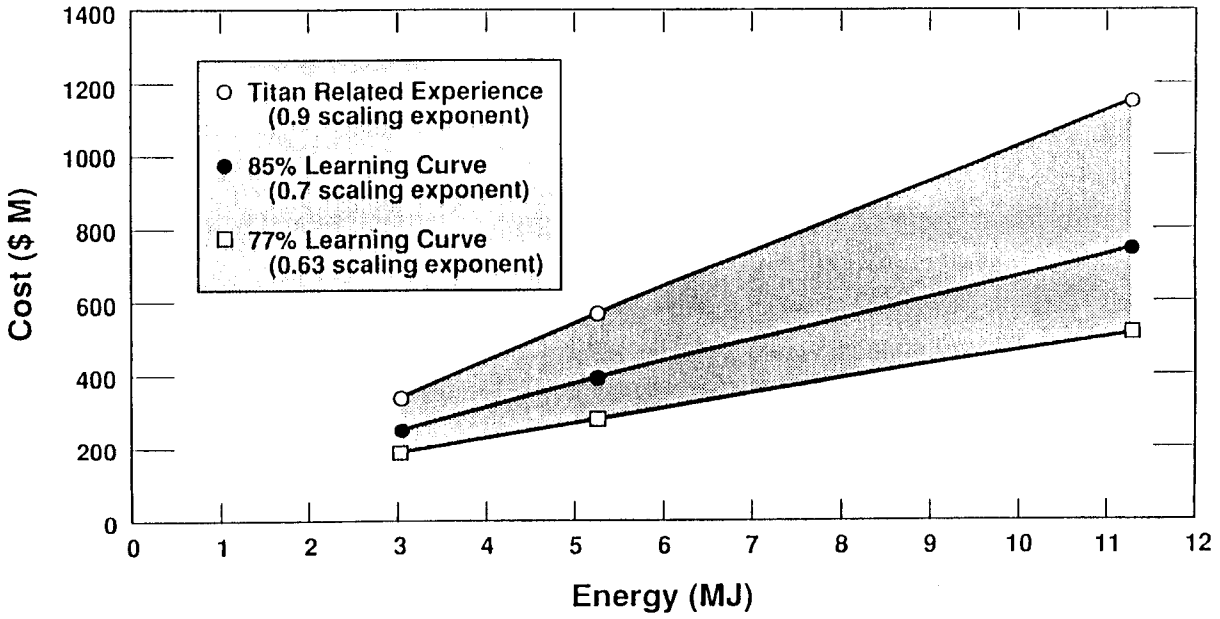

Fig. 12.1. Total KrF laser driver cost as a function of driver energy.[4]

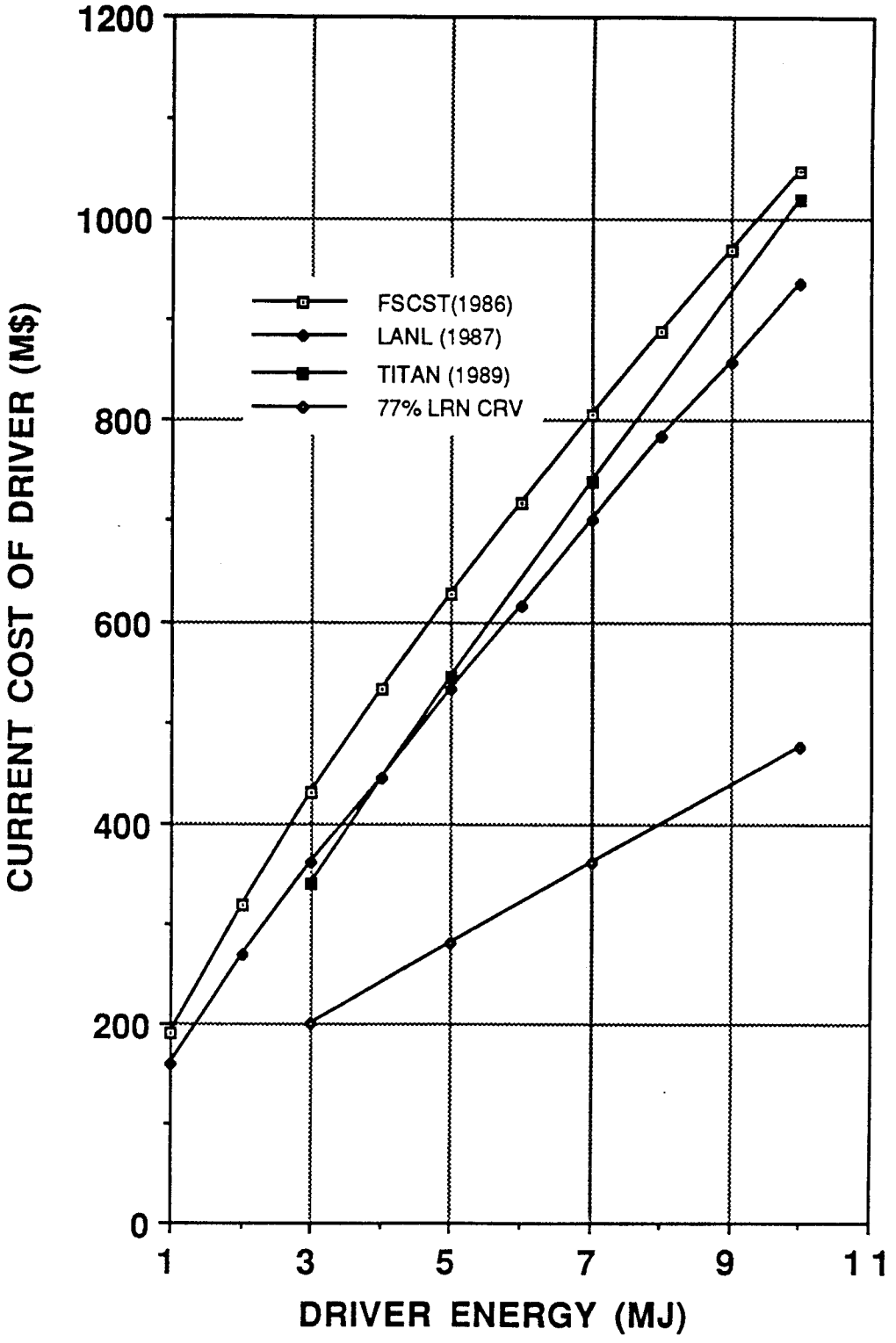

Fig. 12.2. Comparison of the FUSCOST algorithm obtained total KrF laser driver cost as a function of driver energy with TITAN and LANL estimate. LANL data taken from reference 5.

12.4. Annual Component Replacement Cost

There are several replacement components that must be accounted for in the operating costs. They are:

1. First wall tiles
2. Blanket modules
3. Final focusing mirrors
4. Balance of plant reactor components.

First wall tiles have a 2 FPY lifetime and blanket modules have a 3 FPY lifetime. For consistency, we assume that both will be replaced on a 2 FPY schedule or 34.3 calendar months. The direct cost of these components is 66.84 M$ and thus, the prorated annual cost based on a 34.3 CM lifetime is 23.4 M$. It should be mentioned that the original purchase of Be included a surplus of 33%. This allowed 1/3 of the modules to be replaced at one time, with the new modules already loaded with Be, prepared to be placed into the reactor. During the following 11.4 months, the Be is reclaimed from the spent modules and reprocessed for use in replacement modules.

The final focusing mirrors have a projected lifetime of 1 FPY or 16 CM. The total cost of the final focusing mirrors is 8 M$ based on a unit cost of ~$65,000/$m^2$. The prorated annual replacement cost is thus 6 M$.

Finally the replacement cost of the remaining reactor components including the balance of plant is taken as 1% of the direct cost of these components per year, which amounts to 10 M$. The total annual component replacement cost is:

$$23.4 + 6 + 10 = 39.4 \text{ M\$} .$$

12.5. Target Costs

The cost of ICF targets is not well known. In the past, reactor studies have used a canonical value of 100 M$ for a target factory which was included in the direct costs and amortized over the reactor lifetime. This is not very logical since the cost would vary depending on the complexity of the target and the quantity produced, which depends on the repetition rate.

The most comprehensive analysis of ICF target fabrication was performed by J. Pendergrass et al.,[6] in conjunction with the HIFSA study. This study focused on targets for heavy ion beams which require a layer of high Z material on the outer surface. Figure 12.3 shows the cost/target for three different varieties, a direct drive double shell, indirect drive and direct drive single shell.

The SIRIUS-T target is a direct drive single shell target without the high Z material deposited on the outer surface. It is therefore simpler than the HIB direct drive single shell target shown in the bottom curve in Fig. 12.3. At 10 Hz this target is costed at ~$0.2/target. We have used a base cost for the simpler SIRIUS-T target of $0.15/target and bracketed it with a range from $0.1/target to $0.2/target.

It is interesting to note that a 100 M$ target factory for SIRIUS-T, at 5% interest would give a cost of $.05/target if one considered the principal and interest payment for a 43 calendar year amortization. Operation and maintenance would add ~45% to the cost and the material cost would be trivial, since plastics $(CH_2)_x$ would be used. For a government operated facility, a 100 M$ target factory could provide targets at a cost of ~$.08/target. Similarly a 380 M$ factory would provide targets at ~$0.2/target. This seems to cover a wide range of target factory costs and justifies a cost range of $0.1-0.2/target we have used in this study.

12.6. Reactor Material Costs

The unit costs used for the various reactor chamber materials are given in Table 12.2 for the reference year of 1986. The values used in 1990 are escalated/inflated at 4.2% per year, which is the average inflation rate for those years as given by the consumer price index for energy related materials.

12.7. Balance of Plant Costs

The balance of plant (BOP) costs are well known since they are based on present day fossil fuel and fission power reactors. The FUSCOST code uses the algorithms proposed by Scott Thompson of ORNL.[2]

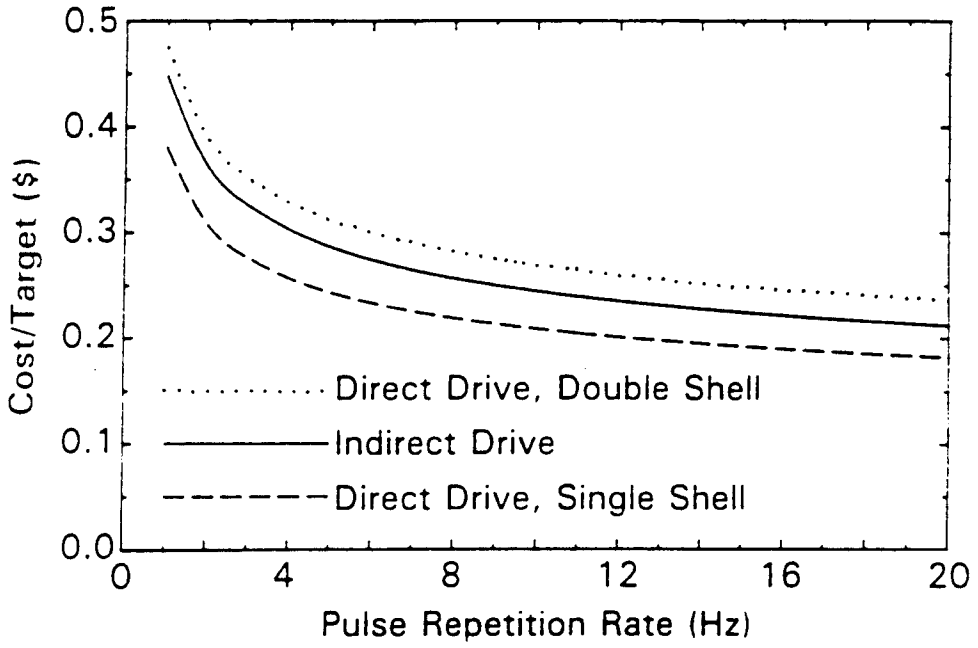

Fig. 12.3. The total cost per target as a function of pulse repetition rate for different target types, with target rejection only after being completed.[6]

Table 12.2. Reactor Materials Unit Costs

	(1986)	(1990)
Graphite ($/kg)	1000	1180
90% ^{6}Li enriched Li ($/kg)	1318	1550
Beryllium ($/kg)	450	530
Vanadium structure ($/kg)	600	700
Concrete ($/m^3)	1000	1180
Target injectors ($ each)*	750×10^3	885×10^3

*Two injectors are used in SIRIUS-T

The following algorithms are used for the BOP, all in 1990$.

Turbine plant (M$) = 0.411 $P_{th}^{0.8}$

Electric plant (M$) = 6.72 $P_g^{0.2}$ $P_{in}^{0.3}$

Maintenance equipment (M$) = 4.83 $P_{th}^{0.3}$

Miscellaneous plant (M$) = 5.95 $P_g^{0.3}$

Heat rejection (M$) = 0.178 $P_g^{0.8}$

Instrumentation and control (M$) = 2.95 $P_{th}^{0.3}$

where P_{th} = thermal power in MW, P_g = gross electric MW_e, P_{in} = laser input power in MW.

The heat transfer equipment account is a complex one and consists of individually costed liquid metal pumps, pipes, heat exchangers, cleanup system and storage tanks, as well as water pumps, pipes, steam generator, storage tank, and auxiliary and laser cooling systems. This account also includes the He circulators for the intermediate loop. Similarly the fuel handling account includes vacuum pumps, exhaust ducts, fuel cleanup systems, isotope separation, U storage beds, cavity gas recycle system, Xe inventory, cryogenic and gaseous storage, all costed separately.

The reactor containment building uses the algorithm:

$$\text{Containment building (M\$)} = 4.5 \times 10^{-3}\ V^{0.8}$$

where V = building volume in m^3.

In addition there are T_2 treatment, control, maintenance, radwaste, administration, diesel generator and hot cell buildings. The laser hall is included in the cost of the driver.

12.8. Annual Tritium Production

One thousand megawatt years of DT fusion power (1000 MWy) consumes 56 kg of tritium. SIRIUS-T has the following relevant parameters:

Availability (%)	70
Tritium breeding ratio (TBR)	1.9
Required TBR	1.05

The per calendar year T_2 surplus is therefore:

(56)(0.7)(1.9 - 1.05) = 33.32 kg/CY

12.9. Cost of T_2 (COT) Production

Table 12.3 gives the SIRIUS-T costs in 1990 dollars for the interest rates of 5% and 10%. The assumptions are:

- Construction period (years) 8
- Debt financing (%) 100
- Reactor life (FPY) 30
- Availability (%) 70
- Target costs ($) 0.15
- Annual T_2 production (kg) 33.3

The total direct costs are the same for the 5% and 10% interest rates. Total overnight costs reflect a 65% increase, accounting for construction factor, home office factor, field office factor and owners cost factor. Interest on capital borrowed during the 8 years of construction amounts to 506 M$ for the 5% interest rate and 1133 M$ for the 10%. Thus the total capital costs are 2838 M$ for the 5% interest and 3465 M$ for the 10% interest rate.

Table 12.3. SIRIUS-T Costs

	Costs in M$ (1990)	
Interest Rate	5%	10%
Reactor chamber	411	411
Driver	375	375
Turbine plant	136	136
Heat transfer equipment	115	115
Electric plant	115	115
Buildings	98	98
Maintenance equipment	43	43
Miscellaneous plant	39	39
Heat rejection	26	26
Instrumentation and control	26	26
Fuel handling	24	24
Land acquisition	6	6
Total direct costs	1,413	1,413
Total overnight costs	2,332	2,332
Total capital costs	2,838	3,465
Annual operation and maintenance	70	70
Annual component repl.	39	39
Annual target costs	33	33
Annual principal and interest	161	352
Total annual payment	303	494
Cost of T_2 production $/g (1990)	9,099	14,835

The annual expenses for tritium production are the operation and maintenance (O&M), component replacement, target costs and the mortgage payments. The principal and interest payments are based on a 43 year amortization period and are very different for the 5% and 10% interest rates. The total annual payment is 303 M$ and 494 M$ for the 5% and 10% interest rates, respectively. From these figures we arrive at the cost of T_2 production (COT) in 1990 dollars of $9,099/g at 5% interest rate and $14,835/g at 10%.

12.10. Discussion of Economic Analysis

Figure 12.4 is a bar chart of the SIRIUS-T direct costs. The two dominant accounts are of the reactor chamber at 411 M$ and the driver at 375 M$. Unfortunately, these two accounts are also the least well known. For this reason, we have been very conservative in costing the driver and reactor chamber. The next four large accounts are all part of balance of plant (BOP) in which there is a lot of confidence. The remaining costs all fall below the 50 M$ level.

Figure 12.5 is a bar chart of the reactor chamber direct costs. It shows clearly that the vanadium alloy and the Be costs dominate, at 189 M$ and 172 M$ respectively. The cost of the 90% enriched ^{6}Li lithium is 41.7 M$. The remaining costs are relatively low. Figure 12.6 is a bar chart of the vanadium costs in the chamber. Most of the structure, amounting to 67%, is in the frame and manifolds, pipes etc. which are lifetime components. The vanadium alloy in the modules and tile backing will be changed out on a 2 FPY schedule.

Figure 12.7 shows the effect of the replacement schedule on the cost of tritium production. The difference between a 2 FPY module and tile replacement as compared to a 3 FPY replacement, while keeping the final focusing mirror at 1 FPY, is only 1.2-2.2% in COT depending on the interest on capital. The reason the effect is so small is because the operating costs are so heavily dominated by the interest on capital payments. Figure 12.8 shows the effect of varying the cost of targets from 10¢ to 20¢ per target increases the COT by 8% at 5% interest rate and by 5% at 10% interest rate.

Finally Fig. 12.9 shows the effect of driver efficiency on the COT. The point to make here is that COT is almost flat between a driver efficiency of 5%-10%. Below 5%, the COT

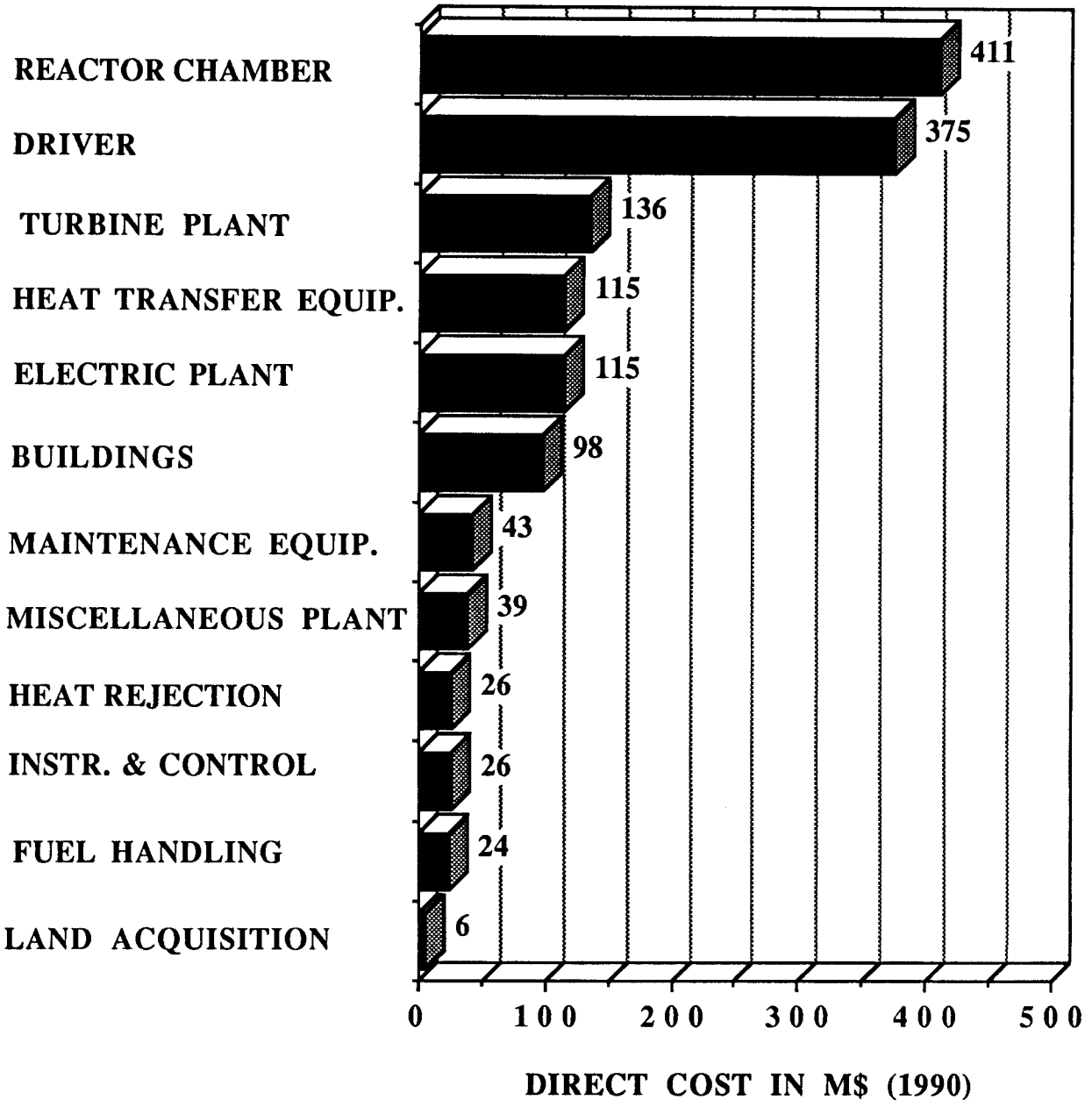

Fig. 12.4. SIRIUS-T direct costs.

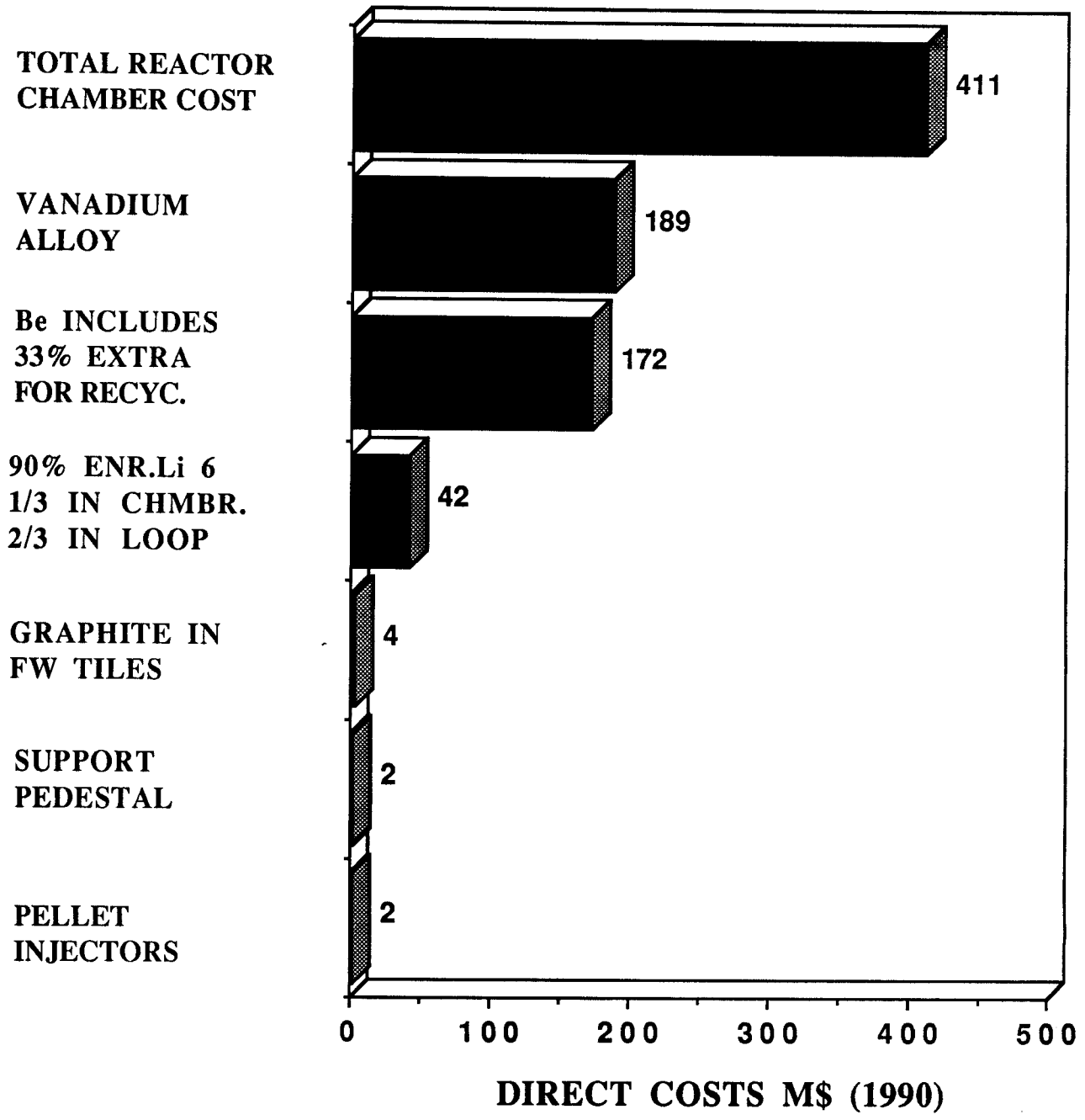

Fig. 12.5. Reactor chamber direct cost breakdown.

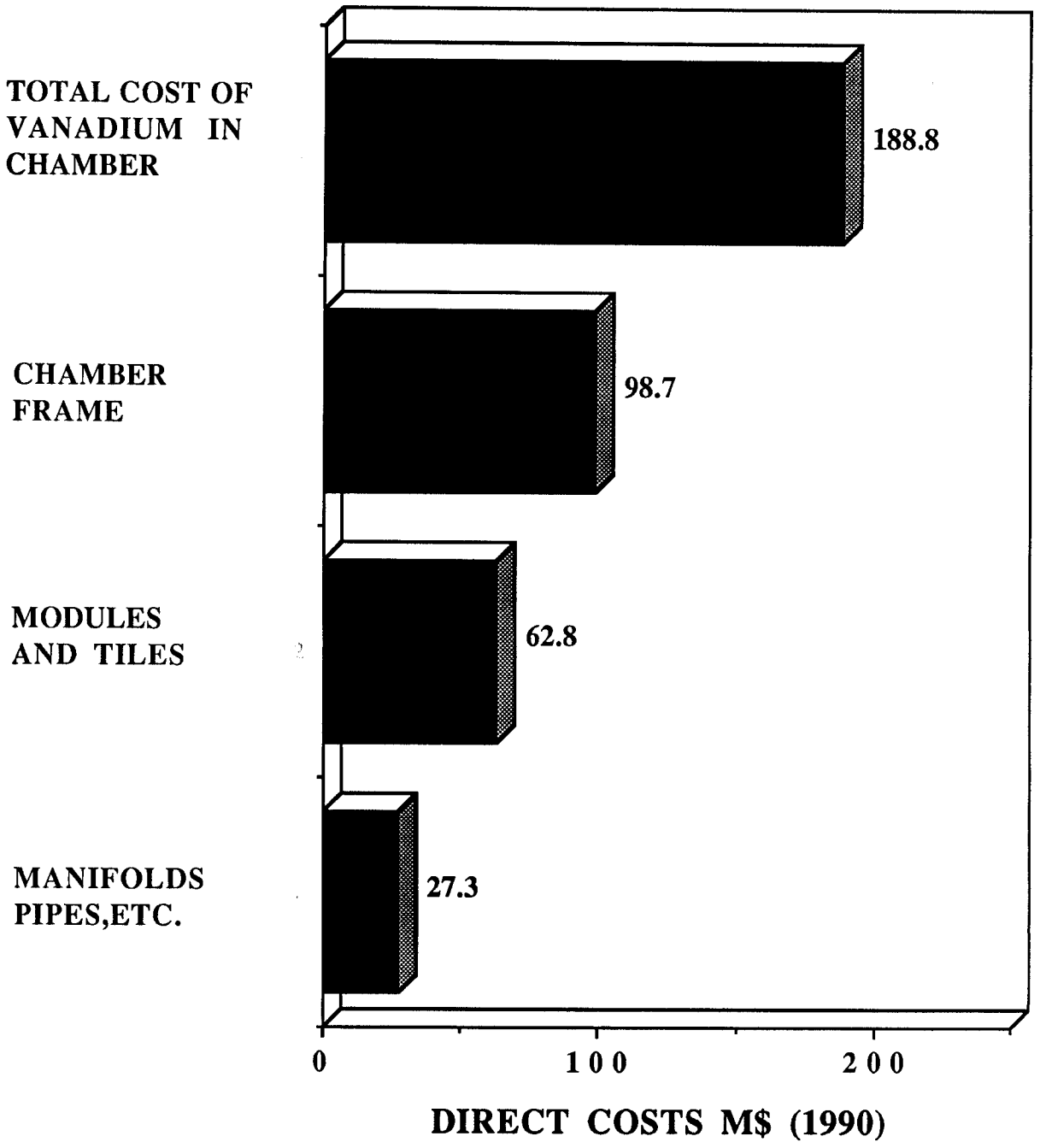

Fig. 12.6. Vanadium cost breakdown in chamber.

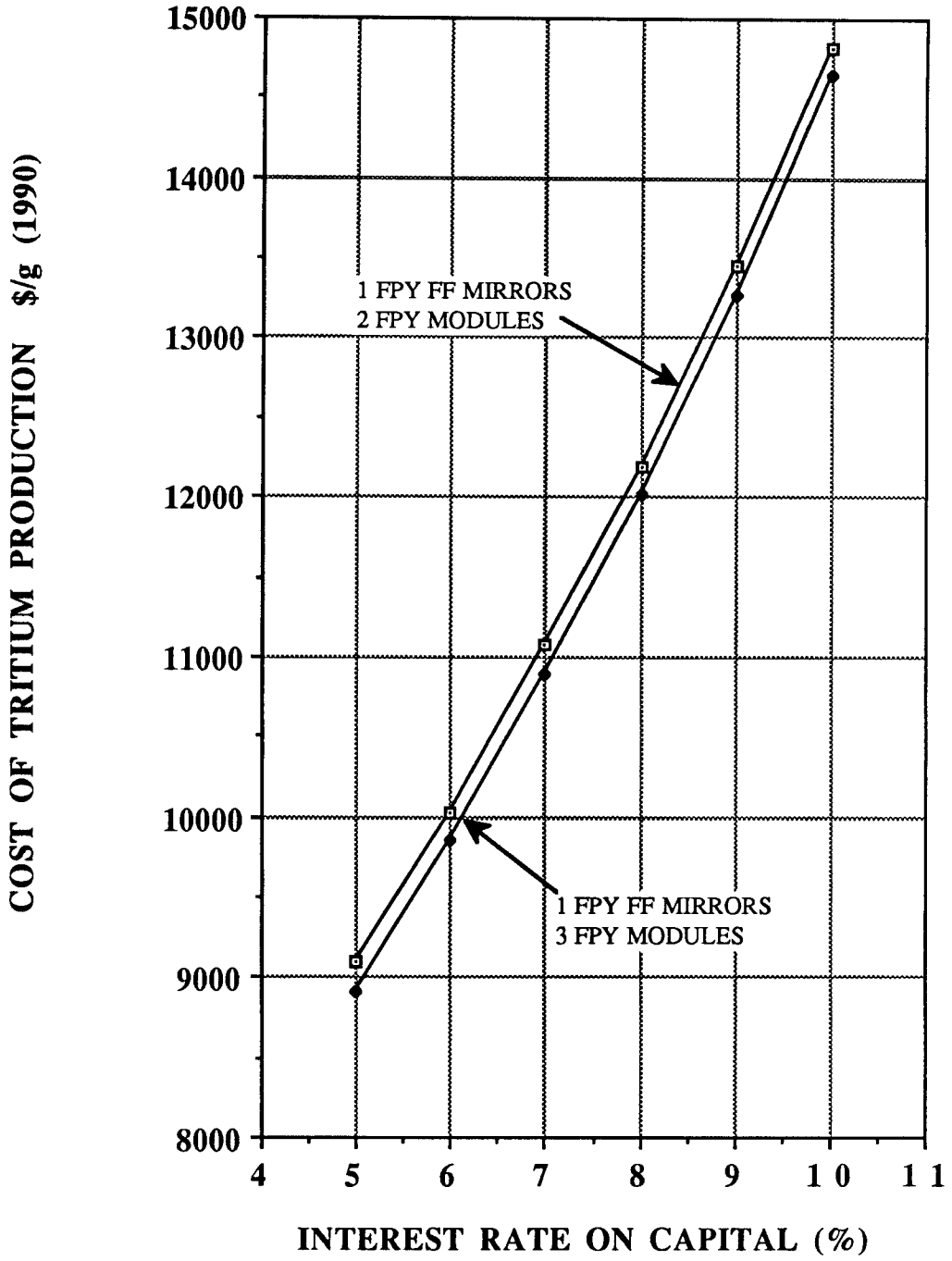

Fig. 12.7. Cost of tritium production as a function of two component replacement schedules for a 15¢ target cost.

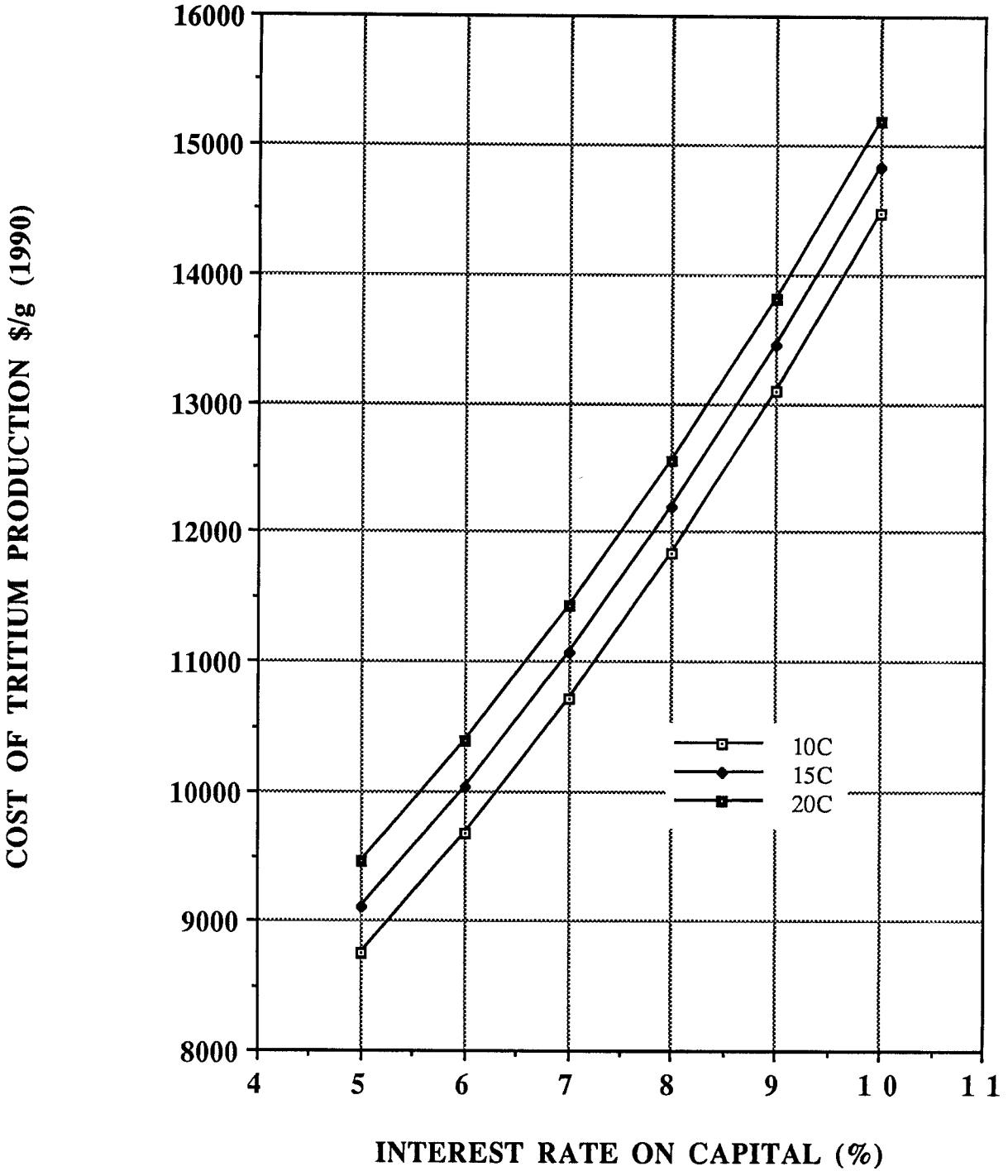

Fig. 12.8. Cost of tritium production as a function of interest rate for 10¢, 15¢ and 20¢ target costs.

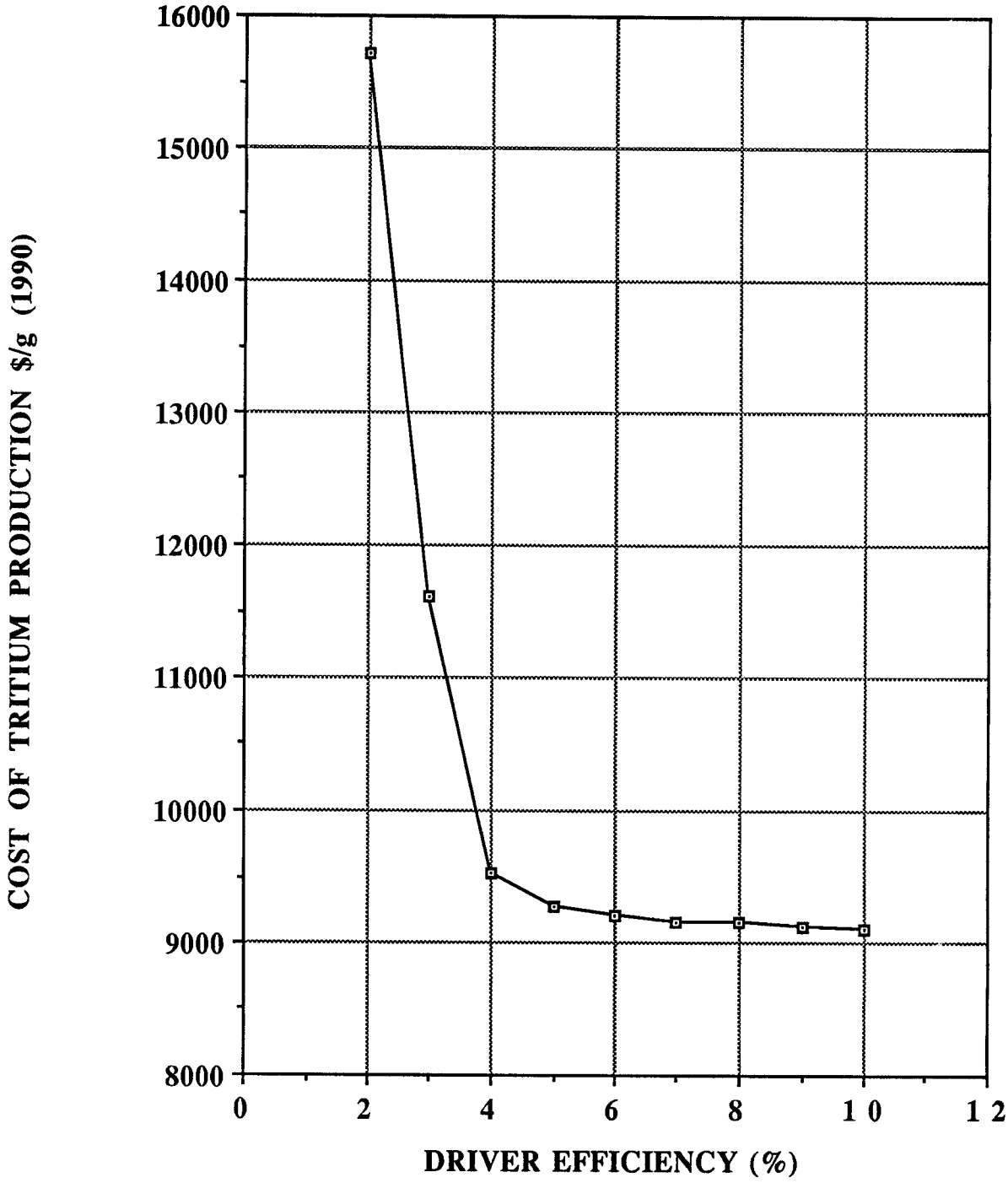

Fig. 12.9. Cost of tritium production as a function of driver efficiency for 5% and 15¢ target costs.

rises dramatically because the reactor is no longer self sufficient with respect to electrical needs, and must purchase electricity to operate. Between 5% and 10% driver efficiency the COT drops <2%. This effect is solely due to the cost of the electric plant which handles less electricity at the higher driver efficiency.

12.11. Summary and Conclusions

A conservative costing estimate for a privately owned SIRIUS-T facility shows that the cost of tritium production is <$10,000/g if the interest on capital is 5% and <$15,000/g if the interest on capital is 10%, both in 1990 dollars. The major cost drivers are the reactor chamber at 411 M$ and the laser driver at 375 M$.

Varying the blanket module replacement schedule from 3 FPY to 2 FPY has a minimal effect on COT. Similarly, doubling the cost of targets from 10¢ to 20¢ increases the COT by <8%. Finally, the efficiency of the driver between 5%-10% has a negligible (<2%) effect on COT.

References for Chapter 12

1. Z. Musicki, "FUSCOST: A PC-Based Menu Driven Program for Economic Analysis of Fusion Facilities," Proc. of 12th Symposium on Fusion Engineering, Oct. 1987, Monterey, CA, Vol. 2, pp. 955-958.
2. Scott Thompson, "Reference Cost Data for Fusion Studies," Revision 1, Sept. 1986, Fusion Engineering Design Center.
3. T.J. McCarville, W.R. Meier, C.F. Carlson, B.B. Glasgow, "SAFIRE - A System Analysis Code for ICF Reactor Economics," LLNL UCRL 15872, Vol. 1, Jan. 12, 1987.
4. "KrF Laser Driven Laboratory Microfusion Facility," Design Concept Review, LANL, January 17, 1990.
5. J. Harris et al., "Future Development and Application of KrF Laser-Fusion Systems," Fusion Technology, Vol. 11, No. 3, 1987.
6. John Pendergrass et al., "Heavy Ion Fusion Target Cost Model," Fusion Technology, Vol. 13, No. 12, 1988.

Figure Captions

Fig. 12.1. Total KrF laser driver cost as a function of driver energy.[4]

Fig. 12.2. Comparison of the FUSCOST algorithm obtained total KrF laser driver cost as a function of driver energy with TITAN and LANL estimate. LANL data taken from reference 5.

Fig. 12.3. The total cost per target as a function of pulse repetition rate for different target types, with target rejection only after being completed.[6]

Fig. 12.4. SIRIUS-T direct costs.

Fig. 12.5. Reactor chamber direct cost breakdown.

Fig. 12.6. Vanadium cost breakdown in chamber.

Fig. 12.7. Cost of tritium production as a function of two component replacement schedules for a 15¢ target cost.

Fig. 12.8. Cost of tritium production as a function of interest rate for 10¢, 15¢ and 20¢ target costs.

Fig. 12.9. Cost of tritium production as a function of driver efficiency for 5% and 15¢ target costs.

13. COMPARISON OF TRITIUM PRODUCTION REACTORS

13.1. Introduction

The U.S. Department of Energy has initiated a New Production Reactors Program which will provide for the design, construction and operation of new facilities for the production of tritium and other special nuclear materials. The preliminary design phase of this mission is currently in progress, leading to construction and operation by the year 2000. Two reactor designs which are being developed utilize thermalized neutrons produced in fissile fueled nuclear piles to irradiate ^{6}Li in target assemblies. These two designs are the heavy water moderated reactor (HWR),[1] operating at low temperature, and the modular high temperature gas-cooled reactor (MHTGR),[2] which will operate at sufficiently high temperature to also provide excess electrical power generation. Safety and environmental impact are high priority considerations in the design, construction, operation and eventual decommissioning of all the new production reactor design programs.[3]

Currently, five conceptual designs of alternative concepts to fissile reactors have been proposed to supply neutrons for tritium production, with the caveat that longer times for research and development would be required than the proposed New Production Reactors Program. These include the Accelerator Production of Tritium (APT)[4] and four thermonuclear reactors which produce neutrons by the fusion of deuterium-tritium fuel. These fusion concepts include two magnetic confinement concepts, a tandem-mirror (TM)[5] and a tokamak (TOK),[6] and two inertially confined concepts initiated by laser drivers, an indirectly driven target design (ICF-TPR),[7] and a directly driven target design,[8] SIRIUS-T.

Each of the production reactor concepts will be described briefly and compared according to their technical operations, safety and environmental impact and projected cost of tritium produced. Such a comparison is difficult because the accelerator and fusion reactors are only conceptual designs; however, such a comparison is instructive to determine if the alternative concepts have improved characteristics which would justify their long-term research and development costs.

The cost of tritium for SIRIUS-T as arrived at in this chapter is different from that reported in the economics analysis (Chapter 12). This is because to compare SIRIUS-T to the other methods of T_2 production, many different economic assumptions needed to be made. The reader should remember that the official cost of tritium production for SIRIUS-T is $9,099/g in 1990 dollars as reported in Chapter 12.

13.2. Comparison of Fission and Fusion Tritium Breeding

13.2.1. Nuclear Reactions

Both fission and fusion reactors produce tritium by the absorption of nearly thermalized neutrons in lithium target materials, via the reaction $^{6}Li(n,\alpha)^{3}H$. In a fission reactor nearly 1.8 neutrons are supplied during the fissioning of ^{235}U which also produces ~200 MeV of energy (Table 13.1). Because 1 neutron is required to continue the chain reaction, only 0.8 neutron/fission is available to react with Li; consequently, the production of one T atom releases ~250 MeV.

In a fusion reactor utilizing the nuclear reaction $^{2}H(^{3}H,n)\alpha$, one neutron is generated per fusion event with the release of 17.6 MeV of energy. In order to increase the production of tritium, this neutron bombards a ^{9}Be atom in a surrounding blanket to produce a neutron multiplication of ~2.3. These secondary neutrons react with Li to produce ~1.9 atoms of T with the release of 9.12 MeV. One T atom must be reserved as new fuel; consequently, in a fusion reactor with low neutron leakage, one net T atom is produced with the simultaneous production of ~28 MeV of energy (Table 13.1).

13.2.2. Thermal Energy Release

As noted above, the production of one atom of T in a fissile reactor releases ~9 times as much thermal energy as compared to a fusion reactor. If this thermal energy is not utilized, it must be released to the environment which may be detrimental to the proposed siting of a fissile reactor as opposed to a fusion reactor. The proposed tritium production reactors, in which no attempt is made to utilize the thermal energy, are water-cooled at <100°C, using low temperature technology, such as aluminum structures and Al-Li alloys as T breeder materials.

Table 13.1. Fission and Fusion Tritium Breeding Reactions[1]

Reactor	Reactions
Fission	$n + {}^{235}U = 2.5\ n$ - 0.7 n (leakage + absorption) - 1 n (fission chain) + 200 MeV + fission products
	$0.8\ n + {}^{6}Li = 0.8\ T + 0.8\ {}^{4}He$
Net Reaction, Nuclear	$n + {}^{235}U + {}^{6}Li = 0.8\ T + 0.8\ {}^{4}He$ + 200 MeV + fission products
Net Reaction, Thermal	~250 MeV/T atom
Fusion	$D + T = n + {}^{4}He$ + 17.6 MeV
	$n + {}^{9}Be = 2.3\ n$ - 2.24 MeV (endothermal reactions) - 0.4 n (blanket absorption)
	$1.9\ n + {}^{6}Li = 1.9\ T$ - 1 T (fusion fuel) + $2\ {}^{4}He$ + 9.12 MeV
Net Reaction, Nuclear	$D + T + {}^{9}Be + {}^{6}Li = 0.9\ T + 2\ {}^{4}He$ + 24.5 MeV
Net Reaction, Thermal	27.2 MeV/T atom

[1]Adapted from Reference 9.

If the thermal energy for either a fission or fusion production reactor is utilized for power production, then the reactor temperature is increased to >300°C so that efficient high pressure steam can be formed for steam-electric power systems. The reactor components in this case must be designed for high temperature operation, using either steel or carbon structures and targets fabricated from either a Li ceramic compound or liquid Li.

13.2.3. Safety and Environmental Impact

All the production reactors are being designed to high safety standards and to minimize their environmental impact during routine operations and accidental events. All of the devices will be enclosed in containment structures which mitigate the release of tritium and other harmful radioactive products following an accident. During routine operations the integrity of the heat exchanger between the reactor coolant and the environmental heat sink is very important because tritium diffuses easily, particularly at high temperatures, through metals used to fabricate heat exchangers. In some of the designs, the reactor coolants may contain tritium which could leak or diffuse through this heat exchanger.

Because the fission reactors utilize ^{235}U fission as the neutron source for tritium production while the fusion reactors do not, the fission reactors must be designed for the containment of the fuel during normal and off-normal operation and for extended periods upon removal of the fuel from the reactor. Eventually, the spent fuel must be processed and the long-lived isotopes disposed of in safe repositories. By contrast, the fuel and fusion products from a fusion reactor are not long-lived radioisotopes. The metallic structure of a fusion reactor contains some long-lived radioisotopes, although some radioactive isotopes can be avoided by the choice of alternative structural materials. Model studies have shown that decommissioned fusion reactor structures can meet Class C waste disposal ratings which requires burial at only 5 m depth and monitoring for 500 years.

13.3. Technical Assessment of Proposed Tritium Facilities

Brief technical aspects of each facility are summarized in Table 13.2.

13.3.1. Heavy Water Reactor (HWR)

The HWR utilizes fissile fuel with the neutrons moderated by D_2O at low temperature so that Al-Li targets can be used. These targets provide the following benefits: low permeability of tritium, low parasitic neutron capture, and low tritium solubility in the Al. The neutron capture cross-section of deuterium is small and the mass of D_2O is kept low so that the breeding of tritium is enhanced. The thermal power rating of the reactor is reported as 2500 MW. Although the tritium producing potential of this reactor has not been declassified, we can estimate from Table 13.1 that ~10 kg of T is produced per full power year (FPY). All the production reactors considered for this study have been rated at 70% availability, yielding ~7 kg of tritium per calendar year (CY).

13.3.2. The Modular High Temperature Gas-Cooled Reactor (MHTGR)

This production reactor concept utilizes 350 MW (thermal) modular high temperature gas-cooled reactors based upon designs for commercial MHTGR's. The proposed design includes four modules combined into a production block that share a spent-fuel storage facility and other support facilities. Two production blocks (8 modules) are combined in the complete facility. Steam generated during normal operation is delivered to a single main turbine and condenser to produce a net output of 135 MWe per module. With the eight MHTGR modules at full power operation, the system would produce 2800 MW (thermal).

The MHTGR uses a graphite-moderated, graphite-reflected annular core formed from prismatic graphite block and helium-cooled. The fuel consists of highly enriched uranium oxycarbide (UCO) microspheres which are coated with successive layers of pyrolytic graphite (PyC) and silicon carbide (SiC). These coated fuel particles are bonded together with a carbonaceous binder to form fuel rods. Enriched ^6Li aluminate microspheres which are coated with successive layers of PyC and SiC form the tritium production targets.

Table 13.2. Tritium Production Reactors - Technology Assessment

	Fission Reactors		Accelerator Study	Magnetic Conf. Fusion		Inertial Conf. Fusion	
	HWR	MHTGC		Tandem Mirror	Tokamak	ICF-TPR	SIRIUS-T
Fuel	^{235}U-Fission		1.6 GeV, p-beam Pb (liq.) Target	D/T Fusion		D/T Fusion	
Tritium Production Reactions	Fission - n Thermal Moderator LiAl Breeder Li Ceramic Batch Process		Spallation - n Thermal Mod. LiAl Breeder Batch Process	Fusion - n Be Multiplier LiAl Breeder Batch Process		Fusion - n Be Multiplier Liq. Li Breeder Continuous T_2 Removal	
TBR (net)[a]	0.8	0.8	40-50	0.67	0.52	1.08	0.90
Reactor Power, MWth	2500	2800	400	540	570	532	1410
Fission/Fusion Power, MWth	2500	2800	-	427	450	400	1000
Aux. Power Req'd., MWe	~50	(Produces 542 MWe)	900	355	560	(Power Self-Sufficient)	
Safety Issues	•Fission Products and Tritium Containment •Afterheat Removal		•Spallation Product Containment	•Tritium Fuel Cycle Containment		•Tritium Fuel Cycle Containment •Afterheat Removal	
Environmental Issues	•Fission Products Storage •Large Waste Heat Disposal		•Spallation Product Disposal; Waste Heat Disposal	•Waste Heat Disposal •Radioactive Structure Storage		•Lower Waste Heat Disposal •Radioactive Structure Storage	
Status	Proven	R&D for Tritium Breeder	Major R&D for p-beams + Pb Target	Requires Long-Term R&D for Fusion Technology			

(a)Tritium breeding ratio for each fission or fusion event, minus one neutron for fission chain or one tritium atom for fusion fuel, or number of neutrons produced per accelerated proton.

13.3.3. Accelerator Production of Tritium (APT)

The conceptual design of the APT facility consists of an accelerator system, a beam transport system, a target system, a tritium extraction system and a waste processing and handling system. In such a facility, a proton beam is accelerated to an energy of 1.6 GeV and a current of 250 mA by use of a radio-frequency current drive. These protons are focused on Pb targets to yield 40-50 neutrons per proton by spallation and evaporation reactions. These neutrons are moderated by water and subsequently captured in Li-Al fertile rods cooled by flowing water to maintain 90°C. The target rods are periodically removed and the tritium extracted in a separate facility. The use of lead for primary neutron production instead of a fissionable material provides lower decay heat with reduced safety concerns, as well as a lower amount of radioactive waste without the concern for the long-lived actinide wastes.

The APT target receives ~400 MW (thermal) and yields (6 to 7) $\times 10^{19}$ neutrons/s, giving a thermal energy to neutron yield ratio of ~40 MeV/neutron. The accelerator would require 900 MWe to drive the proton beam with an assumed efficiency of 44% for the conversion of electrical power to particle acceleration.

13.3.4. Magnetic Fusion Energy Reactors

Preconceptual designs have been investigated to utilize DT fusion reactions to produce neutrons by use of magnetically confined plasmas. Two confinement geometries were considered, namely, (1) the tokamak design (TOK) and (2) the tandem mirror design (TM).

The neutrons produced in either of these devices are emitted randomly from the plasmas and penetrate into a blanket structure containing a Be neutron multiplier (Table 13.1). The neutrons are absorbed in Li breeder materials to yield tritium. When the neutron losses, parasitic captures and one T atom is reserved for refueling were considered, the TM had an excess of 0.67 and the TOK 0.52 T atoms/incident neutron. Both the TOK and the TM fusion reactor concepts utilized ^{6}Li-Al alloys as the tritium breeding materials with the targets cooled and moderated by water at <100°C.

The fusion power is 427 MW for the TM and 450 MW for the TOK producing 10.8 and 9.1 kg of tritium per CY. All the current drive for the plasma has to be supplied by external power sources which requires 355 MWe and 560 MWe for the TM and TOK, respectively.

13.3.5. Inertial Confinement Fusion

Two preconceptual designs have been proposed for the production of tritium by neutrons released from inertially confined fusion reactions, namely the Inertial Confinement Fusion-Tritium Production Reactor (ICF-TPR)[7] and the reactor study[8] "SIRIUS-T". Both of these devices use laser beams to compress small, spherical targets of D/T solid to very high density and heat the compressed fuel to high temperatures in order to initiate the thermonuclear reaction. Both of these designs use Be in a surrounding chamber to multiply the neutrons. These neutrons are captured in a flowing stream of liquid lithium to produce tritium. The tritium in the lithium is extracted outside of the reaction chamber. The moderation and capture of neutrons in the lithium and the structure produces thermal energy which is also transferred by the lithium to a steam-electric turbine outside of the reactor. The electrical power generated is used solely to provide power to the laser and other auxiliary systems.

The shape of the reaction chamber is influenced by the type of target. For instance, the ICF-TPR uses an "indirect-drive" target which requires only two laser beams from opposite directions. Consequently, this chamber is cylindrical, 6 m OD by 9 m high. By contrast, SIRIUS-T uses a simple target design in which the D/T "ice" is contained in a thin shell. For this target to "ignite" the target must be illuminated very symmetrically, which requires 92 laser beams. The direct-drive chamber is, therefore, a sphere of 4 m ID, composed of hexagonal and pentagonal modules, which accommodate the 92 beams.

Following the target ignition, the nuclear fusion reactions continue until the inertia in the compressed target has been exceeded and the target disintegrates, hurling x-rays, α-particles, unburned fuel and target debris throughout the chamber. Two different techniques have been used in order to attenuate these photons and particles before they impact the first structure surrounding the target, because this structure would be severely damaged. In the ICF-TPR, which is cylindrical,

a fall of liquid Li, ~5 cm thick, extends from the top to the bottom of the chamber at 1.5 m from the target and protects the breeding blankets behind the fall. In the SIRIUS-T spherical chamber, xenon gas at a pressure of 133 Pa is used to protect the first structure. In a chamber of 4 m radius, all the photons and debris (but not the neutrons) are stopped before impacting the first structure. The shock wave of Xe gas at this low pressure is small; however, because all the x-rays and ions are attenuated by the Xe, it reaches a high temperature. This thermal energy is then re-radiated to the first wall at a sufficiently slow rate so that the first wall shield, a graphite composite, can withstand the thermal shock.

The tritium breeder blankets were approximately the same thickness, 1.5 m for the ICF-TPR and 1.0 m for SIRIUS-T. The ICF-TPR breeder used Be as a structural material with very little steel which gave 2.08 tritium atoms/incident neutron, or a excess tritium yield of 1.08 per fused T atom in the target. The SIRIUS-T breeder used a vanadium alloy as a structural material with a somewhat smaller amount of Be which gave an overall ratio of 1.90 tritium atoms/incident neutron or 0.90 T atom per T fused in the target.

The tritium production rate in an ICF chamber is a function of the rate of target "burns" and is limited by the rate of debris removal from the chamber and is not constrained by the repeatability of the laser system. For the ICF-TPR the target ignition rate is 2 Hz producing 400 MW of fusion power and 16.9 kg of tritium/CY at 70% availability. For SIRIUS-T the ignition cycle is 10 Hz, producing 1000 MW of fusion power, and 33.3 kg of T/CY at 70% availability.

The technical status of these fusion production reactor concepts places them in the long-term time frame for potential use in the years 2010-2020. In the near-term research and development tasks related to the required laser power, target testing and laser-target interactions will be conducted.

13.3.6. Safety and Environmental Impact

The salient features of each reactor in regard to safety (accidents) and environmental impact are summarized in Table 13.2.

13.4. Economic Assessments of Tritium Production Reactors

This task is difficult because the costing information was supplied by diverse groups and the level of detail varied. The HWR, the MHTGR and the APT followed the NPR capacity cost evaluation guidelines[10] supplied in 1988. The fusion reactors were costed by their designers without any guidelines and would be very difficult to reevaluate. For this comparison, the NPR guidelines were used, as defined below, and the missing fusion reactor cost items were added as noted in Table 13.3.

13.5. Investment Capital

Direct Capital Costs: The total capital costs include all the structures and the equipment installed, as given by the authors of each design.

Indirect Cost: The project management cost is set at 10% of the Direct Capital Costs. The contingency cost is determined as a percent of Direct Capital Cost. This contingency cost reflects an assumption of the maturity of the system to achieve a completed plant which has a 50/50 probability of producing the required production on the required schedule.

Spares and Fission Fuel: This category includes extra parts or equipment which are purchased at the time of construction and the initial fuel core for the fission reactors. For the SIRIUS-T fusion reactor extra Be was purchased for recycle but this cost was included in the Direct Capital Cost.

Operational Costs: This category is given on an annual cost basis.

Cost of Capital: This represents the annual payback of the investment plus interest over the 40 year assumed lifetime of the plant. The long-term "real" interest rate was judged to be 4% and used in this study.

Operation and Maintenance: This line includes the operational staff expenses and expendable items for operation of (1) the reactor, (2) the tritium plant, and (3) waste management. A separate line is used for general site management.

Contingency: This category reflects the maturity of the design and is highest for the APT and the 4 fusion reactor designs.

Table 13.3. Economic Assessment of NPR's (in Million $U.S.)

Categories	HWR	MHTGR	APT	TM	TOK	ICF-TPR	SIRIUS-T
Design Year	1988	1988	1989	1982	1982	1985	1986
Direct Capital	2970	3107	3380	1115	1095	1190	1413
Indirects							
Project Management	296	315	340	112	110	119	141
Contingency Risk/$	9%/294	24%/741	30%/1120	30%/336	30%/330	30%/357	(30%)423
Spares and Fission Fuel	66	245	280	-(a)	-(a)	-(a)	-(b)
Total Investment	3626	4408	5120	1563	1535	1666	1977
Annual Costs							
Capital	183	223	259	79	78	84	100
O&M, Plant + T Fac.	255	225	155	66	66	37	70
General Support	168	168	130	55**	55**	31**	58**
Contingency (Risk/$)	0.5%/2	8%/32	15%/40	15%/17	15%/17	15%/10	15%/19
Capital Upgrade	38	24	140	17	21	12**	30
Target Purchase	-	-	-	-	-	-(c)	35
Electric Power	9	271*	335	61	96	-(d)	-(d)
Total	655	401	1059	295	333	174	312
$/1990	709	434	1101	406	442	207	365
Production, T (kg/CY)	7	7.8	6.8	10.8	9.1	16.9	33.3
Tritium Cost, $/g	101,000	55,600	162,000	37,600	48,600	12,300	10,960†

*Revenue, **Amounts added by author, †This value to be used for a consistent comparison with the other systems in Table 13.3 only. The official cost of tritium from SIRIUS-T is $9,099/g as given in Chapter 12.

(a)Not available, (b)Included in direct capital, (c)Target facility included during construction, (d)Power self-sufficient

Capital Upgrade: The NPR cost evaluation study recommends at least 1% of direct capital be used each year for upgrading the facility.

Target Purchase: The designers of SIRIUS-T proposed that fuel targets be purchased as an annual operational cost @ 15¢ per target while the ICF-TPR constructed a 100 $M facility to accomplish this task.

Electric Power: For the designs which were not self-sufficient in electrical power, this power is purchased from a power grid at costs which varied from 28 mills/kWh for the TM and TOK up to 56 mills/kWh for the APT and depended upon the site selection.

Inflation: The total operational costs were compared in 1990 dollars by use of the consumer price index from the original date of each design to CY 1990.

Cost Comparison: The cost per gram of tritium was obtained when the annual cost of operation was divided by the proposed annual production of tritium.

13.6. Results and Conclusions

A meaningful comparison is obtained when the alternative facilities are compared with the HWR, which is an existing technology, and shows the following: (1) the cost of tritium from a new HWR will be ~3 × the current selling price of $29,000/g, (2) the MHTGR supplies tritium at a 45% lower cost, because of the sale of electricity, (3) the APT cost is a factor of 160% higher, (4) the magnetic fusion facilities are ~36 to 50% of the current cost, and (5) the two ICF facilities are ~11 to 12% of the current cost of tritium as compared to the HWR.

The HWR is based upon existing technology, it provides tritium at a reasonable cost, and it can be built within a ten-year time frame. The MHTGR produces tritium at a significantly lower cost and, also, electrical power which may be valuable at the chosen site; however, the containment of the tritium in the target assemblies during irradiation and the processing of the targets to release the tritium must be demonstrated within the proposed time schedule.

The APT requires major developments in the RF accelerator design, beam propagation, spallation physics and target development. In addition, the cost of tritium appears to be high.

For the long-term supply of tritium and other special isotopes which can be produced by neutron irradiation, the four fusion reactors should be considered. Their advantages are: (1) the amount of waste heat for disposal is only 15% as compared to the fissile reactors, (2) the radioactive wastes are not as hazardous (no actinides) and require much reduced internment facilities, (3) the radioactive heating of the fusion reactors at shutdown is much less than in the fission reactors which reduces the potential for post-accident melting and vaporization of the reactor components, (4) especially the ICF designs are able to support their own power requirements, and (5) the unit cost of tritium is significantly lower. Admittedly, the costs for a fusion reactor contain many tenuous assumptions. These costs should be viewed as indicators rather than as absolute values until a new costing model[11] for fusion reactors which is being developed is accepted.

The development costs needed for a fusion TPR might be considered, but would be difficult to quantify. For instance, if $10 million/yr for 20 years were spent for the tritium production components in the development of the SIRIUS-T reactor, and this investment at 4% interest rate were charged to the eventual tritium product, its cost would increase by only $500/g. The spending of larger amounts of money to drive the fusion program specifically for tritium production might be an option; however, in this case, the development costs would need to be amortized amongst all fusion reactors built for any purpose.

In summary, long-term support is economically and environmentally justified to develop the technology and test these fusion reactor concepts.

References for Section 13

1. J.J. Jicha, Jr., "Heavy-Water Program: Technical Requirements, Conceptual Design Phase Process, and Reactor Characteristics," Trans. Amer. Nucl. Soc., 61, 153 (1990).
2. J.D. Nulton, "The Modular High-Temperature Gas-Cooled Reactor - A New Production Reactor," Trans. Amer. Nucl. Soc., 61, 153 (1990).
3. K.A. Klein, "New Production Reactor Safety," Trans. Amer. Nucl. Soc., 61, 154 (1990).
4. "Accelerator Production of Tritium," DOE/S-0074, Energy Research Advisory Board to the United States Department of Energy (1990).

5. J.D. Lee, "Economic Analysis of a Magnetic Fusion Production Reactor," J. Fusion Energy, 6, 59 (1987).
6. J.D. Lee, "Tritium Breeding Analysis of a Tokamak Magnetic Fusion Production Reactor," J. Fusion Energy, 8, 89 (1989).
7. W.R. Meier, T.J. McCarville, D.H. Berwald, J.D. Gordon, and W.G. Steele, "An ICF Tritium Production Reactor," Fusion Technology, 8, 1208 (1985).
8. I.N. Sviatoslavsky et al., "SIRIUS-T, An Advanced Tritium Production Facility Utilizing Symmetrically Illuminated Inertial Confinement Fusion," submitted to Fusion Technology (in press).
9. W.A. Lokke and T.K. Fowler, "Stockpile Tritium Production for Fusion," UCRL-94003, Lawrence Livermore National Laboratory (1986).
10. "New Production Reactors Capacity Cost Evaluation," DOE DP-0052, Oak Ridge National Laboratory (1988).
11. J. Delene, "Updated Comparisons of Economics of Fusion Reactors with Advanced Fission Reactors," submitted to Fusion Technology (in press).

14. SUMMARY AND CONCLUSIONS

14.1. Summary of SIRIUS-T Salient Features

- SIRIUS-T is a symmetrically illuminated direct drive ICF tritium production facility utilizing 92 beams of a 2 MJ KrF laser with a repetition rate of 10 Hz.
- The reactor design utilizes conservative target performance parameters.
- First wall protection is provided by 4 torr-m of xenon gas and actively cooled graphite tiles.
- The spherical reactor chamber has a 4 m inner radius which provides a comfortable margin of safety with respect to thermal stresses even for irradiated graphite.
- The structural material is the vanadium alloy V-3Ti-1Si, the breeding/cooling material is 90% ^{6}Li enriched Li and the neutron multiplier is Be.
- The optimized breeding blanket is 1 m thick and yields an overall tritium breeding ratio of 1.9 and an energy multiplication of 1.4.
- The containment building is spherical, 22 m in radius and shares the same vacuum environment as the reactor chamber.
- Biological shielding is provided by a 3.2 m thick reinforced concrete containment building wall providing a dose of 2.5 mr/h during reactor operation.
- The final focusing mirrors are mounted at a 20 m radius from the target and have an estimated lifetime of one full power year assuming that the damage recovery fraction by annealing is 85%.
- A lifetime of two full power years is projected for the graphite material in the first wall tiles based on presently available radiation damage data.
- A lifetime of three full power years is projected for the structure in the breeding blanket modules.
- Replacement of the breeding modules and the tiles occurs every two full power years to make it consistent with the lifetime of the graphite tiles.
- The structural frame, also of V-3Ti-1Si is designed to last the 30 full power year lifetime of the reactor.

- The conservatively designed structural frame minimizes deflection and facilitates module replacement even under the worst loading conditions. The mechanical stresses under those conditions are substantially below the design limit.
- The maximum steady state temperature of the V-3Ti-1Si backing of the first wall tiles is 687°C, the breeding blanket structure is 650°C and the Be <720°C.
- The annual SIRIUS-T tritium production at a 70% reactor availability is 33.3 kg/CY.
- The routine tritium release of <30 Ci/d meets acceptable environmental guidelines.
- The maximum accidental tritium release of <20 g does not call for emergency public evacuation according to NRC guidelines.
- The total capital costs in current 1990 dollars for an eight year construction period using conservative assumptions are:

  2,838 M$ (1990) at 5% interest rate

  3,465 M$ (1990) at 10% interest rate
- It is assumed that targets are purchased at 15¢/unit. Sensitivity analysis is performed varying the cost from 10-20¢/unit.
- The cost of T_2 production in current 1990 dollars using a reference 15¢/target is:

  9,100 $/g (1990) at 5% interest rate

  14,835 $/g (1990) at 10% interest rate

14.2. Major Conclusions

- The cost of T_2 production in SIRIUS-T is very competitive with other tritium production schemes under consideration. This conclusion must be qualified by the statement that ICF systems contain advanced technologies which will require considerable research and development as well as time (e.g. 10-20 years) to realize.
- The design shows that practical solutions do exist to the problem of integrating a large number of symmetrically distributed beams in a direct drive ICF reactor configuration.
- The scheme for breeding blanket replacement and maintenance of the final focusing mirrors is reasonable and practical.

- Replacement of blanket modules on a 2 FPY or a 3 FPY schedule has only ~2% impact on the cost of T_2.
- Varying the target cost between 10¢/unit to 20¢/unit has <8% impact on the cost of tritium.
- Driver efficiency above 5% has negligible impact on the cost of tritium. Below 5% efficiency, the cost of tritium rises exponentially because the reactor ceases to be electrically self-sufficient and electricity must be purchased.

14.3. Critical Issues in SIRIUS-T

- The area identified in which there is the least amount of confidence in the design is the survivability of the final focusing mirrors and the degree of recovery that might be expected by high temperature annealing.
- All the issues relating to the lifetime of the graphite in the tiles under the synergistic effects of radiation damage, repeated shock loading and cyclic thermal stresses should be investigated.
- Issues relating to the survival of a single shell target with no high Z coating during injection at 10 Hz are very important.